



(YIP 11) Concurrent Structural Fatigue Damage Prognosis Under Uncertainty

Yongming Liu
CLARKSON UNIVERSITY

04/30/2014
Final Report

DISTRIBUTION A: Distribution approved for public release.

Air Force Research Laboratory
AF Office Of Scientific Research (AFOSR)/ RTA
Arlington, Virginia 22203
Air Force Materiel Command

REPORT DOCUMENTATION PAGE				<i>Form Approved</i> OMB No. 0704-0188	
Public reporting burden for this collection of information is estimated to average 1 hour per response, including the time for reviewing instructions, searching existing data sources, gathering and maintaining the data needed, and completing and reviewing this collection of information. Send comments regarding this burden estimate or any other aspect of this collection of information, including suggestions for reducing this burden to Department of Defense, Washington Headquarters Services, Directorate for Information Operations and Reports (0704-0188), 1215 Jefferson Davis Highway, Suite 1204, Arlington, VA 22202-4302. Respondents should be aware that notwithstanding any other provision of law, no person shall be subject to any penalty for failing to comply with a collection of information if it does not display a currently valid OMB control number. PLEASE DO NOT RETURN YOUR FORM TO THE ABOVE ADDRESS.					
1. REPORT DATE (DD-MM-YYYY) XX-XX-2014		2. REPORT TYPE Final report		3. DATES COVERED (From - To) From April, 2011 to March, 2014	
4. TITLE AND SUBTITLE Concurrent structural fatigue damage prognosis under uncertainties				5a. CONTRACT NUMBER FA9550-11-1-0025	
				5b. GRANT NUMBER	
				5c. PROGRAM ELEMENT NUMBER	
6. AUTHOR(S) Liu, Yongming				5d. PROJECT NUMBER	
				5e. TASK NUMBER	
				5f. WORK UNIT NUMBER	
7. PERFORMING ORGANIZATION NAME(S) AND ADDRESS(ES) Clarkson University 8 Clarkson Avenue Potsdam, NY 13699-1401				8. PERFORMING ORGANIZATION REPORT NUMBER	
9. SPONSORING / MONITORING AGENCY NAME(S) AND ADDRESS(ES) Air Force Office of Scientific Research, Arlington, Va				10. SPONSOR/MONITOR'S ACRONYM(S) AFOSR	
				11. SPONSOR/MONITOR'S REPORT NUMBER(S)	
12. DISTRIBUTION / AVAILABILITY STATEMENT UU					
13. SUPPLEMENTARY NOTES					
14. ABSTRACT This project proposes a fundamentally different and innovative fatigue prognosis methodology based on a small time scale formulation is proposed for the real-time concurrent structural damage prognosis. The proposed novel damage model overcomes the inherent difficulties in existing fatigue theories. One of the most important benefits is that concurrent fatigue analysis across multiple spatial and temporal scales becomes feasible. Pervasive prognosis capability is addressed in this study, from material level up to structure level. Rigorous validation of model hypotheses and prediction will be performed using state-of-the-art experimental techniques, such as in-situ fatigue testing under scanning electron microscopy combined with digital image analysis. A special focus in the proposed study is on the systematic uncertainty modeling through multilevel computational simulations. Advanced reliability methods, Bayesian statistics and information theory are proposed to capture the stochastic nature of fatigue damage accumulation.					
15. SUBJECT TERMS					
16. SECURITY CLASSIFICATION OF:			17. LIMITATION OF ABSTRACT	18. NUMBER OF PAGES	19a. NAME OF RESPONSIBLE PERSON
a. REPORT	b. ABSTRACT	c. THIS PAGE			19b. TELEPHONE NUMBER (include area code)

Concurrent structural fatigue damage prognosis under uncertainties

Final report submitted to AFOSR

(Contract No. FA9550-11-1-0025, Project Manager: Dr. David Stargel)

Technical Contact: Yongming Liu, Principal Investigator
Arizona State University
Tempe, AZ 85287
Phone: 480-965-6883
Email: yongming.liu@asu.edu

Table of contents

Summary of Accomplishments.....	3
Accomplishment for Task 1.1	3
Accomplishment for Task 1.2 and Task 1.3	3
Accomplishments for Task 2.1.....	4
Accomplishments for Task 2.2.....	4
Accomplishments for Task 2.3.....	4
Publications generated from the project.....	4
Appendix 1: Accomplishments for Task 1.1	7
Appendix 2: Accomplishments for Task 1.1	35
Appendix 3: Accomplishments for Task 1.1	64
Appendix 4: Accomplishments for Task 1.2 &1.3	88
Appendix 5: Accomplishments for Task 2.1	127
Appendix 6: Accomplishments for Task 2.2	158
Appendix 7: Accomplishments for Task 2.2	180
Appendix 8: Accomplishments for Task 2.3	204

Summary of Accomplishments

(April 1, 2011 – March 31, 2014)

In the proposed concurrent structural fatigue damage prognosis framework, a general methodology for structural level prognosis has been investigated and developed in real time. Two main tasks have been proposed: Task 1 Concurrent structural fatigue damage prognosis framework and Task 2 Uncertainty modeling and probabilistic analysis. Each task includes several subtasks and detailed information is shown below.

Task 1.1 Small time scale fatigue formulation;

Task 1.2 Hierarchical coupled state-space model for concurrent analysis;

Task 1.3 Structural damage prognosis integrating sensor data;

Task 2.1 Rigorous uncertainty quantification;

Task 2.2 Efficient probabilistic damage prognosis;

Task 2.3 Reliability updating

All proposed tasks have been finished and deliverables have been submitted during the past years' progress report or are included in this final report.

Accomplishment for Task 1.1

Since the crack closure concept was introduced into the crack growth analysis, many fatigue crack growth models have been developed based on the crack closure hypotheses. Direct and comprehensive experimental observations of fatigue crack growth behavior at the very small scales is of great importance to verify the crack closure hypotheses and to investigate the underlying fatigue damage mechanism. In this report, the in-situ SEM experiments for Al 7075-T6 and steel 4340 specimens compared and very different phenomena are observed. It observed that significant crack closure is observed for aluminum alloys but not for steels. This strongly suggests that the very careful consideration must be taken for the different materials when the fatigue evaluation is performed. Novel in-situ SEM testing under both constant amplitude and variable amplitude loadings are investigated and details can be found in appendix 1- appendix 3.

Accomplishment for Task 1.2 and Task 1.3

Another major focus of the proposed project is to formulate a state-space framework for dynamics analysis and integration for sensor data. A new scheme for the dynamic load reconstruction and integration with the proposed time-based fatigue crack growth formulation is developed. The strain measurement from the sensors and finite element of the structure is used to estimate the dynamic stress response and is used for the fatigue crack growth analysis. The concurrent structural and material damage coupling can be solved. Details can be found in appendix 4.

Accomplishments for Task 2.1

Task 2.1 focuses on rigorous uncertainty quantification for probabilistic fatigue prognosis. An experimental study is proposed to investigate the uncertainty effect caused by random loading sequence on the fatigue crack growth behavior of Al 7075-T6. The testing matrix includes different overload cycle percentage, overload ratios, and deterministic and random loading sequences in the current investigation. The proposed experimental study suggests that extreme value distribution is a good approximation of fatigue life distribution. The effect of uncertain loading is different under different loading spectrums. Finally, all experimental observations are reported in table format in the appendix for future numerical model development and validation for interested readers. Details of this research progress can be found in Appendix 5.

Accomplishments for Task 2.2

Task 2.2 focuses on an efficient and accurate prediction methodology for the fatigue crack prognosis. First, a methodology based-on a subset simulation method using Bayesian principle has been proposed to evaluate the fatigue life at an arbitrary reliability level. An efficient sampling algorithm for fatigue life prediction is developed to find the corresponding fatigue life variable at a certain confidence level. Numerical examples using direct Monte Carlo simulation and the proposed inverse subset simulation method are compared for algorithm verification. Various experimental data for metallic materials are used for model prediction validation. Details are shown in Appendix 6.

An efficient equivalent stress transformation method is developed for the real time fatigue damage prognosis. The key idea is to match the fatigue life distribution of the time-by-time calculation with the equivalent constant stress amplitude fatigue crack growth curves. The inverse first-order reliability method (IFORM) is used solve the probabilistic life distribution without sampling. The proposed method is compared with existing methods and a significant computational efficiency is observed. Details of this research progress can be found in Appendix 7.

Accomplishments for Task 2.3

Bayesian updating is proposed to update the reliability estimation using continuous SHM or NDE observations. The focus on the proposed study is on the demonstration of the developed small time scale fatigue crack growth model for the prognosis. A demon problem is illustrated using plate specimen with embedded piezo sensor detection. Details can be found in Appendix 8.

Publications generated from the project

The project has generated several journal articles and peer-reviewed conference proceedings. They are listed below.

- Zhang, W. and Y. Liu (2012). "In situ SEM testing for crack closure investigation and virtual crack annealing model development." *International Journal of Fatigue* 43(0): 188-196.
- He, J., X. Guan, et al. (2012). "Structural response reconstruction based on empirical mode decomposition in time domain." *Mechanical Systems and Signal Processing* 28(0): 348-366.
- Lu, Z. and Y. Liu (2011). "Experimental investigation of random loading sequence effect on fatigue crack growth." *Materials & Design* 32(10): 4773-4785.
- Jian Yang, Wei Zhang, Yongming Liu, Existence and Insufficiency of the Crack Closure for Fatigue Crack Growth Analysis, *International Journal of Fatigue*, 2014, 62, 144 - 153
- He, J.; Guan, X. & Liu, Y. Structural response reconstruction based on empirical mode decomposition in time domain, *Mechanical Systems and Signal Processing* , 2012, 28, 348 – 366.
- He, J., Guan, et al. (2013). "Time domain strain and stress reconstruction for concurrent fatigue damage prognostics" *Mechanical Systems and Signal Processing* (under review)
- Xiang, Y., Liu, Y. An Equivalent Stress Transformation for Efficient Probabilistic Fatigue Crack Growth Analysis under Variable amplitude Loadings, *ASCE Journal of Aerospace Engineering*, 2013. (under review)
- Zhang, W. and Y. Liu . "Time-based subcycle fatigue crack growth modeling. Part I: analytical approximation for crack tip displacement", *International Journal of Fatigue*. (under preparation)
- Zhang, W. and Y. Liu . "Time-based subcycle fatigue crack growth modeling. Part II: crack growth simulation and validation", *International Journal of Fatigue*. (under preparation)
- Enqiang Lin, Hailong Chen, Yongming Liu, "atomistic simulations of fatigue crack growth in single crystal aluminum", *ASME 2013 International Mechanical Engineering Congress & Exposition*, San Diego, CA.
- Jian Yang, Wei Zhang, Yongming Liu, "Subcycle fatigue crack growth mechanism investigation for aluminum alloys and steels", *International Conference of Fracture*, 2013, Beijing, China.
- Jingjing He; Xuefei Guan; Yongming Liu, "Concurrent structural and material fatigue damage prognosis integrating sensor data", *AIAA SDM conference*, 2013, Boston, MA.
- Wei Zhang; Yongming Liu, "A time-based formulation for real-time fatigue damage prognosis under variable amplitude loadings", *AIAA SDM conference*, 2013, Boston, MA.
- Jian Yang; Wei Zhang; Yongming Liu, "Subcycle Fatigue Crack Growth Mechanism Investigation for Aluminum Alloys and Steels", *AIAA SDM conference*, 2013, Boston, MA.
- Wei Zhang, Yongming Liu, "Subcycle fatigue damage mechanism investigation using In-situ SEM testing", *ASME 2012 International Mechanical Engineering Congress & Exposition*, Houston, TX.
- H. Li, Y. Xiang, Y. Liu, "Probabilistic fatigue life prediction using Subset Simulation", *53rd Structures, Structural Dynamics, and Materials and Co-located Conferences*,

Honolulu, Hawaii , April, 2012.

- W. Zhang, Y. Liu, “In-situ fatigue testing on the existence and insufficiency of the crack closure”, International Conference on Fatigue Damage of Structural Materials IX, Hyannis, MA, USA, September, 2012.
- Jian yang, wei zhang, yongming liu, “A Multi-Resolution Experimental Methodology for Fatigue Mechanism Verification of Physics-Based Prognostics”, Annual Conference of the Prognostics and Health Management Society 2012. ISBN: 978-1-936263-05-9

Appendix 1: Accomplishments for Task 1.1

In-Situ SEM Testing for Crack Closure Investigation and Virtual

Crack Annealing Model Development

Wei Zhang, Yongming Liu*

Clarkson University, Potsdam, NY, 13699, USA

Abstract: In this report, an in-situ scanning electron microscope (SEM) fatigue testing is proposed to investigate the crack closure phenomenon within one cyclic loading under plane stress conditions. One objective of this experimental study is to verify the existence and significance of crack closure by directly measuring the variation of crack tip opening displacement (CTOD) and evaluating the crack opening stress levels. During the testing, the loading cycle is divided into a certain number of levels. At each level, high resolution images are taken around the crack tip region by SEM. Following this, imaging analysis is used to process these images in order to quantify the crack tip behavior at any time instants. Four constant amplitude loading cases with different stress ratios are investigated. Crack closure phenomenon is directly observed and measured. A simple mechanical model (named virtual crack annealing model) is developed based on the in-situ SEM testing observations. The calculated crack opening stress level is compared with experimental observations. A detailed discussion is given based on the current investigation to explain some well-known issues in the classical fatigue theory.

Keywords: crack closure, fatigue crack growth, in-situ SEM, virtual crack annealing

* Corresponding author, Tel.: 315-268-2341; Fax: 315-268-7985; Email: yliu@clarkson.edu

1. Introduction

Many approaches have been proposed to correlate the fatigue damage with the applied driving forces. The earliest effort can be traced back to Wholer [1] and Basquin [2,3], who correlated the applied stress ranges with the final failure life of non-precracked specimens. In 1960's, a significant contribution was made by Paris [4], who proposed to correlate the fatigue crack growth rate per cycle to the applied stress intensity factor range. The Paris' model becomes the most widely-used fracture mechanics-based method for fatigue life prediction. Many modifications of the Paris' model have been proposed in the open literature. One of the most important modifications is the inclusion of the crack closure concept, which was first introduced into the crack growth analysis by Elber [5]. Elber [5] pointed out that fatigue cracks remain closed during part of the loading process and proposed an effective stress intensity factor range to account for the crack closure effect. Many related studies have been done on the crack closure using experimental investigation, numerical analysis as well as theoretical studies [6-15]. Budiansky and Hutchinson [6] estimated the plasticity-induced crack closure in small-scale yielding conditions using theoretical analysis under constant cyclic loadings. Newman [11,12] analyzed the crack closure problems using a strip yield model and numerical simulations.

Crack closure has long been an argument in the fatigue community. Some studies strongly support the crack closure effect on the fatigue crack growth [6,14,16]. There are several studies that indicate the non-existence or negligibility of the crack closure [17-21]. Sadananda and Vasudevan stated [17] that the plasticity-induced

closure is negligible in the plane strain condition. Zhang and Meng [18] observed that faster small crack growth rates are attributed to stronger crack tip plasticity around the small crack tips rather to the fatigue crack closure. Kujawski [19] shown that the plasticity-induced closure is not observed. Riemelmoser and Pippan [20] and Davidson [21] found that roughness induced closure cannot be observed. Bowman et al. [22] showed that the "roughness induced closure" disappears when the alignment of the test system is such that known linear systems produce reproducible and linear load-displacement records even when the specimen is flipped about horizontal and vertical axes. Additionally, it should be noted that the ASTM round robin problem on crack closure measurement failed to produce laboratory-independent results.

The experimental determinations of crack closure are commonly based on load-displacement measurements. Crack closure, if it exists, will affect the crack tip stress field and the compliance of the specimen. As reviewed by James et al. [23], the compliance-based crack closure measurement is not reliable due to many reasons. For example, the alignment of the specimen will affect the crack closure measurement. Many alternative techniques are proposed to measure the crack contact [23], such as ultrasonic diffraction [24], potential drop [25,26], X-ray computed tomography [26]. The proposed study uses scanning electron microscopy to directly observe the crack contact.

There are very few studies about direct observations and measurements of the crack closure within one loading cycle. Some researches use in-situ SEM testing to study crack closure of the small fatigue cracks [18,28] and long crack growth

behavior [29]. Most of in-situ testing methodologies focus on the observation of crack growth and tip deformation between different cycles, for example, between ten thousand and hundred thousand cycles. Detailed investigations of the crack growth kinetics during a single loading cycle are rarely found in the open literature. Zhang and Liu [30] proposed a novel in-situ SEM fatigue testing to investigate the fatigue crack growth mechanisms within a single cyclic loading in the plane stress condition. In [30], the crack opening stress level was directly measured and it was shown that crack closure (or crack opening stress) had a direct relationship with the starting point of the crack growth. Only one stress ratio ($R=0.1$) was performed. In this report, the main objective of the experimental study is to verify the existence and significance of crack closure by measuring CTOD variation directly under constant amplitude loadings with different R ratios. Based on the experimental observations, a new virtual crack annealing (VCA) model is proposed to predict the crack opening stress level analytically. The proposed model is validated using experimental observation of crack opening stress under different R ratios.

The report is organized as follows. First, the in-situ fatigue testing procedure in SEM and experimental results are presented. The measurements of the crack opening stress level and the crack tip deformation behavior are discussed in detail. Next, a new virtual crack annealing model is developed and validated with our experimental observations. Following this, several well-known issues in fatigue crack growth analysis are discussed according to the new observations from the proposed

experimental study. Finally, some conclusions and future work are given based on the current investigation.

2. In-situ SEM experiments and observations

2.1 Experimental set-up

An in-situ SEM fatigue testing is performed to achieve the high resolution investigation for the hypothesis verification of crack growth kinetics and crack deformation in the vicinity of the crack tip. Some details of the experimental set-up for the in-situ SEM experiment are shown in Fig. 1. It consists of a palm-sized tensile stage installed in a field emission SEM (JEOL-7400F). The tensile stage is manufactured by Ernest F. Fullam Inc., which is now merged to MTI Instruments Inc.. The maximum gage length between mechanical grips is about 27 mm, and the load capacity is 5 kN. The sub-stage is fixed in the SEM and the cyclic loading is applied during the experiment. During the testing, the vacuum level is remained to be less than 9.3×10^{-5} MPa (gage reading). Multiple resolution images are recorded during the testing for the measurements of crack length and the crack tip deformation behavior. Since the stage will prevent the coupon from getting closer to the pole piece, the shortest working distance available is 16.5 mm.

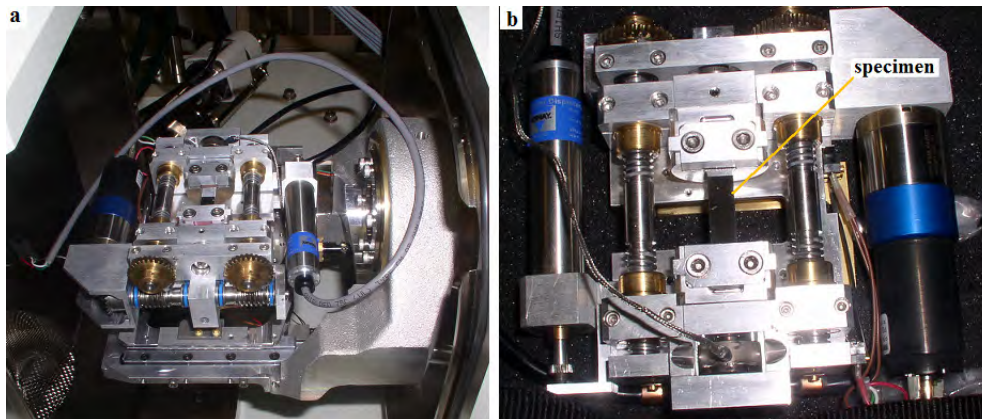


Fig. 1 In-situ SEM fatigue testing setup a) loading stage installed in SEM ;b) specimen installed in loading stage;

2.2 Specimen design

Single edge notched plate specimens with width $W = 8$ mm, length $L = 52$ mm and thickness $T = 0.86$ mm made of aluminum alloy sheet (Al7075-T6) were tested. Due to the small thickness of specimens, it is assumed to be under the plane stress conditions for a relatively long crack. The specimen design is shown in Fig. 2. An edge notch of length 1mm is machined on the specimen. After machining, the specimens are pre-cracked using a hydraulic testing machine INSTRON 1331 until the initial crack reaches about 1 mm. The pre-cracking procedure follows the ASTM standard E647-08. Following this, both surfaces of the specimen are polished with the sandpaper whose average particle diameter is smaller than 10 μm . The final polishing is done using a vibration polishing machine with 1~3 μm polishing suspension. The mechanical properties and the chemical composition of the investigated material are given in Table 1 and Table 2 respectively, which are reported by the manufacturer.

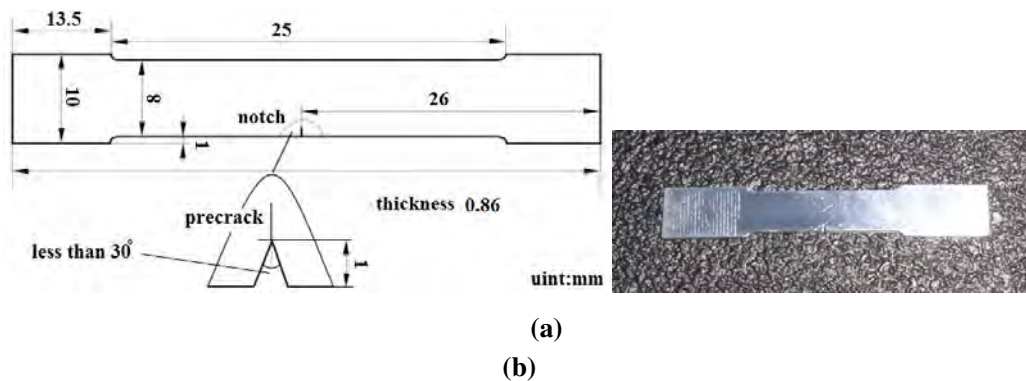


Fig. 2. Geometry of test specimen (a) the specimen design; (b) polished specimen.

Table. 1 7075-T6 mechanical properties

Ultimate tensile strength	573~582 MPa
Tensile yield strength	502~516 MPa
Young's Modulus	71.7 GPa

Table. 2 Chemical composition of 7075-T6

	Si	Fe	Cu	Mn	Mg	Cr	Zn	Ti	V	Zr	Other	Max
Min % weight	0.00	0.00	1.2	0.00	2.1	0.18	5.1	0.00	0.00	0.00	Each	0.05
Max % weight	0.4	0.50	2.0	0.30	2.9	0.28	6.1	0.20	0.05	0.05	TOT	0.15

2.3 Experimental procedure

The specimen is loaded in the tensile stage under cyclic loading and observed in-situ under SEM. The K calculation is based on the solution for clamped ended specimen [31,32]. In this report, the stress ratios of the applied constant amplitude loading are 0.05, 0.1, 0.33, and 0.5, respectively. The measurements are usually after 50 to 100 cycles loading in SEM to ensure the crack growth is stable. During the testing, one loading cycle is divided into many steps, shown as Fig. 3. The applied loading increases/decreases at a very slow rate. During the loading/unloading path the stage will hold at each step (shown as rectangle points) for investigation.

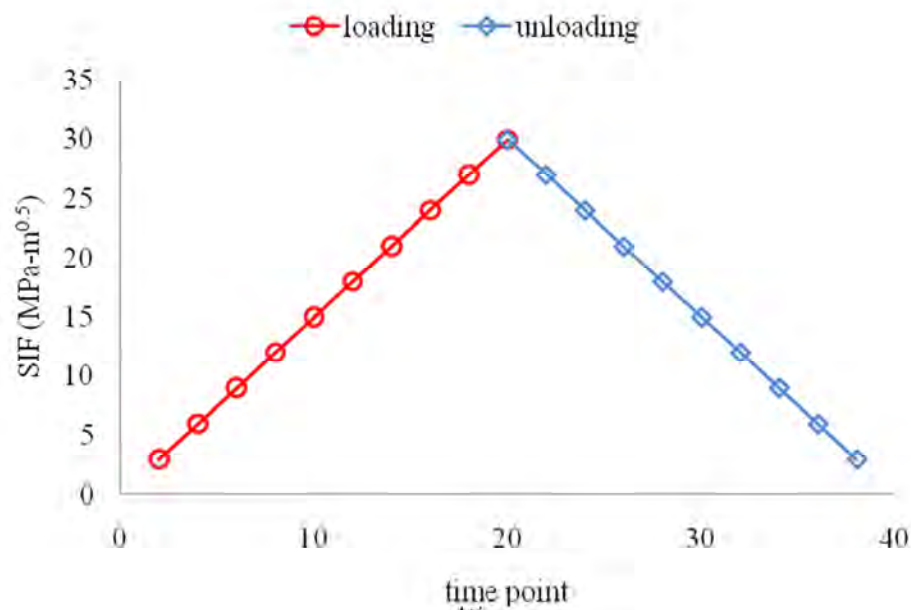


Fig. 3 Schematic representation of imaging recording points in complete loading cycles

At each loading level, images of the crack tip are taken under very high magnification. Imaging analysis and measurements are performed for the crack tip opening displacement (CTOD) which is directly related to crack opening stress level. Reference points on the crack surface in the minimum loading image are selected and the CTOD in other images are quantified by measuring the distance between the two crack faces in the position of the original crack tip. This procedure is repeated for all images recorded during the in-situ testing and the crack opening stress level can be evaluated [30]. An illustration of this procedure is shown in Fig. 4, where $R=0.025$. Figs. 4.1-5.15 show the selected images from the minimum loading to the maximum loading. Only 15 images are selected and are shown here to save the space. In Fig. 4.1, the horizontal arrows indicate the direction of applied loading. It is clearly seen that the crack growth is accompanied with the CTOD increments. Several interesting things are observed from these images. First, crack closure is directly observed from images. There are no obvious CTOD increments during Fig. 4.1 to Fig. 4.4 although the loading increases to about 30% of the maximum loading. After that, the crack tip starts to open and the CTOD gradually increases, as shown in Fig. 4.5~4.9. Then, a significant crack blunting phenomenon is observed at the later stage of the loading (see Figs. 4.10-4.15 where the applied loading is close to the maximum loading)

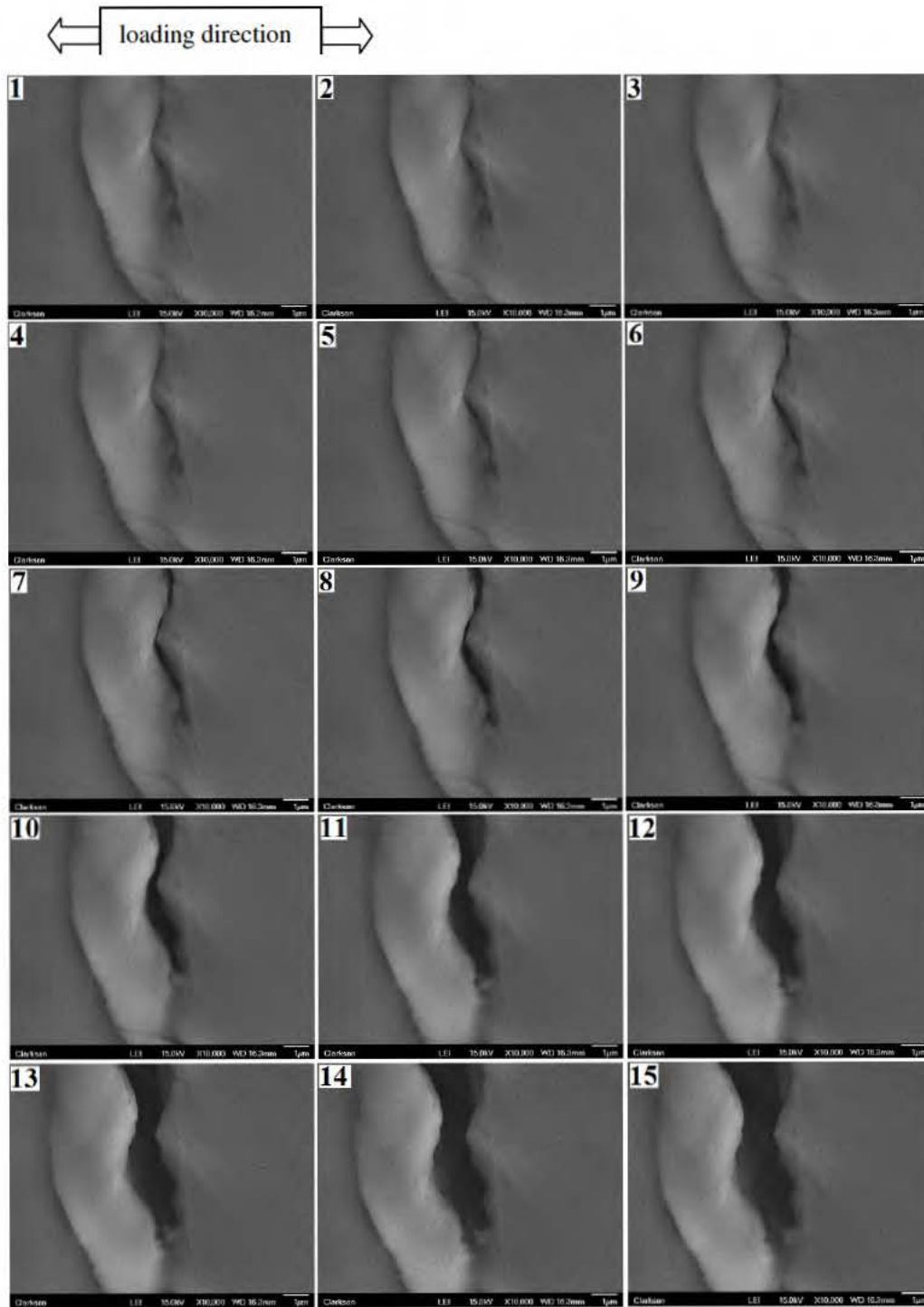


Fig. 4. Illustration of crack CTOD measurements, $R=0.025$, $K=0.7$, 4.4, 5.8, 8.0, 9.5, 10.9, 12.4, 13.9, 15.3, 16.0, 20.4, 21.9, 23.3, 24.8, and 26.3 $\text{MPa}\cdot\text{m}^{0.5}$ for Figs. 4.1 to 4.15, respectively (magnification 10,000)

The above example visually validates the crack closure hypotheses for a low R ratio case. Similarly, an illustration of a high R ratio case is shown in Figs. 5, where $R=0.5$. Figs. 5.1-5.6 also show the images from the minimum loading to the maximum

loading. It is clear that the crack tip remains closed (shown in Fig. 5.1-5.3) until the applied load reaches 67% of the maximum loading (shown in Fig. 5.4). Similar observations with other maximum loading levels and R ratios are also observed in other specimen testing's. Details and quantitative measurements will be discussed in the following sections.

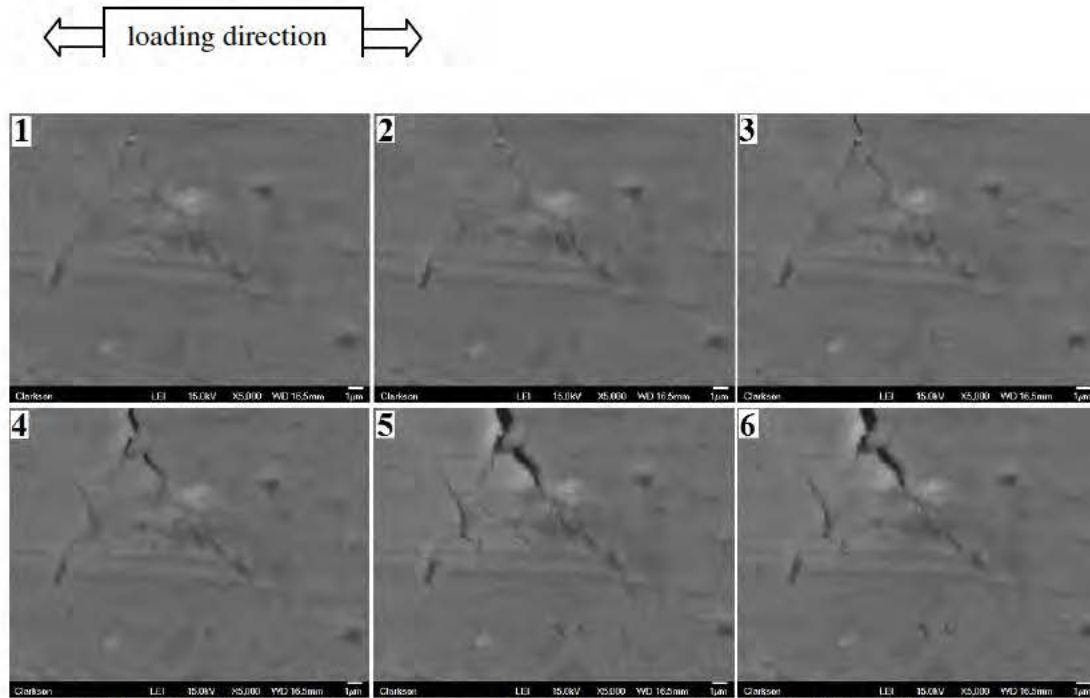


Fig. 5. Illustration of crack closure with high R ratio, $R=0.5$, $K=10.4, 12.5, 13.8, 16.6, 19.1$, and $20.8 \text{ MPa-m}^{0.5}$ for Figs. 5.1 to 5.6, respectively (magnification 5,000)

2.4 Experimental results and analysis

The above discussion is based on images to see the crack closure phenomenon qualitatively. In this section, quantitatively measurement of CTOD variation is shown for the post-testing data analysis. CTOD measurements with different R ratios are plotted in Figs. 6-9. The x -axis is the applied stress intensity factor. Y -axis is the measured CTOD variation corresponding to the applied loading level. Multiple

measurements are performed to verify the observed phenomenon are not random and to minimize the measurement errors. In Fig. 6, different shapes of data points represent the loading paths of different loading cycles. It is shown that the crack tip starts to open when the SIF exceeds a certain loading level (crack opening stress level). After that, the CTOD increases as the loading increases. During the unloading path, the crack tip will be closed when the loading decreases less than a certain level (crack closing stress level). The crack opening stress level is slightly larger than crack closing stress level. Because the crack growth only takes place in the loading path [30], only the CTOD in the loading path and crack opening stress level is studied here. From Figs. 6-9, the crack open stress level for each R ratio can be evaluated using linear interpolation. It should be noted that the y-scales in Figs. 6-7 and in Figs. 8-9 are different due to very different CTOD observations. In this report, the normalized crack opening stress is used, which is the ratio between the crack opening stress level to the corresponding maximum loading. The mean values are reported as shown in Table. 3. As the R ratio increases, the crack opening stress will increase.

Table. 3 crack opening stress ratios

R ratio	0.025	0.1	0.33	0.5
crack opening stress ratio	0.32	0.45	0.56	0.67

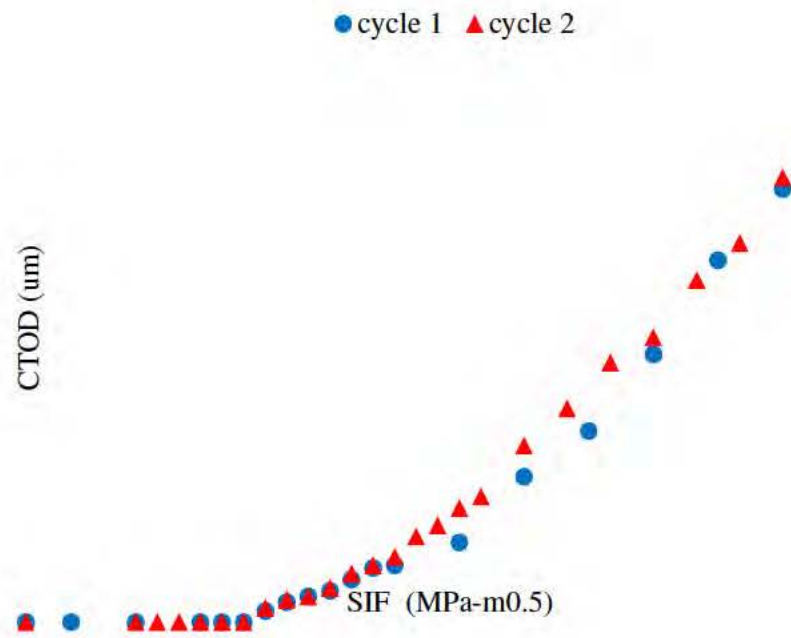
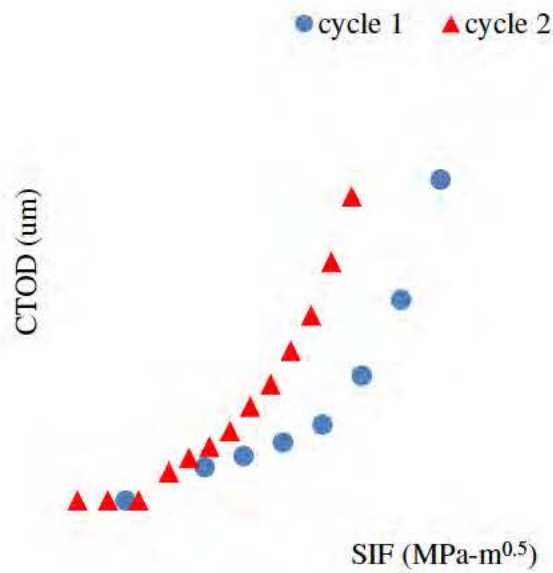


Fig. 6. CTOD measurement for complete cycle(R = 0.025)



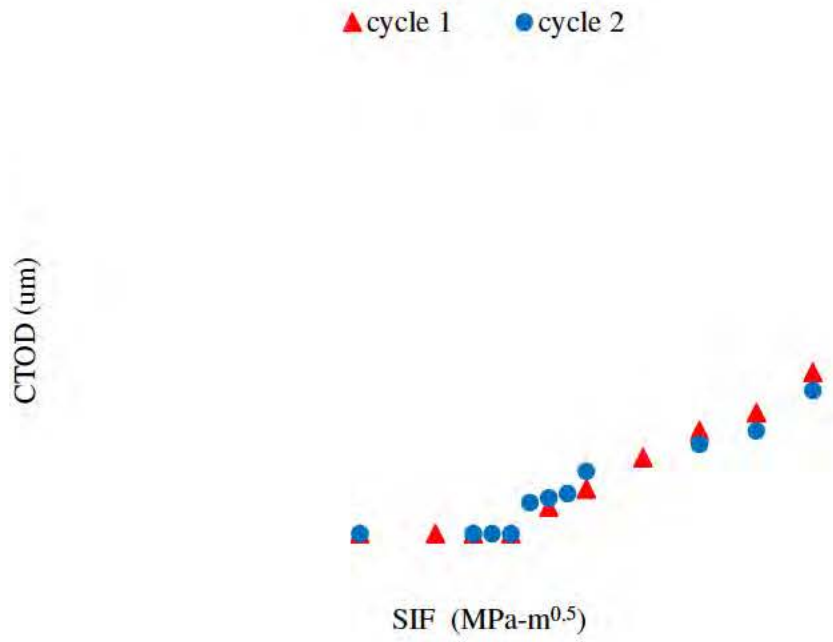


Fig. 8. CTOD measurement (R = 0.33)

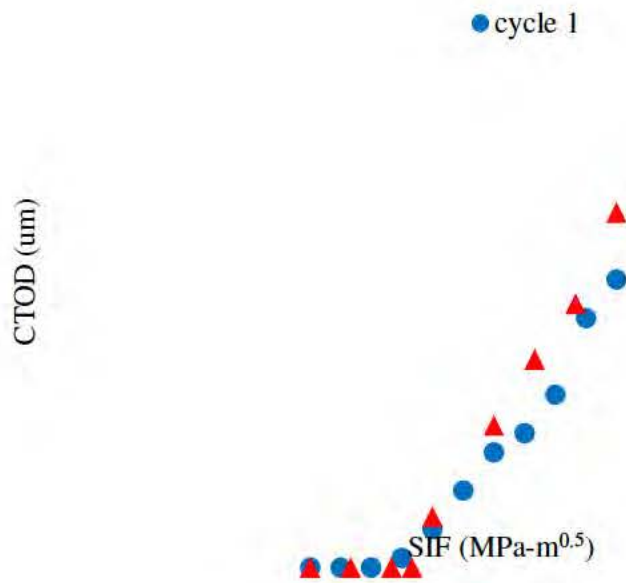


Fig. 9. CTOD measurement (R = 0.5)

All crack tip opening displacement (CTOD) measurements are plotted against the K_{eff} in Fig. 10. K_{eff} is defined as the difference of the current K level and the opening K level. In Fig. 10, it can be observed that some differences can be seen under different loading conditions. The curves under $R=0.025$ and $R=0.5$ are very similar. The other two curves under $R=0.1$ and $R=0.33$ are different. This observation could be caused by at least two reasons. First, the local material properties ahead of the crack tip may be different due to Inconsistencies in the aluminum specimen used. Second, the CTOD range may not be uniquely determined by the effective ΔK and is also related to the maximum K in the previous loading history. Detailed investigation is required to draw a consistent conclusion using more specimens and statistical analysis.

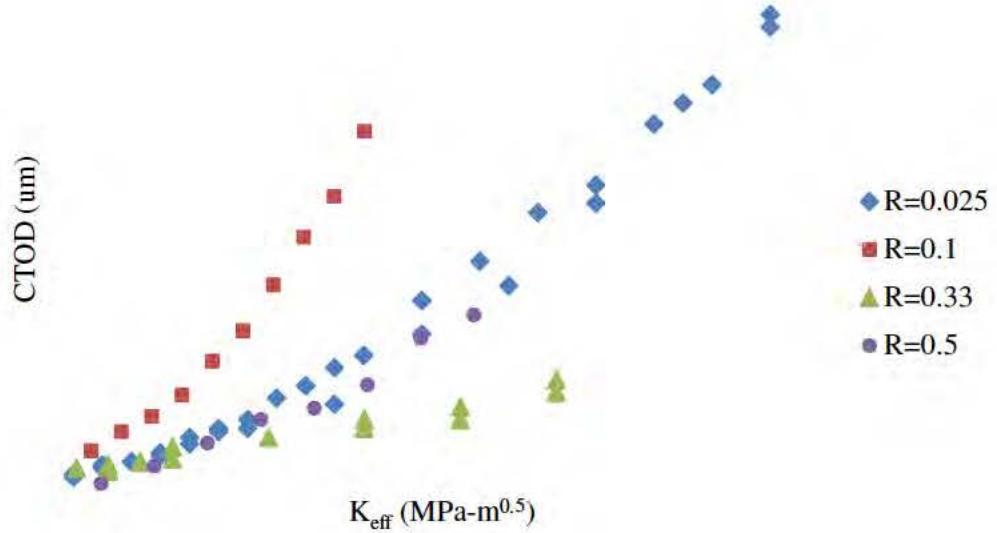


Fig. 10. CTOD vs. K_{eff} under different stress ratios

3. Virtual crack annealing model for crack closure calculation

The crack closure calculation is usually not very easy since it involves the highly nonlinear analysis of cyclic plasticity and contact analysis. Several studies have used finite element method to track the crack closure variation [33-35]. A simplified one dimensional spring model proposed by Newman [36] is the most commonly used one since it reduces computational cost significantly compared to the true 3D FEM analysis. Even with the simplified spring model, the direct tracking of crack closure at any time instant during a variable amplitude loading is not possible and the crack closure analysis is only performed during a certain time period for the computational efficiency. A simple analytical crack closure solution is proposed in this report to avoid the complex contact analysis of crack closure. This approximation is inspired from the in-situ SEM testing that the crack surfaces behind the crack tip fully closed during the cyclic loading. When the crack is fully closed, it appears no differences compared to the non-fractured material. In other words, the crack seems to be “annealed” when closed. One assumption in the proposed analytical solution is the crack “annealing” happens once it is fully closed. This assumption avoids the contact analysis and the fracture surface can be removed. Another assumption is the validity of the Dugdale model, where it assumes the small scale yielding conditions and the superposition principle can be used. The Dugdale model assumes the low strain hardening and is used in the current work. This represents a first-order approximation and additional hardening correction factor can be used. In a previous study [30], the experimental results showed that the material hardening effect is not large and the low

strain hardening is assumed in the current study.

The proposed approximation model is named as Virtual Crack Annealing (VCA) model since it assumes that the overlapped length of crack closure is annealed and acts as virgin materials. The basic principles of fracture mechanics can still be applied to the artificially annealed crack. In order to illustrate the basic idea of this model a schematic illustration is shown in Fig. 11. A real crack after the unloading is shown first. The crack length is a and the crack closure length is d . Ahead of the crack tip, there is a reversed plastic zone with compressive residual stress. In the crack closure zone, the compressive residual stress transfers through the contact surface. Using the assumption of crack annealing, a virtual crack can be assumed to have the length of $(a-d)$ and the reversed plastic zone size will be (d_r+d) . The real crack and the annealed virtual crack are equivalent in the sense that they have the same length of compressive residual stress zone. For the virtual crack, the reloading will cause the crack tip compressive residual stress to be reversed. When the residual stress within the distance d ahead of the virtual crack becomes zero, the crack is fully open. In order to simulate this, the superposition principle is used, which uses the second assumption for the small scale yielding.

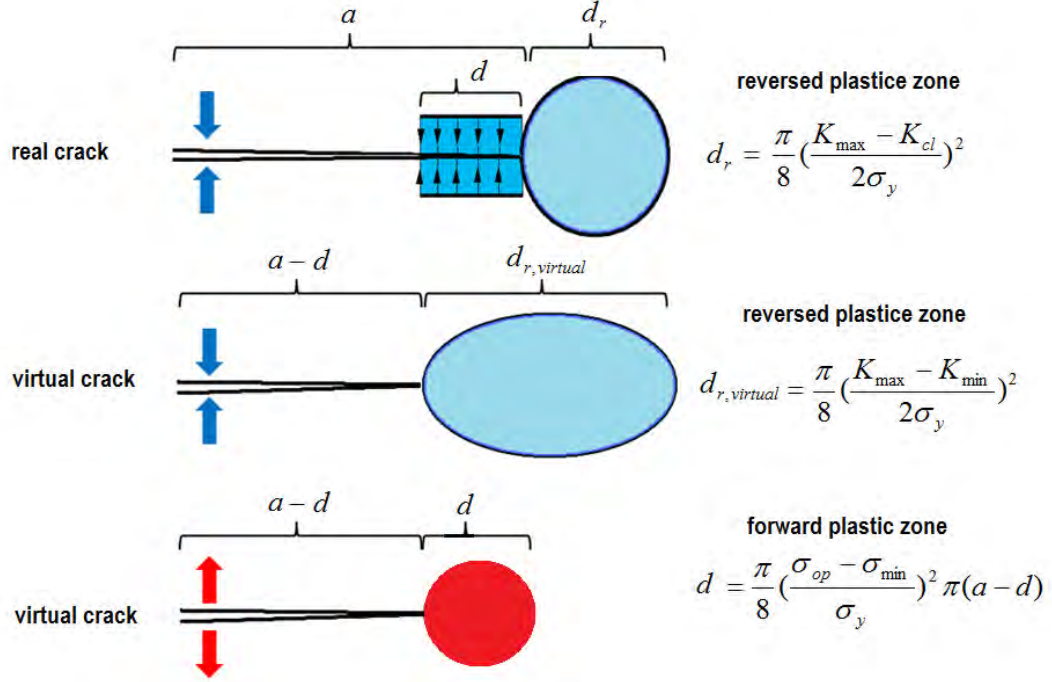


Fig. 11. Schematic illustration of real crack and virtual crack model

For the ease of discussion, a crack under constant amplitude loading is discussed first. If the crack is unloaded from its current maximum loading, the crack remains open initially. The reversed plastic zone and the CTOD change until the crack closure happens. If crack closure happens, the CTOD remains the same and the reversed plastic zone size ahead of the crack tip stops increasing. The CTOD and reversed plastic zone can be expressed as [37]

$$\delta = \begin{cases} \delta_{\max} - \frac{(K_{\max} - K)^2}{2E\sigma_y} = \delta_{\max} - \frac{\lambda}{2} (\sigma_{\max} - \sigma)^2 a & K \geq K_{cl} \\ \delta_{\max} - \frac{(K_{\max} - K_{cl})^2}{2E\sigma_y} = \delta_{\max} - \frac{\lambda}{2} (\sigma_{\max} - \sigma_{cl})^2 a & K < K_{cl} \end{cases} \quad (4)$$

where K_{cl} and σ_{cl} are the SIF and stress level at the crack closure, respectively.

Similarly, the reverse plastic zone considering crack closure can be expressed as

$$d_r = \begin{cases} \frac{\pi}{8} \left(\frac{K_{\max} - K}{2\sigma_y} \right)^2 & K \geq K_{cl} \\ \frac{\pi}{8} \left(\frac{K_{\max} - K_{cl}}{2\sigma_y} \right)^2 & K < K_{cl} \end{cases} \quad (5)$$

The above discussion is for the real crack with crack closure. If the virtual crack with length of $(a-d)$ is under the same loading conditions, classical fracture mechanics can be used to calculate the CTOD and plastic zone since no crack surface contact occurs for the virtual crack. As shown in Fig. 10, the overlapped length d can be estimated as

$$\begin{aligned} d = d_{r,virtual} - d_r &= \frac{\pi}{8} \left(\frac{K_{\max} - K_{\min}}{2\sigma_y} \right)^2 - \frac{\pi}{8} \left(\frac{K_{\max} - K_{cl}}{2\sigma_y} \right)^2 \\ &= \frac{\pi}{8} \left(\frac{\sigma_{\max} - \sigma_{\min}}{2\sigma_y} \right)^2 \pi(a-d) - \frac{\pi}{8} \left(\frac{\sigma_{\max} - \sigma_{cl}}{2\sigma_y} \right)^2 \pi(a) \end{aligned} \quad (6)$$

In the above equation, the plastic zone size for the virtual crack is calculated from classical fracture mechanics. If the virtual crack is under reloading from the minimum stress, the overlapped length will gradually reduce until a certain stress level (σ_{op}). Below the opening stress level, the CTOD at the real crack tip will remain constant since the crack is not fully open. Above the crack opening level, the crack behaves like a regular crack. The CTOD variation during the reloading path considering crack closure can be expressed as

$$\delta = \begin{cases} \delta_{\min} + \frac{(K - K_{op})^2}{2E\sigma_y} = \delta_{\min} + \frac{\lambda}{2} (\sigma - \sigma_{op})^2 a & K \geq K_{op} \\ \delta_{\min} & K < K_{cl} \end{cases} \quad (7)$$

Now the issue comes to how to calculate the crack opening and closure stress level. Consider the virtual crack with length $(a-d)$ under the reloading. The stress at the overlapped length will change from $-\sigma_y$ at the fully closure to zero at the fully open

stage. If the Dugdale model concept can be still used, the forward plastic zone of the virtual crack at the opening stress will equal to the overlapped length (i.e., make the crack fully open, see Fig. 10) and can be expressed as

$$d = \frac{\pi}{8} \left(\frac{K_{op} - K_{min}}{\sigma_y} \right)^2 = \frac{\pi}{8} \left(\frac{\sigma_{op} - \sigma_{min}}{\sigma_y} \right)^2 \pi(a - d) \quad (8)$$

In the current in-situ SEM testing, it is shown that the crack opening closure stress is similar or slightly larger than the crack opening stress level. As a first order approximation, the identical value of opening stress and closure stress in one loading cycle is assumed. Under this hypothesis, analytical approximation of crack opening stress can be obtained by combining Eq. (8) and Eq. (6).

$$\frac{\pi}{8} \left(\frac{\sigma_{max} - \sigma_{min}}{2\sigma_y} \right)^2 \pi(a - d) - \frac{\pi}{8} \left(\frac{\sigma_{max} - \sigma_{op}}{2\sigma_y} \right)^2 \pi(a) = \frac{\pi}{8} \left(\frac{\sigma_{op} - \sigma_{min}}{\sigma_y} \right)^2 \pi(a - d) \quad (9)$$

Eq. (9) assumes the material has elastic perfect plastic material properties. For most engineering materials, strain hardening happens and makes the problem more complex. If the kinematic hardening is assumed for the investigated material, Eq. (9) is modified as

$$\frac{\pi}{8} \left(\frac{\sigma_{max} - \sigma_{min}}{2\sigma_y} \right)^2 \pi(a - d) - \frac{\pi}{8} \left(\frac{\sigma_{max} - \sigma_{op}}{2\sigma_y} \right)^2 \pi(a) = \frac{\pi}{8} \left(\frac{\sigma_{op} - \sigma_{min}}{\sigma_y / \eta} \right)^2 \pi(a - d) \quad (10)$$

where η is the material hardening factor. If hardening happens, η should be larger than 1. For materials without significant hardening, 1 is a good estimate.

If the crack overlapping length is very small compared with the true crack length (i.e., $d \ll a$), its effect on the SIF calculation can be ignored. Eq. (10) can be rewritten as

$$(1 + 4\eta^2)\sigma_{op}^2 - (8\eta^2\sigma_{min} + 2\sigma_{max})\sigma_{op} + (4\eta^2\sigma_{min}^2 + 2\sigma_{max}\sigma_{min} - \sigma_{min}^2) = 0 \quad (11)$$

Eq. (11) is the general solution using the virtual crack annealing model for the crack opening stress calculation under constant amplitude loadings. If the material has no significant hardening (i.e., $\eta = 1$), Eq. (11) can be further simplified as

$$(\sigma_{op} - \sigma_{min})(5\sigma_{op} - 2\sigma_{max} - 3\sigma_{min}) = 0 \quad (12)$$

It is interesting to see that Eq. (12) gives two possible solutions for the opening stress level under the proposed virtual crack annealing model. One solution is $\sigma_{op} = \sigma_{min}$, which indicates that there is no crack closure and the overlapped length is zero. Another solution is $\sigma_{op} = \frac{1}{5}(2\sigma_{max} + 3\sigma_{min})$. This observation indicates that either there is no crack closure or a unique crack closure level under constant amplitude loadings. A discussion of this solution will be given later in this report by comparing with other analytical solutions and experimental data.

4. Discussions

The crack closure has been a long time argument in the fatigue research. Most of existing cracks closure measurements are based on the compliance measurements during the cyclic loading, which is an indirect experimental validation of the crack closure hypothesis. The crack closure is directly observed in the in-situ SEM testing in the proposed experimental study. Data analysis shows that crack only opens after a certain stress level. It also confirms that crack only grows after the crack is fully open, which is one of the major hypotheses originally proposed by Elber. The hysteresis loop of the CTOD variation confirms the analytical predictions using the crack closure assumptions [6]. All these direct observations confirm the validity of crack closure.

Paris, Tada and Donald [38] proposed a new concept of partial crack closure model. They stated that a significant contribution to fatigue damage may occur in the load range below the opening load, P_{op} , as measured by the compliance method. It is assumed that the interference between crack faces at a small distance behind the crack tip only partially shields the crack tip from fatigue damage. According to the partial crack closure model, the crack surfaces contact each other at a distance behind the tip, but not immediately behind the tip. In Fig. 12, the partial crack closure model is schematically shown. It shows that two added shadowed layer of material inserted into a smooth crack to model the interference caused by roughness. The very vicinity behind the crack tip remains open and only a partial crack closure happens during the loading. Fig. 12(a) shows the crack under the minimum loading and the Fig. 12(b) represent crack tip under the crack opening stress.

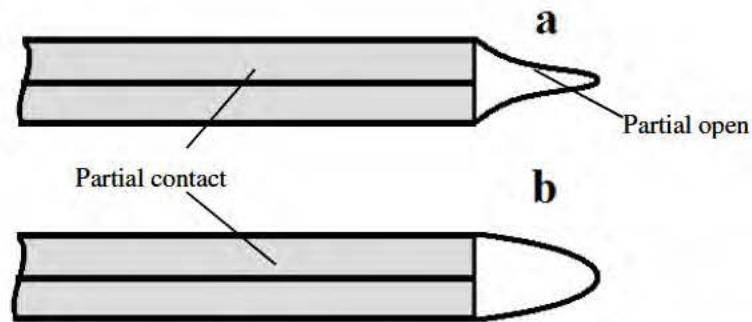


Fig. 12. Schematic illustration of the “partial crack closure model” (a) with the crack closed at minimum load; (b) with opening load applied.

The proposed in-situ SEM testing results does not support the partial crack closure hypotheses. As shown in Fig. 13, the closing process of the crack tip during unloading is shown for one specimen. In these figures, the white arrows indicate

loading direction and the loading decreases from maximum (Fig. 13.1) to minimum (Fig. 13.6). It can be seen that the crack surfaces contact each other immediately behind the tip. In other words, the crack tip is fully closed in Figs. 13.5-13.6. This indicates that the partial closure model is not correct for the Al-7075-T6 material in the current investigation.

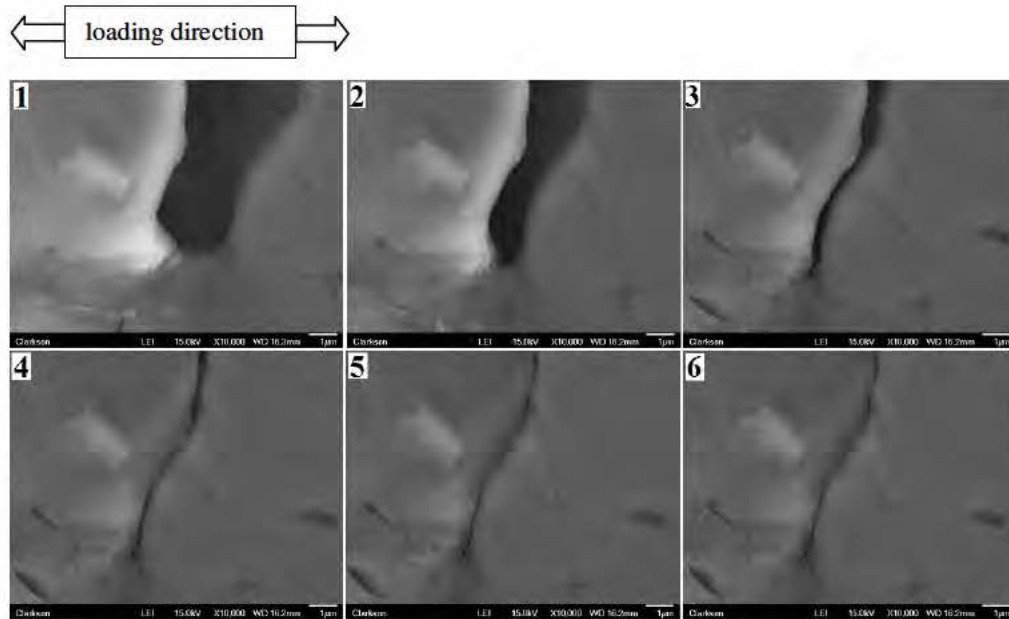


Fig. 13. Illustration of crack closing process (magnification 10,000)

Fig. 14 shows the loading process of the same crack. During the loading process, the crack surfaces immediately behind the crack tip will open first in Fig. 14.3. Following this, the crack tip will finally open as shown in Figs. 14.4- 14.9. This phenomenon is also against the partial closure model hypotheses.

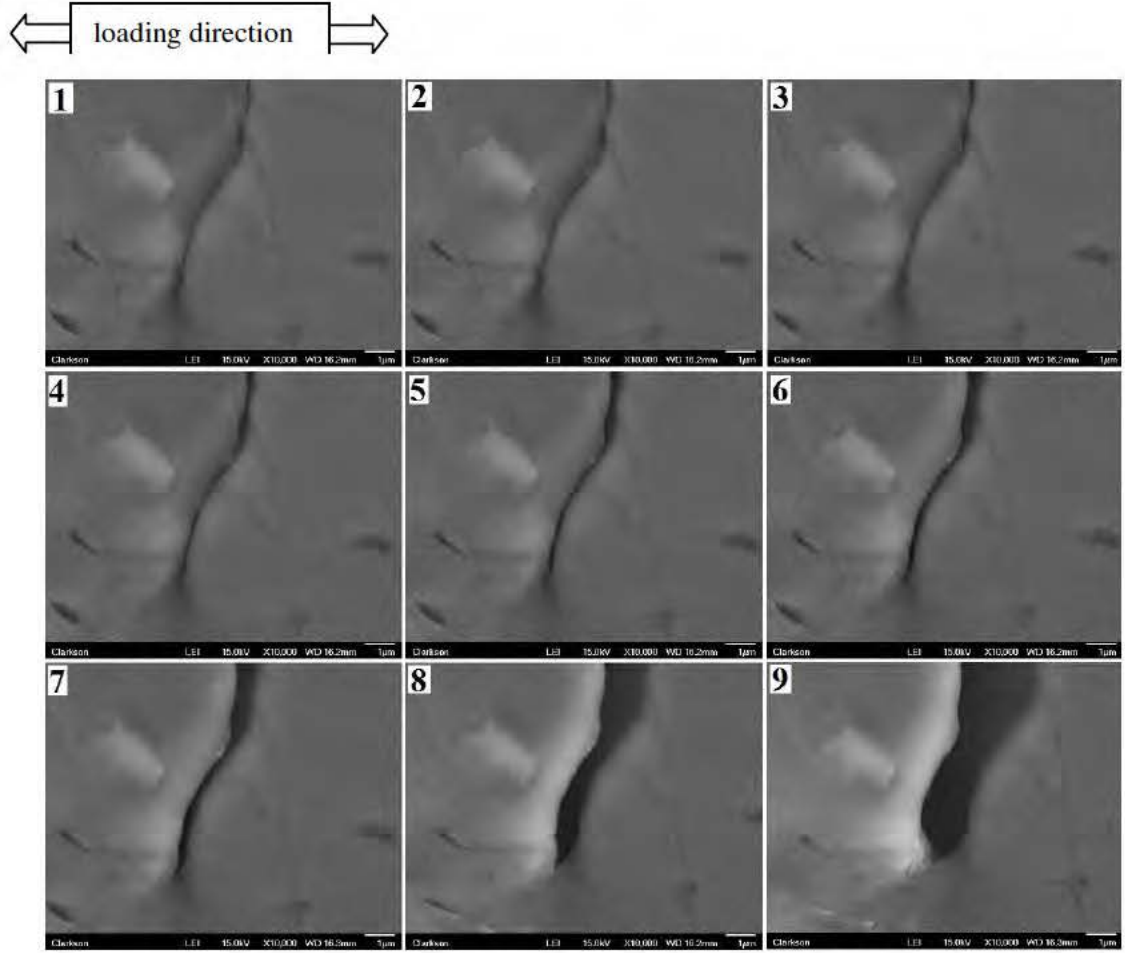


Fig. 14. Illustration of crack opening process (magnification 10,000)

Another discussion shown here is on the crack opening stress calculation. There are many studies available in the literature for the calculation of crack opening stress levels. Among them, the model proposed by Newman [39] is most widely used. Under constant amplitude loadings, the crack opening stress for the plane stress can be expressed as

$$\sigma_{op} / \sigma_{\max} = K_{op} / K_{\max} = 0.535 + 0.069R + 0.139R^2 + 0.257R^3 \quad (12)$$

where $\sigma_{\max} / \sigma_0 \approx 0.2$ and σ_0 is the flow stress of the material.

In the current experimental study, the specimen thickness is very small and the plane stress condition is assumed. The crack opening stress level predicted using the

Newman's model, the proposed virtual crack annealing model (with hardening factor of 1.1), and in-situ SEM testing results are shown in Fig. 15. It is shown that both models give similar estimation at high R ratios. For low R ratios (e.g., $R < 0.4$) the predictions are different. The testing results are in good agreement with the proposed model predictions. In the current investigation, the predictions using Newman's model overestimates the crack opening stress at low R ratios. It should be noted that the constraint factor in Newman's model is taken as 1 for plane stress conditions.

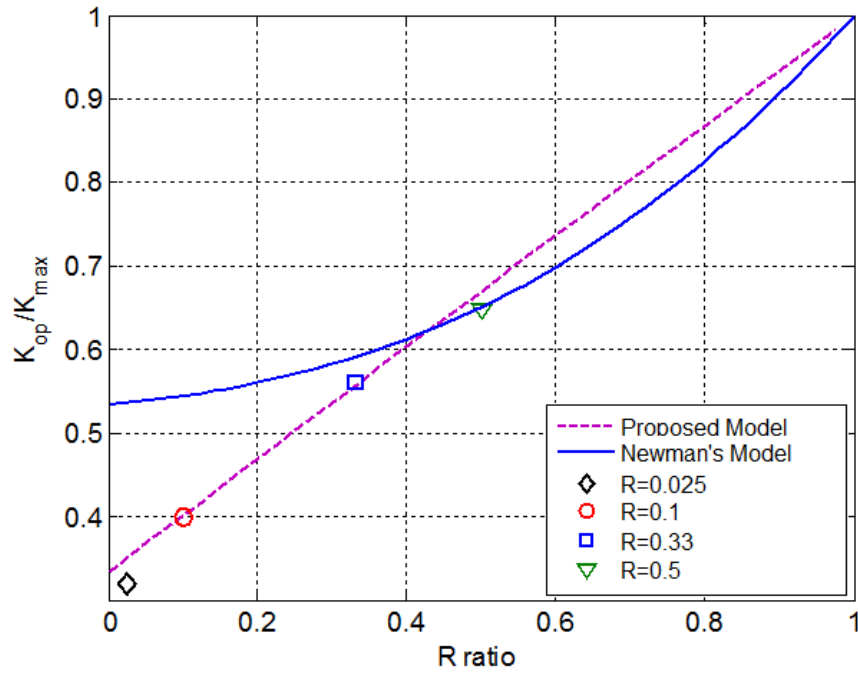


Fig. 15. Comparison of experimental measured crack opening stress with model predictions

5. Conclusions and future work

An innovative experimental methodology using in-situ SEM testing and imaging analysis is proposed in this study. Experimental testing is performed under four different R ratios for the hypotheses verification of the crack closure. A simple virtual

crack annealing (VCA) model is proposed for the calculation of the corresponding crack opening stress level is proposed in this report. Several conclusions can be drawn from the current study.

- Crack closure is directly observed during the in-situ SEM testing under different R ratios for the investigated material;
- Both the experimental testing and the proposed model predictions show that the crack opening stress level increases as the R ratio increases. The variation is almost linear in the investigated R ratio regime (from 0 to 0.5);
- The current experimental data does not support the partial crack closure model hypotheses for the investigated material;
- The crack opening stress level prediction using Newman's model agree well with experimental data at the two high R ratios (i.e., 0.33 and 0.5), but overestimates the opening stress level at relatively low R ratios (i.e., 0.025 and 0.1).

Current experimental study and the model validation focus on the constant amplitude loadings. Experimental and theoretical study under general variable amplitude testing needs further study. The extension of the proposed study to other material systems, such as steel and titanium alloys, needs further investigation.

In a previous study using the similar instrumentation under optical microscopy and the digital image correlation [40], the authors have shown that stress/strain redistributed at the stress level similar to the crack surface contact stress observed in this study. Detailed correlation study under scanning electron microscopy will

additional experimental study for both testing design and image post-processing technique.

Acknowledgments

The research reported in this part was supported by funds from Air Force Office of Scientific Research: Young Investigator Program (Contract No. FA9550-11-1-0025, Project Manager: Dr. David Stargel). The support is gratefully acknowledged.

References

1. Wohler A., Über die Festigkeits-Versuche mit Eisen und Stahl [On strength tests of iron and steel]. Z Bauwesen Vol. 20, 1870, pp.73–106.
2. Basquin OH., "The exponential law of endurance tests", Proc Am Soc Test Mater ,Vol. 102, 1910, pp. 625–639.
3. Schutz W., "A history of fatigue", Eng Fract Mech , Vol. 54, 1996, pp. 263–300.
4. Paris P., Erdogan F., "A critical analysis of crack propagation laws", J Basic Eng , Vol. 90, 1963,pp.528–534.
5. Elber W., "Fatigue crack closure under cyclic tension", Eng Fract Mech , Vol. 21, 1970, pp.37–45.
6. Budiansky B., Hutchinson JW., "Analysis of closure in fatigue crack growth", ASME J Appl Mech , Vol. 45, 1978, pp 267–76.
7. Zhang JZ., Bowen P., "On the finite element simulation of three-dimensional semi-circular fatigue crack growth and closure", Eng Fract Mech , Vol. 60, 1998, pp.341–360.
8. Llorca J., Saez Gavez V., "Modeling plasticity-induced fatigue crack closure", Eng Fract Mech , Vol. 37, 1990, pp. 185–196.
9. Gdoutos EE., "Modeling fatigue crack closure using dislocation dipoles", 2006, pp. 249–250.
10. Kim JH., Lee SB., "Behavior of plasticity-induced crack closure and roughness induced crack closure in aluminum alloy", International Journal of Fatigue, Vol. 23, 2001, pp. 247–251.
11. Newman JC., "A crack-closure model for predicting fatigue crack growth under aircraft spectrum loading", In: NASA Technical Memorandum 81941; 1981, pp. 1743–1751.
12. Newman JC., "A crack opening stress equation for fatigue crack growth", International Journal of Fatigue, Vol. 24, 1984, pp.131–135.
13. Chang T., Guo W., "Effects of strain hardening and stress state on fatigue crack closure", International Journal of Fatigue, Vol. 21, 1999, pp. 881–888.
14. Chang T., Guo W., "A model for the through-thickness fatigue crack closure", Eng Fract Mech , Vol. 64, 1999, pp. 59–65.

15. Pommier S., Bompard P., "Bauschinger effect of alloys and plasticity-induced crack closure: a finite element analysis", *Fatigue Fract Eng Mater Struct* , Vol. 23, 2002, pp. 129–139.
16. Newman JC., A crack opening stress equation for fatigue crack growth. *Int J Fatigue*, Vol.24, 1984, pp. 131-135.
17. Vasudevan A., Sadananda K., and Louat N., "Reconsideration of fatigue crack closure", *Scripta Metall. Mater.*, Vol.27, 1992, pp. 1673-1678.
18. Zhang JZ., and Meng ZX., "Direct high resolution in situ SEM observations of very small fatigue crack growth in the ultra-fine grain aluminium alloy IN 9052", *Scripta Materialia*, Vol. 50(6), 2004, pp. 825-828.
19. Kujawski, D. "ΔK_{eff} parameter under re-examination", *International Journal of Fatigue*, Vol. 25, 2003, pp.793–800.
20. Riemelmoser, F. and R. Pippan, "Crack closure: a concept of fatigue crack growth under examination", *Fatigue Fract Eng Mater Struct*, Vol. 20, 1997, pp. 1529-1540.
21. Davidson, David L., *Fatigue crack closure*, *Engineering Fracture Mechanics*, Vol.38, Issue 6, 1991, pp. 393–402.
22. Bowman R., Stephen D. Antolovich, R.C. Brown, A demonstration of problems associated with crack closure measurement techniques, Vol. 31, Issue 4, 1988, pp. 703–712
23. M.N. James, M.N. Pacey, L.W. Wei, E.A. Patterson, Characterisation of plasticity-induced closure crack flank contact force versus plastic enclave, Vol. 70, Issue 17, 2003, pp. 2473–2487
24. S. Golan, R. Arone, Measuring of closure forces with ultrasonic diffracted waves, P. Höller (Ed.), *New Procedures in Nondestructive Testing*, Springer-Verlag, Berlin (1983)
25. C.K. Clarke, G.C. Cassatt, A study of fatigue crack closure using electric potential and compliance techniques, *Engng. Fract. Mech.*, Vol. 9, 1977, pp. 675–688
26. V. Bachmann, D. Munz, Fatigue crack closure evaluation with the potential method, *Engng. Fract. Mech.*, Vol.11, 1979, pp. 61–71
27. Guvenilir, T.M. Breunig, J.H. Kinney, S.R. Stock, Direct observation of crack opening as a function of applied load in the interior of a notched tensile sample of Al–Li 2090, *Acta Mater.*, Vol.45, 1997, pp. 1977–1987
28. Halliday MD., Poole P., and Bowen P., "In situ SEM measurements of crack closure for small fatigue cracks in aluminum 2024-T351", *Fatigue Fract. Eng. Mater. Struct.*, Vol. 18 (6), 1995, pp. 717–729.
29. Andersson H., and Persson C., "In-situ SEM study of fatigue crack growth behavior in IN718", *International Journal of Fatigue*, Vol. 26 (3), 2004, pp. 211-219.
30. Zhang W. and Liu Y., "Investigation of incremental fatigue crack growth mechanisms using in situ SEM testing", *International Journal of Fatigue*, 2011, in press
31. John, R. and Rigling, B., "Weight Function for a Single Edge Cracked Geometry with Clamped Ends", *International Journal of Fracture*, Vol. 72,, 1998, pp.145-158.
32. Jones I.S., "A wide range weight function for a single edge cracked geometry with clamped ends", *International Journal of Fracture*, Vol. 89, Number 1, 1998, pp. 1-18(18)

33. Fleck NA., "Finite element analysis of plasticity induced crack closures under plane strain condition" Engineering Fracture Mechanic, Vol. 25, 1986, pp.441-449.
34. McClung RC. and Sehitoglu H., "On the finite element analysis of fatigue crack closure—2. Numerical results", Engineering Fracture Mechanics, Vol. 33, Issue 2, 1989, pp. 253-272
35. Zapatero J., Moreno B. and Gonzalezherrera A., "Fatigue crack closure determination by means of finite element analysis", Engineering Fracture Mechanics Vol. 75, 2008 , pp. 41-57
36. Newman JC., "Finite Element Analysis of Fatigue Crack Propagation Including the Effects of Crack Closure", Ph.D thesis, Virginia Polytechnic Institute and State University, Blacksburg, VA, May 1974.
37. McClung RC. and Sehitoglu H., "On the finite element analysis of fatigue crack closure", Engineering fracture mechanics, Vol.33, 1989, pp.237.
38. Paris PC., Tada H. and Donald J.K., "Service load fatigue damage—a historical perspective". International Journal of Fatigue, 1999, pp. S35–S46.
39. Newman JC., Jr."A crack opening stress equation for fatigue crack growth" International Journal of Fatigue, Vol.24, 1984, pp.131.
40. Zhang W. and Liu Y., "Plastic zone size estimation under cyclic loadings using in situ optical microscopy fatigue testing", Fatigue & Fracture of Engineering Materials & Structures, Vol. 34, Issue 9, 2011, pp. 717–727.

Appendix 2: Accomplishments for Task 1.1

Existence and Insufficiency of the Crack Closure for Fatigue Crack

Growth Analysis

Jian Yang, Wei Zhang and Yongming Liu
Arizona State University, Tempe, AZ 85287

Abstract: In this paper, the multi-resolution in-situ experiment, optical microscopy experiment and SEM experiment are used to investigate the existence of crack closure and its sufficiency for crack growth prediction. In-situ optical microscopy testing and the digital image correlation analysis are used to measure the plastic zone size in front of the crack tip. In-situ scanning electron microscopy testing is used to measure the crack tip opening displacement and crack growth kinetics. Crack closure behavior under constant loading with a single overload is studied under SEM. The experimental methodology is applied to two different metallic materials (aluminum alloys and steels). Detailed imaging analysis and experimental results are presented and compared. It is found that the crack closure phenomena exist for aluminum alloys, but not for steels in the current investigation. If the crack closure happens, it will significantly alter the crack tip plasticity behavior. Under constant amplitude loading, the crack closure concept is able to uniquely correlate the crack growth kinetics. However, under single overload loading, the crack closure is not able to uniquely correlate with the crack growth kinetics; statistical crack growth experiment also shows the inefficiency of crack closure. Finally, a discussion about the necessity and the insufficiency of crack closure for crack growth prediction is given.

Key words: crack closure; existence; insufficiency; crack growth; in-situ; multi-scale.

1. Introduction

In the past half century, many existing studies have been done on fatigue crack growth mechanism and prediction models. The most famous and successful model should be Paris' Law, which based on the applied stress intensity range [1]. However, Paris' model cannot be applied to loadings with different load ratio and modification is required. In 1970, Elber introduced a crack closure mechanism and modified the applied stress intensity factor range in order to characterize the effect of load ratio [2]. Since Elber's discovery provides a physical meaning to the modification, many researches have been done to get crack-opening load in theoretical method or experimental way. In 1978, Budiansky and Hutchinson provided an analytical estimation of crack opening load with the assumptions of long crack and small scale yielding according to the ideally plastic Dugdale-Barenblatt model [3]. In 1984, Newman analyzed the crack closure problems by developing a strip yield model, which employs a strip yield type plastic zone for leaving residually stretched material in the wake of the crack, causing plasticity-induced closure [4]. However, it is found that the measurement is difficult and the result depends on the measuring location and technique employed such as by traditional gauge and acoustic method [5]. Others methods like electrical potential method [6], ultrasonic method [7][8], and numerical method [9] are also used to measure crack opening load. These methods mentioned are indirectly way to observe crack closure and measure the crack opening loading, and it might be affected by many other factors, for example, it is found that

commonly employed notch-mouth clip-gauge method is not sensitive enough to detect the closure of short cracks in regions of notch plasticity [10].

In this paper, in-situ testing and imaging analysis is used to directly observe the crack closure level and its relationship with crack tip behavior. Compare to the other indirect method, it is non-contact and able to provide direct evidence about the crack closure at very different resolutions. Next, the proposed methodology is applied to two different metallic material systems and the existence of crack closure is investigated in detail. Following the testing under constant loading, a variable loading situation is tested to investigate crack closure effects on crack growth rate. In mechanics, the crack closure behavior under overload loading is investigated in detail. Meanwhile, a statistical crack growth rate under constant loading and overload loading is compared. Finally, a discussion for the existence and insufficiency of crack closure for the fatigue crack growth analysis is given based on the current investigation.

2. In-situ optical microscopy study for crack closure

In in-situ optical microscopy test, a unit load cycle is divided into several steps and images are taken at each step. Then, the strain distribution can be calculated by digital image correlation analysis. When the load is decreasing, the plastic zone is increasing due to the reversed plastic flow. However, if the crack is closed, the crack surfaces will contact and begin to undertake the reversed stress, thus the reversed plastic zone size will stop increasing. The reversed plastic zone size is a better indicator for crack closure than many other methods due to the advantages of non-contact and a stable

precision inherited from digital image correlation method.

2.1 Experiment set-up and procedure

The experimental set-up for in-situ optical microscopy experiment is shown in Fig. 1. It contains two parts: a palm-sized tensile stage and an optical microscope system. The tensile stage is manufactured by Ernest F. Fullam Inc., which has been merged to MTI Instruments Inc. The maximum gage length between mechanical grips is about 27 mm, and the load capacity is 5 kN. The sub-stage is fixed on the microscope and the cyclic loading is applied to the specimen. A Nikon metallurgical microscope is used to monitor the specimen surface and a high resolution imaging acquisition system is used to record images during the testing.

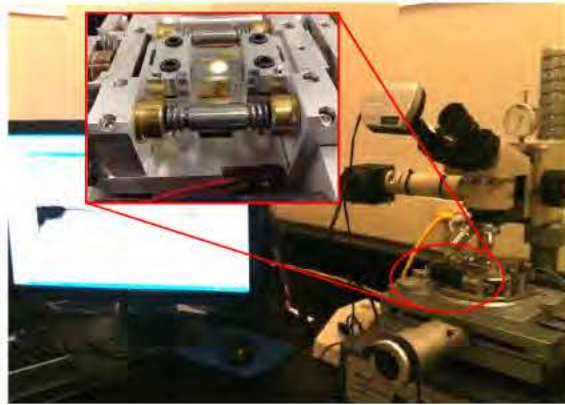


Fig. 1 Experiment setup

The specimen is a single edge notched plate with width $W = 8$ mm, length $L = 52$ mm and thickness $T = 0.86$ mm. Due to the small thickness of specimens, it is assumed to be under the plane stress conditions for a relatively long crack.

The experiment procedure contains four major steps as follows.

Step 1: specimen manufacturing and pre-cracking. Single edge notched plate specimen as described is used for testing. After notching, the specimens are pre-cracked under a hydraulic tension machine INSTRON 1331 until the initial crack reaches about 1 mm. The pre-cracking procedure follows the ASTM standard E647-99;

Step 2: polish the specimen to form randomly distributed small dark regions on the smooth surface, which is a requirement for digital image correlation analysis. Both surfaces of the specimen should be polished with the sandpaper whose average particle diameter is smaller than 10 μm ;

Step 3: apply load on the specimen under the monitoring of a microscope, while image of the crack tip region is taken during the loading and unloading process. A unit load cycle is divided into several steps in the load profile. At each step, the image around the crack region is taken for strain calculation. The step load is set according to the precision requirement and computation resource limitation. An example profile is shown in Fig. 2, which contains 37 steps during the loading and unloading path.

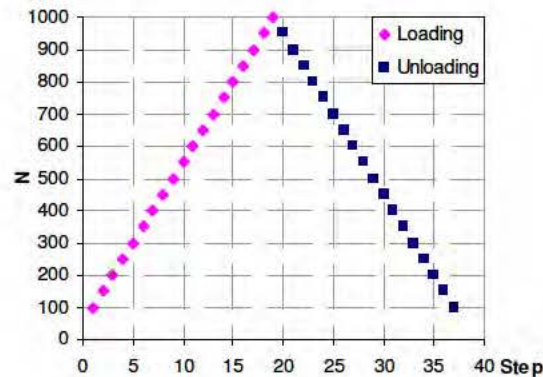


Fig. 2 Load profile

Step 4, process the images by DIC software to get the strain field of the crack tip region and calculate the plastic zone using mechanical analysis. The plastic zone size is defined along the crack propagation direction and it can be measured directly from the processed image.

The theoretical reversed plastic zone under cyclic loading can be estimated by Eq. (1) without the consideration of crack closure [11]

$$\rho = \frac{1}{\pi} \left(\frac{\Delta K}{2\sigma_y} \right)^2, \quad (1)$$

where σ_y is the yielding strength and

$$\Delta K = F \cdot \Delta\sigma \sqrt{\pi a} = F \cdot (\sigma_{\max} - \sigma_{\min}) \sqrt{\pi a}, \quad (2)$$

where F is the geometry factor and

$$F = 1.12 - 0.231 \left(\frac{a}{W} \right) + 10.55 \left(\frac{a}{W} \right)^2 - 21.72 \left(\frac{a}{W} \right)^3 + 30.39 \left(\frac{a}{W} \right)^4 \quad (3)$$

where a is the crack length.

2.2 Case study of Al7075-T6 and Steel 4340

With the above described experiment procedure, two sets of experiments are carried out to investigate the crack closure behavior under constant loading in Al 7075-T6 and Steel 4340 separately.

The chemical composition of aluminum 7075-T6 is listed in Table 1. The aluminum is the balance in the total weight. The basic physical properties are listed in Table 2.

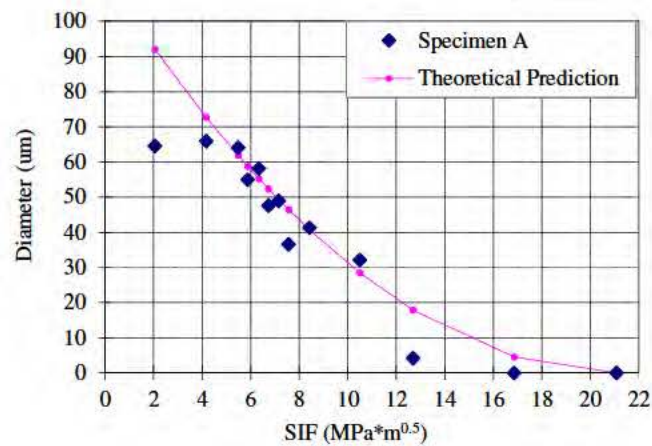
Table 1 Chemical composition of Al 7075-T6 (weight, %)

Element	Zn	Mg	Cu	Fe	Si	Mn	Cr
Min	5.1	2.1	1.2	0	0	0	0.18
Max	6.1	2.9	2.0	0.5	0.4	0.3	0.28

Table 2 Basic mechanical properties of Al 7075-T6

Elastic Modulus /GPa	Yield Strength /MPa	Tensile Strength /MPa
71.7	502~516	573~582

Following the above discussed general experiment methodology, the plastic zone size at each step can be measured using the digital image correlation analysis. Three specimens have been tested and the reversed plastic zone size is shown in Fig. 3. It can be found that there is a plat form when stress intensity factor (SIF) is less than about $3.5 \text{ MPa}\cdot\text{m}^{0.5}$, which indicates the reversed stress is released by the surface contact and the phenomena of crack closes.



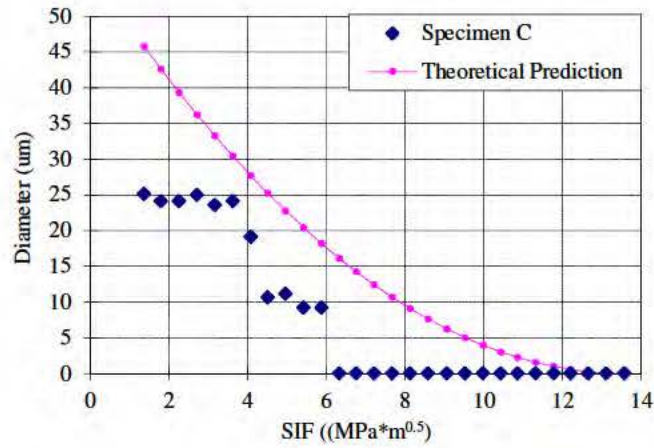
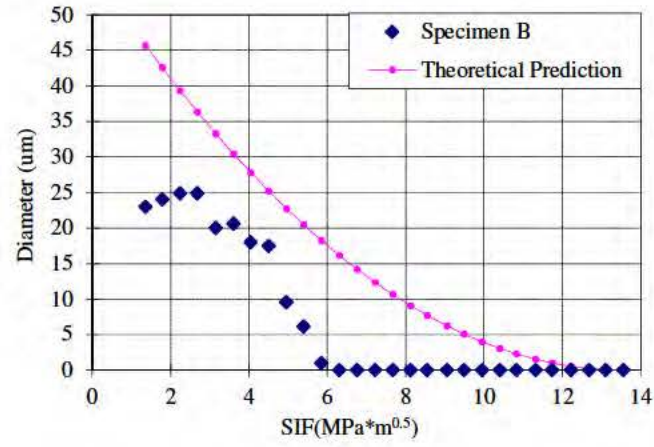


Fig. 3 Plastic zone size of aluminum [12]

The same experiment is carried on AISI 4340 steel. AISI 4340 steel is a heat treatable, low alloy steel containing nickel, chromium and molybdenum. The chemical composition of this material and its basic physical properties are listed in Table 3 and 4.

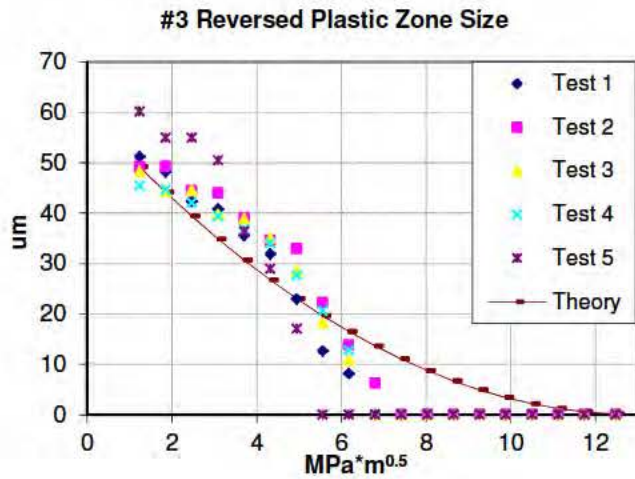
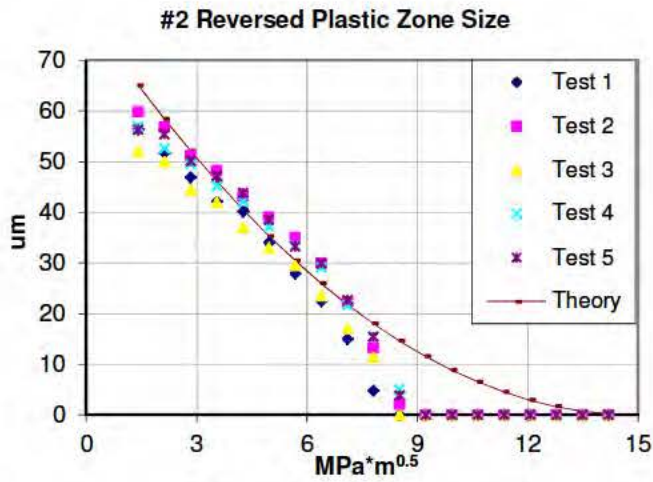
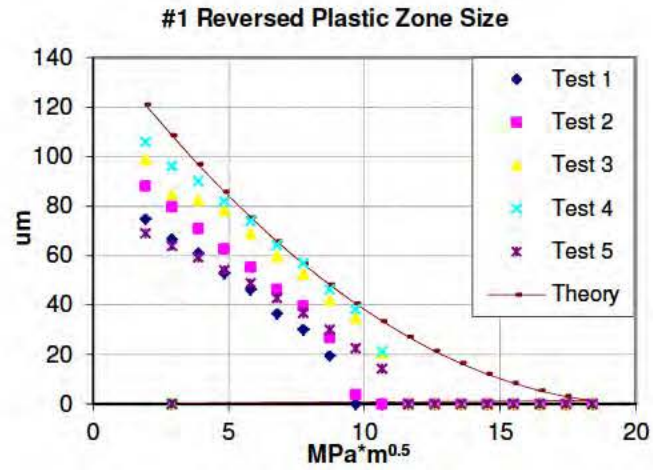
Table 3 Chemical composition of AISI 4340 steel

Element	C	Cr	Mn	Mo	Ni	P	Si	S
Min	0.38	0.7	0.6	0.2	1.65	0	0.15	0
Max	0.43	0.9	0.8	0.3	2	0.035	0.3	0.04

Table 4 Basic physical properties of AISI 4340 steel

Elastic Modulus /GPa	Yield Strength /MPa	Tensile Strength /MPa
190~210	472.3	744.6

In the test, the load starts from 100 N to 1000 N at a step of 50 N. Results of the plastic zone size during the unloading process are obtained as shown in Fig. 4. It is found that the reversed plastic zone size keeps increasing throughout the unloading process and these experiment data shows similar trends to the theory data without plastic closure phenomena. This is very different compared with the results of aluminum alloys and it indicates no crack closure for steel in these tests.



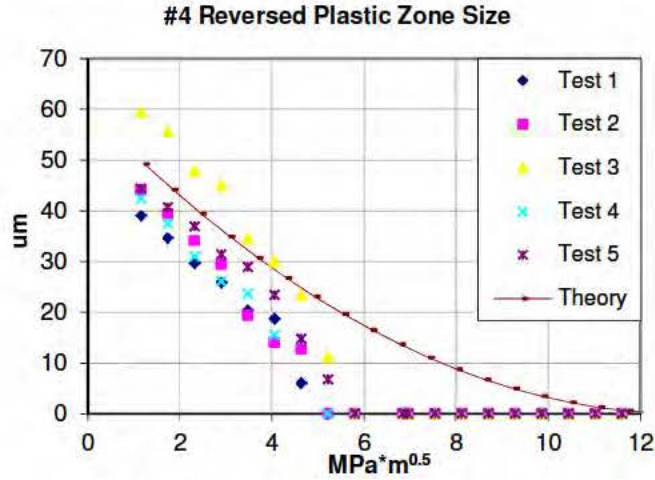


Fig. 4 Plastic zone size of steel specimens

3. In-situ SEM study for crack closure

In order to verify the crack closure indications from optical microscope observation and get further information of the crack tip deformation behavior, in-situ SEM experiment is carried out on the two materials. Further, the behavior of crack closure under variable load is studied for the sufficiency of K_{eff} for crack growth prediction. In mechanics, crack closure behavior under a single overload is studied for the sufficiency of K_{eff} for crack propagation mechanics. In statistics, the crack growth rate under constant loading and overload loading is compared to show the sufficiency of K_{eff} for crack growth prediction. Detailed experimental procedure has been discussed in [13][14] and only a brief description of the experimental methodology is given below.

3.1 In-situ SEM study under constant amplitude loading

An in-situ SEM fatigue testing is performed to achieve the high resolution investigation for the hypothesis verification of crack growth kinetics and crack deformation in the vicinity of the crack tip. Compared with experiment under optical microscope, crack tip opening displacement (CTOD) is measured directly to find the crack is closed or not. Some details of the experimental set-up for the in-situ SEM experiment are shown in Fig. 5. It consists of the tensile sub-stage and a field emission SEM (JEOL-7400F). The sub-stage is fixed in the SEM and the cyclic loading is applied during the experiment. During the testing, the vacuum level is remained to be less than 9.3×10^{-5} MPa (gage reading). Multiple resolution images are recorded during the testing for the measurements of crack length and the crack tip deformation behavior.

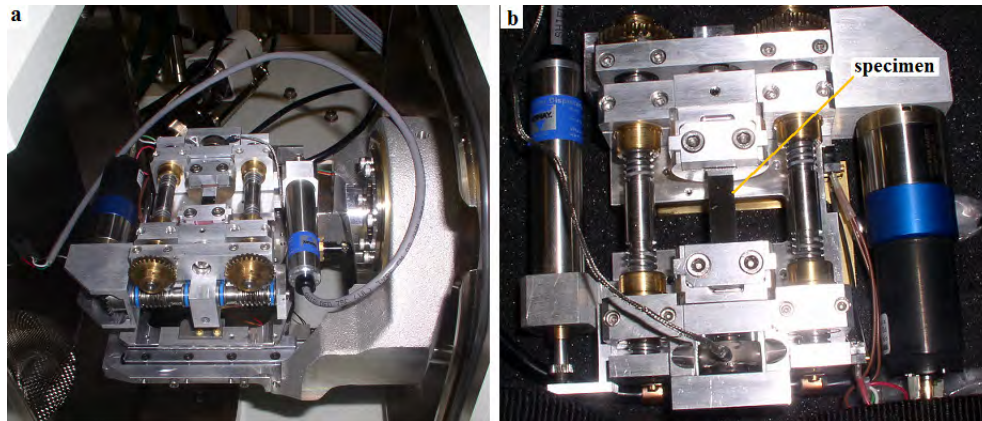


Fig. 5 In-situ SEM fatigue testing setup: a) loading stage installed in SEM; b) specimen installed in loading stage;

The specimen configuration and preparation are almost the same as that in optical

microscope experiment. In this experiment, the final polishing is done by a vibration polishing machine with 1~3 μm polishing suspension.

The specimen is loaded in the tensile stage under cyclic loading and observed in-situ under SEM. In the following comparison for aluminum and steel, the stress ratio of the applied constant amplitude load is 0.1. The measurements are usually after 50 to 100 cycles loading in SEM to ensure the crack growth is stable. During the testing, one loading cycle is divided into many steps, similar with the testing under optical microscopy. The applied loading increases/decreases at a very slow rate. During the loading/unloading path the stage will hold at each step imaging acquisition. CTOD is measured directly from the processed images. The CTOD is defined as the distance of crack surface at the place of crack tip in last cycle. With the same reference, the crack growth rate at each cycle could be measured, as shown in Fig. 6.

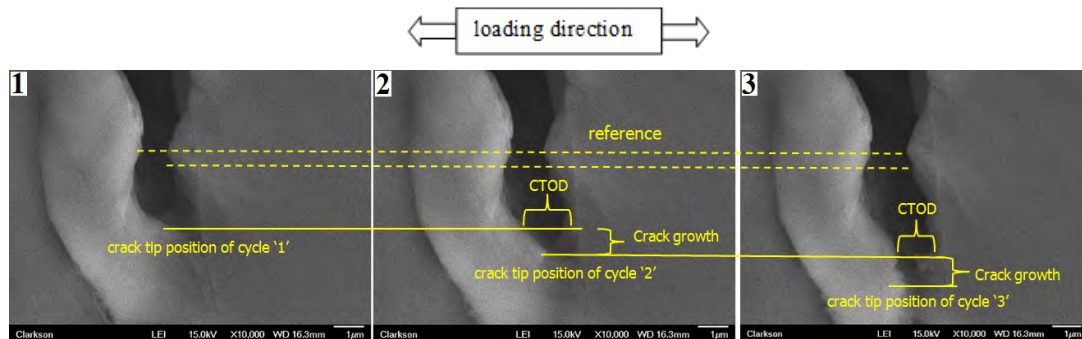
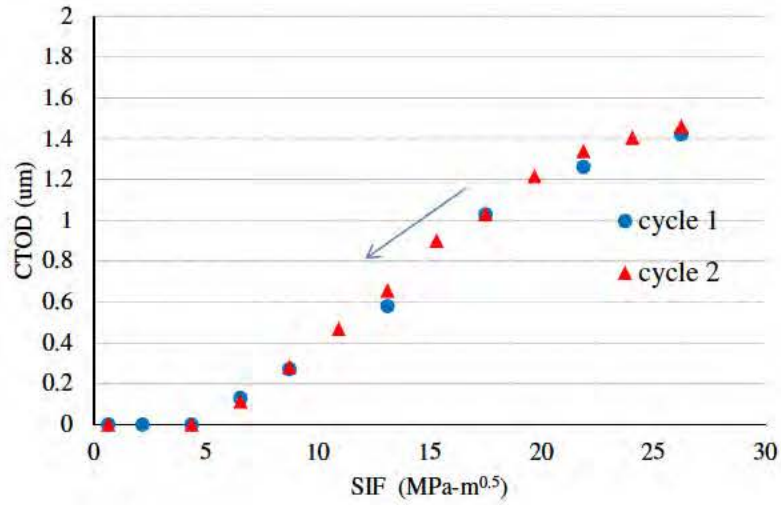


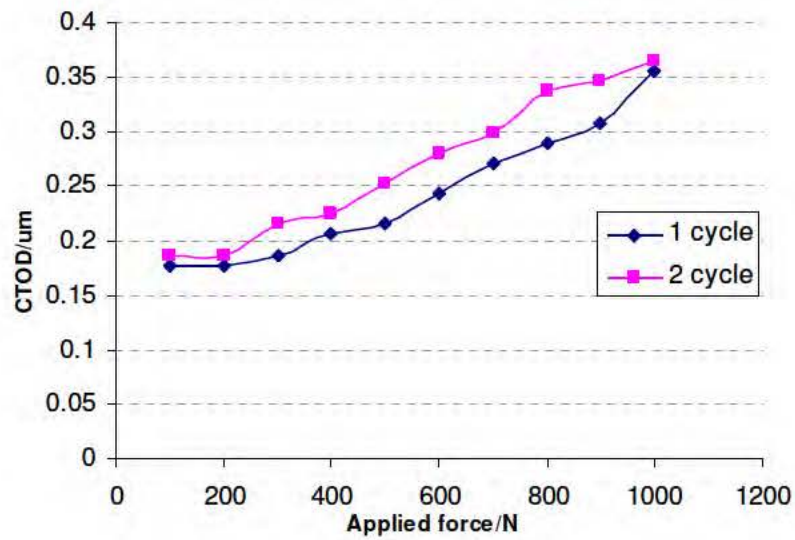
Fig. 6 Images of crack tip position and CTOD under maximum loadings

Using the measuring method, two sets of experiments on steel 4043 and aluminum 7075-T6 have been performed. The results are shown in Fig. 7. It shows that CTOD reduces to zero when SIF is less than $5 \text{ MPa} \cdot \text{m}^{0.5}$ for Al 7075-T6, while for steel 4340, CTOD is not zero under the minimum loading. The crack tip details are shown in Fig.

8. It shows the crack closure in Al 7075-T6 clearly but the crack remains open for steel 4340.

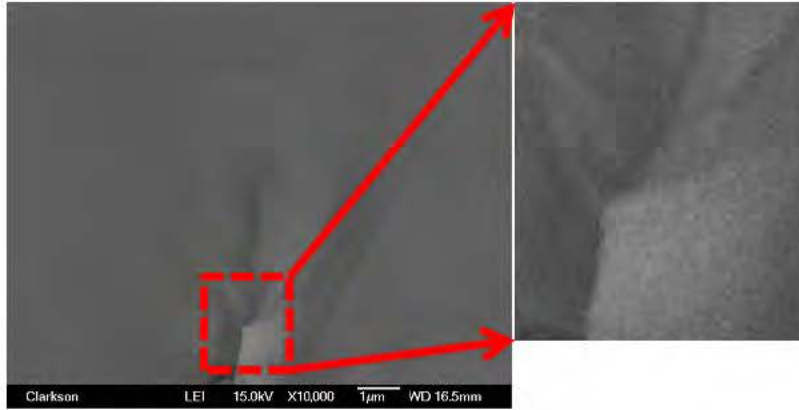


(a) Al 7075-T6

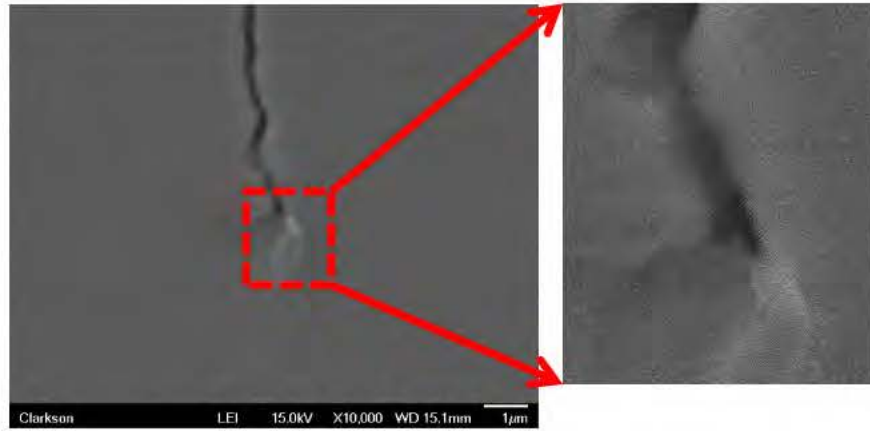


(b) Steel 4340

Fig. 7 CTOD during unloading process on Al 7075-T6 and steel 4340



(a) Al 7075-T6



(b) Steel 4340

Fig. 8 Crack tip under minimum loading of Al 7075-T6 and steel 4340

This result is consistent to the experiment under optical microscope and they show that the existence of crack closure in Al 7075-T6, but it is not observed in steel 4340 at this stage.

3.2 In-situ SEM study under variable loading with single overload

As crack closure is observed both under optical microscope and SEM, its effects on crack growth rate is not negligible for fatigue crack growth prediction for some

metallic materials, if it happens. However, it is not clear that the crack closure is the only/dominant mechanisms for aluminum materials, especially under different loading conditions. Thus, the crack closure effect on crack growth rate under variable loading is investigated and is shown below.

3.2.1 Experiment procedure

The procedure of SEM experiment under variable loading is the same with that under constant loading. The only difference is the loading profile. In this experiment, a cycle of over-load is inserted in a constant loading spectrum. The constant loading ranges from 10 to 30 $\text{MPa}\cdot\text{m}^{0.5}$ and the overload ranges from 10 to 36 $\text{MPa}\cdot\text{m}^{0.5}$. Thus the over load ratio is 1.2 as the ratio of two maximum load. A schematic plot is shown in Fig. 9.

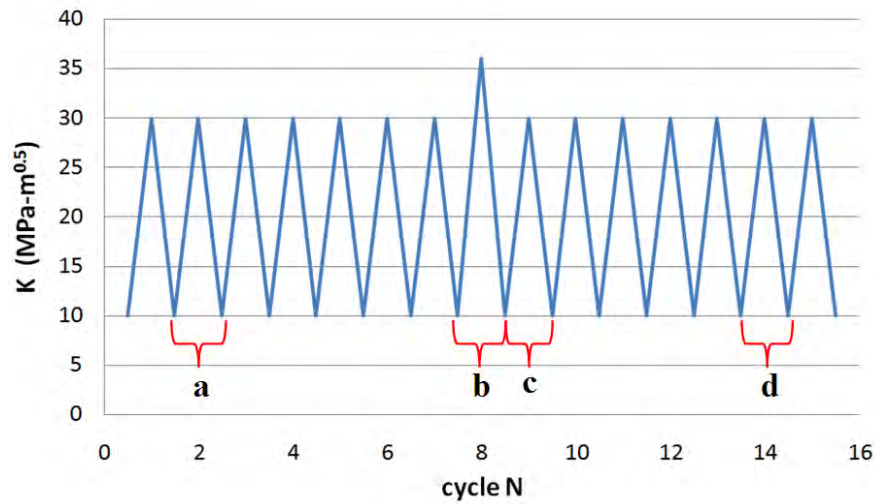


Fig. 9 Schematic representation of single overload spectrum

In order to observe and compare the effects of overload loading, four types of loading cycle are chosen for observations. The first type is the constant loading cycles before

the over load (cycle **a** in Fig. 9), which provides the baseline information of the crack propagation kinematics. The second and the third type are the overload cycle and the cycle right after it. The last type is the cycle 5~20 cycles after the overload. In this study, two experiments data are obtained. In the first experiment, the background stress ratio is 0.33 and the overload ratio is 1.2. In the second experiment, the background stress ratio is 0.025 and the overload ratio is 1.1. In the following discussion, the result of the first experiment will be discussed in detail and the second one will be given as a comparison.

3.2.2 Result and discussion

Following the experiment procedure and the loading profile, the details of crack growing before, during, and after overload under SEM is obtained and compared.

As described before, two cycles before the overload is observed and the crack tip condition during the first loading cycle is shown in Fig. 10. By examining the crack tip, it could be found that the crack is opened between Fig. 10(4) and (5), with the corresponding stress intensity factor $17.68 \text{ MPa}\cdot\text{m}^{0.5}$ and $19.28 \text{ MPa}\cdot\text{m}^{0.5}$. Then, the CTOD is measured at each step in the loading portion of the two cycles, as plotted in Fig. 11. These two series of data show a similar behavior, indicating the stable state of crack under constant loading. It should be noticed that the crack opens when the stress level reaches $(57\pm 2.5)\%$ of the maximum loading.

Then the crack tip deformation behavior is observed during the overloading cycle. In this cycle, the loading process can be divided into two stages as shown in Fig. 12:

stage 1 is the process when the load is equal or less than the maximum of the previous constant loading; stage 2 is the over loading session. It is observed that the crack opening load is similar to the constant loading process and it is about 57% of the maximum loading as shown in Fig. 13. In stage 2, the slope variation of the CTOD is observed. The reason for this change is that the compressive plastic zone is fully reversed by the large overload and the CTOD is controlled by the monotonic plastic zone size rather than the reversed plastic zone size, which is consistent with the classical fracture mechanics and finite element simulation result.

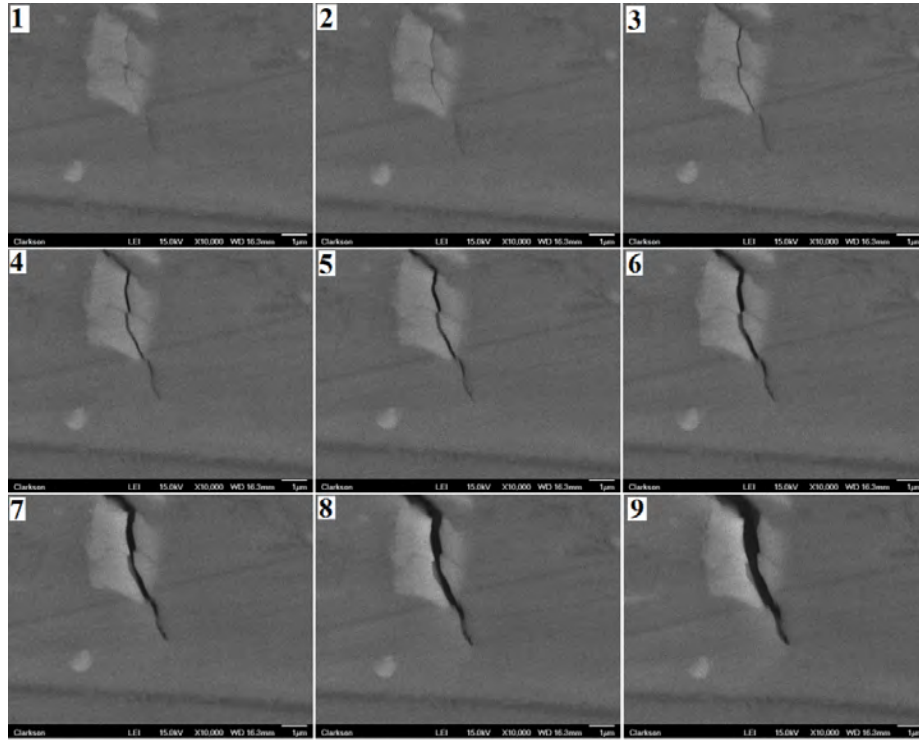


Fig. 10 Illustration of crack tip behavior ($R=0.33$, $K= 9.68, 12.88, 14.48, 16.08, 17.68, 19.28, 21.68, 24.16$, and $28.96 \text{ MPa} \cdot \text{m}^{0.5}$ respectively)

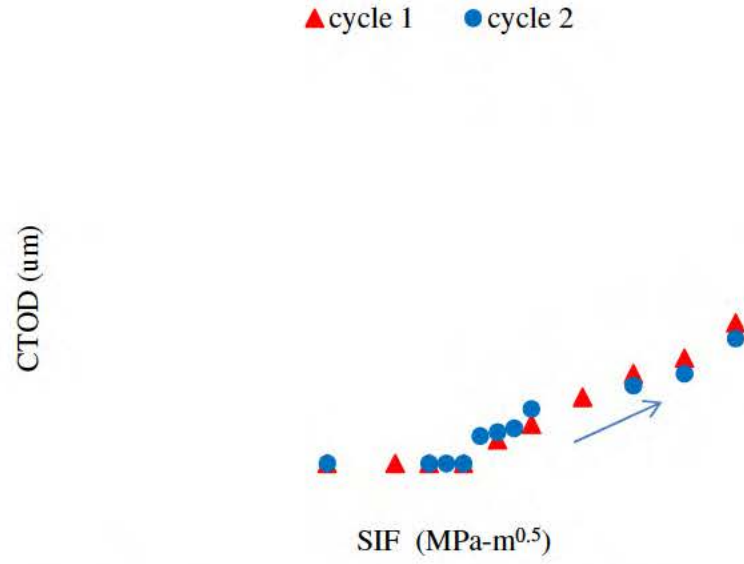
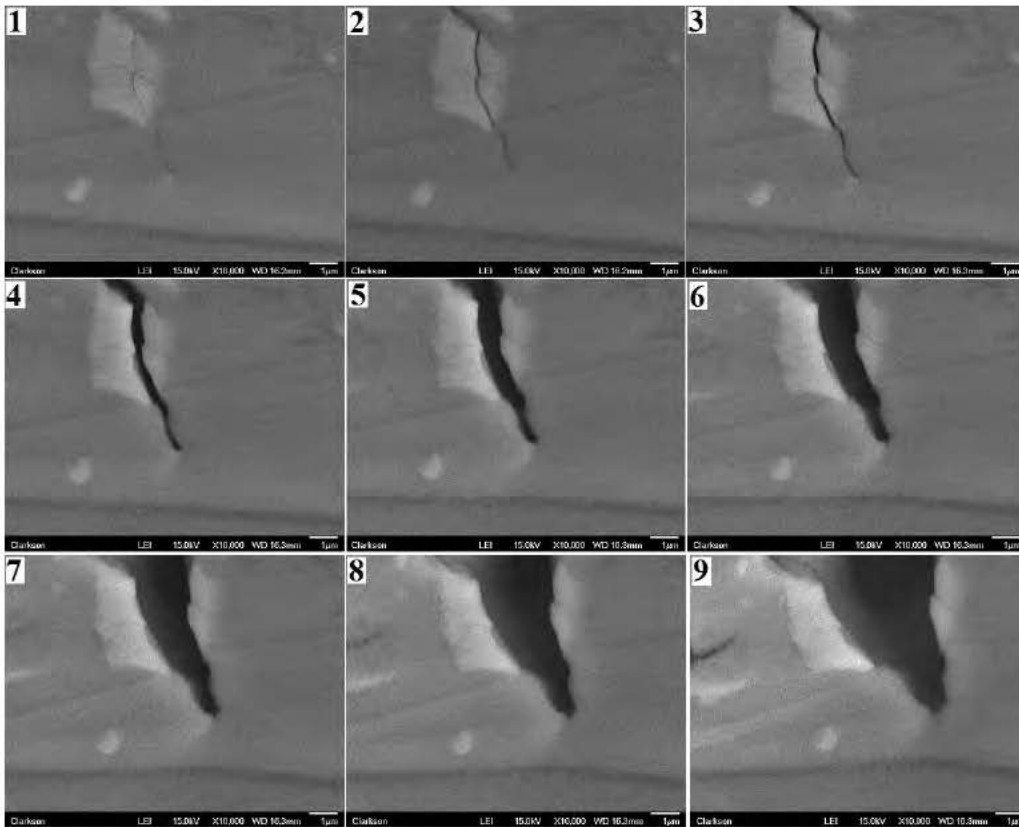


Fig. 11 CTOD variation at each loading step before overload



Figs. 12 Illustration of crack tip behavior under overload ($R=0.33$, $K= 9.68, 16.08, 17.68, 19.28, 24.16, 28.96, 31.36, 32.96, \text{ and } 34.72 \text{ MPa} \cdot \text{m}^{0.5}$ respectively)

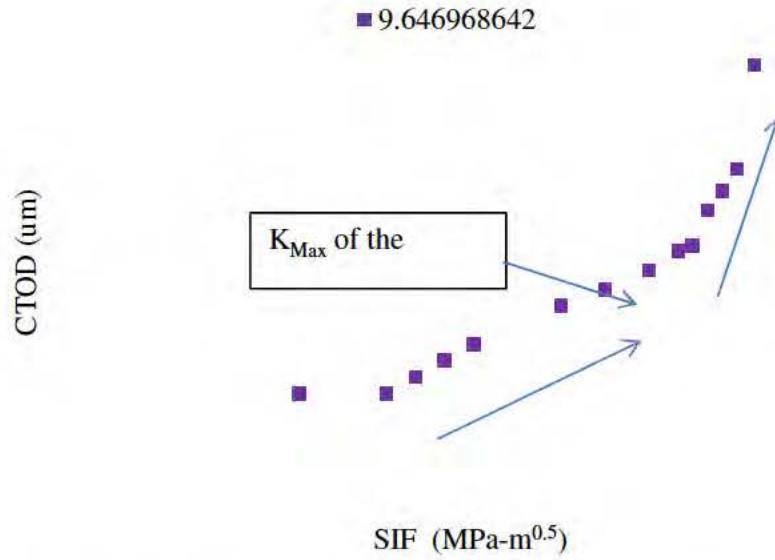
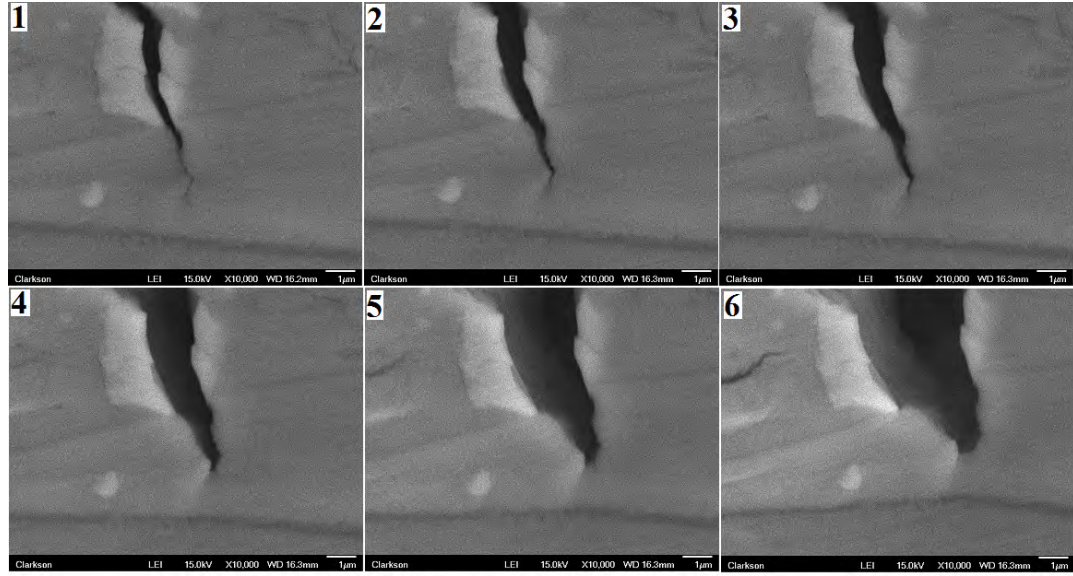


Fig. 13 CTOD variation at each loading step under overload

Next, the cycle follows the overload cycle is investigated. Selected SEM images are shown in Fig. 14 and the CTOD at each loading step is shown in Fig. 15. It is observed that the crack is opened a little earlier than previous. The opening SIF is $13 \text{ MPa} \cdot \text{m}^{0.5}$ but during the constant cycles and the overloading cycle, the opening SIF is $14.5 \text{ MPa} \cdot \text{m}^{0.5}$. On the other hand, the maximum CTOD at peak loading is $7 \mu\text{m}$, much larger than that during the constant loading before the overload, which is $3.5 \mu\text{m}$.



Figs. 14 Illustration of crack tip behavior next to the overload ($R=0.33$, $K= 9.68, 12.88, 16.08, 19.28, 24.16$, and $28.96 \text{ MPa}\cdot\text{m}^{0.5}$ respectively)

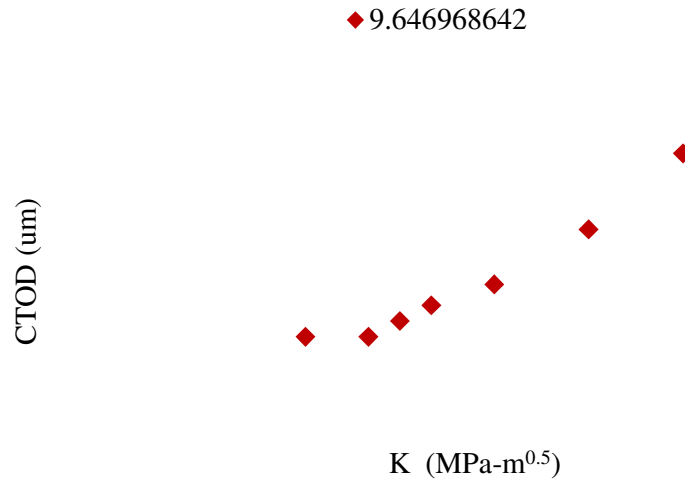
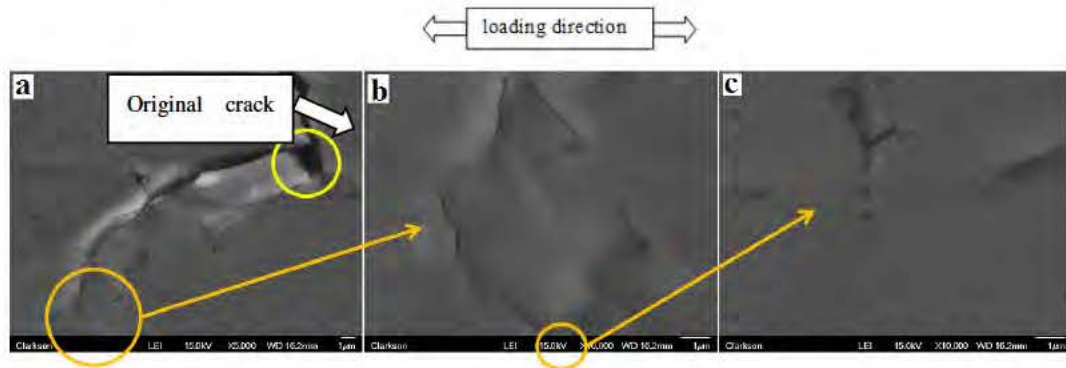


Fig. 15 CTOD variation at each loading step of the next cycle

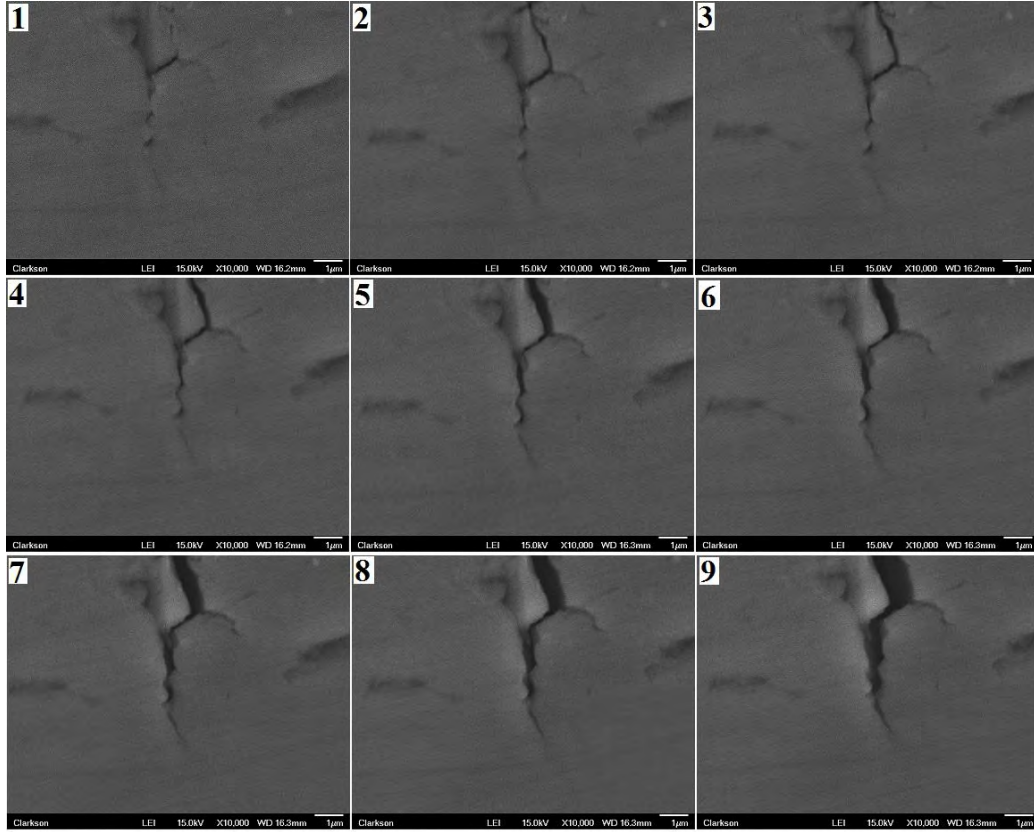
In the following several cycles, the crack growth becomes unstable and very fast, as shown in Fig. 16. The large white arrow and yellow circle indicate the crack tip position under the overload. The crack kinks and bifurcates after the overload within about 10 cycles. The kinks can be seen in both of Figs. 16 (a) and (b), and the bifurcation can be seen in Fig. 16 (b). The relative position between these figures is marked by orange circles and arrows. Fig. 16 (c) focuses on the new crack tip which

is stable after 11 cycles (about 25 microns unstable growth). This observation supports the conclusion that the extra damages caused by the overload will lead to a rapid and unstable crack growth right after the overload. This also supports one of the mechanism models for the crack retardation after the single overload cycle using the crack kinking hypothesis [15].



Figs. 16 Crack path after the overload (11cycles)

The unstable state of crack growth right after the overload cycle lasts only for about 5 cycles. It is mainly because the crack has grown beyond the damaged plastic region caused by the overload, and then the growing process becomes stable again. A cycle which is 11 cycles after the overloading is investigated in this test and the result is shown in Fig. 17 and 18. Different from the cycle right after the overloading cycle, the crack opening SIF is much larger, but the maximum CTOD is smaller. Thus the effective stress intensity factor is smaller than the constant loading condition, which is part of the mechanism for the crack growth retardation in the current investigation.



Figs. 17 Illustration of crack CTOD measurement after overload ($R=0.33$, $K= 9.68, 12.88, 14.48, 16.08, 17.68, 19.28, 21.68, 24.16$, and $28.96 \text{ MPa}\cdot\text{m}^{0.5}$ for figures 1-9, respectively)

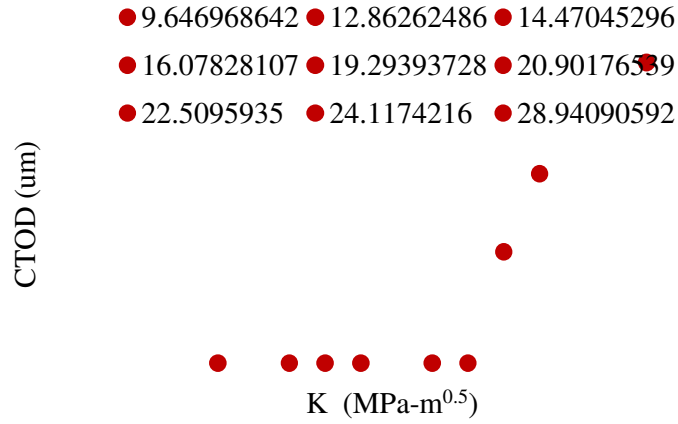


Fig. 18 CTOD variation at each loading eleven steps after overload

For all testing measurements, the crack opening stress intensity factor at each observing cycle are plotted in Fig. 19. The X axis is cycle number and Y axis is the ratio of crack opening SIF over the maximum SIF ($K_{\text{open}}/K_{\text{max}}$). It is shown that during

the constant loading in stage 1, K_{open}/K_{max} is 0.57. Right after the overload cycle, the crack opening slightly decreases and increases to about 75% after 11 cycles.

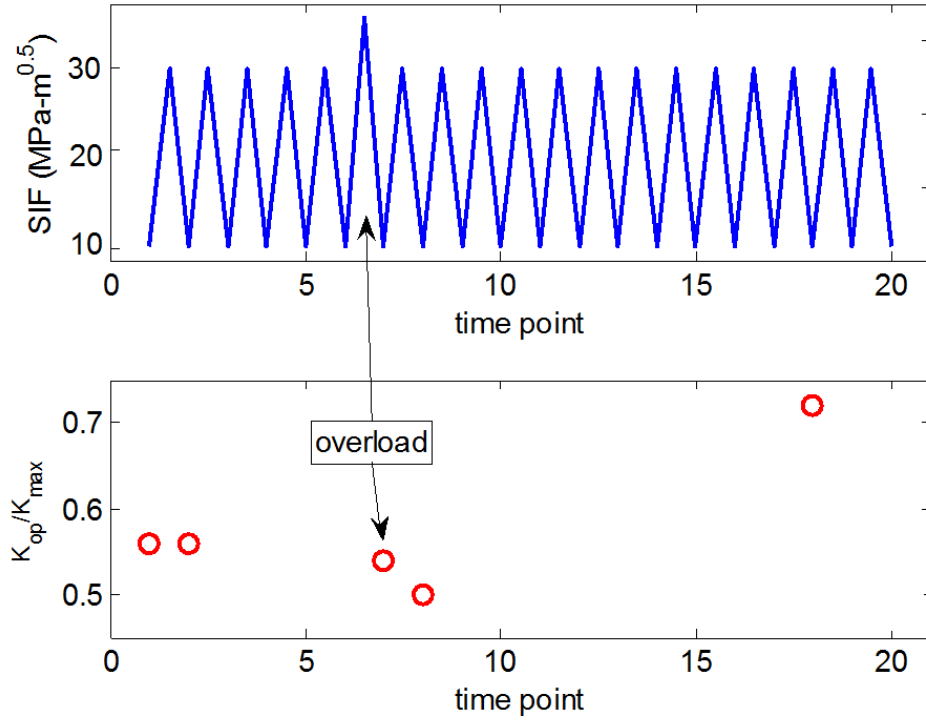


Fig. 19 Illustration of the crack opening stress level variation (R=0.33)

Another experiment has been performed with stress ratio $R=0.025$, the maximum SIF of the constant loading is $26.26 \text{ MPa} \cdot \text{m}^{0.5}$ and the overload ratio 1.1. Very similar result is observed as shown in Fig. 20.

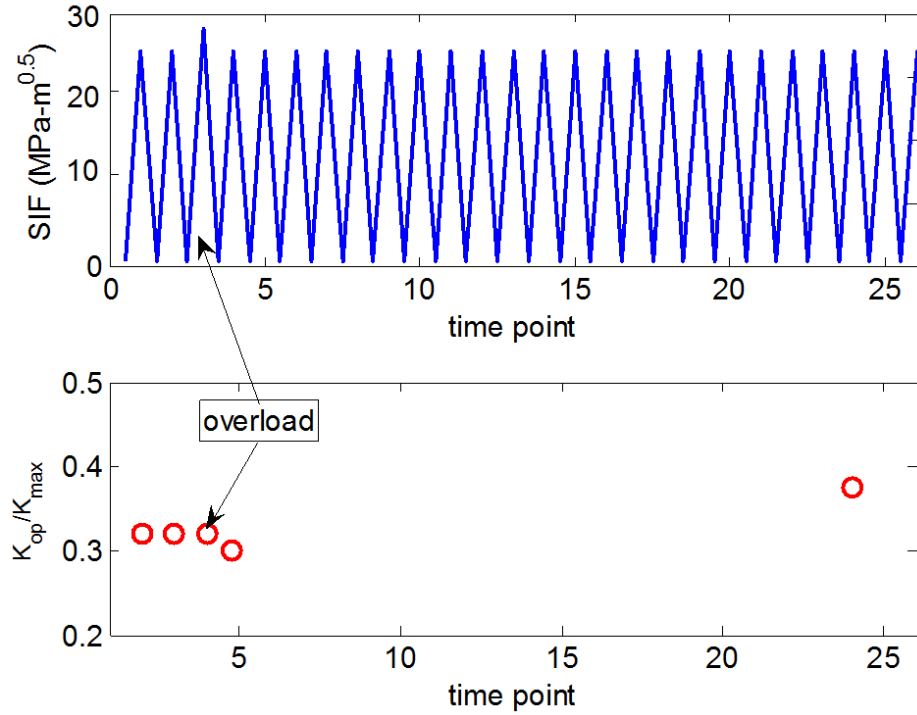
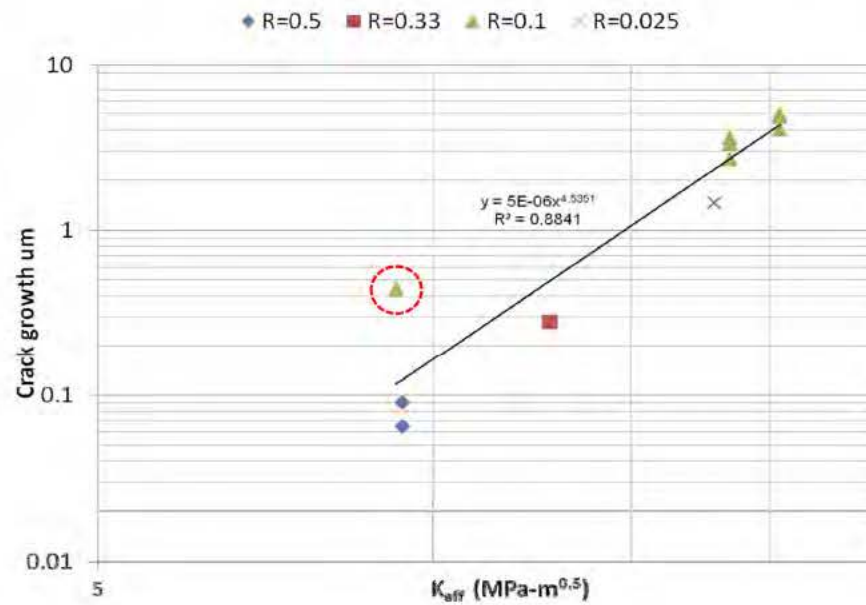


Fig. 20 Illustration of crack opening stress level variation (R=0.025)

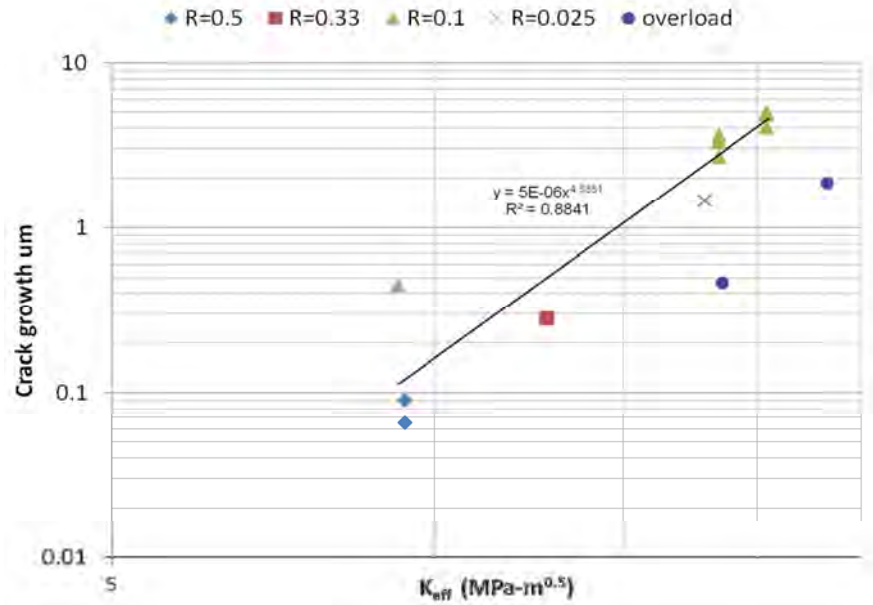
One important hypothesis in the classical crack closure theory is that the effective stress intensity factor range (defined as the maximum SIF minus the opening SIF) can be used to uniquely correlate with crack growth rate under different loadings. However, this experiment shows that under single overload loading, crack opening SIF becomes variable and crack starts to kink and bifurcate. These mechanics cannot be explained only by the phenomena of crack closure.

On the other hand, a statistical study of crack growth rate under constant load and overload loading is conducted to verify this hypothesis. Several experiments have been completed at stress ratio $R=0.5$, 0.33 , 0.1 and 0.025 , and the result of crack growth rate with the effective SIF is plotted in Fig. 21. Fig. 21 (a) only shows the result under constant loading. It can be found that all the data shows a good linear relationship in log-log scale, except one data in red dashed circle. Fig. 21(b) shows the data together

with the single overload testing. It is observed that the two data points are not consistent with the linear trend from the constant amplitude loading data. This observation further indicates that other mechanism also contributes to the crack growth under single overload loading, such as crack branching and blunting as observed from the images.



(a) Constant load



(b) Constant loading and overload loading

Fig. 21 Crack growth rate with SIF under constant load and overload loading

4. Conclusions

In this paper, in-situ experiment at micrometer scale and nanometer scale has been introduced and the observation of crack closure behavior of steel 4340 and aluminum 7075-T6 under constant loading has been obtained. Further, preliminary crack closure behavior under single overload on aluminum 7075-T6 has been studied. Several conclusions can be made from the experiments as follows.

1. Crack closure is directly observed in Al 7075-T6 under both constant and variable loads, but it is not observed in steel 4340 under constant loading at stress ratio 0.1.
2. The crack closure can significantly change the plasticity distribution in front of the crack tip;
3. K_{eff} defined as the difference of K_{max} and K_{open} in the classical fracture theory

correlates with the unique crack growth rate under constant loading, but it not enough for crack growth prediction under variable loading. Additional parameter for the mechanism is need for the prediction;

The proposed study focus on simple variable loadings and more complex loading conditions require additional study. The current imaging analysis is for surface measurements and 3D imaging technique will be very helpful for the investigation of subsurface behavior near a crack tip.

5. Acknowledgements

The research was supported by funds from Air Force Office of Scientific Research: Young Investigator Program (Contract No. FA9550-11-1-0025, Project Manager: Dr. David Stargel). The support is gratefully acknowledged.

6. Reference

- [1] P.C. Paris, M.P. Gomez, W.E. Anderson, A Rational Analytic Theory of Fatigue, *Trend in Engineering*. 13 (1961) 9–14.
- [2] E. Wolf, Fatigue crack closure under cyclic tension, *Engineering Fracture Mechanics*. 2 (1970) 37–45.
- [3] B. Budiansky, J. Hutchinson, Analysis of closure in fatigue crack growth, *Journal of Applied Mechanics*. 45 (1978) 267–276.
- [4] J. J.C. Newman, A crack opening stress equation for fatigue crack growth, *International Journal of Fracture*. 24 (1984) R131–R135.
- [5] D.E. Macha, D.M. Corbly, J.W. Jones, On the variation of fatigue-crack-opening load with measurement location, *Experimental Mechanics*. 19 (1979) 207–213.
- [6] T.T. Shih, R.P. Wei, A study of crack closure in fatigue, *Engineering Fracture Mechanics*. 6 (1974) 19–32.
- [7] D. Bouami, D. De Vadder, Detection and measurement of crack closure and opening by an ultrasonic method, *Engineering Fracture Mechanics*. 23 (1986) 913–920.
- [8] D.S. Singh, A. Srivastav, S. Gupta, E. Keller, A. Ray, Ultrasonic measurement of crack opening load for life-extending control of mechanical structures, in:

- 2009 American Control Conference, IEEE, Piscataway, NJ, USA, 2009: pp. 210–215.
- [9] W. Riddell, R. Piascik, M. Sutton, W. Zhao, S. McNeill, J. Helm, Determining Fatigue Crack Opening Loads from Near-Crack Tip Displacement Measurements, ASTM SPECIAL TECHNICAL PUBLICATION. 1343 (1999) 157–174.
 - [10] N. Fleck, C. Shin, Fatigue crack growth under compressive loading, *Engineering Fracture Mechanics*. 21 (1985) 173–185.
 - [11] J. Rice, A path independent integral and the approximate analysis of strain concentration by notches and cracks, *Journal of Applied Mechanics*. 35 (1968) 379–386.
 - [12] W. Zhang, Y. Liu, Plastic zone size estimation under cyclic loadings using in situ optical microscopy fatigue testing, *Fatigue & Fracture of Engineering Materials & Structures*. 34 (2011) 717–727.
 - [13] W. Zhang, Y. Liu, Investigation of incremental fatigue crack growth mechanisms using in situ SEM testing, *International Journal of Fatigue*. 42 (2012) 14–23.
 - [14] W. Zhang, Y. Liu, In-Situ SEM Fatigue Crack Growth Testing of Al7075-T6, *International Journal of Fatigue*. (2011) accepted.
 - [15] S. Suresh, Micromechanisms of fatigue crack growth retardation following overloads, *Engineering Fracture Mechanics*. 18 (1983) 577–593.

Appendix 3: Accomplishments for Task 1.1

Crack Closure Investigation under Simple Variable Amplitude

Loading Using In-Situ SEM Testing

Wei Zhang, Yongming Liu*

Clarkson University, Potsdam, NY, 13699

Abstract: In this report, the in-situ scanning electron microscopy (SEM) experiments for Al7075-T6 are performed under the variable amplitude loading (single overload) in order to investigate the crack opening stress variation. During the testing, several loading cycles of interest are selected and divided into a certain number of steps. At each step, high resolution images around the crack tip region are taken under the SEM. Imaging analysis is used to quantify the crack tip opening displacement (CTOD) at each corresponding time instant in a loading cycle. In the current experimental work, the crack closure phenomenon is not only directly observed under constant amplitude loadings, but also under the variable amplitude loading. The experimental results provide the evidence that the transient crack opening stress or effective stress intensity factor ranges played a significant role in the transient crack growth. And some observations imply that the crack closure is not the only factor which controls fatigue crack growth. A detailed discussion is given based on the current investigation.

Keywords: fatigue crack, closure, opening stress, in-situ SEM

1. Introduction

In 1960's, Paris' law [1] was proposed which becomes the most popular fracture

mechanics-based method for fatigue life prediction. Many modifications of Paris' law have been proposed in the literature. One of the most significant modifications is the crack closure concept [2], which was first introduced into the crack growth analysis by Elber [2]. Elber pointed out that fatigue cracks remained closed during part of the loading process and proposed an effective stress intensity factor range to account for the crack closure. Since Elber's studies on crack closure showed great promise for fatigue crack growth prediction, there has been extensive numerical and experimental studies on the determination of crack opening stress which is the critical parameter of many fatigue crack growth model. So far much related work has been done on that using experimental investigation, numerical analysis as well as theoretical studies. Budiansky and Hutchinson [3] computed the plasticity-induced crack closure in plane stress case under small-scale yielding condition in their theoretical study. Wheeler [4] and Wilenbourg [5] developed empirical methods based on reduced rate of crack growth for cracks crossing a plastic zone caused by previous overload. Zhang and Bowen [6] discussed three-dimensional semi-circular fatigue crack growth and closure using the finite element simulation. Llorca and Sanchez Gavez [7] established the plasticity-induced fatigue crack closure model based on finite difference method. Gdoutos [8] studied fatigue crack closure model using dislocation dipoles Newman [9,10] analyzed the crack closure problems by developing a strip yield model, which employs a strip yield type plastic zone for leaving residually stretched material in the wake of the crack, causing plasticity-induced closure. Kim and Lee [11] performed the testing with center-cracked tension specimens under the constant

amplitude loading to investigate the fatigue crack closure. Sutton, et al. [12] proposed an experimental methodology for estimating crack closure.

The above mentioned experimental works are all indirect measurements of crack closure, which might be also affected by other factors other than crack closure. There are very few studies on direct observation and measurement of crack closure which can reveal the detailed variation of the crack tip opening/closing behavior with applied loading. Most of existing in-situ SEM testing methodologies are only able to focus on the observation of crack growth and tip deformation between different cycles [28,29]. The detailed investigations of the crack growth kinetics within one loading cycle are rarely found in the open literature. Zhang and Liu [15] proposed a novel in-situ SEM fatigue testing to investigate the fatigue crack growth mechanisms continuously within one cyclic loading. In Zhang and Liu [15], the crack opening stress (crack closure level) and subcycle crack growth rate are directly measured under the constant amplitude loading with $R=0.1$, which shows that crack closure has a significant impact on the fatigue crack growth. In this report, the in-situ SEM experiments for Al7075-T6 are performed under the variable amplitude loading in order to investigate the crack opening stress variation caused by single overload.

The report is organized as follows. First, the experimental equipment and the main procedure of the in-situ SEM fatigue crack growth testing are presented. Following this, the experimental results (the measurements of crack closure) are discussed in detail. Next, some conclusions and future work are given based on the current observations from the proposed experimental study.

2. In-Situ SEM Experiment

Experimental System and Specimen

The experimental set-up for the in-situ SEM experiment is shown in Fig. 1. It consists of a palm-sized tensile stage installed in a field emission SEM (JEOL-7400F). The tensile stage is manufactured by Ernest F. Fullam Inc., which is now merged to MTI Instruments Inc.. The maximum gage length between mechanical grips is about 27 mm, and the load capacity is 5 kN. The sub-stage is fixed in the SEM and the cyclic loading can be applied during the experiment. During the testing, the vacuum level is remained to be less than 9.3×10^{-5} MPa (gauge reading). Multiple resolution images are recorded during the testing for the measurements of crack length and the crack tip deformation behavior. However, because the stage will prevent the coupon from getting closer to the pole piece, the shortest working distant available is 16.5 mm. Post-processing of images is performed using a high performance workstation and the software package ImageJ [16].

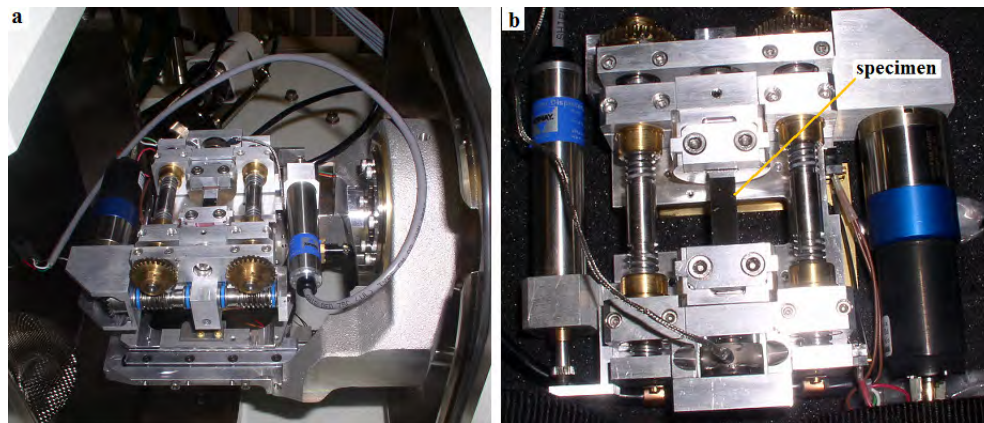


Fig. 1 In-situ SEM fatigue testing setup a) loading stage installed in SEM ;b) specimen installed in loading stage;

Single edge notched plate specimens with width $W \approx 8\text{mm}$, length $L \approx 52\text{mm}$ and thickness $T \approx 0.86\text{mm}$ made of aluminum alloy sheet (Al7075-T6) were tested. Due to the small thickness of specimens, it is typically under the plane stress conditions. The specimen design is shown in Fig. 2. An edge notch of length 1mm is machined on the specimens by slow saw cutting. After machining, the specimens are pre-cracked using a hydraulic testing machine INSTRON 1331 until the initial crack reaches about 1 mm. The pre-cracking procedure follows the ASTM standard E647-99. Following this, both surfaces of the specimen are polished with the sandpaper whose average particle diameter is smaller than 10 μm . Then the final polishing is done using a vibration polishing machine with 1~3 μm polishing suspension. The mechanical properties the chemical compositions of the investigated material are given in Table 1 and Table 2 respectively, which are reported by the manufacturer.

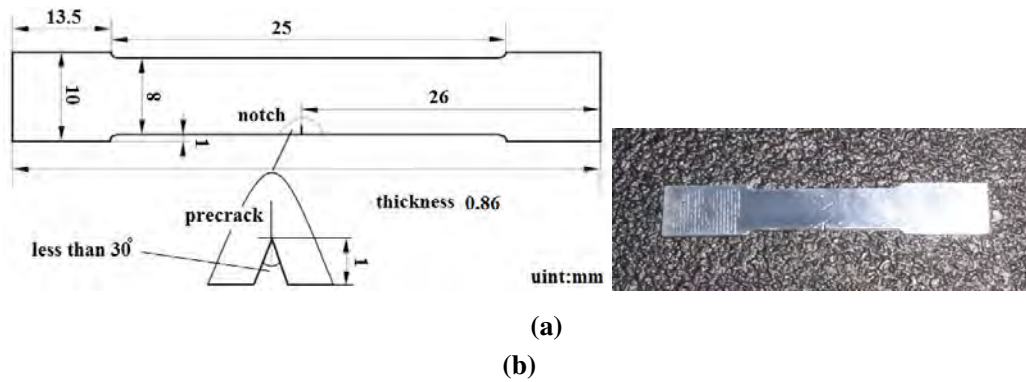


Fig. 2. Geometry of test specimen (a) the specimen design; (b) polished specimen.

Table.1 7075-T6 mechanical properties

Ultimate tensile strength	573~582 MPa
Tensile yield strength	502~516 MPa

Young's Modulus	71.7 GPa
-----------------	----------

Table.2 Chemical composition of 7075-T6

	Si	Fe	Cu	Mn	Mg	Cr	Zn	Ti	V	Zr	Other	Max
Min % weight	0.00	0.00	1.2	0.00	2.1	0.18	5.1	0.00	0.00	0.00	Each	0.05
Ma % weight	0.4	0.50	2.0	0.30	2.9	0.28	6.1	0.20	0.05	0.05	TOT	0.15

Experimental Procedure

Unlike the classical fatigue crack growth testing which usually uses cycle-based crack growth approaches, such as the well-known Paris law which defines the relationship between the average crack growth rate per cycle and the range of applied stress intensity factor, the proposed fatigue crack growth testing is based on a subcycle crack growth concept. It is to define the change in fatigue crack extension continuously throughout a cycle as a function of the change in the applied loading instead of using the cycle averaged crack growth. The proposed in-situ SEM testing is developed to investigate the crack tip behavior in the continuous time-domain and to measure the crack opening stress at the subcycle scale.

The specimen is loaded in the tensile stage under cyclic loading and observed in-situ under SEM. Considering the vacuum environment in SEM, the stage was run about 50 to 100 loading cycles in the chamber before the image acquisition.

A schematic loading profile for our the is shown in Fig. 3. This loading spectrum is a single overload spectrum, which consists of three parts: constant loading before the overload, single overload, and the constant load after the single overload. In the first part, R ratio is equal to 0.33, and the maximum applied stress intensity factor is

30 MPa-m^{0.5}. In the overload part, the overload ratio is 1.2. The overload ratio is defined as the maximum loading of the overload to the maximum loading of the constant amplitude loading. After the overload, the loading resumes to be the constant amplitude loading as before.

Due to the long time for the imaging acquisition, a proper experimental design is required to obtain the necessary information and minimizing the experimental durations. As shown in Fig. 3, four typical cycles (a~d) are designed to be investigated and recorded. Cycle 'a' represents the constant amplitude loading before the overload. The measurements of this cycle can serve as a baseline. Cycle 'b' is the overload cycle, and cycle 'c' is the constant loading right after the overload. From the comparison between cycle 'a' and cycle 'c', the effects left by the single overload can be obtained. The large plastic deformation and defects ahead of crack tip caused by overload may affect the CTOD observation in the cycle 'c' (the following cycle), and the crack growth in this cycle may be not stable. The cycle 'd' shown in Fig. 3 is used to measure the crack deformation and growth behavior 5-20 cycles after the single overload cycle.

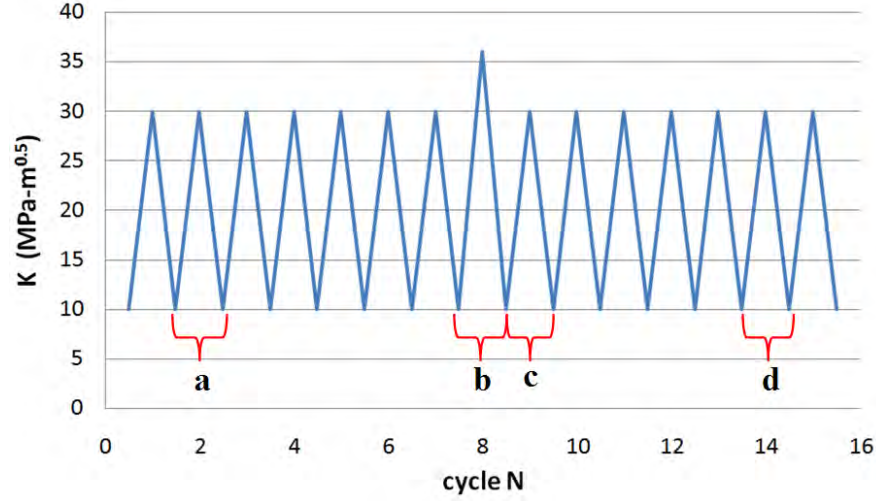


Fig. 3. Schematic representation of single overload spectrum

Each loading cycle of interest is divided into many steps as shown in Fig. 4. The applied loading increases/decreases at a slow rate. During the loading/unloading path, the stage will hold at each step for investigation. At each loading level, images of the crack tip are taken under very high magnification. Imaging analysis is performed to extract the useful information from these pictures, such as the crack tip position and crack tip opening displacement (CTOD). To obtain more accurate baseline cycle 'a', more than one constant loading cycles are investigated to observe the average behavior of the crack under the constant amplitude loading. In the experiment in the current study, three images at the continuous three peak loading levels are measured in the experiment, as shown in Figs. 5. The loading direction is indicated on the top of the images. Several reference markers along the crack surface are identified in images. Digital measures are performed to measure the distance between the new crack tip locations to old crack tip positions, as well as the CTOD. From these images, the average value of CTOD and crack growth per cycle can be obtained. In this report, we

are interested in the crack opening stress level, which can be evaluated by measuring the CTOD variation at the old crack tip position at each loading step, as shown in Figs. 6. In the figures, the brackets indicate the CTOD at the current loading level. The applied loading keeps increasing from the minimum (Fig. 6.1) to the maximum (Fig. 6.6). It is shown that the crack tip remains closed at the beginning of the loading path (see Fig. 6.1 and Fig. 6.2). After that, the crack tip starts to open and become wider gradually (see Figs. 6.3-6.6).

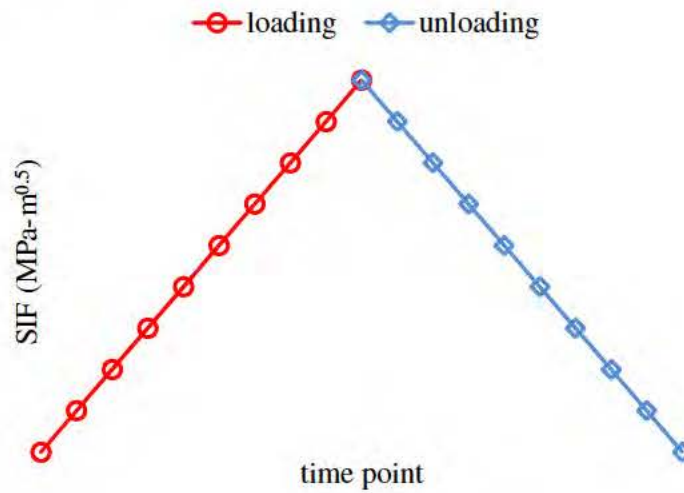
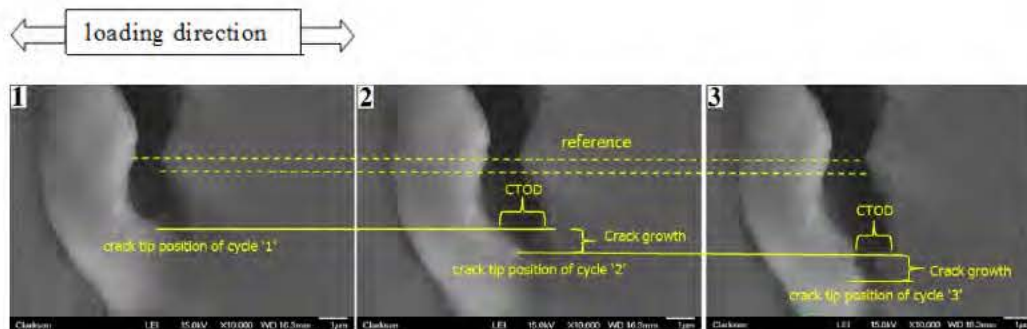
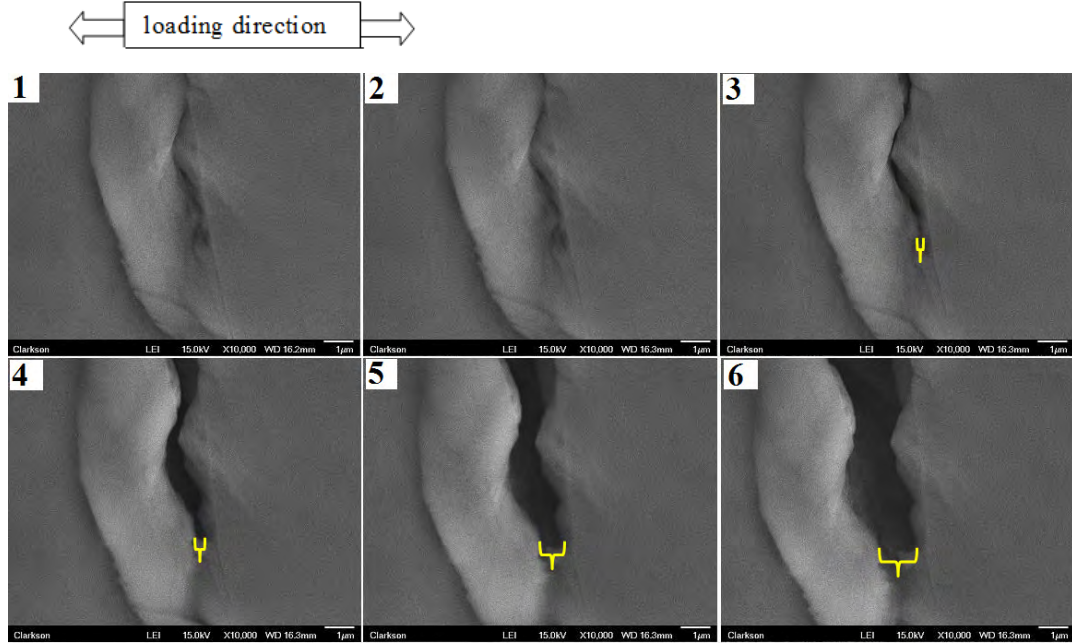


Fig. 4. Schematic representation of imaging recording points in a complete loading cycle



Figs. 5. Images of crack tip position and CTOD under maximum loadings

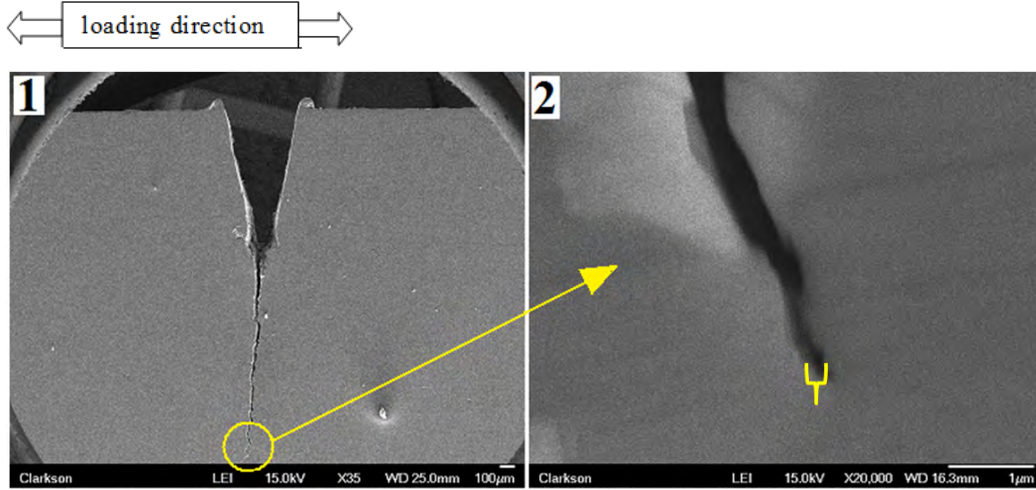


Figs. 6. Images of CTOD variation at different loading steps

3. Experimental Results and Discussions

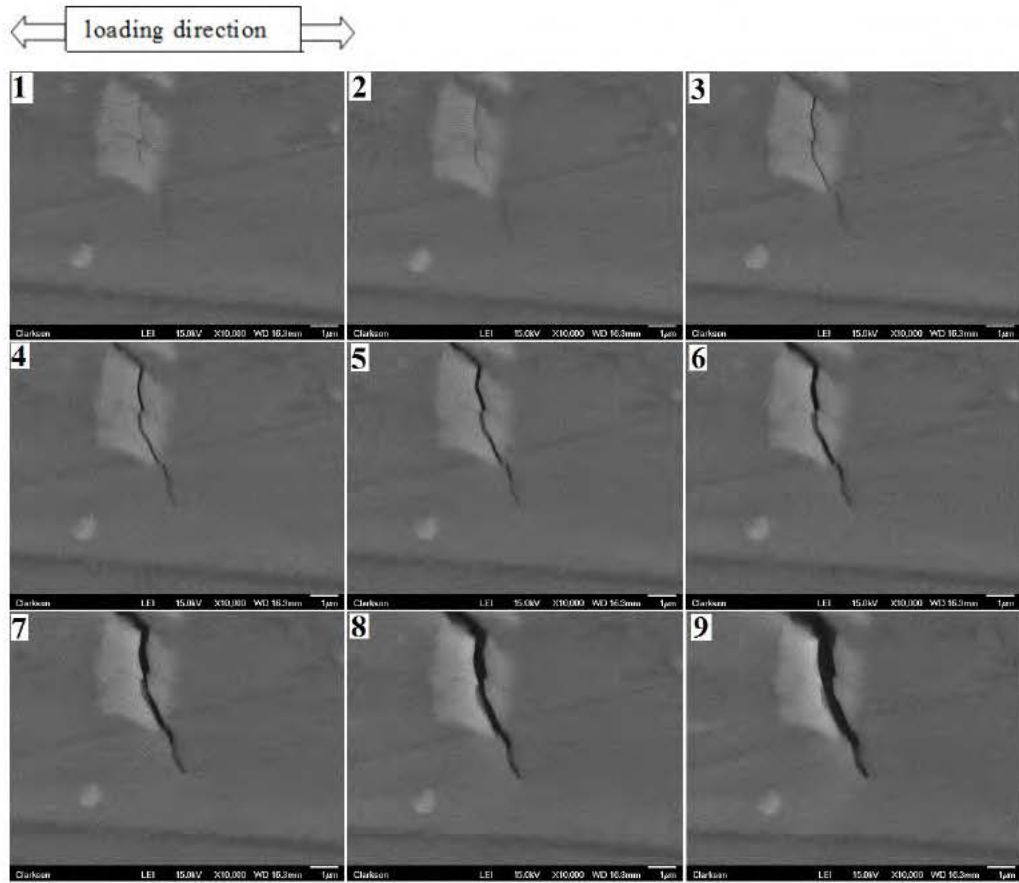
In this section, experimental observations and imaging analysis results of two variable loading cases are presented: 1) stress ratio of 0.33 with an overload ratio of 1.2; 2) stress ratio of 0.025 with an overload ratio of 1.1. The first case is discussed in detail. Following this, similar findings from the second cases are also discussed.

Figs. 7 shows the overview and the detailed tip images of the first case. In this testing, the R ratio of the constant amplitude part is 0.33. The overload ratio is 1.2. The maximum stress intensity factor is about $K_{\max}=36.2\text{MPa}\cdot\text{m}^{0.5}$.



Figs. 7. Multi-resolution SEM images of crack ($R=0.33$, $K_{\max}=36.2\text{MPa}\cdot\text{m}^{0.5}$)

According to the previously discussed experimental procedure, two constant amplitude loading cycles before the single overload are firstly investigated as the baseline. Fig. 8 shows the details of the crack tip behavior during the loading path of the first cycle. It is clear that the crack starts to open between the loadings of Fig. 8-4 and Fig. 8-5. Collecting all the measurements of CTOD of these two cycles, two curves are obtained as shown in Fig. 9. The y -axis is the CTOD and the x -axis is the corresponding stress intensity factors. Different symbols represent different cycles. The trend and maximum values of both two plots are almost the same which indicates the acceptable error of the measurements. It can be seen clearly that the crack tip opens at the stress level approximately $(57\pm 2.5)\%$ of the maximum loading.



Figs. 8. Illustration of crack tip behavior ($R=0.33$, $K= 12.1, 16.1, 18.1, 20.1, 22.1, 24.1, 27.1, 30.2$ and $36.2 \text{ MPa}\cdot\text{m}^{0.5}$ for figures 1-9, respectively)

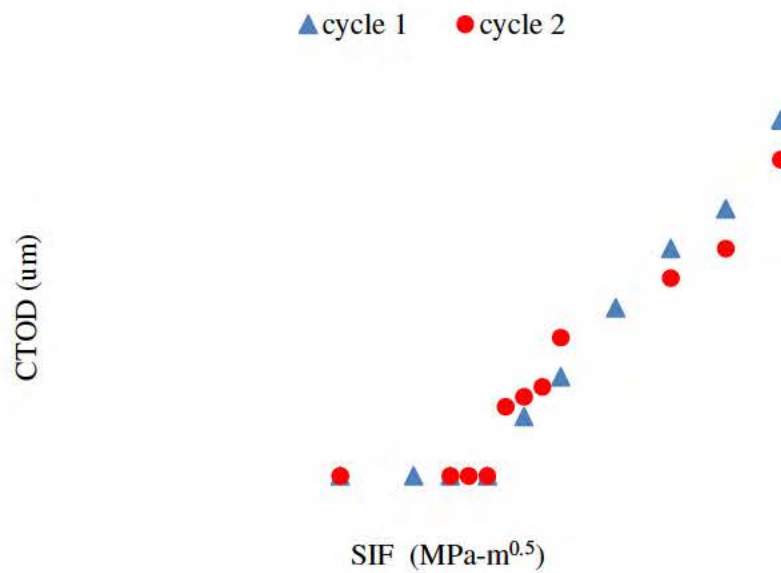
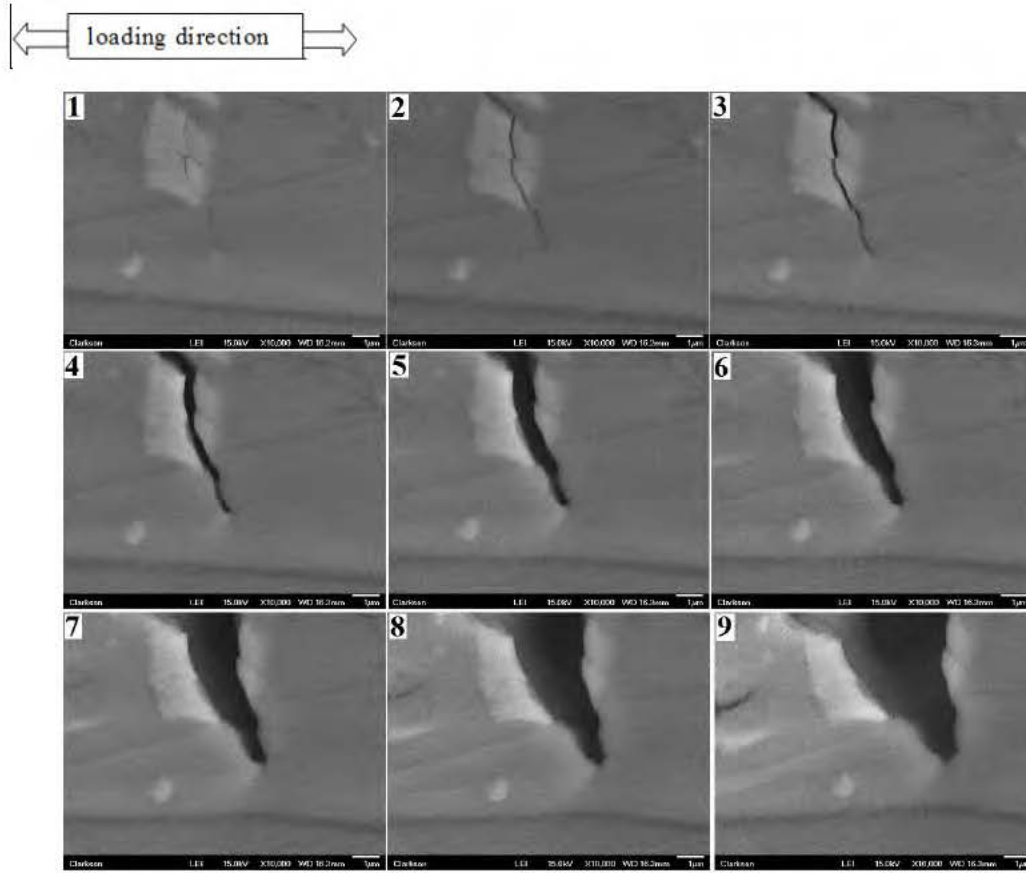


Fig. 9. CTOD variation at each loading step before overload

The crack tip deformation behavior during the single overload is also investigated. Fig. 10 shows the crack tip behavior under the single overload. It is observed that the crack starts to open between the loadings of Fig. 10-2 and Fig. 10-3 (approximate 57% of the maximum loading), which is consistent with the above observations under constant amplitude loading. Once the applied loading exceeds the maximum loading level of the previous constant loading, as shown in Figs. 10.7-10.9, the CTOD increases very fast and the crack tip becomes very blunt. The corresponding measurements are illustrated in Fig. 11. This behavior is consistent with the classical fracture mechanics and finite element simulations [17]. The reason for the fast CTOD change is because the compressive plastic zone is fully reversed by the large overload and the CTOD is controlled by the monotonic plastic zone size rather than the reversed plastic zone size.



Figs. 10. Illustration of crack tip behavior under overload ($R=0.33$, $K=12.1, 20.1, 22.1, 24.1, 30.2, 36.2, 39.2, 41.2$ and $43.4 \text{ MPa}\cdot\text{m}^{0.5}$ for figures 1-9, respectively)

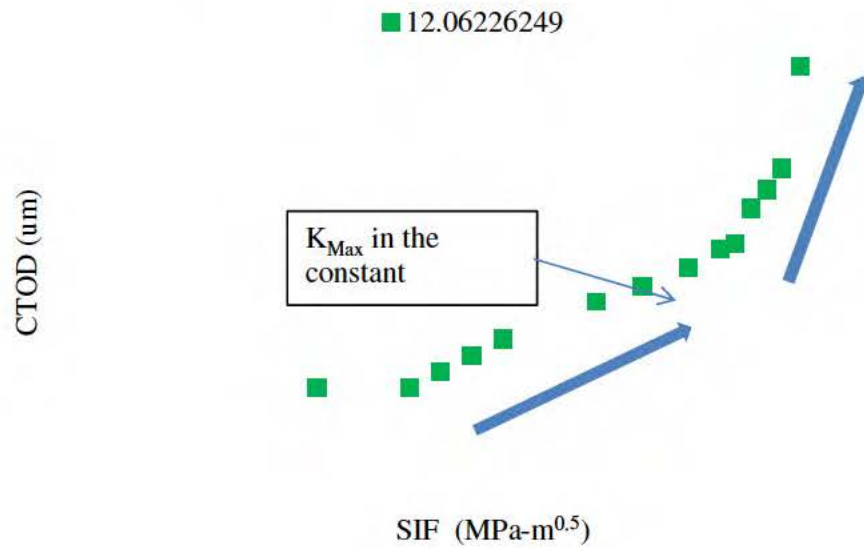
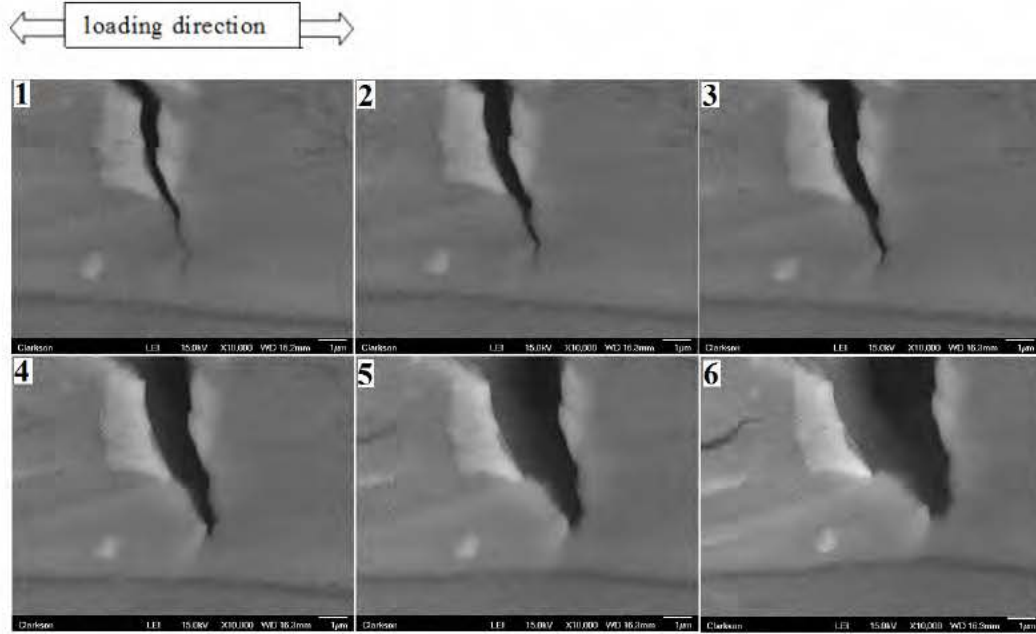


Fig. 11. CTOD variation at each loading step under overload

From the images, it is observed that very large plastic deformation occurs ahead of the crack tip during the overload although the material is not fractured yet. The large plastic deformation causes extra damage and makes the material “weaker” than the virgin materials. This weakened material will affect the crack growth behavior after the overload cycle significantly. The images for the cycle following the overload are observed, as shown in Figs. 12. One interesting thing is observed that the crack closure happens only in the very vicinity behind the crack tip. If Fig. 10 and Fig. 12 are compared with each other at the same loading level, it is clearly seen that the crack closure behavior largely diminished. The crack surfaces behind the crack tip (to about 1~2 μm) still contact and the crack opening stress is similar to the previous constant amplitude loading cycles, as shown in Fig. 13. Fig. 13 also shows that the maximum CTOD value is much larger than that under the constant amplitude loading before the overload cycle (see Fig. 13 and Fig. 10). This behavior could be caused by two reasons: 1) the material ahead of the crack tip is weakened during the overload and its resistance to deformation is less; 2) the largely reduced crack closure causes the increased CTOD since load cannot be transferred through the crack surfaces. It is likely the increased CTOD value is caused by both of them.



Figs. 12. Illustration of crack tip behavior next to the overload ($R=0.33$, $K= 12.1, 18.1, 20.1, 24.1, 30.2$ and $36.2 \text{ MPa-m}^{0.5}$ for figures 1-6, respectively)

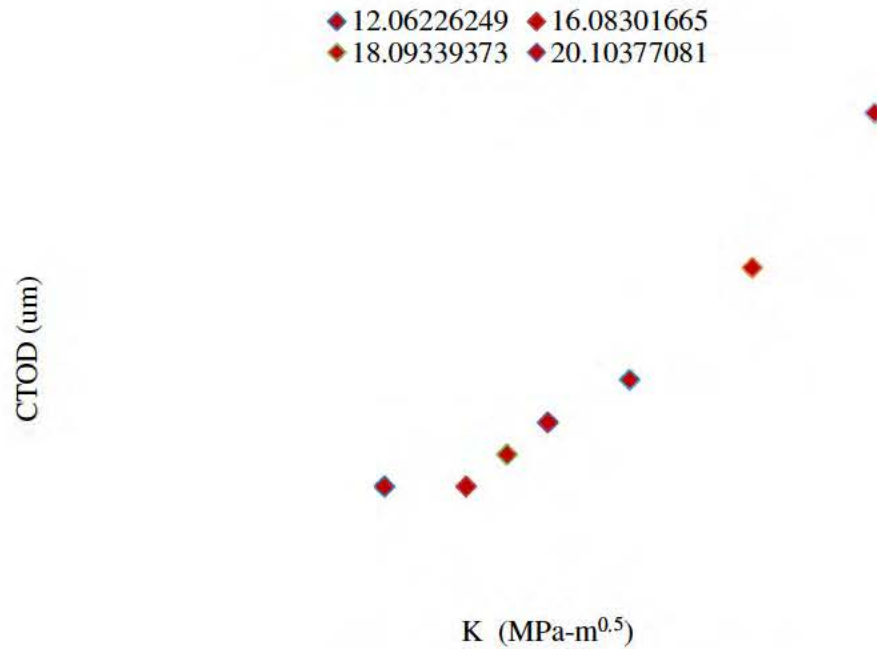
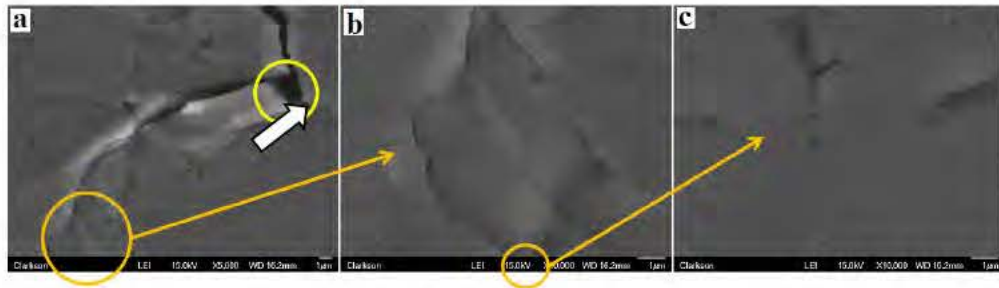


Fig. 13. CTOD variation at each loading step of the next cycle

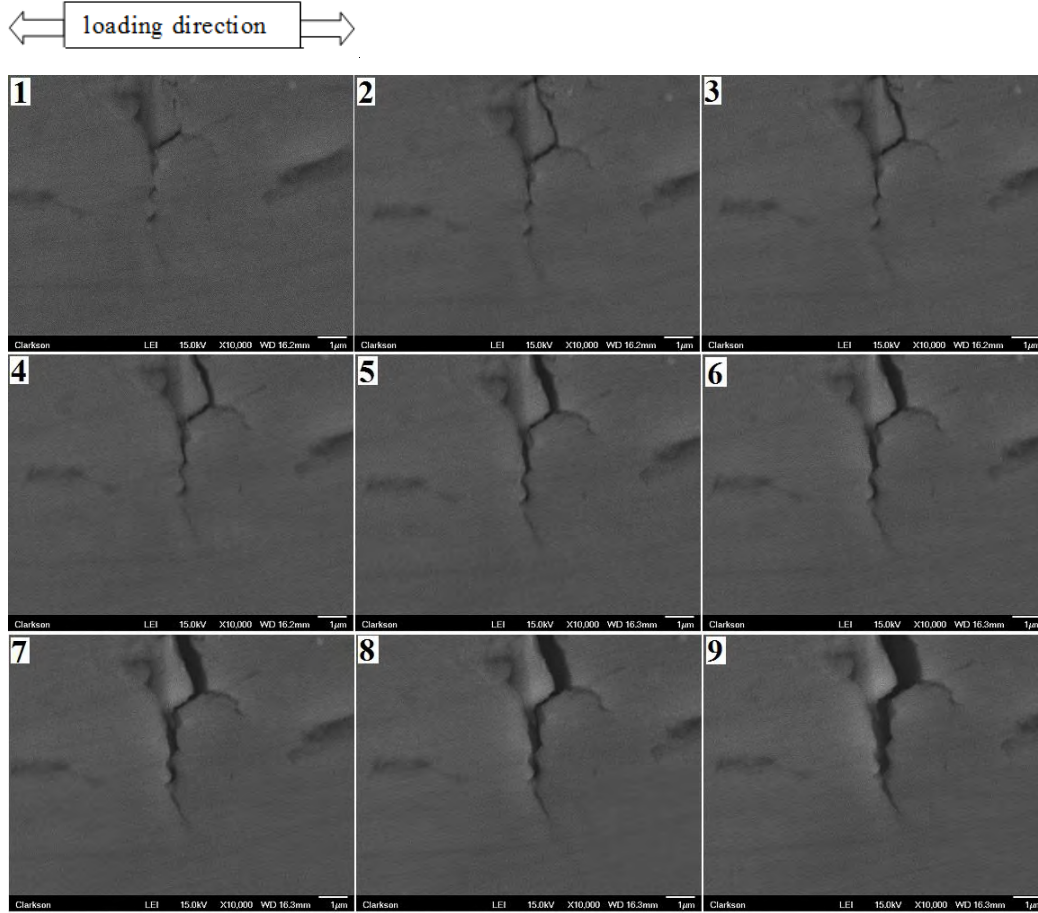
In the following several cycles, the crack growth becomes unstable and very fast, as shown in Fig. 14. The large white arrow indicates the crack tip position of the

overload. The crack kinks and bifurcates after the overload within about 5 cycles. Figs. 14 (c) show a stable crack tip forms again after 11 cycles (about 25 microns unstable growth). This observation supports that the extra damages caused by the overload will lead to a rapid and unstable crack growth in a small area. This also supports one of the mechanism models for the crack retardation after the single overload cycle using the crack kinking hypothesis [18].



Figs. 14. Crack path after the overload (11cycles)

The unstable crack growth right after the overload is considered to be very short time transient process and it will only last for a very short length. This is mainly due to the remaining damage from the overload cycle. After the crack grows out of the affected damaged zone and becomes stable again, the crack tip behavior should be examined to observe the effect from the large plastic zone/residual stress left from the overload cycle. Images 10 cycles after the overload are shown in Figs. 15-16. As shown in Figs. 15 and Fig. 16, it is observed that the crack opening stress level increases significantly and the CTOD values becomes smaller. As a result, the crack growth is slowing down and is known as crack growth retardation.



Figs. 15. Illustration of crack CTOD measurement after overload ($R=0.33$, $K= 12.1$, 16.1, 18.1, 20.1, 22.1, 24.1, 27.1, 30.2 and 36.2 $\text{MPa}\cdot\text{m}^{0.5}$ for figures 1-9, respectively)

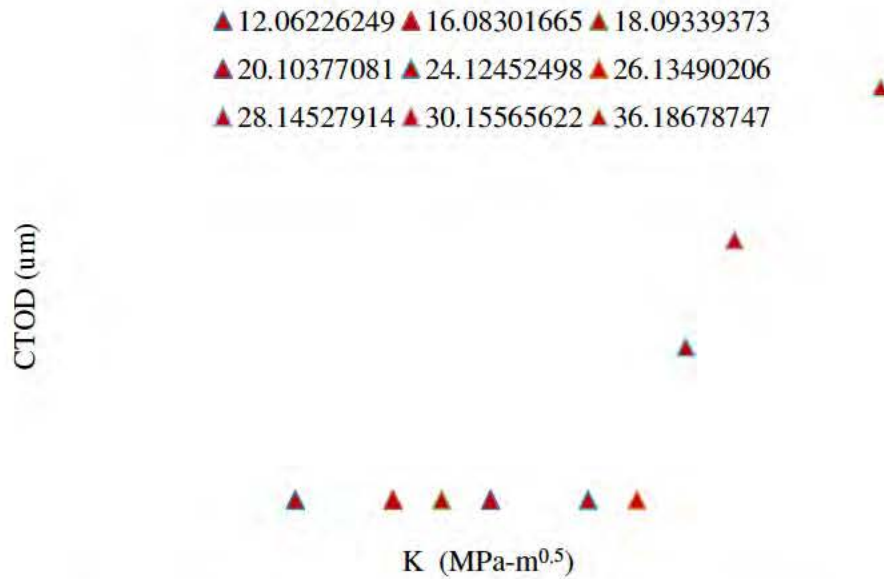


Fig. 16. CTOD variation at each loading step after overload (11cycles)

To compare the variation of crack opening stress level before and after the single overload more quantitatively, all measured crack opening stress levels are plotted in Fig. 17. The y-axis is the ratio between the crack opening stress level and the maximum loading level. The x-axis is the corresponding loading cycle numbers. The rectangular symbol represents the overload cycle and is marked in the Figure. From the first three data points, it is clear that the crack opening stress level is approximately 57% of the maximum loading without effects left by the overload. The forth diamond symbol is slightly smaller than before (the cycle right after the overload). After a dramatically fast growth, the crack growth resumes the stable crack growth. It shows that the increased crack opening stress level is about 75% of the maximum loading. Before the overload, the observed crack growth per cycle is always larger than 0.1 um, but after the unstable crack growth after the overload, it is

hard to measure the crack growth per cycle which is smaller than 20 nanometers based on the current experimental instrumentation.

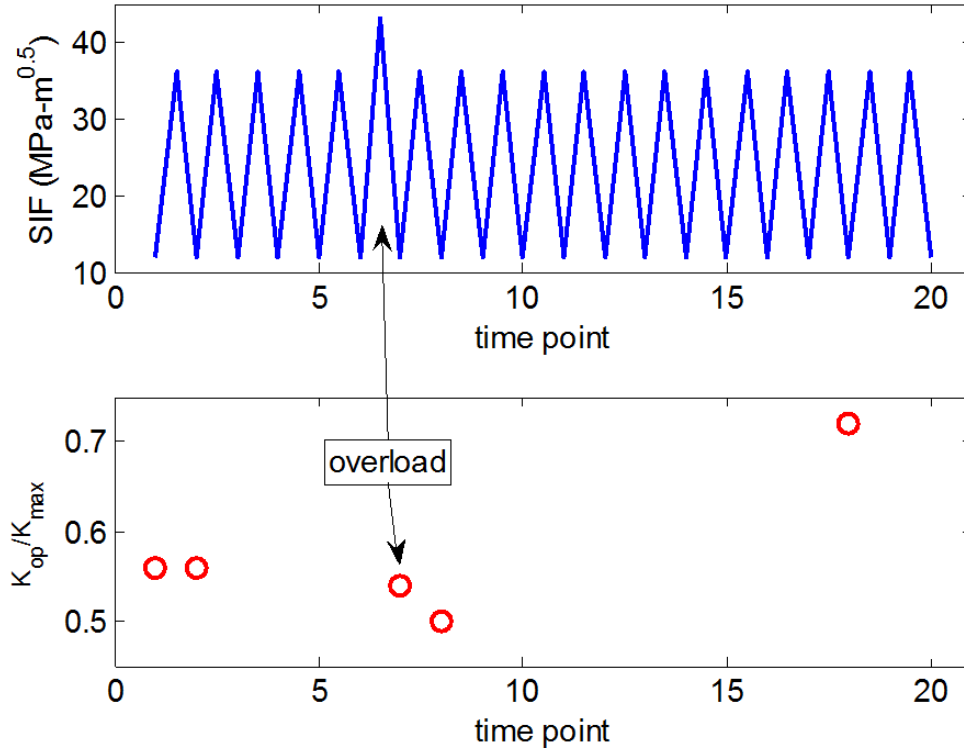


Fig. 17. Illustration of the crack opening stress level variation (R=0.33)

A similar testing is performed with different R ratio and overload ratio. In this testing, R ratio is 0.025 and the maximum loading is $34 \text{ Mpa-m}^{0.5}$. The overload ratio is 1.1. Very similar behaviors are observed, i.e., unstable crack growth right after the overload due to large plastic deformation and increased crack opening stress level after the unstable crack growth. In Fig. 18, it is shown that before the overload the crack opening stress level is 32% of the maximum loading. After the single overload and another 20 cycles, the measured crack opening stress level is about 37% of the maximum loading. Before the overload, the observed crack growth per cycle is

around 1.4 μm . After the unstable crack growth after the overload, it is approximately about 1 μm .

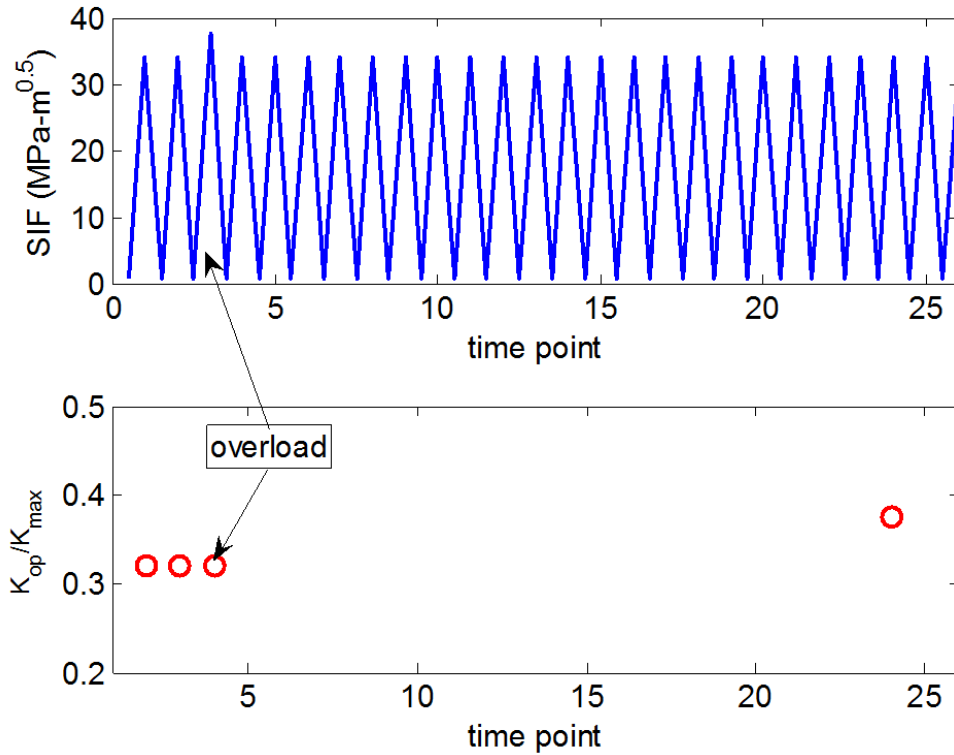


Fig. 18. Illustration of crack opening stress level variation ($R=0.025$)

4. Conclusion and Future Work

An innovative experimental methodology using in-situ fatigue testing under SEM is performed in this report. Experimental testing are designed and performed for Al-7075-T6 under both constant amplitude loading and single overload spectrums. Extensive imaging analysis is performed to measure the crack tip deformation and crack growth behavior. Several major conclusions can be drawn based on the proposed experimental study.

- Crack closure phenomenon is observed under both constant amplitude loading and single overload spectrums;
- CTOD increases very fast during the overload cycle after the loading exceeds the maximum loading level in the previous constant amplitude loading;
- Very large plastic deformation is observed during the overload cycle and makes the crack growth right after the over load unstable;
- Crack growth right after the overload is fast and unstable. Crack kinking and bifurcation is also observed;
- Crack closure disappears or is largely reduced right after the overload. Most crack surfaces remain open during the entire loading cycle;
- After the unstable crack growth right after the overload, the crack opening stress increases compared to the value in the pure constant amplitude loading, which is accompanied with the reduced crack growth rate.

The proposed study focuses on the constant amplitude loading and simple variable loading spectrums. More complex loading spectrums need further study. The application of the proposed technique and procedure to other material systems will greatly help the fundamental understanding of fatigue mechanism at the sub-cycle scale. Other experimental instrumentation designs suitable for very high resolution (i.e., around 1 nanometer scale) will be very valuable when the crack growth per cycle is extremely small (i.e., near the threshold regime). In addition, the statistical effects of the sub-cycle crack

growth measurements and analysis needs further study.

Acknowledgements

The research reported in this part was supported by funds from Air Force Office of Scientific Research: Young Investigator Program (Contract No. FA9550-11-1-0025, Project Manager: Dr. David Stargel). The support is gratefully acknowledged.

References

1. Paris P, Erdogan F. A critical analysis of crack propagation laws. *J Basic Eng* 1963; 90:528–534.
2. Elber W. Fatigue crack closure under cyclic tension. *Eng Fract Mech* 1970; 21:37–45.
3. Budiansky B, Hutchinson JW. Analysis of closure in fatigue crack growth. *ASME J Appl Mech* 1978; 45:267–76.
4. Wheeler, O. (1972). "Spectrum loading and crack growth". *Journal of basic engineering*. 94: pp. 181-186.
5. Willenborg, J., Engle, R.M. and Wood, H.A. 1971. "A Crack Growth Retardation Model Using an Effective Stress Concept". Air Force Flight Dynamics Laboratory: Wright-Patterson Air Force Base, Ohio.
6. Zhang JZ, Bowen P. On the finite element simulation of three-dimensional semi-circular fatigue crack growth and closure. *Eng Fract Mech* 1998;60(3):341–60.
7. Llorca J, Sanchez Gavez V. Modelling plasticity-induced fatigue crack closure. *Eng Fract Mech* 1990;37(1):185–96.
8. Gdoutos EE. Modelling fatigue crack closure using dislocation dipoles; 2006. p. 249–50.
9. Newman JC. A crack-closure model for predicting fatigue crack growth under aircraft spectrum loading. In: *NASA Technical Memorandum* 81941; 1981, pp. 1743–51.
10. Newman JC. A crack opening stress equation for fatigue crack growth. *Int J Fatigue* 1984, Vol. 24, pp.131-135.
11. Kim JH, Lee SB. Behavior of plasticity-induced crack closure and roughness induced crack closure in aluminum alloy. *Int J Fatigue* 2001;23 (Suppl. 1):247–51.
12. Sutton, M.A., Zhao, W, McNeill, S.R., Helm, J.D., Riddell, WT., and Piascik, R.S., "Local Crack Closure Measurements: Development and Application of a Measurement System Using Computer Vision and a Far-Field Microscope," *ASTM STP 1343 on Crack Closure Measurements*, K. Smith and J. McDowell, eds., 145-156 (1999).

13. Halliday MD., Poole P., and Bowen P., "In situ SEM measurements of crack closure for small fatigue cracks in aluminum 2024-T351" , *Fatigue Fract. Eng. Mater. Struct.*, Vol. 18 (6), 1995, pp. 717–729.
14. Andersson H., and Persson C., "In-situ SEM study of fatigue crack growth behavior in IN718", *International Journal of Fatigue*, Vol. 26 (3), 2004, pp. 211-219.
15. Zhang W. and Liu Y., "Investigation of incremental fatigue crack growth mechanisms using in situ SEM testing ", *International Journal of Fatigue*, 2011, in press .
16. <http://rsbweb.nih.gov/ij/>
17. Becker W., "Closed-form modeling of the unloaded mode I Dugdale crack", *Engineering Fracture Mechanics*, 1997. 57(4): p. 355-364.
18. Suresh S., "Micromechanisms of fatigue crack growth retardation following overloads", *Engineering Fracture Mechanics*, 1983. 18(3): p. 577-593.

Appendix 4: Accomplishments for Task 1.2 &1.3

Time domain strain and stress reconstruction for fatigue damage

prognostics

Jingjing He¹, Xuefei Guan², Wei Zhang¹, Yongming Liu^{1*}

¹ *School for Engineering of Matter, Transport, and Energy, Arizona State University,
Tempe, AZ 85281, USA*

² *Siemens Corporate Research, Princeton, NJ 08540, USA*

ABSTRACT: In this study, a novel structural fatigue prognosis method is developed to provide prompt, informed fatigue damage predictions of the structures based on strain gauge measurements at remote locations. The method is based on the structural responses reconstruction at the hot spots and a mechanism-based fatigue crack growth formulation. The structural responses measured from usage monitoring system or sensors at available locations are decomposed into modal responses using empirical mode decomposition. Transformation equations based on finite element modeling are derived to extrapolate the modal responses from the measured locations to critical locations where direct sensor measurements are not available. The evolution of fatigue damage within structures can then be performed using the reconstructed stress responses. A numerical two-span beam example is used to demonstrate the overall reconstruction method. Following this, a practical structure scale problem is provided to validate the effectiveness and the accuracy of the proposed method. Fatigue damage prognosis using the reconstructed stresses from remote strain gauge measurement data is also demonstrated with detailed error analysis.

KEYWORDS: Strain response reconstruction; Stress response reconstruction; Fatigue damage prognostics; Empirical mode decomposition.

1. Introduction

Structural health monitoring (SHM) is one of the key components in recent engineering systems, civil infrastructures, and smart structures [1-3]. Due to the increasing complexity and high reliability demand of those systems, damage and system performance degradation need to be quantified accurately for maintenance purposes [4, 5]. To monitor the status of a target system, measurements about system condition variables are taken either by sensors installed on the system or field non-destructive inspections [6-8]. In particular, using smart sensors for structural health monitoring has drawn a lot of attentions in the SHM community due to flexibilities of smart sensors and advances in composite materials [8-11]. A commonly used classification system for damage identification methods defines four levels of damage identifications: 1) determine the existence of the damage in the structure; 2) identify the location of the damage; 3) quantify the severity of the damage; and 4) estimate the remaining life the system [12]. The difficulty of having a reliable result increases as the system complexity increases. Therefore, obtaining an accurate estimation of the remaining useful life of a damaged system is a practical challenge. For most mechanical systems subject to fatigue loads, fatigue crack propagation is one of major failure mechanisms. Fatigue damage is highly dependent on the applied stress history under realistic service conditions. The practical challenge for fatigue life prediction in such cases is that the stress and fatigue load in the vicinity of the fatigue crack is very difficult to infer. Direct measurement of the stress

or strain in the damaged location is very difficult because the damage location is not known a priori [13]. Furthermore, it is highly nontrivial to place additional sensors at the damaged spot because the local geometry of the damage spot may be very complex to install a new sensor and the service condition of the system may not allow one to install new sensors. Using measurements from pre-installed sensors to infer the information about the critical spot, i.e., a fatigue crack damaged location without direct sensor measurements, may be the only practical option in realistic situations. Therefore, extrapolation to a critical spot from measurements located in a remote spot is a mandatory step for fatigue prognostics and the remaining life prediction. Recent advances of dynamical response extrapolation include frequency-domain methods and direct time-domain methods. Several studies suggest using the concept of transmissibility [14-16]. The basic idea is to define a transformation function between the measurement spot and the desired spot. The method requires a minimal number of locations to obtain the dynamical responses of the desired spot. Direct time domain reconstruction of dynamical responses for acceleration, velocity and deflection includes empirical mode decomposition (EMD)-based method [13]. The basic idea of EMD-based time-domain reconstruction method is to decompose the measurement data using EMD approach [17] with the intermittency criteria. The extrapolation function from a measurement spot to a desired spot is based on the ratio of the two positions in the mode shape of the structural model. Because strain and stress has no direct correspondence in mode shape matrix, these methods cannot be directly applied to obtain the strain and stress responses for fatigue crack growth analysis.

The objective of the study is to develop a direct time domain strain and stress reconstruction method for fatigue damage prognostics using sparse and remote sensor measurements. The proposed method extends the previous EMD-based time-domain reconstruction method by using the finite element model to derive a strain transformation function in modal coordinates. EMD method with intermittency criteria is first employed in the proposed method to decouple the remote strain measurements into modal coordinates, and the extrapolation of the strain and stress responses is made using the strain and stress transformation function. Mode superposition is used to obtain the strain and stress responses of the critical spot for fatigue crack growth analysis and fatigue life prediction. The overall method is demonstrated using a two-span beam-like structure. A more complex 216-degree of freedom (DOF) spatial frame structure is used to further investigate the effectiveness and performance of the method under different signal-to-noise ratios. Reconstruction results are compared with theoretical solutions.

The paper is organized as follows. First, the EMD method for signal decomposition is briefly introduced, and the required signal filtering process using the intermittency criteria is discussed. Next, the transformation equation for strain and stress is derived using the FE model of the structure. Following this, a numerical two-span beam-like structure and a spatial frame structure are used to demonstrate and validate the proposed method. The fatigue crack growth analysis and fatigue life prediction using the reconstructed stress is calculated and compared with theoretical solutions. Finally, conclusions are drawn based on the current study.

2. Strain and stress reconstruction methodology

The proposed strain and stress reconstruction method is based on three pieces of information: The measurement data from one or multiple strain gauges, the structural model, and locations of measurement locations and the sensor inaccessible locations. The overall process for the reconstruction involves several steps, as illustrated in Fig. 1. Details of each of the calculation steps are discussed in this section.

2.1 Extraction of modal responses from measurement data using EMD method

The first step of the reconstruction method is to decompose the measured time domain signals from strain gauges into a set of responses in the modal coordinates. This step can be made using empirical mode decomposition (EMD) method with intermittency criteria. For the completeness of the paper, the EMD method with intermittency criteria is briefly introduced.

The basic idea of EMD method is to break down the original signal into a set of intrinsic mode functions (IMF) and a residual term. An IMF is a function that has a mean value of zero and only one extreme between zero crossings. The IMFs form a complete and nearly orthogonal basis for the original signal, allows for varying frequency in time to be preserved, which is hidden in the Fourier domain or in wavelet coefficients [17]. For a given time series data $y(t)$, the EMD method uses the following sifting process to obtain IMFs [17]:

1. Identify the local maxima or minima of $y(t)$, denoted by y_+ and y_- respectively.
2. Cubic-spline interpolate using y_+ and y_- to obtain two envelopes $e_+(t)$ and $e_-(t)$, denote the mean of the two envelopes as $m_1(t) = [e_+(t) + e_-(t)]/2$

3. Compute $h(t) = y(t) - m(t)$
4. If $h(t)$ is not an IMF, continue the sifting process using $h(t)$ as the new signal data through Steps 1-3. The stopping criterion is

$$\sum_t \frac{[h_k(t) - h_{k-1}(t)]^2}{h_{k-1}^2(t)} < \varepsilon,$$

where $h_k(t)$ is the sifting result in the k th iteration, and ε is a small value between 0.2 and 0.3. The resulting $h_k(t)$ is an IMF, denoted as $f_1(t)$.

Repeat the above steps to get the second IMF $f_2(t)$ from the residue $y(t) - f_1(t)$.

Continue the computation to obtain up to the n th IMF until the remaining of the signal

$r(t) = y(t) - \sum_{i=1}^n f_i(t)$ is a mono-component, which indicates that the number of

up-crossings (or down-crossings) of zero is equal to the number of peaks. The original signal $y(t)$ now can be expressed as the summation of n IMFs and a residual term, as shown in Eq. (1).

$$y(t) = \sum_{i=1}^n f_i(t) + r(t), \quad (1)$$

where $f_i(t)$ is the i th IMF and $r(t)$ is the residue. Term $r(t)$ also represents the mean trend or constant for this signal [18].

Each of the IMFs obtained from the above standard sifting process may contain several frequency components, and is not a good approximation to the modal responses. To ensure each of the IMFs contains only one frequency component (i.e., the modal responses corresponding to some natural frequency), an intermittency frequency denoted by ω_{int} must be imposed in the sifting process. The idea is to

remove all frequency components lower and larger than ω_{int} , and this can be done prior to or within the sifting process using a band-pass filter. The process to obtain the modal response corresponding to the i th natural frequency ω_i is discussed in [18] and is summarized here:

1. An approximate range for ω_i , $\omega_{iL} < \omega_i < \omega_{iH}$ is estimated either by Fourier transform of $y(t)$ or finite element model computations.
2. Process the signal data $y(t)$ using a band-pass filter with a frequency range $\omega_{iL} < \omega_i < \omega_{iH}$.
3. Process the filtered signal using the standard sifting process described above.

By repeating the above procedure with different frequency ranges for different natural frequencies, all modal responses can be obtained. These IMFs have several characteristics: 1) Each IMF contains the intrinsic characteristics of the signal; 2) Once an IMF is obtained, the next IMF will not have the same frequency at the same time instant [19, 20]; and 3) The first IMF for each IMFs series is considered to be the approximation of modal response. Using the sifting process with intermittency criteria, the original signal expression can be written as Eq. (2).

$$y(t) \approx \sum_{i=1}^m x_i(t) + \sum_{i=1}^{n-m} f_i(t) + r(t), \quad (2)$$

where $x_i(t)$ is the modal response (that is also an IMF) for the i th mode. Terms $f_i(t)$ ($i = 1, \dots, n-m$) are other IMFs but not modal responses.

2.2 Transformation equations for strain and stress responses

To reconstruct the strain and stress responses at a location (without direct measurements) using strain gauge measurement data from a remote location, transformation equations are needed to establish the physical relationship between the two locations. For a general structure, finite element model (FEM) can be used as the structural model to derive transformation equations. Consider a general FEM describing a structure under analysis, the system dynamics equation can be expressed as

$$\mathbf{M}\ddot{\mathbf{X}} + \mathbf{C}\dot{\mathbf{X}} + \mathbf{K}\mathbf{X} = \mathbf{F}, \quad (3)$$

where \mathbf{M} , \mathbf{K} and \mathbf{C} are mass, stiffness, and damping matrices, respectively. \mathbf{X} is the displacement vector and \mathbf{F} is the load vector. For practical structures subject to stochastic excitations, \mathbf{F} is unknown and direct solving Eq. (3) to obtain the dynamical responses of a sensor inaccessible location is not possible. However, the finite element method allows for correlating displacement responses of two different DOFs in the modal coordinates through the mode shape matrix. The mode shape matrix can readily be obtain by solving the eigenvalue problem of

$$[\Phi, \lambda] = \text{eig}([\mathbf{M}^{-1}\mathbf{K}]), \quad (4)$$

where Φ and λ are the eigenvectors and eigenvalues, respectively. Φ (Eq. (5)) is also referred to as the mode shape matrix. λ corresponds to the natural frequencies of the structure, i.e., $\lambda = (2\pi\mathbf{f})^2$ where \mathbf{f} is the vector of natural frequencies.

$$\Phi = \begin{bmatrix} \phi_{11} & \cdots & \phi_{n1} \\ \vdots & \ddots & \vdots \\ \phi_{1n} & \cdots & \phi_{nn} \end{bmatrix} \quad (5)$$

The physical meaning of Φ can be interpreted as follows: each column of Φ represents a mode and each component in the column represents the displacement contribution of a DOF in the structure. For example, ϕ_{ij} represents the displacement contribution from DOF j under mode i . Since the model shape matrix is a constant once the number of the DOF and the discretization topology of the structure are determined, the ratio of displacement contribution of one DOF to that of another DOF is also a constant. This characteristic indicates that the responses of one DOF under modal coordinates allows for the calculation of responses of another DOF under modal coordinates. Denote the responses under modal coordinates as δ_{ij} , where i and j represents the mode index and the DOF index, respectively, The physical meaning of the modal response relationship between two DOFs can be expressed as

$$\frac{\phi_{ie}}{\phi_{iu}} = \frac{\delta_{ie}}{\delta_{iu}}, \quad (6)$$

where the subscript e represents the DOF (location) which physical responses can be measured by sensors and u represents the DOF that is inaccessible for sensor measurements. $\delta_{ij}(t)$ corresponds to the modal responses components for the overall physical displacement responses of $\mathbf{X}_j(t)$ for DOF j at a time index t . If the physical displacement responses of the DOF e having sensor measurements can be decomposed into its modal responses, i.e., $\mathbf{X}_e(t) \approx \sum_{i=1 \dots m} \delta_{ie}(t)$, using Eq. (6), the physical displacement responses of the sensor inaccessible DOF u can be obtained as

$$\mathbf{X}_u(t) \approx \sum_{i=1 \dots m} \left[\delta_{ie}(t) \left(\frac{\phi_{ie}}{\phi_{iu}} \right)^{-1} \right], \quad (7)$$

where $i = 1 \dots m$ denotes the participating modes. It should be noted that Eq (7) holds for displacement $\mathbf{X}(t)$, velocity $\dot{\mathbf{X}}(t)$, and acceleration $\ddot{\mathbf{X}}(t)$, but it cannot be directly applied to reconstructions for strain and stress responses. Since Eq. (6) holds true for any arbitrary two DOFs, a more general equation can be obtained for any given time index t :

$$\Phi_i = \alpha \delta_i, \quad (8)$$

where Φ_i is the i th column vector in the mode shape matrix Φ , δ_i is the i th modal responses for all DOFs, α is a scalar constant for a given time index t .

Denote the strain and stress responses for an element (in the FE model) indexed by k at time index t as $\boldsymbol{\epsilon}^{(k)}$ and $\boldsymbol{\sigma}^{(k)}$. From the finite element formulation, the strain and displacement has the following relationship:

$$\boldsymbol{\epsilon}^{(k)} = \mathbf{B}^{(k)} \cdot \mathbf{X}^{(k)}, \quad (9)$$

where $\mathbf{B}^{(k)}$ is the *strain-displacement* matrix for element k and $\mathbf{X}^{(k)}$ is the displacement response vector consisting of all DOFs of element k . The expression of $\mathbf{B}^{(k)}$ usually has the format of

$$\mathbf{B}^{(k)} = \mathbf{L} \mathbf{N}^{(k)}, \quad (10)$$

where \mathbf{L} is the differential operator and $\mathbf{N}^{(k)}$ is the matrix of shape functions for element k . Using Eq. (8), the following equation is obtained under modal coordinates:

$$\mathbf{B}^{(k)} \Phi_i = \alpha \mathbf{B}^{(k)} \delta_i \quad (11)$$

The term $\mathbf{B}_k \delta_i^{(k)}$ (for simplicity, denoted the term as $\eta_i^{(k)}$) is the strain response vector associated with i th mode and k th element under modal coordinates. The

transformation equation for strain responses under i th mode between two elements indexed by e and u can be obtained by using Eq. (11) as

$$\frac{\mathbf{B}^{(e)}\boldsymbol{\Phi}_i^{(e)}}{\mathbf{B}^{(u)}\boldsymbol{\Phi}_i^{(u)}} = \frac{\alpha\mathbf{B}^{(e)}\boldsymbol{\delta}_i^{(e)}}{\alpha\mathbf{B}^{(u)}\boldsymbol{\delta}_i^{(u)}} = \frac{\eta_i^{(e)}}{\eta_i^{(u)}}. \quad (12)$$

The result of Eq. (12) indicates that if the physical strain responses are measured at one location (represented by element e in the FE model) can be decomposed to its modal responses, i.e., $\boldsymbol{\varepsilon}^{(e)} \approx \sum_{i=1\dots m} \eta_i^{(e)}$, the physical strain responses at a sensor inaccessible location (represented by element u in the FE model) can be reconstructed using the following transformation equation:

$$\boldsymbol{\varepsilon}^{(u)}(t) \approx \sum_{i=1\dots m} \left[\eta_i^{(e)}(t) \left(\frac{\mathbf{B}^{(e)}\boldsymbol{\Phi}_i^{(e)}}{\mathbf{B}^{(u)}\boldsymbol{\Phi}_i^{(u)}} \right)^{-1} \right], \quad (13)$$

where $i = 1\dots m$ denotes the participating modes and all other notations are defined as before. Once the physical strain responses are reconstructed using Eq. (13), the stress responses can be readily calculated using the following constitutive equation:

$$\boldsymbol{\sigma}(t) = \mathbf{c}\boldsymbol{\varepsilon}(t), \quad (14)$$

where \mathbf{c} is the *material matrix*. The constitutive equation for isotropic materials can be written explicitly as

$$\begin{Bmatrix} \sigma_{xx} \\ \sigma_{yy} \\ \sigma_{zz} \\ \sigma_{yz} \\ \sigma_{xz} \\ \sigma_{xy} \end{Bmatrix} = \begin{bmatrix} c_{11} & c_{12} & c_{12} & 0 & 0 & 0 \\ & c_{11} & c_{12} & 0 & 0 & 0 \\ & & c_{11} & 0 & 0 & 0 \\ & & & (c_{11}-c_{12})/2 & 0 & 0 \\ sym. & & & & (c_{11}-c_{12})/2 & 0 \\ & & & & & (c_{11}-c_{12})/2 \end{bmatrix} \begin{Bmatrix} \varepsilon_{xx} \\ \varepsilon_{yy} \\ \varepsilon_{zz} \\ \varepsilon_{yz} \\ \varepsilon_{xz} \\ \varepsilon_{xy} \end{Bmatrix}, \quad (15)$$

where $c_{11} = \frac{E(1-\nu)}{(1-2\nu)(1+\nu)}$, $c_{12} = \frac{E\nu}{(1-2\nu)(1+\nu)}$, and $(c_{11} - c_{12})/2 = G$. Terms E ,

ν , and G are Young's modulus, Poisson's ratio, and the shear modulus of the material, respectively. The relationship between the three material constants is

$$G = \frac{E}{2(1+\nu)}. \quad (16)$$

Based on above discussions and derivations, the overall procedure for strain responses reconstruction is summarized in Fig. 1.

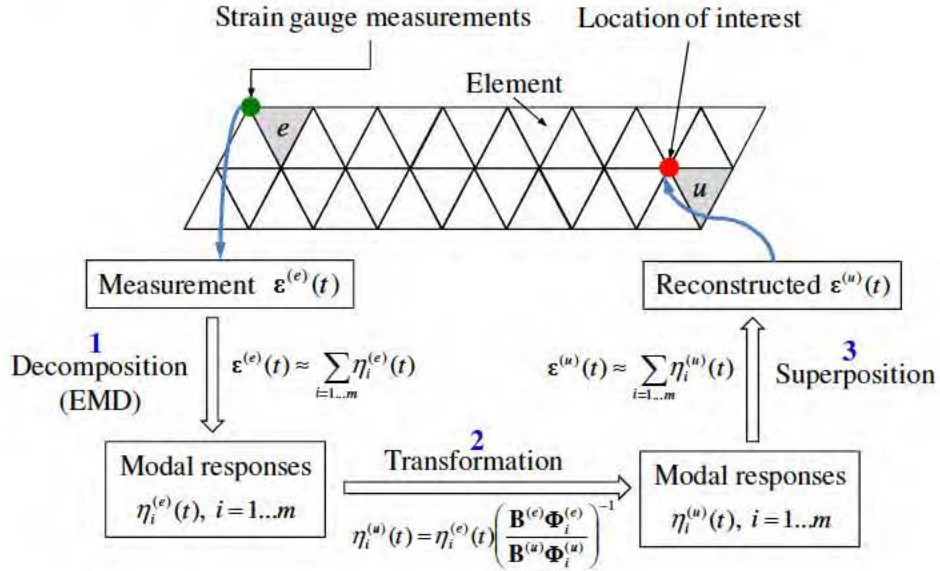


Fig. 1 Flowchart of the overall strain reconstruction procedure using remote strain gauge measurements.

Once the strain and stress responses of locations of interest are obtained using the proposed reconstruction method, the stress responses can be used in the fatigue crack growth models based on fracture mechanics or the concept of S-N curves. The fatigue

life prediction integrating the strain and stress reconstruction method is presented next.

3. Fatigue life prediction integrating strain and stress reconstruction method

One of the critical components in fatigue life prediction analysis is the loading information. The knowledge of the loading information of a structure allows for reliable and accurate fatigue life prediction. It is frequently seen that the critical spots for fatigue damage usually have no direct sensor measurements. One of the objectives of the proposed reconstruction methodology is to provide accurate loading information for fatigue life prediction using sparse and remote strain gauges installed in the structure. The proposed reconstruction methodology can be readily integrated into existing structural health monitoring systems for prognostics.

Stress responses of a location of interest can be obtained using Eq. (14) in which the strain responses for the location are reconstructed using the procedure in Fig. 1 with remote strain gauge measurements. The reconstructed stress responses form a spectrum loading for the location of interest. In practice, the spectrum loading for a mechanical part is a complex and often stochastic sequence of load amplitudes. The calculation of fatigue life is different for crack-damaged and normal mechanical parts. For a component without fatigue cracks, the calculation of fatigue life based on the S-N curve [21] and Miner's rule [22] can be adopted. In such cases, the following procedure is widely used:

1. Reduce the stochastic loading spectrum to a set of simple cyclic loadings using the rainflow counting method [23, 24].

2. Perform statistical analysis for the results from the rainflow analysis to create a histogram of cyclic stress and form a fatigue damage spectrum.
3. For each stress level in the fatigue damage spectrum, calculate the degree of cumulative damage using the S-N curve (of the material).
4. Combine the damage contributions of each stress level using Miner's rule.

For a part with an existing fatigue crack subject to a stochastic spectrum loading, fatigue crack growth models involving the stress intensity factor should be used. For example, fatigue crack growth models reported in [25-27] can deal with stochastic spectrum loadings and the reconstructed stress responses can be directly used.

4. Examples

Two numerical examples are presented here. The first example is a two-span beam structure subject to random forces. The second example is a complex spatial frame structure with 216 DOFs. The first example demonstrates the reconstruction methodology, and the second example demonstrates the reconstruction methodology integrating the fatigue damage prognosis.

4.1: A numerical beam structure example

A beam structure is used to demonstrate the overall reconstruction methodology and to investigate the performance of the proposed method under different measurement noises. The beam is 5m long, 0.5m wide and 0.05m thick. The Young's modulus is 69600MPa and the density is 2730kg/m³. The beam structure is divided into 10 equal segments in the FE model, as shown in Fig. 2. Random forces are applied at all vertical direction DOFs of the FE model. The random forces are modeled as Gaussian white noise processes passed through a sixth order low-pass Butterworth filter with a

100Hz cutoff. One percent of modal damping is considered. Displacement responses are calculated by solving the equation of motion of the beam based on its finite element model using mode superposition method. The sampling frequency is 1000Hz. Strain responses are calculated using the strain-displacement matrix and Eq. (9). The beam is modeled using Euler–Bernoulli beam theory and the 1×4 strain-displacement matrix is given by

$$\mathbf{B}^{(k)} = -\frac{y^{(k)}}{[L^{(k)}]^2} \cdot \begin{bmatrix} 6\left(-1 + \frac{2x^{(k)}}{L^{(k)}}\right) & 2L^{(k)}\left(-2 + \frac{3x^{(k)}}{L^{(k)}}\right) & 6\left(1 - \frac{2x^{(k)}}{L^{(k)}}\right) & 2L^{(k)}\left(-1 + \frac{3x^{(k)}}{L^{(k)}}\right) \end{bmatrix} \quad (17)$$

where the superscript (k) denotes the k th element, $L^{(k)}$ is the length of the element, $x^{(k)}$ and $y^{(k)}$ are the horizontal and vertical locations (within the element dimension) that the strain is computed, respectively. The displacement responses at a given time index t , $\mathbf{X}^{(k)}(t)$, is a 4×1 matrix

$$\mathbf{X}^{(k)}(t) = [u_1^{(k)}(t) \quad \theta_1^{(k)}(t) \quad u_2^{(k)}(t) \quad \theta_2^{(k)}(t)], \quad (18)$$

where $u_1^{(k)}(t)$, $\theta_1^{(k)}(t)$, $u_2^{(k)}(t)$ and $\theta_2^{(k)}(t)$ are the vertical and rotational displacements of the four DOFs of the element. The result of $\epsilon^{(k)}(t) = \mathbf{B}^{(k)}\mathbf{X}^{(k)}(t)$ is the x-direction strain of the location specified by $(x^{(k)}, y^{(k)})$ in the element. After the strain response generations, noise signals are added to each point in the strain responses to represent the noisy sensor measurements. The noise signals are Gaussian pulse process with root mean square (RMS) setting to a percentage of the largest RMS of the acceleration responses. The noise terms are specified using the noise level in this study, for example, a 10% noise level refers to the noise elements are Gaussian pulse processes with RMS 10% of the largest RMS of the strain responses.

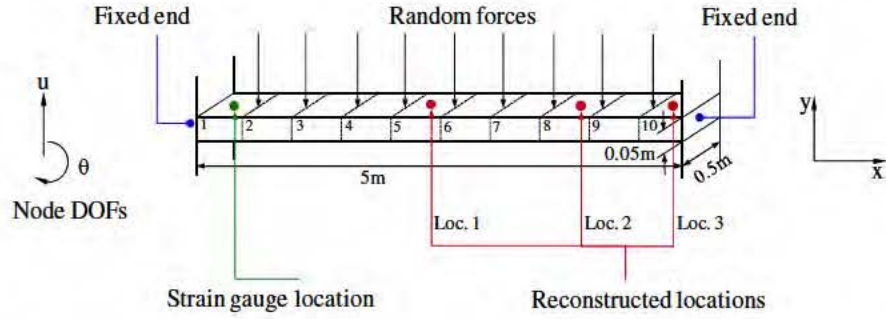


Fig. 2 FE diagram of a beam structure with both ends fixed and applied forces.

Synthesized strain gauge measurement locations and the three reconstructed locations are the geometry centers of the surfaces of elements 1, 5, 8, and 10, respectively.

To demonstrate the overall reconstruction methodology, 10-second noisy (10% RMS) sensor measurement data are generated using the above described procedure. The location of the assumed sensor is at (0.25m, 0.05m) of the element close to the left fixed end (labeled 1 in the figure). The synthesized strain gauge measurement data are shown in Fig. 3(a) and the Fourier spectra of the data is shown in Fig. 3(c), where four frequencies can be easily identified. The identified frequencies from the Fourier spectra are (10.38Hz, 28.69Hz, 56.22Hz, 93.15Hz), and they are used to design the band-pass filters. Frequency ranges for each band-pass filter are given in Table 1. EMD method with intermittency criteria are employed first to obtain modal responses corresponding to the four natural frequencies from the measurement data. Fig. 4 presents the results of modal responses of the strain measurement data in Fig. 3(a). For clear demonstration, the middle portion (4-6s) data are shown.

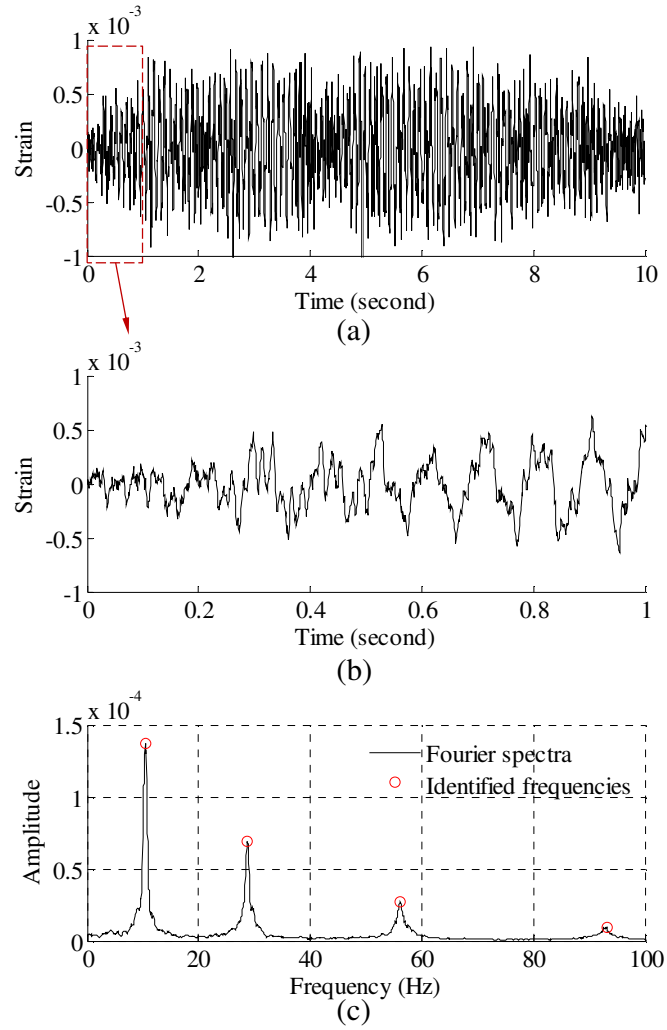


Fig. 3 The synthesized strain gauge measurement data and the Fourier spectra of the data. (a) Entire 10s measurement data, (b) measurement data (0-1s), and (c) Fourier spectra of the measurement data.

Table 1 Frequency ranges for each band-pass filters for the beam problem

Mode	1	2	3	4
Identified frequency	10.38	28.69	56.22	93.15
Passband corner frequency (Hz)	[8 9]	[22 26]	[46 52]	[80 87]

Stopband corner frequency (Hz)	[11.5 13]	[31 36]	[61 67]	[98 105]
--------------------------------	-----------	---------	---------	----------

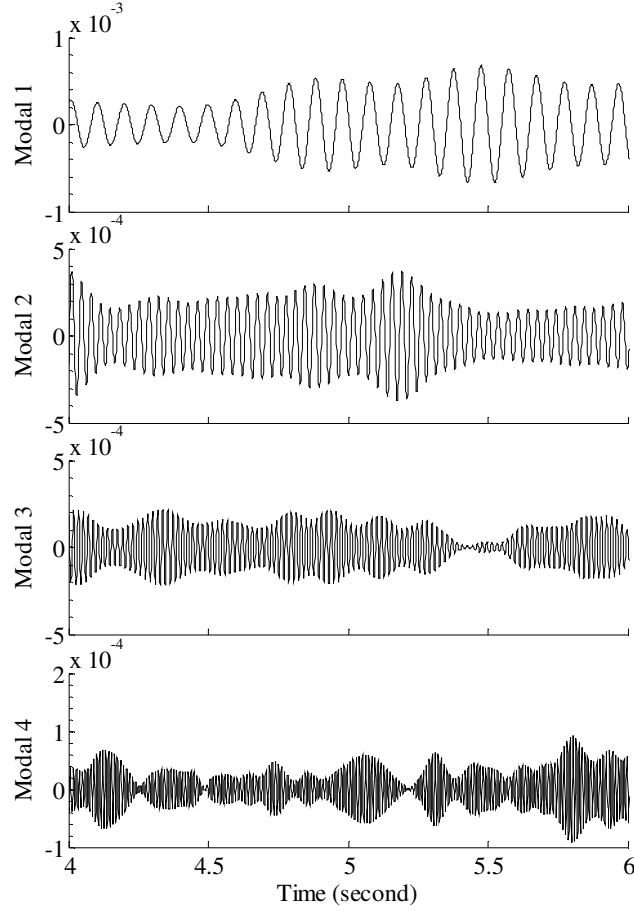


Fig. 4 Four modal responses of the strain gauge measurement data obtained using EMD method with intermittency criteria.

The four modal response results are used in Eq. (13) to obtain the strain responses for the three locations of interest shown in Fig. 2. The 1×4 matrix $\mathbf{B}_k = [0 \ 0.05 \ 0 \ -0.05]$ for all elements (i.e., $k=1 \dots 10$) due to the uniform discretization of the beam. Reconstructed strain responses for the three locations are

presented in Fig. 5. It can be observed that the reconstructed results are very close to the theoretical results for the three locations, considering the measurement data with 10% RMS measurement noises. Correlation coefficients between the reconstructed strain responses and the theoretical strain responses for the three locations are 0.981, 0.978, and 0.981, respectively, indicating the proposed methodology produces reliable and accurate results in this example.

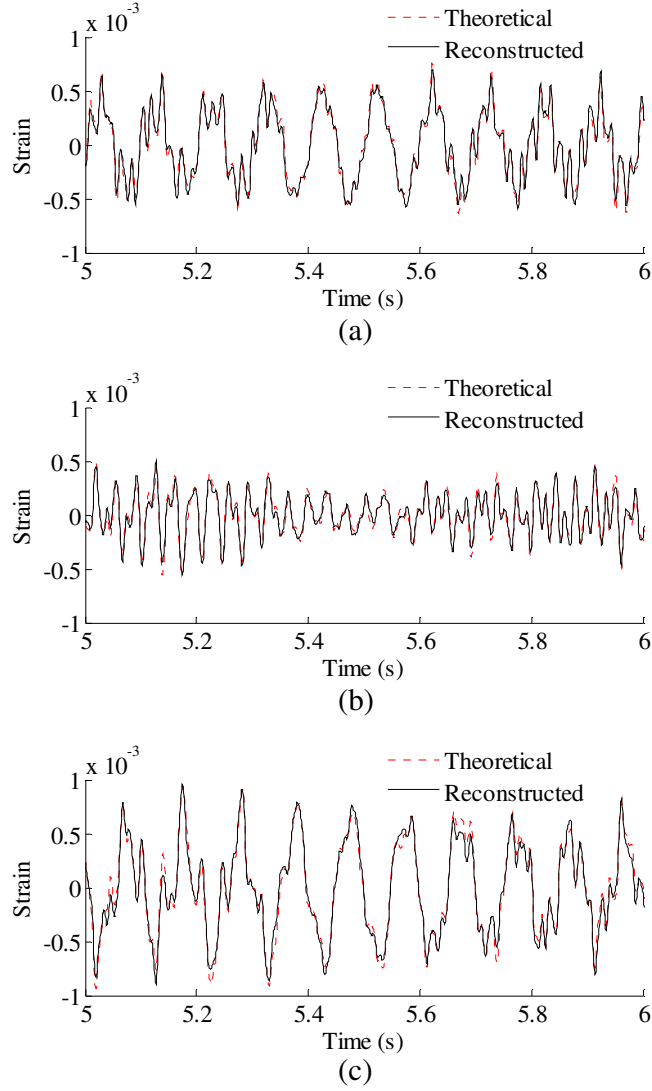


Fig. 5 Reconstructed and theoretical strain responses for three locations (Loc. 1-3) in Fig. 2. Results are concentrated on 5-6s for clear presentation. (a) Results for Loc. 1, (b) results for Loc. 2, and (c) results for Loc. 3.

To reconstruct the stress responses, the reconstructed strain responses are used in Eq. (14). The material matrix for this 1D beam problem is a 1×1 matrix (a scalar) of

$\mathbf{c} = [E]$ in which E is the Young's modulus of the material. The reconstructed stress results are shown in Fig. 6.

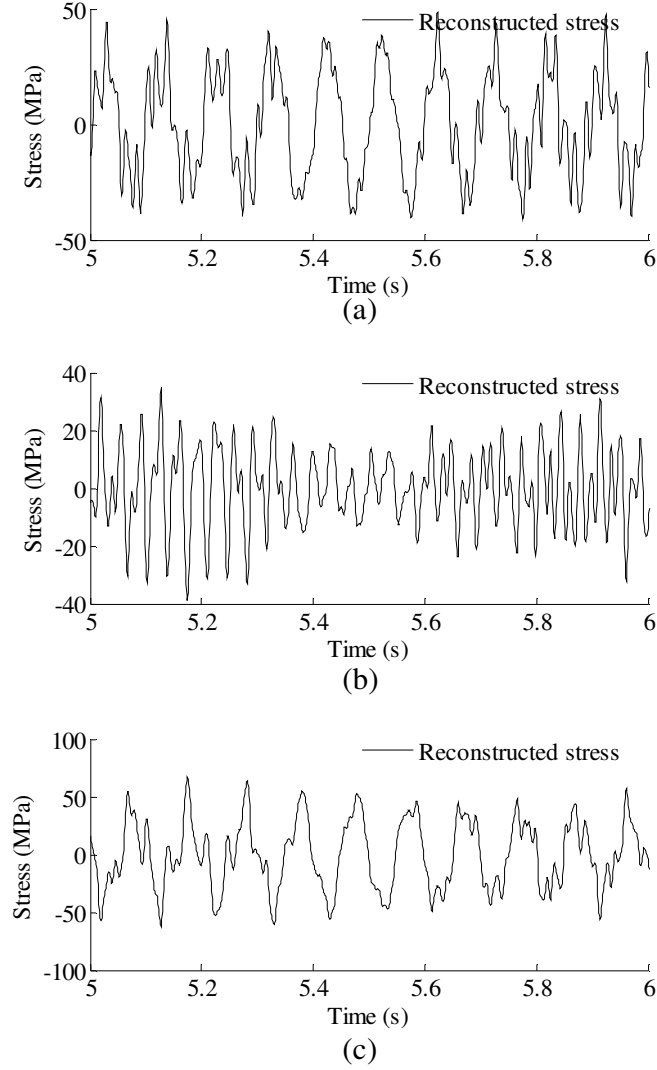


Fig. 6 Reconstructed stress responses for three locations (Loc. 1-3) in Fig. 2. Results are concentrated on 5-6s for clear presentation. (a) Results for Loc. 1, (b) results for Loc. 2, and (c) results for Loc. 3.

The beam example demonstrates the overall reconstruction procedure and the effectiveness of the proposed method. Next, a practical structural scale example is

presented to investigate the performance of the method for realistic problems and the fatigue damage prognosis using the reconstructed stress responses is illustrated.

4.2: A three-dimensional frame structure example

The proposed methodology can be directly applied to structural level reconstruction analysis. To demonstrate the basic idea, a 216-DOF spatial frame structure is used here. The finite element model diagram of the structure and its dimensions are shown in Fig. 7. The structure is a four-story steel structure and it has extents of $2m$, $1m$, and $5m$ in x -axis direction, y -axis direction, and z -axis direction, respectively. Each story has a height of $1.25m$. In the figure nodes are labeled using nearby numbers and elements are labeled with numbers in round brackets. Each of the elements has two nodes and 12 DOFs in total. Each node has 6 DOFs, namely the displacements of x , y , and z directions and the rotations along x , y , and z axes. All the nodes attached to the ground (i.e., $z=0$) are prescribed and the structure has 216 DOFs. Required properties of the structural member element for FE modeling are listed in Table 2.

Table 2 Properties of structural member elements

Property	Value
Cross-section area B (m^2)	0.01
Moment of inertia I_y (m^4)	8.3333×10^{-6}
Moment of inertia I_z (m^4)	8.3333×10^{-6}
Torsion constant J (m^4)	6.6667×10^{-5}

Young's modulus E (GPa)	200
Poisson's ratio ν	0.3
Shear modulus G (GPa)	$E/(2+2\nu)$
Mass per unit volume ρ (kg/m ³)	7.8×10^{-3}

At each floor, stochastic forces in the x -axis direction are applied to simulate the ambient excitations. The surface geometry center of the element (78) is used to as the location of the actual strain gauge. Sensor measurements are obtained by solving the dynamical equations of the finite element model and 10% RMS noise terms are added to the deterministic results to represent the measurement uncertainty. The sampling frequency is 1000Hz. The stochastic forces and the noise terms are generated using the same methods in the beam example. Without loss of generality, the element (52) is arbitrarily chosen to represent the location of interest. For this element, strain and stress responses at the geometry center of the surface perpendicular to the y -axis direction can have maximum response amplitudes and this geometry center is the location of interest. Both the strain gauge measurement location and the reconstructed location are shown in Fig. 7. For illustration purposes, only the normal strain and stress is considered to be significant. The reconstruction for shear strain and stress responses can be obtained using the same methodology.

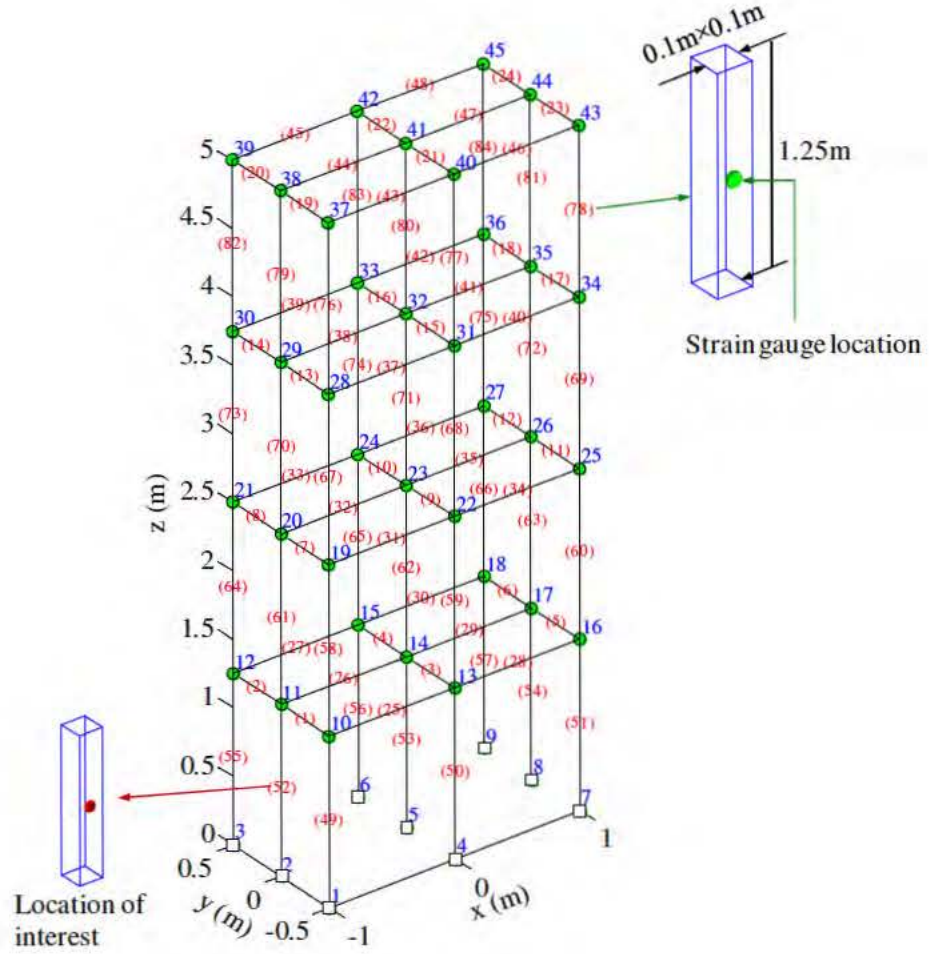


Fig. 7 FE model of the spatial frame structure

4.2.1 Strain and stress response reconstruction

Sixty seconds of synthesized strain gauge measurement data with 5% RMS noise terms are presented in Fig. 8(a). The Fourier spectra of the strain gauge measurement data indicate four significant frequencies as shown in Fig. 8(c). Those four frequencies are used to design band-pass filters for the modal responses extraction. Fig. 9 presents the modal responses obtained by the EMD method with intermittency criteria. The reconstructed strain gauge responses for the location of interest in

element (52) and the theoretical results are compared in Fig. 10. The reconstructed stress responses based on the reconstructed strain results are shown in Fig. 11. The correlation between the reconstructed strain responses and the theoretical strain calculation results is 0.9768.

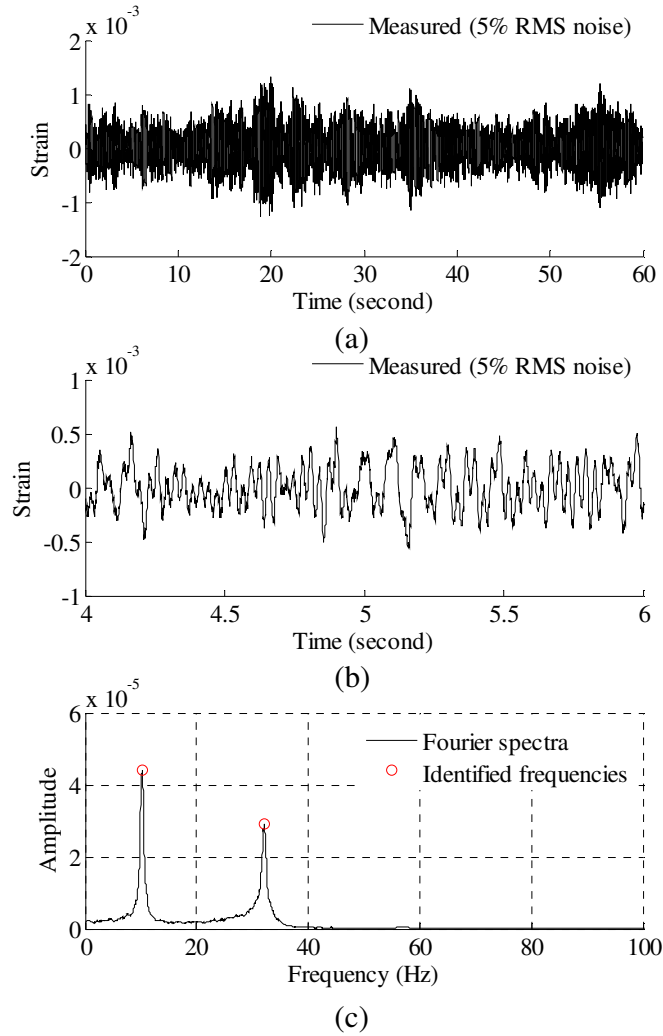


Fig. 8 Strain gauge measurement data and Fourier spectra of the data. (a) Strain gauge measurement data (0-60s), and (b) concentrated on 4-6s for clear presentation, and (c) Fourier spectra of the measurement data (0-60s).

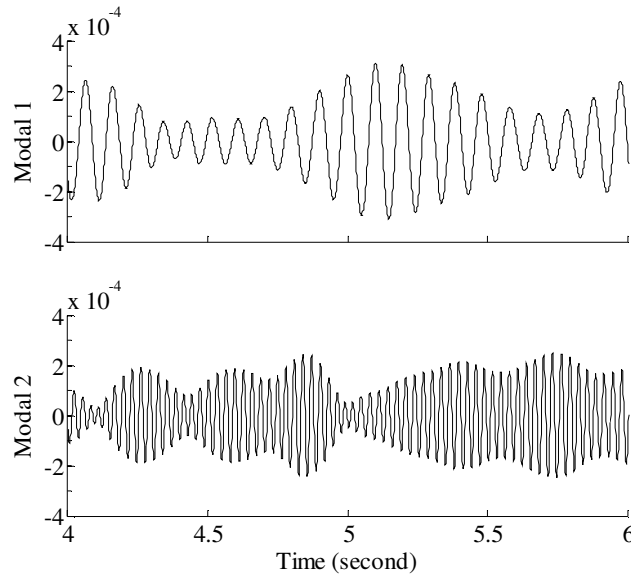


Fig. 9 Modal responses of the strain gauge measurement data obtained by EMD method with intermittency criteria.

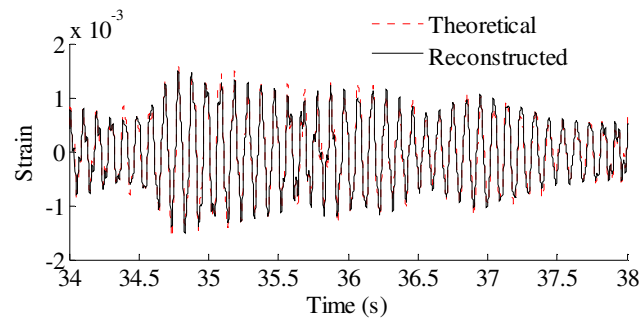


Fig. 10 Reconstructed and theoretical strain responses for the location of interest shown in Fig. 7. Results are concentrated on 4-6s for clear presentation.

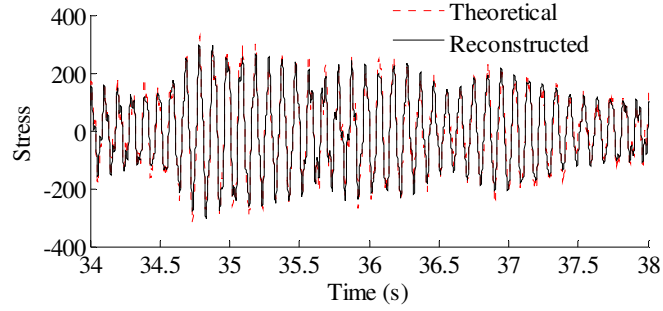


Fig. 11 Reconstructed and theoretical bending stress responses for the location of interest shown in Fig. 7. Results are concentrated on 36-37s for clear presentation.

4.2.2 Effect of measurement noise to reconstructed strain and stress responses

To investigate the effect of measurement noise to the reconstructed strain and stress responses, several numerical cases are studied. To represent realistic situations, the noise signals are Gaussian pulse processes with root mean square (RMS) setting to a percentage of the largest RMS of the calculated strain responses. The percentage value is defined as noise level. For example, a 5% noise level is to generate noise components from Gaussian pulse processes with RMS setting to 5% of the largest RMS of the strain responses. The noise components are added to the strain responses and the results are used as the representative noisy strain measurement data. Correlation coefficient is used as a metric to evaluate the similarity between the theoretical responses and the reconstructed responses for bending stresses. RMS is set to taking value from 0% to 10% with 1% increment. At each of the RMS settings, bending stress responses at element 52 (as shown in Fig. 7) are reconstructed based on the strain measurement at element 78 (as shown in Fig. 7). The correlation coefficient between the reconstructed stress responses at element 52 and the theoretical stress

responses (also with noise components) at element 52 is calculated. Results for all RMS settings are presented in Fig. 12.

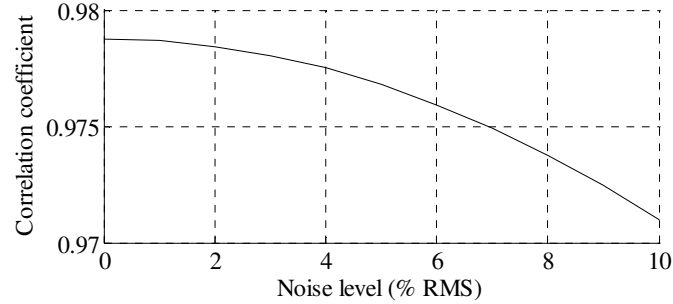


Fig. 12 Reconstruction performance measured in correlation coefficient under different noise levels.

It can be seen that the performance is degraded with the increase of noise level. The overall performance of the reconstruction method is about larger than 97% in similarity for noise levels not larger than 10% RMS for the case example. Next, the fatigue prognosis integrating the reconstructed stress responses is presented.

4.2.3 Fatigue damage prognosis using the reconstructed stress responses

The fatigue crack growth model used in this study is a small time scale model. Since the development of the fatigue crack growth model is beyond the scope of this paper, only a brief introduction is given here. Detailed derivation and model validation for the new material fatigue crack growth model can be found in the referred article [28].

The small time scale model is developed based on the geometric relationship between the crack tip opening displacement (CTOD) and the instantaneous crack growth kinetics. The geometric relationship between the CTOD and the instantaneous

crack growth kinetics is shown in Fig. 13. The schematic illustration in Fig. 13 is for a through thickness crack in an infinite plate. Only the tip region is shown. As shown in Fig. 13, the crack will extend a distance (da), after a small time increment (dt) and the crack tip will extend from O to O' . Considering the geometry of crack tips at two time points (t and $t+dt$), the crack growth rate da/dt for an infinitesimal crack growth is derived as it is shown in Eq. (19), where θ is the crack tip opening angle (CTOA).

$$da = \frac{\cot(\theta)}{2} d\delta = Cd\delta \quad (19)$$

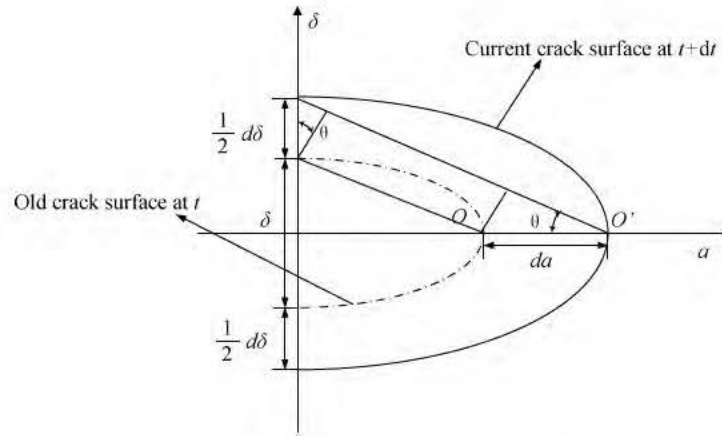


Fig. 13 Schematic representation of crack tip geometry profiles during fatigue crack growth.

The CTOD can be approximately expressed as Eqs. (20-21) using the plastic zone model proposed by Irwin [29]. Eq. (20) is for elastic-perfect-plastic material behavior and ignores the hardening effect [30].

$$\delta = \frac{1}{2} \frac{K^2}{E\sigma_y} = \lambda\sigma^2 a \quad (20)$$

$$\lambda = \frac{\pi}{2E\sigma_y} \quad (21)$$

where E is the Young's modulus. σ_y is the yield strength. It should be noted that σ in Eq. (20) is the nominal stress. According to Fig. 13, the crack propagated from O to O' during a small time increment. The crack length increment is da and the CTOD increment is $d\delta$. The CTOD increment $d\delta$, is expressed as Eq. (22)

$$d\delta = \lambda(2\sigma da + \sigma^2 da) \quad (22)$$

Substituting Eq. (22) into Eq. (19) and dividing on both sides by a small time increment dt , the instantaneous crack growth rate is represented as

$$\frac{1}{C\lambda a} \frac{da}{dt} = \frac{2\sigma}{1-C\lambda\sigma^2} \frac{d\sigma}{dt} \quad (23)$$

The proposed methodology describes crack growth rate in terms of time scale instead of cycle, according to Eq. (23). The crack length at any arbitrary time can be calculated by direct time integration. Above discussion is for the case when the crack starts to grow. The crack may not grow during the entire duration of the cyclic loading. A general expression considering the non-uniform crack growth is expressed as

$$\dot{a} = H(\dot{\sigma}) \cdot H(\sigma - \sigma_{ref}) \cdot \frac{2C\lambda}{1-C\lambda\sigma^2} \cdot \dot{\sigma} \cdot \sigma \cdot a, \quad (24)$$

where “ \cdot ” denotes time derivative throughout this paper. H is the Heaviside function. σ_{ref} is the reference stress level where the crack starts to grow. Cracks do not grow during the entire duration of the cyclic loading. For example, crack does not growth during the unloading path due to the energy principle. Also, crack only starts to grow when the applied loading is beyond a certain stress level. The crack length needs to be calculated by performing the integration from the lower integration limit

(e.g., the time when the reference stress level is reached) to the upper integration limit (e.g., the time when the maximum stress level is reached). The crack closure model is essentially contained in the calculation of reference stress level. In this case, the determination of the reference stress level is critical in order to perform the integration. The small time scale model has been validated using the existing experimental data for various materials under both constant loading and variable amplitude loadings [28]. There are several advantages for the developed small time scale model: (1) Comparing with Paris' model, the small time scale model does not need cycle-counting (e.g., only using direct time domain integral) under random variable loadings. Paris' model considers the average crack growth per cycle and cannot include the detailed mechanisms within one loading cycle (e.g., non-uniform crack growth kinetics within one cycle as shown in Eq. (24), (2) Stress ratio effect has been included in the small time scale model since the direct stress state instead of stress range is used; and (3) One unique advantage of the small time scale model is that it can be seamlessly coupled with structural analysis and has great potential for concurrent structural dynamic analysis and multilevel (e.g., structural level and material level) fatigue damage prognosis. This capability makes it an ideal model for real-time damage analysis and on-line decision-making [31].

To demonstrate the fatigue prognosis with reconstructed stress responses, a numerical crack growth analysis using the original and reconstructed signal with different noise levels are performed. The initial crack is assumed to be 5mm. Comparisons of crack length vs. time curves are shown in Fig. 14. The x -axis is the

time points in the numerical simulation. The y-axis is the simulated crack length using the proposed small time scale fatigue crack growth model. As shown in Fig. 14, all crack length curves agrees with each other. Quantitative error analysis is performed and is shown in Fig. 15. The x-axis is the noise level (i.e., percentage of the RMS). The y-axis is the maximum absolute error of the crack length prediction normalized by the crack length. The error definition is

$$Error = \frac{\max |\hat{a}(t) - a(t)|}{a_e(t)} \quad (25)$$

where $\hat{a}(t)$ is the crack length at time t using reconstructed stress responses. $a(t)$ is the crack length at time t using theoretical stress responses. $a_e(t)$ is the final crack length of calculation. It is shown that the prediction error of crack length does not have a monotonic trend with respect to the introduced noise level. The maximum error is less than 0.8% with all the stress histories investigated in the current study. It should be noted that the proposed study focuses on the theoretical development of the stress reconstruction methodology. Further investigation is required for the experimental validation studies.

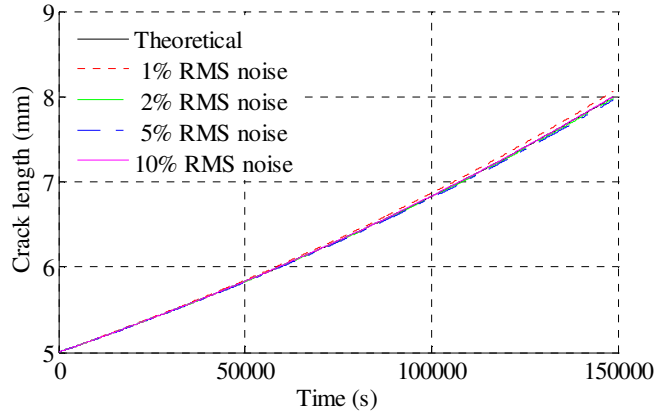


Fig. 14 Crack growth trajectories calculated using theoretical and reconstructed stress responses under different RMS noise levels.

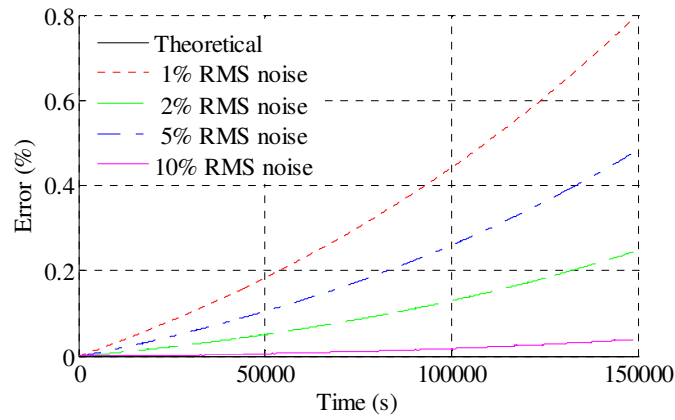


Fig. 15 Error analysis of crack length predictions using theoretical and reconstructed stress responses under different RMS noise levels.

5. Conclusions

In this study, a direct time domain strain and stress reconstruction method integrating fatigue damage prognostics methodology was developed. Sparse and remote strain gauge measurements from the existing structural health monitoring (SHM) system can be directly used to reconstruct the strain and stress responses for critical spots without direct sensor measurements. The proposed method extends the

previous EMD-based time-domain reconstruction method by using the finite element model to derive a strain transformation function in modal coordinates. EMD method with intermittency criteria is first employed in the proposed method to decouple the remote strain measurements into modal coordinates, and the extrapolation of the strain and stress responses is made using the derived strain and stress transformation function. Mode superposition is used to obtain the strain and stress responses of the critical spot for fatigue crack growth analysis and fatigue life prediction. The overall method is demonstrated using a beam structure and a more complex 216-DOF spatial frame structure. Reconstruction results are compared with theoretical solutions. Fatigue analysis using the reconstructed stress responses was performed to demonstrate the effectiveness of the overall method. Based on the current study, several conclusions are drawn:

1. A universal transformation for modal responses was derived based on the FE modeling of the target structure. The transformation allows for efficient reconstruction of strain/stress modal responses in time domain.
2. According to numerical analysis results, the proposed method can produce results very close to theoretical solutions considering a practical noisy measurement system. The reconstructed results have an overall correlation coefficient larger than 0.97 under 10% RMS noise settings.
3. Fatigue crack growth analysis using the reconstructed stress responses agrees well with the crack length predictions using the original stress responses. The

crack length prediction using the reconstructed stress responses is not sensitive to the introduced noise at the investigated levels.

The current study focuses on the theoretical development and further study is required to experimentally validate the proposed methodology. Only mode I planar crack is considered in the demonstrated examples and curvilinear or 3D cracks need further investigations. The multiscale analysis in the proposed study focuses on the structural and macro materials level. The extension to include material microstructure effect for the fatigue prognosis needs further investigations.

Acknowledgements

The research was supported by funds from Air Force Office of Scientific Research: Young Investigator Program (Contract No. FA9550-11-1-0025, Project Manager: Dr. David Stargel). The support is gratefully acknowledged.

Reference

1. Johnson, T.J., et al., *Distributed structural health monitoring with a smart sensor array*. Mechanical Systems and Signal Processing, 2004. **18**(3): p. 555-572.
2. Hurlebaus, S. and L. Gaul, *Smart structure dynamics*. Mechanical Systems and Signal Processing, 2006. **20**(2): p. 255-281.
3. Doebling, S.W., et al., *Damage Identification and Health Monitoring of Structural and Mechanical Systems from Changes in their Vibration Characteristics: A Literature Review*. 1996, LOS ALAMOS NATIONAL LAB NM.
4. Kulkarni, S. and J. Achenbach, *Structural health monitoring and damage prognosis in fatigue*. Structural Health Monitoring, 2008. **7**(1): p. 37-49.
5. Beral, B. and H. Speckmann. *Structural health monitoring (SHM) for aircraft structures: a challenge for system developers and aircraft manufactures*. in *Structural Health Monitoring 2003: From Diagnostics & Prognostics to Structural Health Management : Proceedings of the 4th International Workshop on Structural Health Monitoring*. 2003. Stanford University, Stanford, CA.
6. Verboven, P., et al., *AUTONOMOUS STRUCTURAL HEALTH MONITORING--PART I: MODAL PARAMETER ESTIMATION AND TRACKING*. Mechanical Systems and Signal Processing, 2002. **16**(4): p. 637-657.
7. Parloo, E., et al., *Autonomous structural health monitoring—part II:*

- vibration-based in-operation damage assessment*. Mechanical Systems and Signal Processing, 2002. **16**(4): p. 659-675.
8. Giurgiutiu, V. and A. Cuc, *Embedded non-destructive evaluation for structural health monitoring, damage detection, and failure prevention*. Shock and Vibration Digest, 2005. **37**(2): p. 83.
 9. Chang, P.C., A. Flatau, and S. Liu, *Review paper: health monitoring of civil infrastructure*. Structural Health Monitoring, 2003. **2**(3): p. 257-267.
 10. Katsikeros, C.E. and G. Labeas, *Development and validation of a strain-based Structural Health Monitoring system*. Mechanical Systems and Signal Processing, 2009. **23**(2): p. 372-383.
 11. Farrar, C.R. and K. Worden, *An introduction to structural health monitoring*. Philosophical Transactions of the Royal Society A: Mathematical, Physical and Engineering Sciences, 2007. **365**(1851): p. 303.
 12. Rytter, A., *Vibrational based inspection of civil engineering structures*. 1993, Department of Building Technology and Structural Engineering, University of Aalborg.
 13. He, J., X. Guan, and Y. Liu, *Structural response reconstruction based on empirical mode decomposition in time domain*. Mechanical Systems and Signal Processing, 2012. **28**: p. 348-366.
 14. Law, S., J. Li, and Y. Ding, *Structural response reconstruction with transmissibility concept in frequency domain*. Mechanical Systems and Signal Processing, 2011. **25**(3): p. 952-968.
 15. KAMMER, D., *ESTIMATION OF STRUCTURAL RESPONSE USING REMOTE SENSOR LOCATIONS*. Journal of Guidance, Control, and Dynamics, 1997. **20**(3): p. 501-508.
 16. Ribeiro, A., J. Silva, and N. Maia, *On the generalisation of the transmissibility concept*. Mechanical Systems and Signal Processing, 2000. **14**(1): p. 29-36.
 17. Huang, N.E., et al., *The empirical mode decomposition and the Hilbert spectrum for nonlinear and non-stationary time series analysis*. Proceedings of the Royal Society of London. Series A: Mathematical, Physical and Engineering Sciences, 1998. **454**(1971): p. 903-995.
 18. Yang, J.N., et al., *System identification of linear structures based on Hilbert-Huang spectral analysis. Part 1: normal modes*. Earthquake Engineering & Structural Dynamics, 2003. **32**(9): p. 1443-1467.
 19. Bao, C., et al., *Time-varying system identification using a newly improved HHT algorithm*. Computers & Structures, 2009. **87**(23-24): p. 1611-1623.
 20. Huang, N.E., Z. Shen, and S.R. Long, *A new view of nonlinear water waves: The Hilbert Spectrum I*. Annual Review of Fluid Mechanics, 1999. **31**(1): p. 417-457.
 21. Stephens, R.I. and H.O. Fuchs, *Metal Fatigue in Engineering*. Second Edition ed. 2001, New York: John Wiley & Sons, Inc.
 22. Miner, M.A., *Cumulative Damage in Fatigue*. J. Applied Mechanics, 1945. **12**: p. A159-A164.
 23. Matsuishi, M. and T. Endo, *Fatigue of metals subjected to varying stress*. paper presented to Japan Society of Mechanical Engineers, 1968: p. 37-40.

24. Downing, S.D. and D. Socie, *Simple rainflow counting algorithms*. International Journal of Fatigue, 1982. **4**(1): p. 31-40.
25. Newman Jr, J.C., *A crack-closure model for predicting fatigue crack growth under aircraft spectrum loading*. ASTM STP, 1981. **748**: p. 53-84.
26. He, J., Z. Lu, and Y. Liu, *A new method for concurrent dynamic analysis and fatigue damage prognosis of bridges*. Journal of Bridge Engineering, 2011. **1**: p. 196.
27. De Koning, A., *A simple crack closure model for prediction of fatigue crack growth rates under variable-amplitude loading*. ASTM STP, 1981. **743**: p. 63-85.
28. Lu, Z. and Y. Liu, *Small time scale fatigue crack growth analysis*. International Journal of Fatigue, 2009. **32**(8): p. 1306-1321.
29. Janssen, M., J. Zuidema, and R.J.H. Wanhill, *Fracture Mechanics*. 1 ed. 2004: VSSD. 378.
30. Skorupa, M., *Load interaction effects during fatigue crack growth under variable amplitude loading—a literature review. Part II: qualitative interpretation*. Fatigue & fracture of engineering materials & structures, 1999. **22**(10): p. 905-926.
31. He, J., Z. Lu, and Y. Liu, *New Method for Concurrent Dynamic Analysis and Fatigue Damage Prognosis of Bridges*. Journal of Bridge Engineering, 2012. **17**(3): p. 396-408.
32. Pommier, S., *Cyclic plasticity and variable amplitude fatigue*. International Journal of Fatigue, 2003. **25**(9-11): p. 983-997.
33. Mikheevskiy, S. and G. Glinka, *Elastic-plastic fatigue crack growth analysis under variable amplitude loading spectra*. International Journal of Fatigue. **31**(11-12): p. 1828-1836.
34. Corbly, D.M. and P.F. Packman, *On the influence of single and multiple peak overloads on fatigue crack propagation in 7075-T6511 aluminum*. Engineering Fracture Mechanics, 1973. **5**(2): p. 479-497.
35. Venkateswara Rao, K.T. and R.O. Ritchie, *Mechanisms for the retardation of fatigue cracks following single tensile overloads: behavior in aluminum-lithium alloys*. Acta Metallurgica, 1988. **36**(10): p. 2849-2862.
36. Mohanty, J.R., B.B. Verma, and P.K. Ray, *Prediction of fatigue crack growth and residual life using an exponential model: Part II (mode-I overload induced retardation)*. International Journal of Fatigue, 2009. **31**(3): p. 425-432.
37. Willenborg J, E.R., Wood RA, *A Crack Growth Retardation Model Using an Effective Stress Concept*. 1971, Air Force Flight Dynamics Laboratory: Wright-Patterson Air Force Base, Ohio.
38. Wheeler, O.E., *Spectrum loading and crack growth* J. Basic Eng., Trans. ASME, 1972. **94**(1): p. 181-186.
39. Elber, W., *The significance of fracture crack closure*. ASTM Special Technical Publication 486, American Society for Testing and Materials ed. Damage tolerance in aircraft structures. 1971, Philadelphia. 230-242.
40. Newman, J.C., *A crack closure model for predicting fatigue crack growth under aircraft spectrum loading*. Methods and models for predicting fatigue crack growth under random loading, ASTM Special Technical Publication 748, American Society for Testing and Materials. 1981, Philadelphia 53-84.

41. Koning, A.U.d. *A simple crack closure model for prediction of fatigue crack growth rates under variable-amplitude loading*. in *Fracture Mechanics: Thirteenth Conference, ASTM STP 743*. 1981: American Society for Testing and Materials.
42. Ray, A. *A state-space model of fatigue crack growth for real-time structural health management*. in *Digital Avionics Systems Conferences*. 2000.
43. de Koning AU, v.d.L.H., *Prediction of fatigue crack growth rates under variable loading using a simple crack closure model*. 1981, NLR MP 81023U Amsterdam.
44. Liu, Y. and S. Mahadevan, *Efficient methods for time-dependent fatigue reliability analysis*. AIAA Journal, 2009. **47**(3): p. 494-504.
45. Liu, Y. and S. Mahadevan, *Probabilistic fatigue life prediction using an equivalent initial flaw size distribution*. International Journal of Fatigue, 2009. **31**(3): p. 476-487.
46. Kujawski, D., *A fatigue crack driving force parameter with load ratio effects*. International Journal of Fatigue, 2001. **23**(Supplement 1): p. 239-246.
47. NASA, *Fatigue crack growth computer program NASGRO Version 3.0-Reference manual*. JSC-22267B, NASA, Lyndon B. Johnson Space Center, Texas, 2000.
48. Xiang, Y. and Y. Liu, *Application of inverse first-order reliability method for probabilistic fatigue life prediction*. Probabilistic Engineering Mechanics. **26**(2): p. 148-156.
49. Paris, P. and F. Erdogan, *A critical analysis of crack propagation laws*. J. Basic Eng. Trans. ASME, 85, 1963: p. 528-553.
50. Paris, P. and M. Gomez, *A rational analytic theory of fatigue*. Trends Eng, 1961. **13**(9-14).
51. Dowling, N.E., *Mechanical behavior of materials : engineering methods for deformation, fracture and fatigue*. 3rd ed. 2007, Upper Saddle River, NJ, London: Pearson Prentice Hall ; Pearson Education. xvii, 912 p.
52. NASA, *Fatigue crack growth computer program NASGRO Version 3.0-Reference manual*. JSC-22267B, NASA, Lyndon B. Johnson Space Center, Texas, 2000.
53. Lu, Z. and Y. Liu, *Small time scale fatigue crack growth analysis*. International Journal of Fatigue. **32**(8): p. 1306-1321.
54. Zizi Lu and Y. Liu, *Small time scale fatigue crack growth analysis*. International Journal of Fatigue, 2010. **32**(8): p. 1306-1321.
55. Thorndahl, S. and P. Willems, *Probabilistic modelling of overflow, surcharge and flooding in urban drainage using the first-order reliability method and parameterization of local rain series*. Water Research, 2008. **42**(1-2): p. 455-466.
56. Cheng, J. and Q.S. Li, *Reliability analysis of a long span steel arch bridge against wind-induced stability failure during construction*. Journal of Constructional Steel Research, 2009. **65**(3): p. 552-558.
57. Val, D.V., M.G. Stewart, and R.E. Melchers, *Effect of reinforcement corrosion on reliability of highway bridges*. Engineering Structures, 1998. **20**(11): p. 1010-1019.
58. Skaggs, T.H. and D.A. Barry, *Assessing uncertainty in subsurface solute transport: efficient first-order reliability methods*. Environmental Software, 1996. **11**(1-3): p. 179-184.
59. Cizelj, L., B. Mavko, and H. Riesch-Oppermann, *Application of first and second*

- order reliability methods in the safety assessment of cracked steam generator tubing*. Nuclear Engineering and Design, 1994. **147**(3): p. 359-368.
60. Kam, T.Y., K.H. Chu, and S.Y. Tsai, *Fatigue reliability evaluation for composite laminates via a direct numerical integration technique*. International Journal of Solids and Structures, 1998. **35**(13): p. 1411-1423.
61. Liao, M., X. Xu, and Q.-X. Yang, *Cumulative fatigue damage dynamic interference statistical model*. International Journal of Fatigue, 1995. **17**(8): p. 559-566.
62. Xiang, Y. and Y. Liu, *Inverse first-order reliability method for probabilistic fatigue life prediction of composite laminates under multi-axial loading*. ASCE Journal of Aerospace Engineering, 2011. **24**(2): p. 189-198.
63. Haldar, A. and S. Mahadevan, *Probability, reliability, and statistical methods in engineering design*. 2000, New York ; Chichester [England]: John Wiley. xvi, 304 p.
64. Liu, Y., Mahadevan, S, *Efficient methods for time-dependent fatigue reliability analysis*. AIAA Journal, 2009. **47**(3): p. 494-504.
65. Rackwitz, R.a.F., B, *Note on Discrete Safety Checking When Using Non-Normal Stochastic Models for Basic Variables*. Load Project Working Session, MIT, Cambridge, MA, June 1976.
66. Rackwitz, R.a.F., B, *Structural Reliability Under Combined Random Load Sequences*. Computers & Structures, 1978. **9**(5): p. 484-494.
67. Porter, T.R., *Method of analysis and prediction for variable amplitude fatigue crack growth*. Eng. Fract. Mech, 1972. **4**: p. 717-736.
68. Lu, Z. and Y. Liu, *Experimental investigation of random loading sequence effect on fatigue crack growth*. Materials & Design, 2011. **32**(10): p. 4773-4785.

Appendix 5: Accomplishments for Task 2.1

Rigorous uncertainty quantification prediction

Yibing Xiang and Yongming Liu*

Clarkson University, Potsdam, NY, 13699

Abstract: An integrated experimental and simulation approach is proposed to study the effect of loading uncertainties on the fatigue crack growth behavior of Al-7075-T6. Various loading histories, including constant amplitude loadings, single overload block loadings, and deterministic and random variable spectrum loadings are used in the current investigation. Multiple specimen tests are performed and statistical analysis is used to extract the probability distribution of crack size and fatigue life. A previously developed small time scale model is used as a mechanism model to explain the fatigue crack growth behavior under random variable amplitude loadings. Monte Carlo (MC) simulation is used for the probabilistic fatigue life prediction. Model predictions are compared with the experimental observations for model validation. It is observed that the effect of uncertain loading is different under different loading spectrums. For some cases, the uncertainties of loadings have no major impact on the probabilistic life distribution. For other cases, loading uncertainties have significant impact on the scatter of the life distribution. Model analysis indicates that this behavior is mainly due to the scatter of crack opening stresses produced under different variable amplitude loading spectrums

Key words: Fatigue crack growth, random loading, small time scale model, probabilistic, uncertainty

* Corresponding author, Tel.: 315-268-2341; Fax: 315-268-7985; Email: yliu@clarkson.edu

* Corresponding author, Tel.: 315-268-2341; Fax: 315-268-7985; Email: yliu@clarkson.edu

1. Introduction

Fatigue crack growth process in engineering materials and structures is a complex stochastic process. It has been observed that huge scatter exists even for identical specimens under same loading conditions and environments [1-4]. This may be caused by the uncertainties of material properties, manufacturing process, and residual stresses, etc. More importantly, loadings for realistic structures are random and are different from the design spectrums, although the statistical distributions may be same. The loading uncertainties cause tremendous uncertainties under realistic working conditions and make the life prediction very difficult [5, 6].

Many stochastic fatigue crack growth methods have been proposed to take into account uncertainties for accurate fatigue life predictions [4, 6, 7]. Most of probabilistic analysis focused on the material variability and very few studies focused on the unknown/random loading uncertainties. For the comprehensive statistical analysis of fatigue crack growth, multiple specimen testing under similar conditions are required. Due to the high time and budget cost associated with fatigue testing, very limited data have been reported in the open literature, especially for statistical analysis. Several data sets under constant amplitude loadings were reported [2, 8]. Data sets under general random loadings are rarely found. In this study, experimental investigation under both deterministic and random variable amplitude loadings are designed and performed, which aims to provide a comprehensive data sets for the study of loading uncertainty effect on the fatigue crack growth and life prediction.

A previously developed small time scale model [9] is used for the deterministic

fatigue crack growth prediction. The small time scale model [9] is fundamentally different from the traditional reversal-based fatigue formulation, such as the yield zone model [10, 11] and the crack closure model [12-15]. It is not a cycle-based model and is based on the instantaneous crack growth kinetics within a cycle. One advantage of the proposed small time scale model is that it can be used for fatigue analysis at variable time and length scales. The fatigue crack growth analysis under random variable amplitude loading can be performed without cycle-counting. Another advantage is that the small time scale model includes the stress ratio effect intrinsically since the direct stress state instead of the stress range is used. A detailed derivation and model performance comparison can be found in [18]. Probabilistic crack growth analysis is performed using direct Monte Carlo simulations. Material uncertainties are included by randomizing the model parameters in the small time scale model. Loading uncertainties are included by random process generation following the specified statistical distribution of loadings. Probabilistic crack growth curves and life predictions are compared with obtained experimental data.

This paper is organized as follows. First, probabilistic fatigue crack growth analysis model is discussed. Deterministic mechanism model is briefly discussed and MC simulation-based probabilistic analysis is illustrated. Following this, experimental design and results are presented in detail. Deterministic loading testing is discussed first and compared with model predictions, which aims to check the applicability of the small time scale model in the fatigue crack growth predictions. Random variable amplitude loading testing are discussed and compared with model predictions, which

aims to validate the probabilistic crack growth statistics. Next, detailed discussions are given to correlate the model analysis with experimental observations. Several conclusions are drawn based on the experimental investigations and model analysis.

2. Probabilistic fatigue crack growth analysis

2.1 Deterministic mechanism model for fatigue crack growth

A previously developed small time scale fatigue crack growth formulation is used as the deterministic model to explain the crack growth mechanism. The key idea of the small time scale model is to define the fatigue crack kinetics at any arbitrary time instant (dt) instead of during a complete cycle. A detailed derivation of the developed small time scale formulation for fatigue crack growth simulation under mode I loading can be found in [9]. Only a brief description is shown here. The instantaneous crack growth rate is calculated using the geometric relationship (as shown in Fig. 1) between the Crack Tip Opening displacement (CTOD) and the crack growth and is expressed as

$$da = \frac{ctg\theta}{2} d\delta = Cd\delta \quad (1)$$

where $C = \frac{ctg\theta}{2}$ and θ is the crack tip opening angle (CTOA)

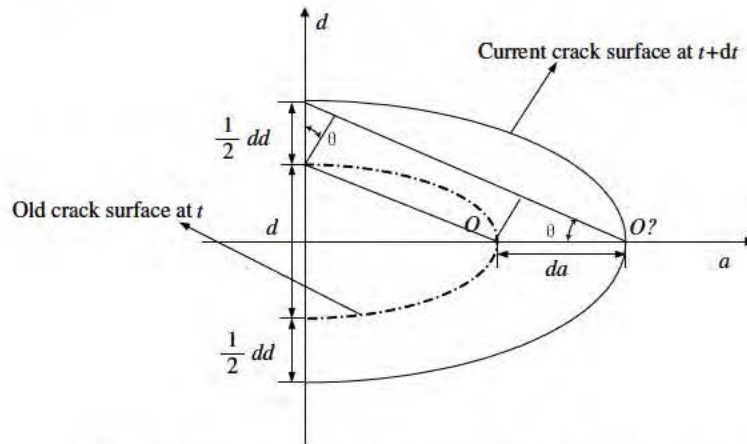


Fig. 1 Schematic representation of crack tip geometry

Using several hypotheses about the non-uniform crack growth kinetics within one loading cycle, a general instantaneous crack growth rate at any time can be expressed as

$$\dot{a} = H(\dot{\sigma}) \cdot H(\sigma - \sigma_{ref}) \cdot \frac{2C\lambda\sigma}{1 - C\lambda\sigma^2} \cdot \dot{\sigma} \cdot a \quad (2)$$

where $H(x) = \begin{cases} 1, & \text{if } x > 0 \\ 0, & \text{if } x \leq 0 \end{cases}$ and σ_{ref} is the lower integration limit. Eq. (2) includes

two hypotheses: 1) there is no crack growth during the unloading path (see the term of $H(\dot{\sigma})$); 2) there is no crack growth during the initial loading path (see the term of $H(\sigma - \sigma_{ref})$). Detailed justification of these hypothesis and validation under uniaxial loadings can be found in [9]. The crack length at any arbitrary time can be calculated via direct time integration over both sides of Eq. (2). This method is fundamentally different from the traditional cycle-based fatigue formulation and is based on the incremental crack growth at any time instant within a loading cycle. Stress ratio effect is intrinsically considered in the proposed fatigue model since the stress state is directly used instead of using the cyclic stress range. It can be used for fatigue analysis at various time and length scales and is very convenient for the fatigue analysis under random variable amplitude loadings without cycle-counting.

Above discussions are for constant amplitude loadings and the idea can be extended to variable amplitude loadings. The concept of forward and reverse plastic zone interaction is used for the variable amplitude loading “memory” effect. Unlike the crack tip plasticity under monotonic loading, there are two plastic zones under fatigue cyclic loading: forward plastic zone during the loading path and reverse plastic

zone during the unloading path [16]. A schematic illustration of the proposed model is shown in Fig. 2. In Fig. 2, the reverse plastic zone is shown as the textured area and the forward plastic zone is shown as the solid shaded area. The reverse plastic zone after the unloading produces a compressive residual stress ahead of the crack tip. Crack will not grow unless the compressive residual stress is reversed, which indicates that crack will only grow beyond a certain stress level σ_{ref} in the loading path, i.e. when the present forward plastic zone size reaches the previous reverse plastic zone size ahead of the crack tip [9].

Under constant amplitude loading, the largest reverse plastic zone size at any time point always comes from the previous nearest unloading process. However, as for the variable amplitude loading, the largest reverse plastic zone size may come from a previous unloading process far from the current time point (e.g., a large overload before the current calculation). The current forward plastic zone has to go beyond the largest reverse plastic zone in order to grow the crack. As it is shown in Fig. 2, an overload is applied when the crack length is a_{ol} and the resulted reverse plastic zone is $\Delta r_{p,ol}$. At the current calculation, the crack length is a and the current forward plastic zone size is r_f . It is seen that the largest reverse plastic zone produced from a previous overload may affect the crack growth many cycles after the overload. This is known as the “memory effect” during the variable amplitude loading crack growth, such as the overload retardation.

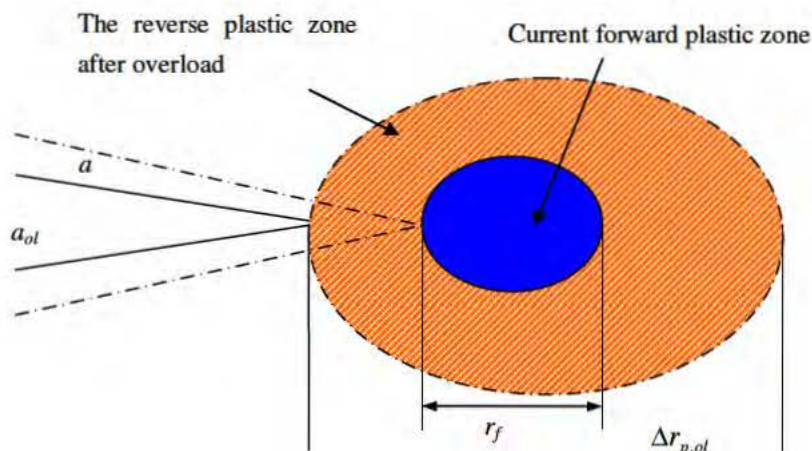


Fig.2 Illustration of forward and reverse plastic zone under variable amplitude loading

In order to represent the mechanism in Fig. 2, a modified limit state function is proposed in determining the σ_{ref} , i.e.,

$$a_{ol} + \Delta r_{p,ol} = a + r_f \quad (3)$$

The left side of Eq. (3) calculates the coordinate of the largest reverse plastic zone boundary and the right side of Eq. (3) calculates the coordinate of the current forward plastic zone boundary. Eq. (3) is also applicable to the constant loading case and is the general limit state function in determining when the crack starts to grow.

Deterministic fatigue crack length at any arbitrary time during the entire loading history can be obtained by the direct time-domain integration of Eq. (2) under both constant and variable amplitude loadings.

2.2 Uncertainty modeling and probabilistic analysis

It is known that the uncertainty of fatigue crack growth may be caused by the variation of mechanical properties of metallic materials such as inhomogeneity, composition, uncertainties in geometrical properties, etc. In this study, experimental investigation under deterministic amplitude loadings is designed to investigate the material uncertainty. In the proposed deterministic crack growth model, three material parameters(i.e., the fracture toughness K_C , the stress intensity factor threshold ΔK_{th} , and the yield strength σ_Y), are treated as random variables, which follow lognormal distributions [17]. Raw material testing data under constant amplitude loadings are used to calibrate the material random variables in the proposed probabilistic fatigue crack growth simulation model. An example is shown here for illustration. One sets of specimens (CT-I in the later experimental investigation

section) are fatigue tested under constant amplitude loading and serves as the training data. The objective is to obtain the statistics of material random variables. For constant amplitude loading testing, seven CT specimens were tested under the sinusoidal load of a maximum tensile force $P_{max}=2000N$ and $P_{min}=200N$ (stress ratio $R=0.1$). Raw material testing data is shown in Fig. 3.. A generalized Bayesian regression/updating method is used to calibrate three parameters in the small time scale model. Details of the method can be found in [18] from the same authors. Three parameters are assumed to follow the lognormal distribution and are independent to each other. 95% confidence bounds using the calibrated material parameters are used to compare with the raw experimental data (Fig. 3). It is shown that the predicted results agree well with the experimental test data which indicates a satisfactory calibration. The distribution parameters are listed in Table. 1. The calibrated statistical distribution parameters will be used for model predictions under general variable amplitude loadings.

Table 1. The calibrated statistics of material random variables

Variable	ΔK_{th} (MPa-m ^{1/2})	K_C (MPa-m ^{1/2})	σ_Y (MPa)
Mean value	0.8	32	520
Standard deviation	0.011	2.72	20.32

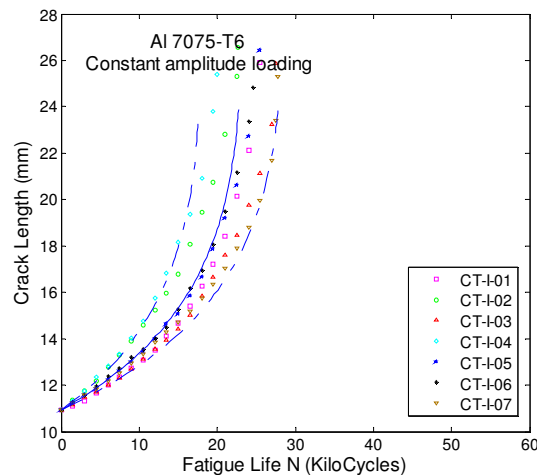


Fig. 3 Raw data and predicted a-N curves under constant amplitude loading

Another type of uncertainties is loading uncertainty. In practice, the statistical distribution for external loadings is usually specified from design or can be extracted from field testing. For example, the distribution can be obtained using classical rain-flow counting method on recorded loading spectrums. Once the statistical distribution of loading is known, random loading spectrums can be generated. In this practice, the random loading sequence becomes the major source of loading uncertainties, which is investigated in this paper. In the current investigation, overload block loading spectrums are used in the experimental investigation. The statistical distribution is a discrete probability distribution with the overload occurrence probability of p . A schematic plot probability mass function of 6% occurrence probability is shown in Fig. 4. ‘Overload’ in the x-axis indicates the occurrence of the overload loading cycle and ‘Regular’ indicate the occurrence of the regular constant amplitude loading cycle.

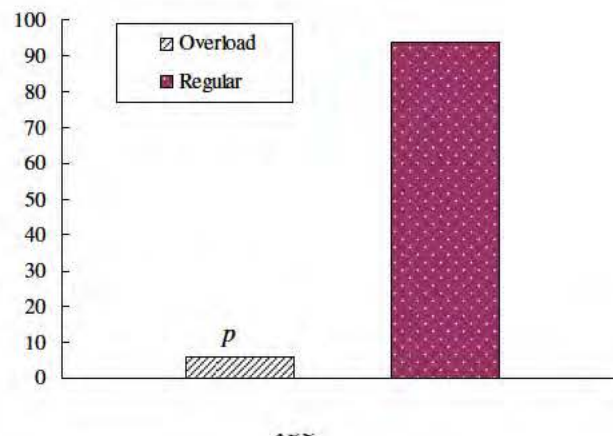


Fig. 4 Schematic plot probability mass function of 6% occurrence probability

For the loading uncertainty study, repeated block loading is used in experimental testing. The loading sequence is randomly generated while keeping the overload distribution the same as the designated one (e.g., distribution in Fig. 4). The random sequence is generated by randomly determine the cycle numbers between each pair of overload cycles, i.e. $n1$, $n2$, $n3$ in Fig. 5. For example, if the number of cycles in one block is 50, the total number of overload cycles is 3 (i.e., $50 \times 6\%$). The number of regular loading cycles is 47 (i.e., the summation of $n1$, $n2$, and $n3$ should be $(50-3)$). A random number $A1$ is first generated following the uniform distribution. $n1$ can be determined by multiplying the generated random number ($A1$) and 47. Following this, another random number ($A2$) is generated following the uniform distribution, too. $n2$ can be determined by multiplying the generated random number ($A2$) and $(47-n1)$. The integer value is used to determine $n1$ and $n2$ since the number of cycles has to be integer. To satisfy the total number of regular cycles (47 in this example), $n3$ must equal to $(47-n1-n2)$. Thus, one complete loading block is generated. Many random sequences can be generated using the above described procedure while keeping the overload distribution unchanged. An illustration of five randomly generated loading spectrums is shown in Fig. 6. The same procedure is also used for generation of other types of overload spectrums.

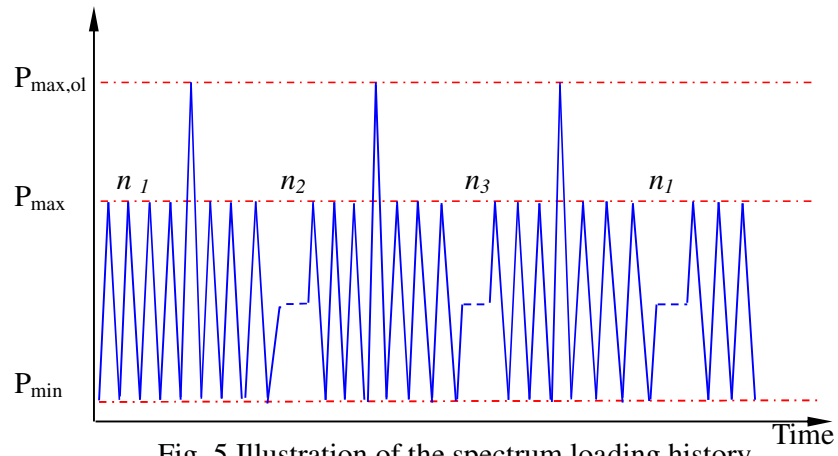


Fig. 5 Illustration of the spectrum loading history

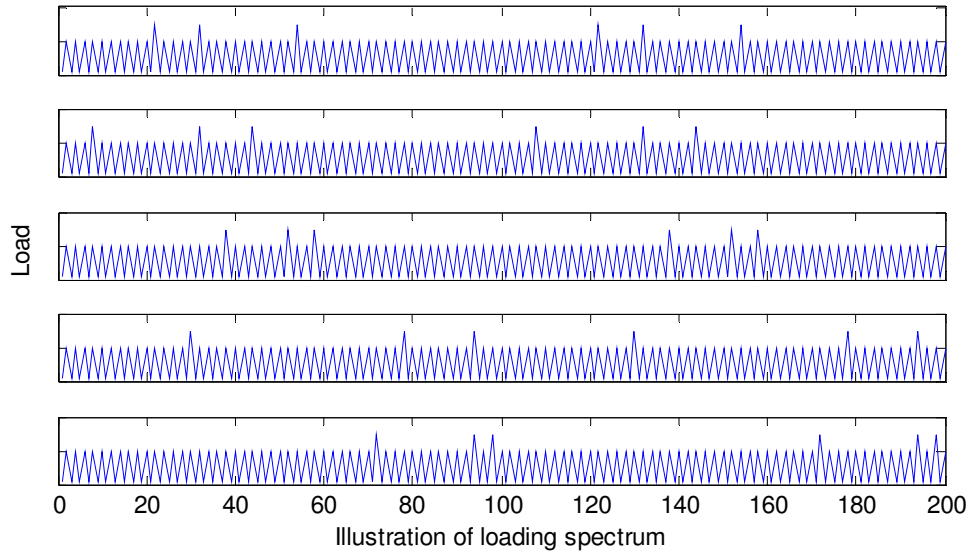


Fig. 6 Illustration of the generated random loading spectrum

Once all uncertainties of material properties are quantified and random loading sequences are generated, direct Monte Carlo simulation is used to obtain the probabilistic crack growth curves. It should be mentioned that advanced probabilistic methods are available for efficient and accurate probabilistic analysis, such as the inverse first-order reliability method [19] developed by the same authors. The key objective in this paper is to illustrate the effect of uncertainty loading on crack growth predictions. Advanced development of new probabilistic methods is beyond the scope of this study. Only direct Monte Carlo simulation method is used for illustration. In

the current study, 10000 MC samples are used for all probabilistic simulations.

3. Experimental investigation and results

3.1 Materials and specimen design

The materials tested in this study are 7075-T6 aluminum, which is one of commonly used metallic materials in aircrafts and rotorcrafts. The chemical composition and mechanical properties of 7075-T6 aluminum were summarized in Tables 2 and 3, respectively. Compact Specimen is used for fatigue crack growth testing under both constant and variable amplitude loadings according to the ASTM E647-08 [20]. A schematic drawing of our CT specimen is shown in Figure 7. The width (W) of the specimen is 40 mm and the thickness (B) is 5 mm.

Table.2 Chemical compositions of 7075-T6 aluminum (in wt.%)

Al7075-T6 Chemistry Limits												
Chemistry	Si	Fe	Cu	Mn	Mg	Cr	Zn	Ti	V	Zr	Other	Max
min	0.00	0.00	1.2	0.00	2.1	0.18	5.1	0.00	0.00	0.00	Each	0.05
max	0.4	0.50	2.0	0.30	2.9	0.28	6.1	0.20	0.05	0.05	TOT	0.15

Table.3 Mechanical properties of 7075-T6 aluminium

7075-T6 mechanical properties	
Ultimate tensile strength	573~582Mpa
Tensile yield strength	502~516Mpa
Young's Modulus	71.7GPa

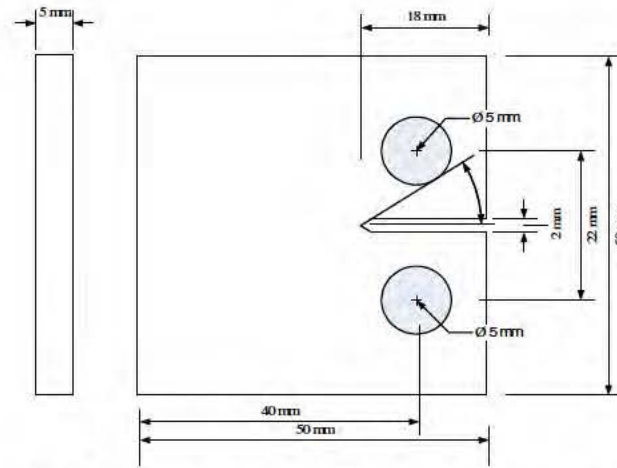


Fig 7. The illustration of the geometry of specimen used for uniaxial tensile testing

3.2 Experimental setup

All tests were conducted on a MTS servo-hydraulic test machine and performed under the load control in accordance with ASTM test specification E647-08 [20]. The surface crack measurement system consists of a stereo microscope, a digital camera and a traveling stage monitored digitally controlled by a desktop. The digital measurement system on the horizontal direction can produce a digital readout with a resolution of 0.0001 inch. The position of the traveling stage is fixed during the testing to eliminate any hysteresis effects. The testing setup is shown in Fig. 8. The surfaces of the specimen were mechanically polished (one micron diamond suspension in the last step), which provides a mirror-like surface to facilitate the optical crack length measurement. The initial crack length is obtained following the precracking procedure detailed in ASTM E647-08 [20] and is about 11 mm in the current investigation. Steady-state fatigue crack growth behavior was then investigated at the R-ratio 0.1 at a frequency of 8 Hz.

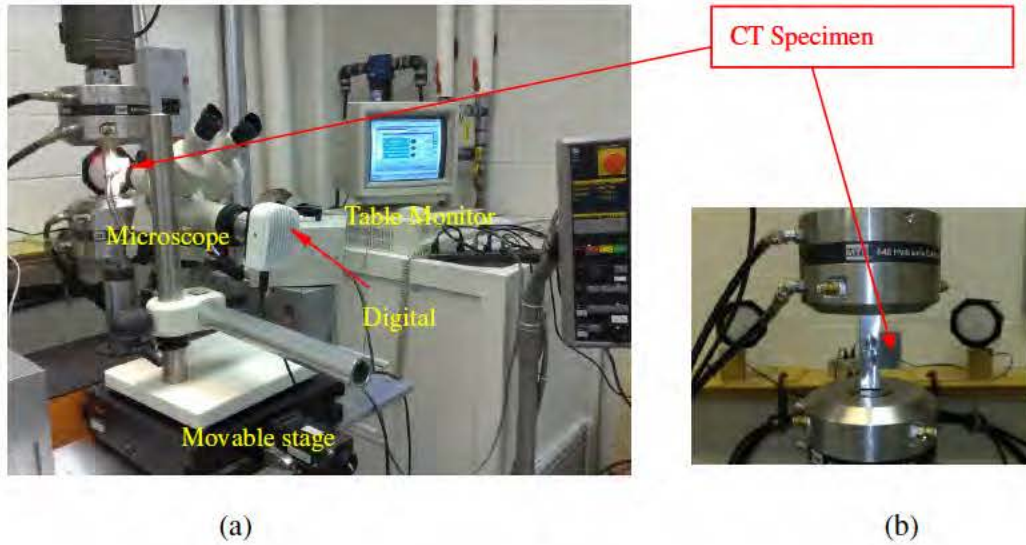


Fig. 8 Experimental testing instrumentations

According to ASTM E647-08 [20], the calculation of stress intensity factor range for the CT specimen calculate is

$$\Delta K = \frac{\Delta P}{B\sqrt{W}} f\left(\frac{a}{W}\right) \quad (4)$$

where, $f\left(\frac{a}{W}\right)$ is the geometrical correction functions, (validity range: $a/W \geq 0.2$)

$$f\left(\frac{a}{W}\right) = \frac{(2 + a/W)}{(1 - a/W)^{3/2}} \left[0.886 + 4.64\left(\frac{a}{W}\right) - 13.32\left(\frac{a}{W}\right)^2 + 14.72\left(\frac{a}{W}\right)^3 - 5.6\left(\frac{a}{W}\right)^4 \right] \quad (5)$$

This SIF solution is used in the model prediction.

3.3 Experimental loading design and results

The main objective of this study is to investigate the effect of loading uncertainties on the fatigue crack growth behavior. Loading profile design is the crucial component in order to achieve this goal. In addition, the current study focuses on the statistical analysis of the fatigue crack growth behavior, a large number of specimen testing is also required.

Table. 4 Summary of testing design

Group name	Loading spectrum	Number of specimens	Overload ratio
------------	------------------	---------------------	----------------

CT-I	Constant amplitude loading	7	N/A
CT-II	Single overload spectrum	4	1.5 to 2.0
CT-III	6% overload block spectrum – deterministic sequence	7	1.2
CT-IV	6% overload block spectrum – random sequence	7	1.2
CT-V	6% overload block spectrum – deterministic sequence	7	1.5
CT-VI	6% overload block spectrum – random sequence	7	1.5
CT-VII	0.15% overload block spectrum – deterministic sequence	7	1.5
CT-VIII	0.15% overload block spectrum – random sequence	7	1.5

Various constant amplitude, deterministic variable amplitude, and random variable amplitude loading tests are designed. The tests design is summarized in Table 4. The schematic representation of different variable amplitude loading is shown in Fig. 5. Details about the testing design and experimental observations are described below under variable amplitude loadings. Testing results under constant amplitude loadings have been discussed in section 2.

3.3.1 CT – II – single overload spectrums

CT-II is under single overload spectrums. The objective is to check the applicability of the deterministic small time scale model under different overload ratios and is not for statistical uncertainty analysis. This test can be considered as a preliminary deterministic validation of the used small time scale fatigue crack growth model.

In this section, overload retardation effect is studied by performing testing on four

CT specimens under single overload loading histories with different overload ratios. The P_{\max} and P_{\min} of regular load are set as same as those for the constant amplitude loading. The maximum load value of overload $P_{\max,ol}$ is set as 3000N, 3400N, 3800N, and 4000N (i.e., overload ratio is 1.5, 1.6, 1.7 and 2.0) , respectively. The overload is inserted into the loading history when the crack is about 14 mm. Raw testing results are shown in Fig. 9(a). It is clearly seen the retardation effect after the overload loading. The retardation effect increases as the overload ratio increases. It is also observed that “crack arrest” happens when the overload ratio is 2.0. Deterministic model predictions using the calibrated mean value of parameters (see the last section under constant amplitude loading) are shown in Fig. 9(b). A very similar trend as those shown in the experimental data is observed from the model prediction. This observation indicates the proposed small time scale model is capable of simulating the overload retardation effect and will be used for other spectrum predictions.

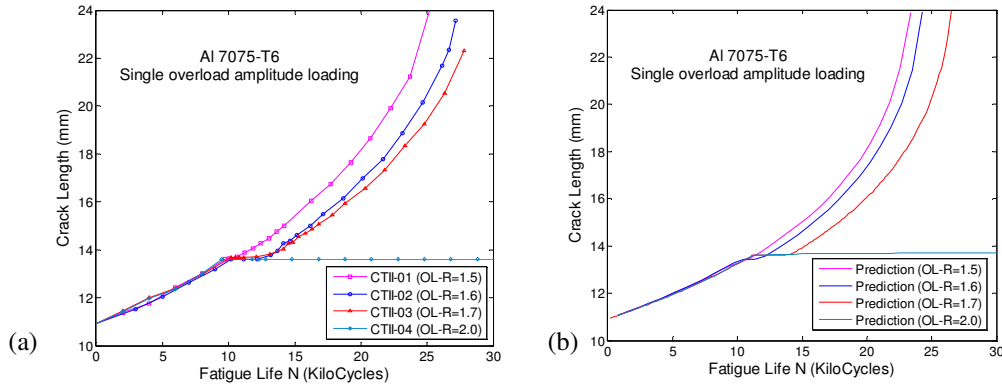


Fig.9 Experimental observations and model predictions under single overload spectrum (a) experimental data; (b) model prediction

3.3.2 CT – III & CT-IV (CT-V & CT-VI)

CT – III & CT-IV (CT-V & CT-VI) testing are under the overload spectrums with

6% overload cycles. CT-III (CT-V) specimens are under the same deterministic loading sequence. CT-IV (CT-VI) specimens are under the random loading sequence. CT – III & CT-IV have the overload ratio of 1.2 and CT-V & CT-VI have the overload ratio of 1.5. The overload ratio is defined as the ratio between the maximum loading level of the overload cycle and the maximum value of the constant load cycle. P_{\max} and P_{\min} of the constant load cycles are 2000N and 200N, respectively. The peak value $P_{\max,ol}$ for the overload cycle is 2400N for the overload ratio 1.2 and is 3000N for the overload ratio 1.5.

All groups have the statistically identical loading (i.e., 6% overload). The block sequences of the two testing groups are listed in Table 5. The random sequence is generated using the methods described in section 2. It should be noted that the confidence levels of crack growth measurements may vary for different sample sizes [21]. Due to limited budget and time, seven specimens are used for each group of testing.

Table. 5 Summary of the loading sequence of 6% overload spectrum

Specimen	Loading sequence*
CT-III-01~07 / (CT-V)-01~07	n1=23, n2=10, n3=14
CT- IV -01 / (CT-VI)-01	n1=23, n2=10, n3=14
CT- IV -02 / (CT-VI)-02	n1=42, n2=3, n3=2
CT- IV -03 / (CT-VI)-03	n1=16, n2=16, n3=15
CT- IV -04 / (CT-VI)-04	n1=30, n2=10, n3=7
CT- IV -05 / (CT-VI)-05	n1=27, n2=20, n3=0

CT- IV -06 / (CT-VI)-06	n1=47, n2=0, n3=0
CT- IV -07 / (CT-VI)-07	n1=12, n2=20, n3=15

* Loading sequence and explanation of n1, n2, and n3 can be found in Fig. 5.

The raw data of measured crack length is shown in Fig. 10 and Fig. 11.

Median and 90% confidence bounds using 10,000 direct Monte Carlo simulations are shown together with the raw experimental data in (a), (b) of Fig. 10~Fig. 11. Overall, a satisfactory agreement is observed between experimental observations and model predictions for the different spectrum loading histories. All experimental observations fall within the 90% confidence bounds for both deterministic and random loading histories. For some cases, the predicted median curve has a small deviation from the median value of the experimental observations. This could be caused by the insufficient number of specimens. Also, this could be due to the inaccuracy of the small time scale model. Future work is required for the improvement of prediction accuracies.

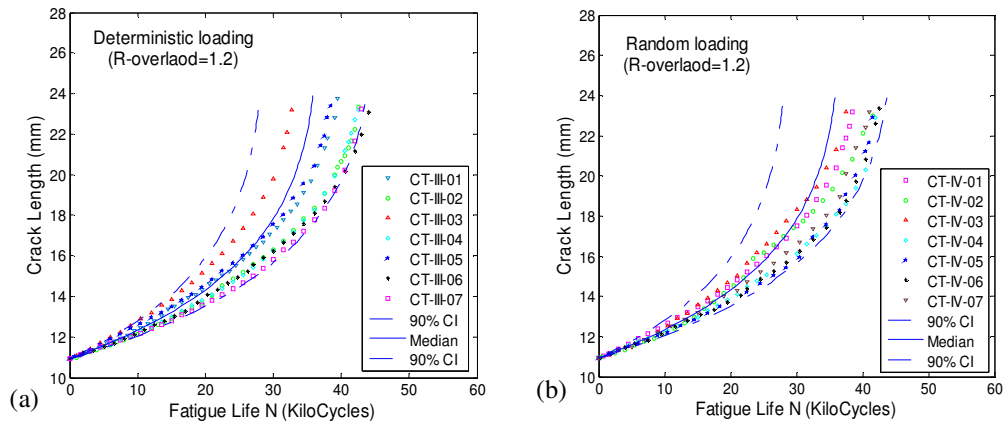


Fig. 10 Raw data and predicted a-N curves under (a) deterministic loading; (b) Raw random loading, (6% overload spectrum, overload ratio=1.2)

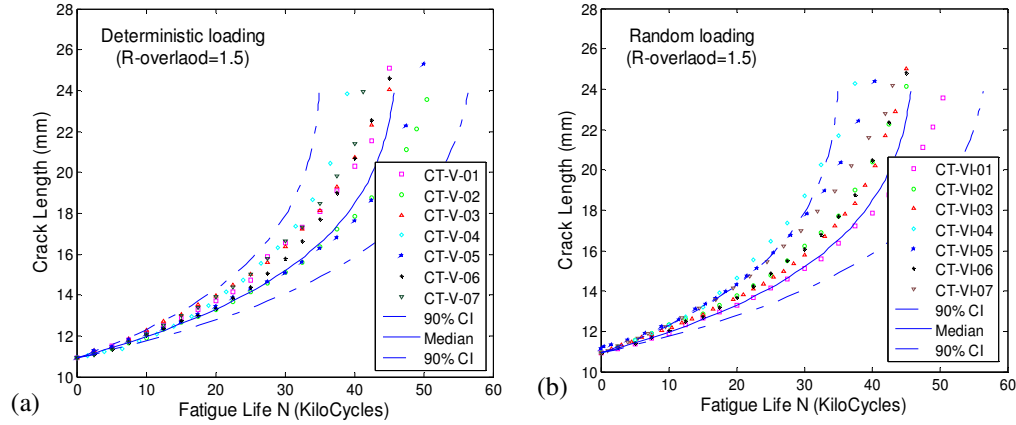


Fig. 11 Raw data and predicted a-N curves under (a) deterministic loading, (b) random loading, (6% overload spectrum, overload ratio=1.5)

3.3.4 CT – VII & CT-VIII

CT – VII & CT-VIII testing are under the overload spectrums with 0.15% overload cycles. Each block has 2000 cycles. CT-VII specimens are under the same deterministic loading sequence. CT-VIII specimens are under the random loading sequence. Both groups have the overload ratio of 1.5. The deterministic and random loading sequences are listed in Table 6.

Table. 6 Summary of the loading sequence of 0.15% overload spectrum

Specimen	Loading sequence*
CT-VII-01~07	n1=100, n2=47, n3=1850
CT-VIII-01	n1=100, n2=47, n3=1850
CT-VIII-02	n1=800, n2=600, n3=597
CT-VIII-03	n1=1997, n2=0, n3=0
CT-VIII-04	n1=517, n2=0, n3=1480
CT-VIII-05	n1=665, n2=665, n3=667
CT-VIII-06	n1=150, n2=668, n3=1179
CT-VIII-07	n1=1887, n2=50, n3=60

* Loading sequence and explanation of n1, n2, and n3 can be found in Fig. 5. The raw data of measured crack length is shown in Fig. 12.

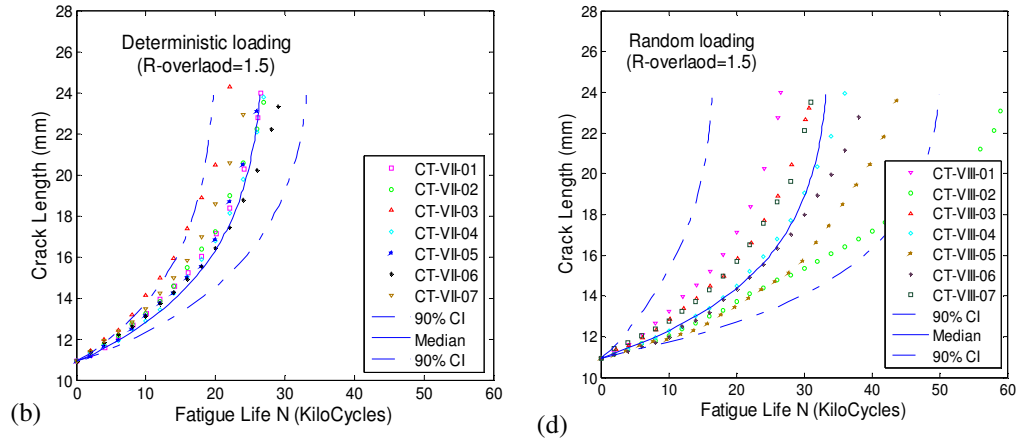


Fig.12 Raw data and predicted a-N curves under (a) deterministic loading; (b) random loading, (0.15% overload spectrum, overload R-ratio=1.5)

The raw data of measured crack length – time (a-N) curves are shown in Fig. 12. Median and 90% confidence bounds using 10,000 direct Monte Carlo simulations are shown together with the raw experimental data. Again, a satisfactory agreement is observed between experimental observations and model predictions for the different spectrum loading histories. One testing data under random loading sequence shows a very different trend with respect to other testing curves.

4. Discussions

A detailed discussion is given in this section based on the experimental and numerical investigations for the loading effect on the probabilistic fatigue crack growth predictions. The focus in the discussion is on the effect of different loading conditions on the median and variance of crack length measurements. The small time scale model is used to explain the experimental observations.

4.1 Overload ratio effects

It is well known that the overload ratio affects the magnitude of “crack growth retardation” [22, 23]. Most existing studies focused on the deterministic (e.g., mean or

median) behavior and very few studies focused on the statistical effects [24]. Experimental testing of multiple specimens under different overload ratios (e.g., 1.2 and 1.5) for 6% overload cycle spectrums were performed. All loadings are deterministic to remove the loading uncertainty effects (e.g., CT-III and CT-V groups). Experimental measured median and variance of crack length under these two loading conditions are shown in Fig. 13(a) and Fig. 13(b), respectively. Fig. 13(a) is for the median crack growth and it clearly shows the effect of different overload ratios. Higher overload ratios causes a higher retardation and slower crack growth. Fig. 13(b) shows the variance variation corresponding to time and it shows that the variance for the higher overload ratio is also larger than that of a lower overload ratio. The median and variance of Monte Carlo simulations using the small time scale model are shown in Fig. 13(c) and Fig. 13(d), respectively. It is shown that the model prediction correctly represents the same behavior as observed in the experiments.

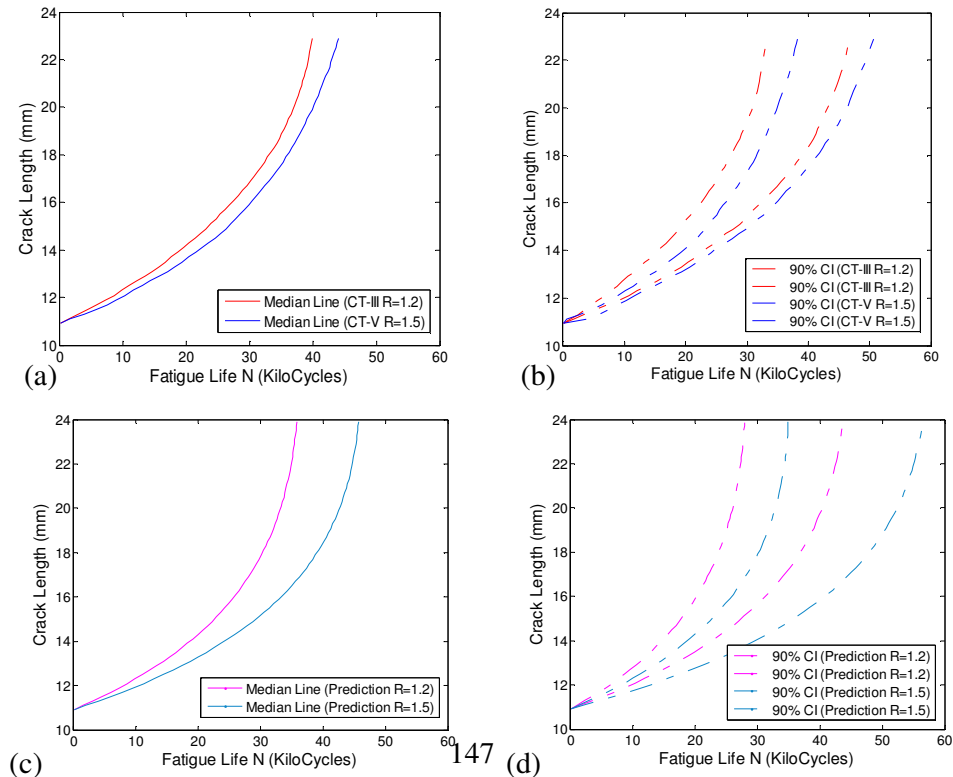


Fig. 13 Crack length under 6%-overload spectrum with different overload ratios (a) Experimentally measured median; (b) Experimentally measured variance; (c) median of Monte Carlo simulations; (d) variance of Monte Carlo simulations

This behavior seen in the experiments and predictions can be explained by the crack closure concept in the small time scale model. The crack length at the any arbitrary time is calculated by integrating the kernel function from crack opening stress level to the maximum stress level. The crack opening stresses under 6%-overload spectrum with two different overload ratios are shown in Fig. 14. It is seen that the higher overload ratio caused a higher crack opening stress level in general, which leads to slower crack growth rate.

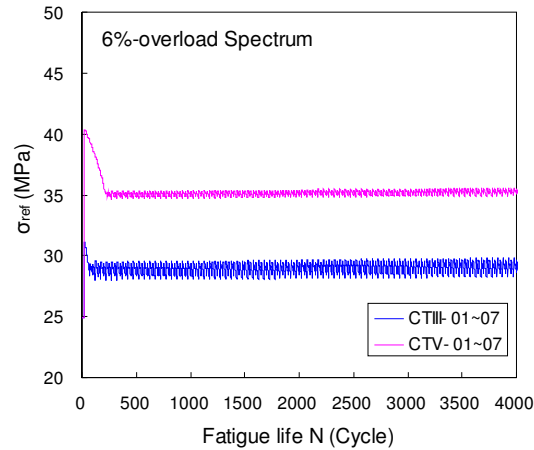


Fig. 14 The crack opening stress under 6% - overload spectrum with two different overload ratios

4.2 Overload cycle percentage effects

This section focuses on the effect of different overload cycle percentage (i.e., probability of occurrence). Experimental testing of multiple specimens under deterministic 6% overload spectrum (CT-V) and deterministic 0.15% overload

spectrum (CT-VII) were performed. Each group includes seven specimens. Experimental measured median and variance of crack length under these two loading conditions are shown in Fig. 15(a) and Fig. 15(b), respectively. It clearly shows that both of the median and variance of fatigue crack growth life under 6%-overload spectrum is much longer than those under 0.15%-overload spectrum. In this investigation, higher overload cycle percentage causes a higher retardation and slower crack growth. The median and variance of Monte Carlo simulations using the small time scale model are shown in Fig. 15(c) and Fig. 15(d), respectively. It is shown that the model prediction correctly represents the same behavior as the experimental observations.

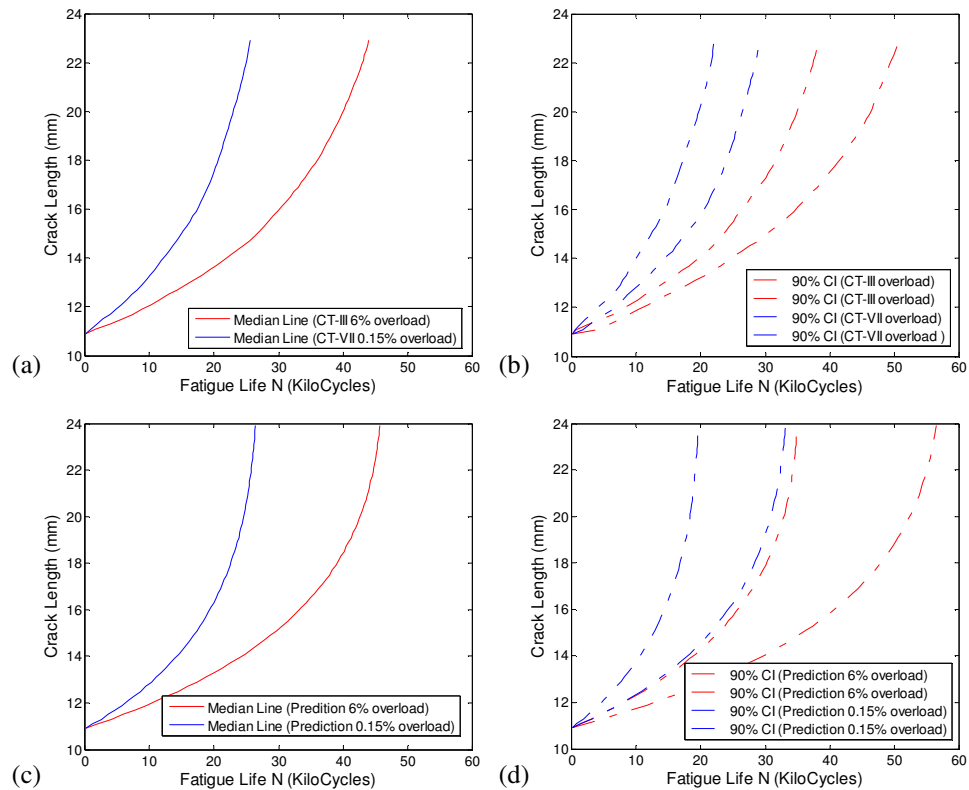


Fig. 15 Crack length under different overload cycle percentage spectrums (a) Experimentally measured median; (b) Experimental measured variance; (c) median of Monte Carlo simulations; (d) variance of Monte Carlo simulations

Again, the reason for this phenomenon seen in the experiments and predictions can be explained by the crack closure concept in the small time scale model. The crack opening stress levels under two different overload percentage spectrums are shown in Fig. 16. It is seen that the crack opening stresses under one 6%-overload spectrum sequence (i.e. CTV-01~07) float around a higher level with smaller variation compared to those under one 0.15%-overload spectrum sequence (i.e. CTVII-01~07), which leads to slower crack growth rates. The reason is that the retardation effect caused by overload cycles has influence on the following thousands of cycles. For 6%-overload spectrum (i.e. CTV-01~07), another overload occurs before the crack opening stress level reduces to its steady state under the constant amplitude loading. While for 0.15%-overload spectrum (i.e. CTVII-01~07), the crack opening stress level reduces significantly before another overload happens (as shown in Fig.17).

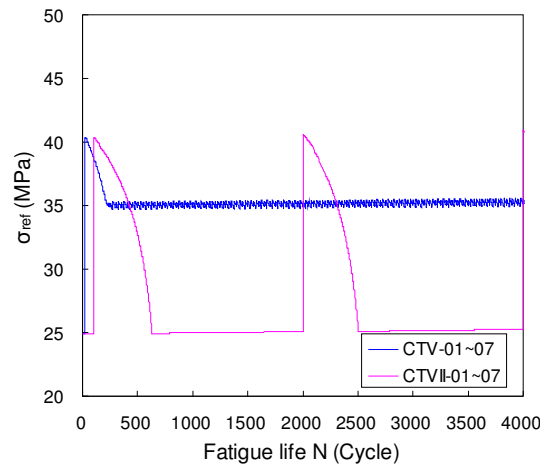


Fig. 17 The crack opening stress under two different overload-percent spectrums: 6%-overload spectrum and 0.15%-overload spectrum

4.3 Deterministic and random loading sequence effect

Previous discussions all focuses on the deterministic loading sequence, i.e., all

specimen are under the same variable amplitude loading. This section focuses on the effect of random loading sequence effect. In order to study the random loading sequence effect, the experimental testing of multiple specimens for random 6% overload cycle spectrums and random 0.15% overload cycle spectrum sequences (CT-IV, CT-VI and CT-VIII groups) were performed corresponding to the testing (CT-III, CT-V and CT-VII groups) under deterministic loading sequences, respectively. Experimental measured medians and variances of crack length under random loading sequences and deterministic loading sequence are plotted together in Fig. 18~ Fig. 20. The median and variance of Monte Carlo simulations using the small time scale model are shown in (c) and (d) of Figs. 18~20, respectively. It is shown that the model prediction correctly reproduces the same behavior as observed in the experiments.

Experimental and simulation results show very different effects of random loading sequence on the fatigue crack growth under 6% overload spectrum and 0.15% overload spectrums. For 6% overload spectrum, no significant difference between deterministic and random loading sequence is observed. Both median and variance measurements are similar under deterministic and random loading sequences. This is confirmed for overload ratio 1.2 (Fig. 18) and overload ratio 1.5 (Fig. 19). Experimental measurements show slight difference, which is likely to be caused by the insufficient number of specimens. MC simulation results are almost the same and curves are overlapped on each other. Thus, it could be concluded that the loading uncertainties from random loading sequence have no major influence on fatigue crack growth under the 6% overload cycle spectrums.

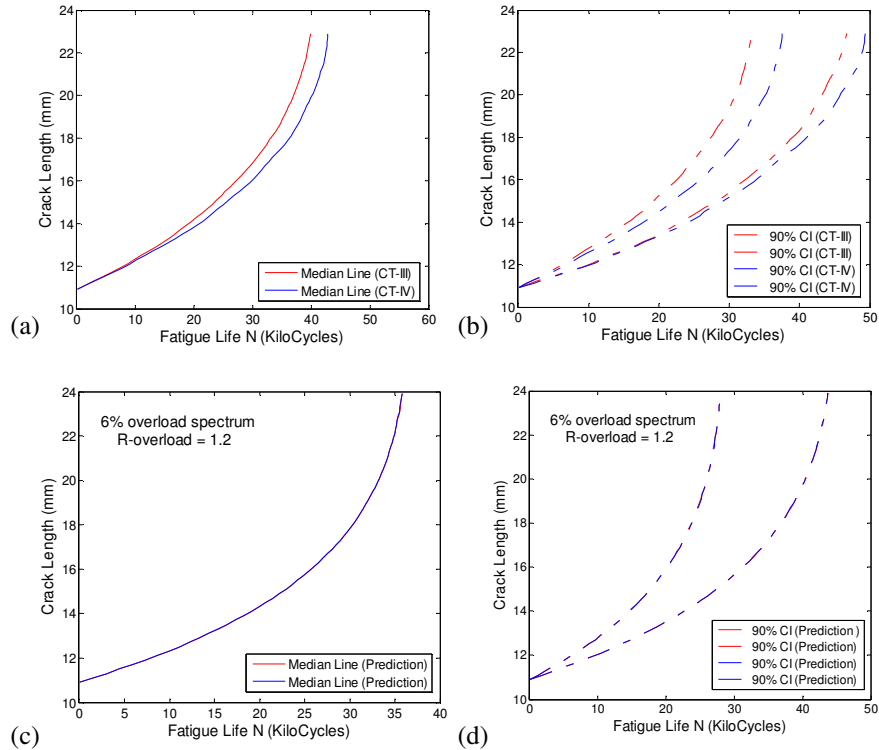


Fig. 18 Crack length under deterministic 6%-overload spectrum loading history and random loading history with overload ratio 1.2 (a) Experimentally measured median, (b) Experimentally measured variance, (c) median of Monte Carlo simulations; (d) variance of Monte Carlo simulations

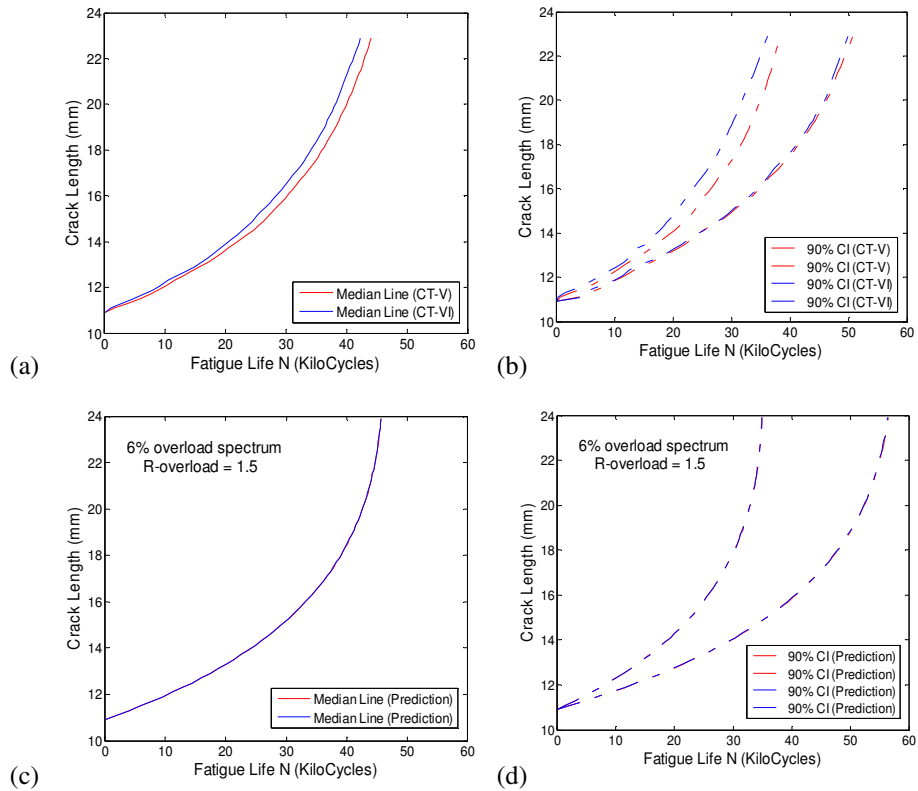


Fig. 19 Crack length under deterministic 6%-overload spectrum loading history and random loading history with overload ratio 1.5 (a) Experimentally measured median, (b) Experimentally measured variance, (c) median of Monte Carlo simulations; (d) variance of Monte Carlo simulations

The conclusion is completely different for 0.15% overload spectrums. Significant effects of loading uncertainties are observed under 0.15% overload spectrums. The median curve under random loading sequence is slightly slower compared to the one under deterministic loading sequence. The variance under random loading sequences is significantly larger than that under deterministic loading sequences (Fig. 20). The data under random loading sequences is much more scatter than that under deterministic loading sequences. Again, the median and variance prediction of Monte Carlo simulation shows the similar behavior as the experimental observations.

The above observations indicate that the effect of loading uncertainties depends on the overload spectrums. This behavior could be explained by the uncertainties associated with the crack opening stress under deterministic and random loading sequences. For random 6%-overload spectrum loading history, the amplitude of crack opening stress level only varies in a small range for different loading sequences, while the amplitude of crack opening stress level changes quite differently for different 0.15%-overload spectrum loading sequences. The opening stress variations of seven specimens for the two different loading spectrums are shown in Fig. 21. It is clearly shown that the scatter of the opening stress is much larger for the 0.15% spectrum, which causes a larger scatter in the fatigue crack growth behavior.

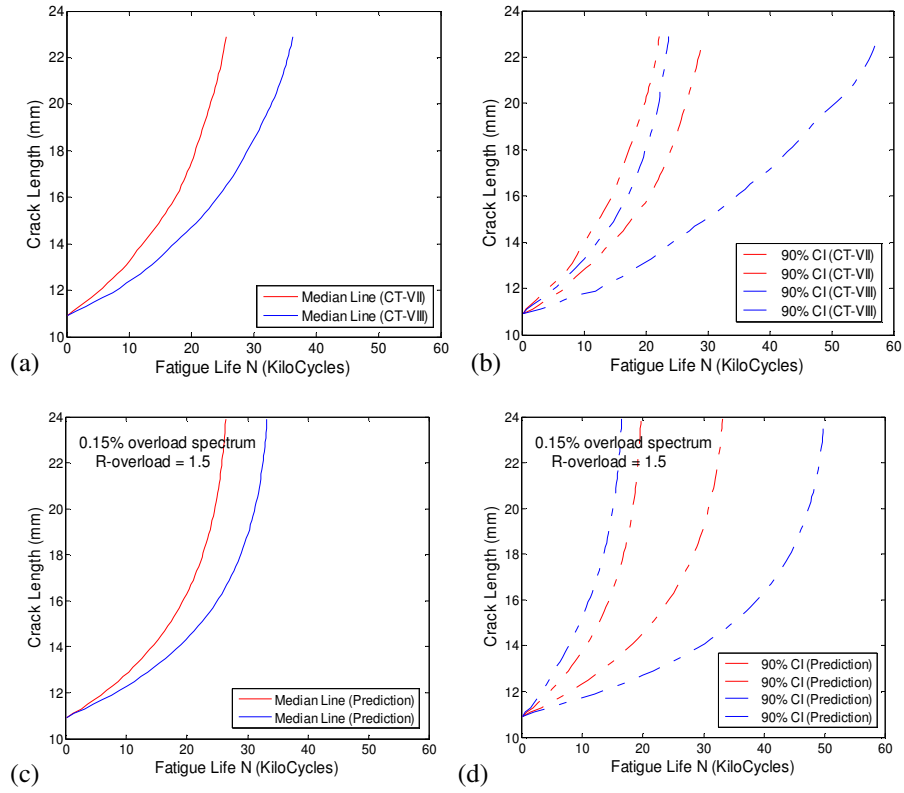


Fig. 20 Crack length under deterministic 0.15%-overload spectrum loading history and random loading history with overload ratio 1.5 (a) Experimentally measured median, (b) Experimentally measured variance, (c) median of Monte Carlo simulations, (d) variance of Monte Carlo simulations

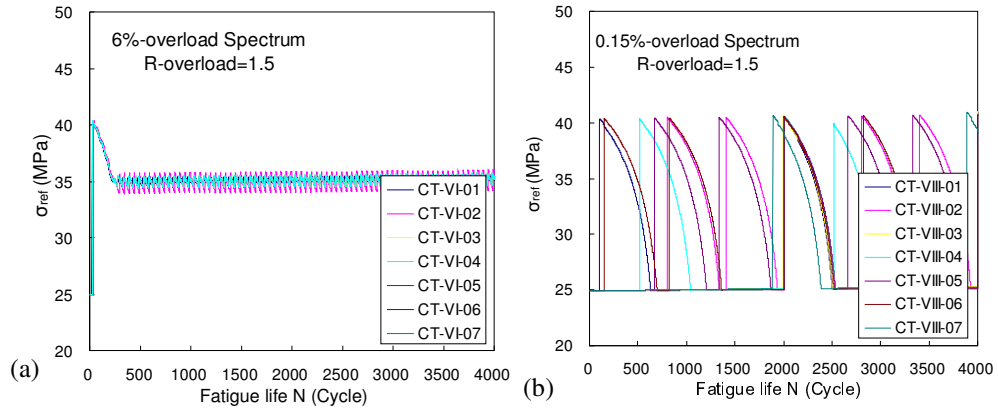


Fig. 21 Crack opening stress variation under two different overload-percentage spectrums (a) 6%-overload spectrum; (b) 0.15%-overload spectrum

5 Conclusions

This study focuses on the experimental and numerical investigation of stochastic fatigue crack growth under variable amplitude loadings. Multiple Compact Tension

(CT) specimens of 7075-T6 aluminum under various loading histories are performed, which includes constant amplitude loading, variable amplitude loading with single overload, and spectrum variable amplitude loading with overload. The scatter and statistical aspect of fatigue crack growth data are investigated. Monte Carlo simulations using a recently developed small time scale model is used for probabilistic crack growth predictions and for explanations of experimental findings. Overall, a satisfactory agreement between experimental observations and model predictions is observed and the proposed model is able to explain most of experimental findings using crack closure-based mechanism.

Several main conclusions from both experimental and numerical study are shown below:

- Both median and variance of crack growth life will increase as the overload ratio increases, which can be explained by the increased crack opening stress level.
- Both median and variance of crack growth life will decreases as the percentage of overload cycle decreases in the current investigation. This behavior is caused by the crack opening stress variation under different stress levels.
- The effect of loading uncertainties from random loading sequence depends on the loading spectrums (e.g., the percentage of overload cycles). In the current investigation, no major effects are identified under the 6% overload cycles for both median and variance of crack growth life. Significant effects are observed

under 0.15% overload spectrums, where the variance of random loading sequence is much larger than that under deterministic loading sequences. This behavior is related to the uncertainties associated with the crack opening stress under deterministic and random loading sequences.

The above conclusions are based on the investigations under specified loadings and materials. For other loading spectrums and materials, further investigation is required. Future work is also required to extend the discussions to general multiaxial loading conditions, where the mixed-mode crack growth occurs.

Acknowledgements

The research reported in this report was supported by funds from Air Force Office of Scientific Research (Contract No. FA9550-11-1-0025, Project Manager: Dr. David Stargel). The support is gratefully acknowledged.

Reference

1. Svensson, T., *Prediction uncertainties at variable amplitude fatigue*. International Journal of Fatigue, 1997. **19**(93): p. 295-302.
2. Wu, W.F. and C.C. Ni, *Statistical aspects of some fatigue crack growth data*. Engineering Fracture Mechanics, 2007. **74**(18): p. 2952-2963.
3. Chen, C.-D., et al., *The effects of material variations on aircraft inspection schedules based on stochastic crack growth model*. International Journal of Fatigue, 2008. **30**(5): p. 861-869.
4. Liu, Y. and S. Mahadevan, *Probabilistic fatigue life prediction using an equivalent initial flaw size distribution*. International Journal of Fatigue, 2009. **31**(3): p. 476-487.
5. Taheri, F., D. Trask, and N. Pegg, *Experimental and analytical investigation of fatigue characteristics of 350WT steel under constant and variable amplitude loadings*. Marine Structures, 2003. **16**(1): p. 69-91.
6. Dominguez, J., J. Zapatero, and J. Pascual, *Effect of load histories on scatter of fatigue crack growth in aluminum alloy 2024-T351*. Engineering Fracture Mechanics, 1997. **56**(1): p. 65-76.
7. Grell, W.A. and P.J. Laz, *Probabilistic fatigue life prediction using AFGROW and accounting for material variability*. International Journal of Fatigue. **32**(7): p.

1042-1049.

8. D.A. Virkler, B.M. Hillberry, and P.K. Goel, *The statistic nature of fatigue crack propagation*. ASME J Engng Mater Technol 1979. **101**: p. 148-153.
9. Zizi Lu and Y. Liu, *Small time scale fatigue crack growth analysis*. International Journal of Fatigue, 2010. **32**(8): p. 1306-1321.
10. Willenborg J., Engle R.M., and W. R.A., *A Crack Growth Retardation Model Using an Effective Stress Concept*. 1971, Air Force Flight Dynamics Laboratory: Wright-Patterson Air Force Base, Ohio.
11. Wheeler, O.E., *Spectrum loading and crack growth* J. Basic Eng., Trans. ASME, 1972. **94**(1): p. 181-186.
12. Elber, W., *The significance of fracture crack closure*. ASTM Special Technical Publication 486, American Society for Testing and Materials ed. Damage tolerance in aircraft structures. 1971, Philadelphia. 230-242.
13. Newman, J.C., *A crack opening stress equation for fatigue crack growth*. International Journal of Fatigue, 1984. **24**: p. 131-135.
14. Koning, A.U.d. *A simple crack closure model for prediction of fatigue crack growth rates under variable-amplitude loading*. in *Fracture Mechanics: Thirteenth Conference, ASTM STP 743*. 1981: American Society for Testing and Materials.
15. Ray, A. *A state-space model of fatigue crack growth for real-time structural health management*. in *Digital Avionics Systems Conferences*. 2000.
16. McClung, R.C., *Crack closure and plastic zone sizes in fatigue*. Fatigue & Fracture of Engineering Materials & Structures, 1990. **14**(4): p. 455-468.
17. GS, W., *Intrinsic statistical characteristics of fatigue crack growth rate* Eng Fract Mech, 1995. **51**: p. 787-803.
18. Guan, X., R. Jha, and Y. Liu, *Probabilistic fatigue damage prognosis using maximum entropy approach*. Journal of Intelligent Manufacturing, 2009: p. 1-9.
19. Yibing Xiang and Y. Liu, *Application of inverse first-order reliability method for probabilistic fatigue life prediction* Probabilistic Engineering Mechanics, 2011. **26**(2): p. 148-156.
20. Materials, A.S.o.T.a., *Standard Test Method for Measurement of Fatigue Crack Growth Rates*, in *Annual Book of ASTM Standards*. 1998: Philadelphia, PA. p. 671-715.
21. Ray, A. and R. Patankar, *A stochastic model of fatigue crack propagation under variable-amplitude loading*. Engineering Fracture Mechanics, 1999. **62**(4-5): p. 477-493.
22. Skorupa, M., *Load interaction effects during fatigue crack growth under variable amplitude loading - a literature review. Part I: empirical trends*. Fatigue Fract Engng Mater Struct 1998. **21**: p. 987-1006.
23. D. Damri and J.F. Knott, *Transient retardations in fatigue crack growth following a single peak overload*. Fatigue Fract Engng Mater Struct 1991. **14**: p. 709-719.
24. Kim, J.K. and D.S. Shim, *A statistical approach for predicting the crack retardation due to a single tensile overload*. International Journal of Fatigue, 2003. **25**(4): p. 335-342.

Appendix 6: Accomplishments for Task 2.2

Subset simulation for inverse reliability problem: application to probabilistic fatigue life prediction

Hongshuang Li, Yibing Xiang, Yongming Liu*
Clarkson University, Potsdam, NY, 13699

Abstract: A general simulation-based methodology is proposed for efficient and accurate inverse reliability analysis, which is applied to solve the problem of probabilistic fatigue life prediction at a specified reliability level. The proposed methodology is based on an inverse formulation of the subset simulation algorithm and an equivalent initial flaw size (EIFS)-based fatigue life prediction model. A parametric study is performed to determine the optimal parameter combination of the subset simulation. The simulation results are compared with direct Monte Carlo simulations for model verification. The proposed method is shown to have similar accuracy with that of direct Monte Carlo simulation and significantly reduces the computational burden.

Keywords: fatigue crack growth, subset simulation, inverse reliability problem, fatigue life prediction

1. Introduction

Fatigue reliability is a time-dependent reliability problem and different metrics can be used to describe the random nature of fatigue damage [1-7]. One common approach is to calculate the reliability/failure probability at a specified life [3, 4]. This approach is very useful for engineering design against fatigue since the service life is usually given in design problems. Both simulation-based method and the FORM

* Corresponding author, Tel.: 315-268-2341; Fax: 315-268-7985; Email: yliu@clarkson.edu

method can be used for this purpose [3, 4]. Another approach is the probabilistic fatigue life prediction, i.e. the remaining life estimation at a specified reliability level, which is formulated as an inverse reliability problem [6, 7]. This measure is very useful for damage prognosis and condition-based maintenance and is the focus of the current study. The inverse reliability methods have been developed and widely used for the reliability-based design optimization (RBDO) problem [8-10]. The RBDO problem is subject to the constraints that the probability of design feasibility is larger than or equal to a specified reliability level. The evaluations of reliability constraints are similar to the probabilistic fatigue life prediction problem (i.e., calculate the life variable under a specified reliability level). Xiang and Liu [6, 7] developed and applied an inverse first-order reliability method (IFORM) for probabilistic fatigue life prediction. The current investigation focuses on the efficient simulation-based method for inverse reliability analysis and probabilistic fatigue life prediction.

Simulation-based method is a widely-used technique for reliability analysis. Direct Monte Carlo simulation (MCS) can be used for probabilistic fatigue life prediction, but is time-consuming for large scale applications. Efficient simulation-based method for the probabilistic fatigue life prediction is the key objective of the presented study. Various sampling technique have been proposed to enhance the computational efficiency of direct MCS, such as importance sampling [11-13], directional sampling [14], and subset simulation [15-19]. Subset simulation is explored in this paper for the probabilistic fatigue life prediction.

Subset simulation is an efficient Monte Carlo technique originally developed for

structural reliability problems [15-19]. The basic idea is to express a small probability as a product of several large conditional probabilities of some intermediate events [15-19]. This allows converting a rare event simulation problem into a series of frequent event simulation problems. The Markov Chain Monte Carlo (MCMC) [20, 21] is employed to evaluate these large conditional probabilities of frequent intermediate events and the Metropolis-Hastings algorithm [20, 21] is adopted to generate the required conditional samples, which is well known as a flexible sampling technique to generate random samples for any arbitrary probability density function (PDF). The original subset simulation is proposed for the forward reliability analysis and is not suitable for the probabilistic life prediction (i.e., an inverse reliability problem). To see this, one new contribution of the proposed study is to develop an inverse formulation of subset simulation algorithm. In addition, the investigation of subset simulation on time-dependent fatigue problem is rarely found in the open literature. The proposed study integrates the inverse version of subset simulation algorithm with a previously developed equivalent initial flaw size (EIFS)-based fatigue life prediction model [3, 22, 23] for efficient probabilistic life prediction.

This paper is organized as follows. First, the basic principles of subset simulation are briefly reviewed. Following this, a mechanical model for the crack growth-based life prediction based on the equivalent initial flaw size (EIFS) concept is briefly discussed. Next, the subset simulation algorithm integrated with the deterministic fatigue model is applied to predict probabilistic fatigue life by treating it as an inverse reliability problem. A parametric study is performed to investigate the effect of

algorithm parameters on the computational efficiency and accuracy. Finally, the proposed methodology is verified by direct Monte Carlo simulation.

2. Background of subset simulation algorithm

In this section, a brief review of subset simulation for the forward reliability analysis is given. Detailed derivation and validation can be found in [15-19].

2.1 Basic principles of the subset simulation

Without loss of generality, it is assumed that the probability of a target event F_T is given by

$$P(F_T) = P(G(\mathbf{x}) > b) \quad (1)$$

where $G(\mathbf{x})$ is a response function of a random vector \mathbf{x} with a joint PDF $f_{\mathbf{x}}(\mathbf{x})$, b is the threshold for the target event. Given a series of intermediate events $F_i, i = 1, 2, \dots, m$, let $F_1 \supset F_2 \supset \dots \supset F_m = F_T$ be a descending sequence of events so that $F_k = \bigcap_{i=1}^k F_i, k = 1, 2, \dots, m$. By the definition of conditional probability and the multiplication theorem in the probability theory, the probability $P(F_T)$ can be expressed as

$$P(F_T) = P(F_m) = P(F_m | F_{m-1}) P(F_{m-1}) = \dots = P(F_1) \prod_{i=2}^m P(F_i | F_{i-1}) \quad (2)$$

In Eq. (2), the probability of a target event F_T is expressed as a production of a series of conditional probabilities $P(F_i | F_{i-1}), i = 2, \dots, m$ and $P(F_1)$.

If the standard Monte Carlo simulation (MCS) is used to evaluate $P(F_T)$ in the original probability space, the number of samples would be very large if $P(F_T)$ is very small. The idea of subset simulation is to replace the evaluation of a small $P(F_T)$ in the original probability space with the evaluation of a series large

conditional probabilities in the conditional probability space. Even if $P(F_T)$ is very small, $P(F_1)$ and the conditional probabilities $P(F_i|F_{i-1}), i = 2, \dots, m$ in Eq. (2) can be made arbitrarily large by appropriate choosing the intermediate events $F_i, i = 1, 2, \dots, m$. Thus, they can be evaluated efficiently by the simulation procedure. The efficiency of simulation-based method can be measured by the coefficient of variance (COV) of the estimator, which is defined by the ratio of its standard deviation and its expectation. For example, if the target probability is $P(F_T) = 10^{-3}$, it requires at least $10^4 \sim 10^5$ samples in the original probability space with given a COV of 10%~30%. By choosing $m = 3$ and $P(F_1), P(F_i|F_{i-1}) = 0.1, i = 2, 3$, about $3 \times 10^2 \sim 3 \times 10^3$ samples are required to evaluate the conditional probabilities according to Au and Beck's study [15], which is much less than the standard MCS.

In Eq. (2), evaluating the conditional probabilities $P(F_i|F_{i-1}), i = 2, \dots, m$ by standard MCS is not efficient because it requires sampling directly from the conditional PDFs $f_{\mathbf{x}}(\mathbf{x}|F_{i-1}) = I_{F_{i-1}}(\mathbf{x}) f_{\mathbf{x}}(\mathbf{x}) / P(F_{i-1})$. $I_{F_{i-1}}(\mathbf{x})$ is an indicator function with a value of 1 if a new sample belongs to F_{i-1} or 0 if a new sample does not belong to F_{i-1} . This indicates that it takes around $1/P(F_{i-1})$ samples before one conditional sample occurs on average. In view of this, the Markov Chain Monte Carlo (MCMC) simulation using the Metropolis-Hastings algorithm [20, 21] is employed to evaluate these conditional probabilities. The algorithm of generating conditional samples by the Metropolis-Hastings algorithm is given in section 0.

Another important issue of the subset simulation is the choice of intermediate events $F_i, i = 1, 2, \dots, m$. The sequence of intermediate events can be expressed as

$$F_i = \{G(\mathbf{x}) > b_i\}, i = 1, \dots, m \quad (3)$$

where $b_1 < b_2 < \dots < b_m$ is a sequence of intermediate event thresholds. It is desirable to choose these intermediate events in an adaptive manner. This can be realized to generate $\{b_1, \dots, b_m\}$ so that the conditional probabilities $P(F_i|F_{i-1}), i = 1, 2, \dots, m$ and $P(F_1)$ equal to the specified probabilities, which can be set to a constant probability p_0 for convenience. The value of p_0 cannot be too small. Otherwise the intermediate events would become rare events again which leads to an increase in the number of samples required in each simulation level (e.g., the simulation procedure that is used to evaluate the constant probability p_0). This also increases the total number of sample $n_t = mn_s$. Here n_s is the number of sample at one simulation level. On the other hand, the value of p_0 cannot be too large. Otherwise the sequence of intermediate event threshold would increase slowly which lead to an increase in the total number of simulation level m in order to reach a target probability. Au and Beck [15] suggested that the conditional probability p_0 take a value of 0.1, which is found to yield good efficiency. The choice of the conditional probability has not been investigated for the inverse reliability problem and the fatigue life prediction. A parametric study is performed in section 5, attempting to find the optimum algorithm parameter combinations for the probabilistic fatigue life prediction.

2.2 Samples generation by the Metropolis-Hastings algorithm

When implementing subset simulation procedure, the conditional samples are generated by the Metropolis-Hastings algorithm. For completeness of the paper, the Metropolis-Hastings algorithm for the MCMC simulation is briefly discussed for the

convenience of readers. Details about the algorithm can be found in [20, 21].

Let $f^*(\xi|x)$ to be a PDF for ξ depending on x . In order to generate the next Markov Chain sample x_{j+1} from the current sample x_j conditional on an intermediate event F_k , the Metropolis-Hasting algorithm is presented as follow:

(1) Generate a candidate state ξ_{j+1} from the proposal PDF $f^*(\xi|x)$

(2) Compute the acceptance ratio:

$$r_{j+1} = \frac{f_X(\xi_{j+1})f^*(x_j|\xi_{j+1})}{f_X(x_j)f^*(\xi_{j+1}|x_j)} \quad (4)$$

(3) Set the new sample x_{j+1} equal to ξ_{j+1} with probability $\min(1, r_{j+1})$, or set

x_{j+1} equal to x_j with probability $1 - \min(1, r_{j+1})$;

(4) When $x_{j+1} \neq x_j$, perform an evaluation of the response function $G(x_{j+1})$. If

$x_{j+1} \in F_k$, accept it as the next state; otherwise reject it and take the current

state x_j as the next one, i.e., set $x_{j+1} = x_j$.

The algorithm presented here is the original Metropolis-Hasting algorithm with an adjustment considering the demand of subset simulation (e.g., step (4)). It works well on low dimension problem. Au and Beck [15] also proposed a modified Metropolis-Hasting algorithm for high dimension problems since the former one encounters difficulties in generating a large number of independent random variables. It has been proved that the next sample x_{j+1} will be distributed as $f_X(x|F_k)$ if the current one x_j follows the stationary distribution of the Markov Chain [15, 21].

3. Deterministic fatigue life prediction methodology

A new fatigue life prediction method based on the equivalent initial flaw size (EIFS) concept has been recently developed [3, 22, 23]. The computation of the EIFS

only requires the fatigue limit data and the fatigue crack threshold intensity factor data without the traditional back-extrapolation procedure. Details about EIFS can be found in [3, 22, 23]. Only a brief review is given here.

The material fatigue crack growth curve can be expressed as

$$da / dN = C(\Delta K - \Delta K_{th})^L \quad C = A \cdot B^R \quad (5)$$

where C and L are fitting parameters. L controls the slope in the Paris regime. C is a function of the applied stress ratio for a specific material. ΔK_{th} is the intrinsic threshold stress intensity factor. It should be noted that the residual stress and environments will affect the crack growth law and the current study does not include these factors explicitly. The ΔK_{th} is extrapolated using the long crack growth testing data. A detailed discussion about the calculation of ΔK_{th} has been shown in [3, 22]. Many available models have been proposed to include the stress ratio effects in the crack growth rate curves, such as the Walker's equation [24] and the FORMAN's model [24]. Detailed study of the stress ratio effect is beyond the scope of this study. A simple fitting function to include the stress ratio effects has been proposed as

$$C = A \cdot B^R \quad (6)$$

where R is the stress ratio. A and B are two fitting parameters and can be fitted using experimental data under different stress ratios. Eq. (6) is just a fitting function to represent the stress ratio effect in the collected experimental data. If other function format is used (e.g., Walker's equation), the same derivation can be used as well. Eq. (5) can be rewritten as

$$dN = \frac{1}{A \cdot B^R [\Delta K - \Delta K_{th}]^L} da \quad (7)$$

Integrating both sides, fatigue life N can be obtained as

$$N = \int_0^N dN = \int_{a_i}^{a_c} \frac{1}{A \cdot B^R [\Delta K - \Delta K_{th}]^L} da \quad (8)$$

where a_c is the critical length at failure, which can be calculated using the fracture toughness and applied stress levels. It depends on the specimen geometry and loading types. In the current study, a_c is assumed to be a constant and a_i is the EIFS determined by the Kitagawa-Takahashi diagram [25] and the El Haddad's model [26] as

$$a_i = \frac{1}{\pi} \left(\frac{\Delta K_{th}}{\Delta \sigma_f Y} \right)^2 \quad (9)$$

where Y is a geometry correction factor and depends on the crack configuration. $\Delta \sigma_f$ is the fatigue limit. This deterministic model is a new life prediction methodology based on the equivalent initial flaw size (EIFS) concept, which does not require back extrapolation to time zero from the crack growth curve [3, 22]. The benefit of this new EIFS calculation is that it is independent of the loading level or crack growth model. The EIFS using classical back-extrapolation method will depend on loading and is not a material property. Once the crack growth curve and the EIFS are determined, Eqs. (8) and (9) can be used for fatigue life prediction.

Different types of uncertainties from material properties, specimen geometric and external loading needs to be included for probabilistic analysis. In the current study, two independent random variables are considered in the fatigue crack growth model: the fatigue limit $\Delta \sigma_f$ and the parameter A in the fatigue crack growth model. It is assumed that both the $\Delta \sigma_f$ and A follow the log-normal distribution. Other

parameters can also be treated as random variables and the proposed inverse subset simulation method has no difficulties in handling multiple random variables. For example, the critical crack length a_c and fracture toughness K_c are also random variables. They will mainly affect the final crack growth and has little effect on the high-cycle to medium-cycle fatigue life prediction because most of the life will be spent during the near-threshold and Paris regime crack growth [3, 22]. For simplicity, they are assumed to be constant in the current study. Exponential power L in the crack growth law could be treated as a random variable, too. The exponent L represents the underlying physics of the crack propagation and usually depends on materials. For example, ductile steels usually have an L close to 2 and aluminum alloys has an L between 3~4. In the present study, L is considered to be a constant. Another important issue is the correlation among random variables, which is critical for the uncertainty analysis. In the current study, $\Delta\sigma_f$ and A are assumed to be independent random variables since each of them is corresponding to very different failure mechanisms (e.g., one is for near-threshold crack growth and one is for Paris regime crack growth). Further studies of the random variable selection and their statistical distributions and correlations are required. The proposed study aims to illustrate the application of the inverse subset simulation method and uses the above mentioned simplifications. For practical applications, detailed investigation on the uncertainty quantification is required. This requires extensive theoretical and experimental work, which is beyond the scope of this study.

4. Subset simulation for inverse reliability analysis and probabilistic fatigue life prediction

The original subset simulation is used to estimate the small failure probability in an engineering system (reliability problem). In this study, we will first explore its application on inverse reliability problems since this is rarely found in the open literature. A reliability problem is to determine the probability $P(F_T)$ if the target event $F_T = \{G(\mathbf{x}) > b\}$ is known, e.g. the threshold value b is known, as shown in Eq. (1). On the other hand, the inverse reliability problem aims to estimate the threshold value b , if the probability $P(F_T)$ is given. In this paper, the probabilistic fatigue life prediction is demonstrated and it belongs to the inverse reliability problem because it estimate the fatigue life under a given a reliability/failure probability level. The original subset simulation needs to be modified for this purpose. The modification is discussed below and illustrated using the probabilistic fatigue life prediction problem.

4.1 Modification for inverse reliability analysis

One constraint in the inverse reliability problem is the target failure probability level., It is straightforward to deal with this constraint in a stopping criterion given the target failure probability level. Therefore, a modified stopping criterion is added to the original subset simulation to represent this reliability constraint. In this case, the procedure of the subset simulation stops when the product of a series of conditional probabilities is less than the target probability p , i.e.

$$p_0^m < p \quad (10)$$

The threshold b can be easily estimated from

$$b = \text{quantile}(g_{m,\cdot}, p/p_0^{m-1}) \quad (11)$$

since it is required to satisfies $p = p_0^{m-1} \times P(G(\mathbf{x}) > b)$. In Eq. (11), the quantile

function is the inverse of the empirical distribution function, and $g_{m\cdot} = \{g_{m,1}, g_{m,2}, \dots, g_{m,n}\}$ is the sorted response function values at the m -th simulation level, i.e., the last simulation level.

The similar idea can be extended if the desired quantity is the confidence bounds for the probabilistic life distribution. The estimated threshold b is the fatigue life under the reliability/failure probability constraint p . Let $p(p < 0.5)$ be the target confidence level, and assume that we are interested in a $(1-2p) \times 100\%$ probabilistic fatigue life confidence bound. N is used to denote the fatigue life. Given the target p level, the fatigue life bound problem can be expressed as

$$1 - 2p = P(N_{1-p} > N > N_p) \quad (12)$$

where N_{1-p} and N_p are the upper confidence bound and the lower confidence bound, respectively. They are defined as

$$p = P(N_{1-p} > N) \quad (13)$$

$$p = P(N > N_p) \quad (14)$$

Now the aim is to estimate the values of N_{1-p} and N_p . The proposed modified subset simulation algorithm can be used to predict both upper and lower life bounds. The deterministic fatigue life prediction method serves as the response function when implementing subset simulation. Thus, the probabilistic fatigue life prediction can be done by estimating the values of N_{1-p} and N_p from Eq. (11).

4.2 Procedure

The implementation procedure of subset simulation for evaluating probabilistic fatigue life is shown as follows in details. Here, we use the problem in Eq. (14) for demonstration. The input random vector is organized as $\mathbf{X} = \{\Delta\sigma_f, A\}$ and \mathbf{x}

denotes an observation of \mathbf{X} .

(1) In the first simulation level, n_s samples are generated by the direct MCS that using the given joint PDF $f_{\mathbf{X}}(\mathbf{x})$;

(2) Predict the fatigue lives using the method described in section 3 and sort them in an ascending sequence $\{N_{1,i}, i=1, \dots, n_s\}$. Here, subscript 1 denotes that these samples belong to the first simulation level. Choose the threshold value $b_1 = N_{1, n_s(1-p_0)}$ so that the first intermediate event

$$F_1 = \{N > b_1\} = \{N > N_{1, n_s(1-p_0)}\} \quad (15)$$

has a probability of p_0 , i.e.

$$P(F_1) = p_0 \quad (16)$$

Here, it is assumed that $n_s(1-p_0)$ is chosen as an integer. It can be seen that $n_s p_0$ samples fall into the first intermediate event F_1 in this step.

(3) In the k -th simulation level, there are $n_s p_0$ samples which belong to the intermediate event F_{k-1} , $k \geq 2$ and can provide "seeds" for generating new samples conditioned on F_{k-1} . Starting from these "seeds", $n_s(1-p_0)$ new samples are generated by the Metropolis-Hastings algorithm.

(4) Compute and sort the fatigue lives corresponding to these n_s samples which are conditioned on F_{k-1} . Choose the threshold value $b_k = N_{k, n_s(1-p_0)}$ so that the conditional probability

$$P(F_k | F_{k-1}) = P\{N > b_k | N > b_{k-1}\} = p_0 \quad (17)$$

and it is easy to know that the probability $P(F_k)$ is

$$P(F_k) = P(F_1) \prod_{i=2}^k P(F_i | F_{i-1}) = p_0^k \quad (18)$$

(5) Repeat step (3) and (4) until p_0^m is less than the target probability p . In another word, the calculation procedure is stopped when the target probability is reached. The lower confidence bound can be estimated by

$$N_p = \text{quantile}(N_{m,}, p/p_0^{m-1}) \quad (19)$$

4.3 The number of simulation level

As mentioned before, the choices of conditional probability p_0 and the number of sample in each simulation level will affect the computational cost and the accuracy of final prediction results. For a given target probability p , the total number of simulation level can be expressed as

$$m = \left\lceil \frac{\log(p)}{\log(p_0)} \right\rceil \quad (20)$$

where $\lceil \cdot \rceil$ means rounding a value to the nearest integer larger than or equal to it. From Eq. (20), it can be seen that the total number of simulation level m is a function of conditional probability p_0 and the given target probability p . If a value of p_0 is chosen, there is a unique value of m corresponding to it. For a fair comparison, the computational cost should be usually measured by the total number of sample since each of them requires one run of the deterministic fatigue life prediction model instead of based on the number of simulation level or on the CPU time. Let n_t be the total number of sample in a subset simulation run and the number of samples at each simulation level is

$$n_s = \frac{n_t}{m} \quad (21)$$

Based on the above discussion, it can be seen that if a target probability p and the desired total number of sample n_t are determined, the possible combinations of the

conditional probability p_0 and the number of samples at each simulation level n_s can be determined. For example, Table 3 summaries different choices with a target probability $p=0.025$, if the desired total number of sample $n_t = 1500$.

Table 3 An example of the parameter combination

p_0	0.05	0.1	0.2	0.3	0.4	0.5
m	2	2	3	4	5	6
n_s	750	750	500	375	300	250

5. Parametric study

A detailed parametric study is performed for probabilistic fatigue life prediction under constant amplitude loading to investigate the effect of algorithm parameters on the efficiency and accuracy of the life prediction. The optimum choice of those parameters is suggested based on the current investigation. The material properties of Al 7075-T6 ($R=-1$) and Al 2024-T3 ($R=0.1$) are shown in Table 2. Distribution of A is obtained from fitting of crack growth rate data in the Paris regime. Distribution of fatigue limit is obtained by fitting the experimental S–N curve data [29-32] in the very long life regime (e.g., at 10^7 – 10^8 cycles) [30]. In the current parametric study, two-sided 95% confidence bounds are selected for investigation. Thus, the target probability p equals to 0.025. The combinations of p_0 and n_s shown in Table 1 are used for the parametric study. The prediction error is defined as

$$error = \frac{\hat{N}_p - N_{MCS}}{N_{MCS}} \times 100\% \quad (22)$$

where \hat{N}_p is the fatigue life prediction computed by the subset simulation. N_{MCS} is the fatigue life prediction obtained from the direct MCS with one million samples. Since the confidence bound 95% is not very high, one million MC simulation is assumed to be the ground truth. For very high confidence level or very low failure probability level (e.g., $p=10^{-6}$), one million MC simulations may not represent the

ground truth. For each combination of p_0 and n_s , 50 independent subset simulation runs were performed. The average mean error of the subset simulation is given in Figure 1.

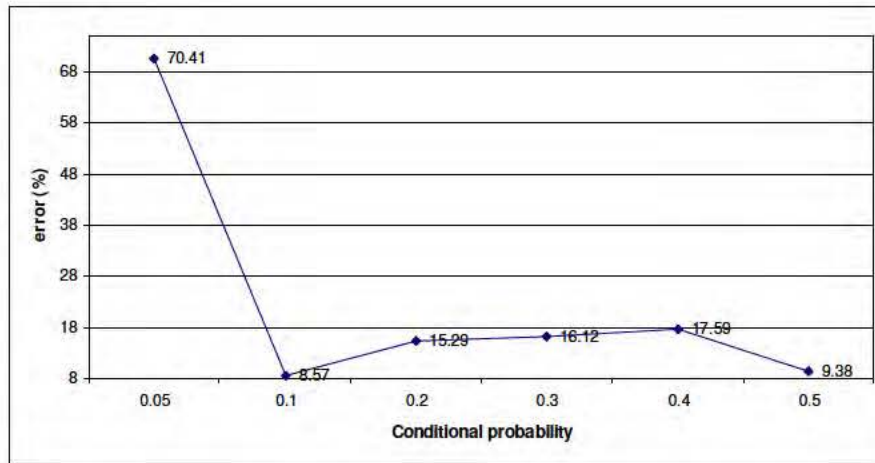


Figure 1. Average mean error of subset simulation for Al 7075-T6 (R=-1)

It is seen that the average prediction accuracy of subset simulation is not a monotonic function as the conditional probability p_0 changes from 0.05 to 0.5. The combination of $p_0 = 0.1$ and $n_s = 750$ produce the best fatigue life prediction accuracy among the investigated six combinations.

Another parametric study is performed for material Al 2024-T3 with stress ratio $R=0.1$. Detailed material properties are shown in Table 2 and Table 3. The parameter combinations are taken from **Error! Reference source not found.**. Based on 50 independent Subset simulation runs, the average prediction error is shown in Figure 2. Different trend for Al 2024-T3 is observed comparing to that for Al 7075-T6. It seems that the selection of the conditional probability level also depends on the specific problem (i.e., material properties of the particular investigation). Nevertheless, the choice of $p_0 = 0.1$ produces the best fatigue life prediction again in this case.

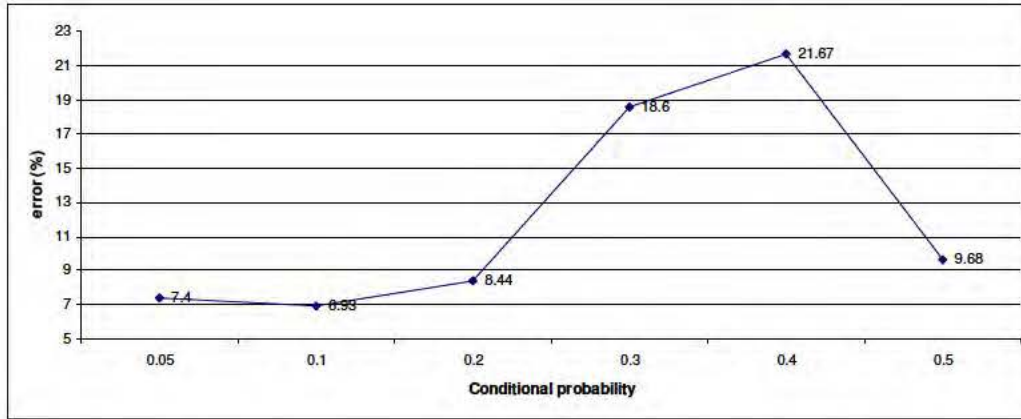


Figure 2 Average mean error of subset simulation for Al 2024-T3 (R=0.1)

In the following parametric study, the conditional probability p_0 is set to 0.1, while the number of sample in each simulation level varies from 100 to 1000. Based on 50 independent simulation runs, the average errors are plotted in Figure 3 and Figure 4, respectively for Al7075-T6 ($R = -1$) and Al 2024-T3 ($R = 0.1$). It is seen that the average error decreases as the total number of sample increases. When the number of samples is larger than 750, the decrease of prediction error is very slow. In the current investigation, 750 samples at each simulation level (i.e., 1500 samples total) is chosen for the tradeoff between efficiency and accuracy.

Table 4 Statistical data of parameter A and fatigue limit $\Delta\sigma_f$

Material	Stress ratio	Parameter	Mean	Std.
Al 7075-T6 [27]	R = -1	A[27]	7.38E-10	1.74E-10
		fatigue limit (MPa) [31]	352	52.24
	R = 0.1	A[27]	2.61E-10	2.87E-10
		fatigue limit (MPa)[30]	176	5.89

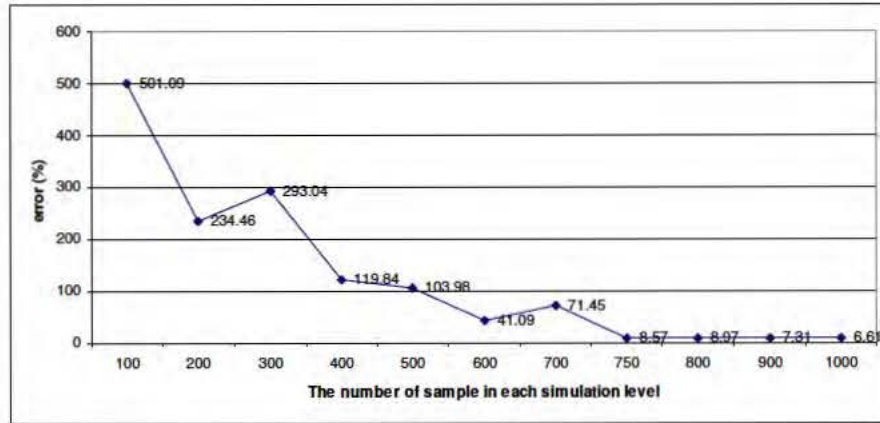


Figure 3 Average error vs. the number of sample in each simulation level for A1
7075-T6 (R=-1)

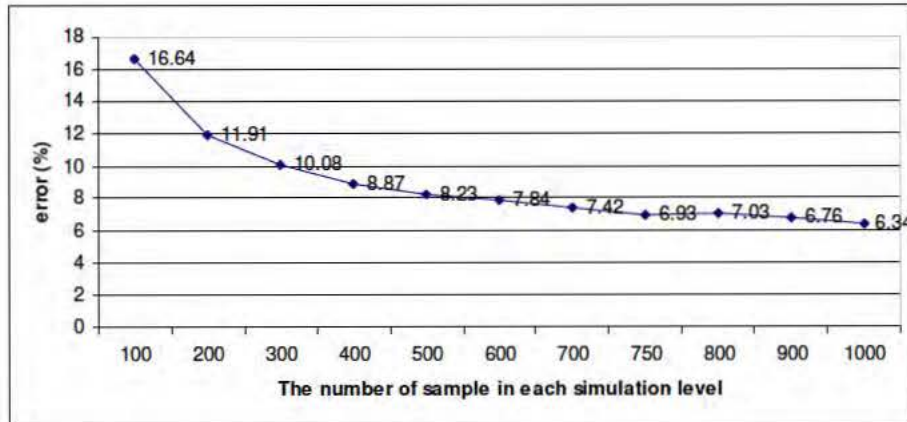


Figure 4 Average error vs. the number of sample in each simulation level for A1
2024-T3 (R=0.1)

For comparison, model predictions using the direct MC method and the proposed inverse subset simulation method is shown in Fig. 5. Generally, the agreement is very good at different stress levels. The computational cost of the proposed inverse subset simulation is several magnitudes less than the standard MC simulation.

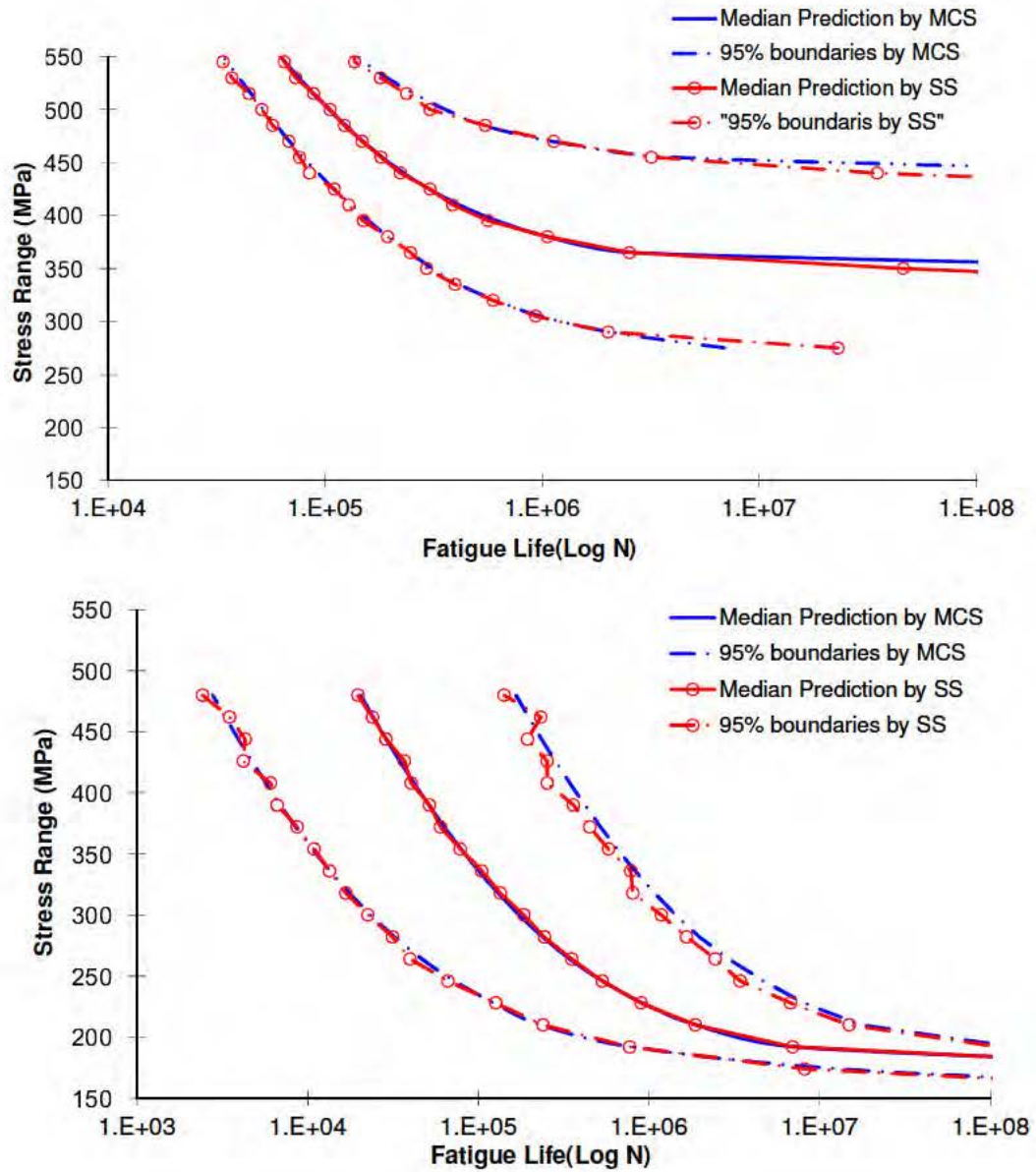


Figure 5 Comparison between numerical results and experimental data for

a) Al-7075 under $R=-1$; b) Al-2024-T3 under $R=0.1$

6. Conclusion

A general simulation algorithm based on subset simulation has been developed for probabilistic fatigue life prediction. It is shown that the proposed method can efficiently calculate the fatigue life with the similar accuracy of the direct Monte Carlo simulation. Parametric studies are used for the optimal algorithm parameter

determination. Several conclusions can be drawn based on the current investigation:

- The subset simulation is capable for the inverse reliability problem by adding a stopping criteria to include the reliability constraint;
- The optimal parameters in the proposed inverse version of subset simulation depends on the specific problem (i.e., different material properties);
- Parametric study suggests that the conditional probability level of 0.1 and the number of simulation samples of 750 at each level give an overall good efficiency and accuracy for the current investigation.

Current study focused on the constant loading case for the coupon level application. Further research is required to extend the proposed algorithm to structural system application under general random loading conditions. Extensive experimental and theoretical studies are required to validate the proposed methodology under realistic applications.

Acknowledgement

The research reported in this paper was supported by funds from Air Force Office of Scientific Research: Young Investigator Program (Contract No. FA9550-11-1-0025, Project Manager: Dr. David Stargel). The support is gratefully acknowledged.

References

- [1] Yao J.T.P., Kozin F., Wen Y.K., Yang J.N., Schuëller G.I., Ditlevsen O., Stochastic fatigue, fracture and damage analysis. *Structural Safety*, 1986;3:231–67.
- [2] Liu, Y. and S. Mahadevan, Stochastic fatigue damage modeling under variable amplitude loading. *International Journal of Fatigue*, 2007. 29(6): p. 1149-1161.
- [3] Liu, Y. and S. Mahadevan, Probabilistic fatigue life prediction using an equivalent initial flaw size distribution. *International Journal of Fatigue*, 2009. 31(3): p. 476-487.
- [4] Liu, Y. and S. Mahadevan, Efficient methods for time-dependent fatigue reliability analysis. *AIAA Journal*, 2009. 47(3): p. 494-504.
- [5] Wei, B.S., Johnson, S., Haj-Ali, R, A Stochastic Fatigue Damage Method for

- Composite Materials Based on Markov Chains and Infrared Thermography. *International Journal of Fatigue*, 2009, 32 (2) 350-360.
- [6] Xiang, Y. and Liu, Y. Inverse first-order reliability method for probabilistic fatigue life prediction of composite laminates under multiaxial loading, *ASCE Journal of Aerospace Engineering*, 2010(In press).
 - [7] Xiang, Y. and Y. Liu, Application of inverse first-order reliability method for probabilistic fatigue life prediction. *Probabilistic Engineering Mechanics*. 26(2): p. 148-156.
 - [8] Der Kiureghian, A., Y. Zhang, and C. C. Li, Inverse reliability problem. *Journal of Engineering Mechanics*, ASCE 1994. 120(5)(1154-9).
 - [9] Li, H., Foschi, R. O., An Inverse Reliability Method and Its Application *Structural Safety*, 1998, 20(3), pp. 257–270
 - [10] P. Ramu, X. Qu, B.D. Youn, R.T. Haftka and K.K. Choi, Inverse reliability measures and reliability-based design optimization, *Int. J. Reliab. Saf.* 1 (1–2) (2006), p. 187–205
 - [11] Melchers RE. Importance sampling in structural systems. *Structural Safety*, 1989, 6(1):3-10
 - [12] Au SK, Beck JL. A new adaptive importance sampling scheme for reliability calculations. *Structural safety*, 1999,21(2):135-158
 - [13] Hurtado JE. Filtered importance sampling with support margin: a powerful method for structural reliability analysis. *Structural Safety*, 2007,29(1):2-15
 - [14] Melchers RE. Structural system reliability assessment using directional simulation. *Structural Safety*, 1994, 16(1-2):23-37
 - [15] Au SK, Beck JL. Estimation of small failure probabilities in high dimensions by Subset simulation. *Probabilistic Engineering Mechanics*, 2001, 16:263-77.
 - [16] Au SK, Beck JL. Subset simulation and its application to seismic risk based on dynamic analysis. *Journal of Engineering Mechanics* 2003; 129(8): 901-917.
 - [17] Au SK. Reliability-based design sensitivity by efficient simulation. *Computers and Structures* 2005; 83:1048–1061.
 - [18] Au SK, Ching J, Beck JL. Application of Subset simulation methods to reliability benchmark problems. *Structural Safety* 2007; 29(3): 183-193.
 - [19] Schuëller GI. Efficient Monte Carlo simulation procedures in structural uncertainty and reliability analysis - recent advances. *Structural Engineering and Mechanics* 2009; 32(1): 1-20.
 - [20] Hastings, W.K., Monte Carlo Sampling Methods Using Markov Chains and Their Applications. *Biometrika*, 1970, 57 (1): 97–109
 - [21] Robert CP, Casella G. Monte Carlo statistical methods (2nd Edition). New York: Springer, 2004.
 - [22] Xiang, Y., Lu, Z., Liu, Y., Crack growth-based fatigue life prediction using an equivalent initial flaw model. Part I: Uniaxial loading. *International Journal of Fatigue*, 2010, 32(2): p. 341-349
 - [23] Lu, Z., Xiang, Y., Liu, Y., Crack growth-based fatigue life prediction using an equivalent initial flaw model. Part II: Multiaxial loading. *International Journal of Fatigue*, 2010, 32(2): p. 376-381

- [24] Dowling, N.E., Mechanical behavior of materials: engineering methods for deformation, fracture and fatigue. 3rd ed. 2007, Pearson Prentice Hall.
- [25] Kitagawa, H. and S. Takahashi, Applicability of fracture mechanics to vary small cracks or cracks in early stage. Proceedings of second international conference on mechanical behavior of materials, ASM International, Metal Park, OH, USA 1976: p. 627-631.
- [26] El Haddad MH, T.T., Smith KN, Prediction of nonpropagating cracks. Engineering Fracture Mechanics, 1979. 11(573-84).
- [27] United States. Federal Aviation Administration. Office of Aviation Research. Fatigue crack growth database for damage tolerance analysis final report. Washington, DC: US Dept. of Transportation. Federal Aviation Administration. Office of Aviation Research. 2005.
- [28] Noroozi AH, Glinka G, Lambert S. A study of the stress ratio effects on fatigue crack growth using the unified two-parameter fatigue crack growth driving force. International Journal of Fatigue 2007;29(9–11):1616.
- [29] Newman JC, Phillips EP, Swain MH. Fatigue-life prediction methodology using small-crack theory. International Journal of Fatigue 1999;21(2):109.
- [30] Rodopoulos CA, Curtis SA, de los Rios ER, SolisRomero J. Optimisation of the fatigue resistance of 2024-T351 aluminium alloys by controlled shot peening—methodology, results and analysis. International Journal of Fatigue 2004;26(8):849–56.
- [31] Zhao T, Jiang Y. Fatigue of 7075-T651 aluminum alloy. International Journal of Fatigue 2008;30(5):834–49
- [32] Naik RA, Lanning DB, Nicholas T, Kallmeyer AR. A critical plane gradient approach for the prediction of notched HCF life. International Journal of Fatigue 2005;27(5):481–92.

Appendix 7: Accomplishments for Task 2.2

An Equivalent Stress Transformation for Efficient Probabilistic Fatigue Crack Growth Analysis under Variable amplitude Loadings

Yibing Xiang and Yongming Liu*

Correspondence: Yongming Liu, Email:yongming.liu@asu.edu

Abstract: A general probabilistic fatigue crack growth prediction methodology for accurate and efficient damage prognosis is proposed in this paper. The methodology is based on an equivalent stress transformation and the inverse first-order-reliability method (IFORM). The equivalent stress transformation aims to transform the random variable amplitude loading to an equivalent constant amplitude loading spectrum. The proposed transformation avoids the cycle-by-cycle calculation under general random variable amplitude loadings. An inverse first-order reliability method (IFORM) is used to evaluate the probabilistic fatigue crack growth behavior and to further enhance the computational efficiency. Computational cost of the proposed study is significantly reduced compared with the direct Monte Carlo simulation. Thus, the proposed method is very suitable for real-time damage prognosis due to its high computational efficiency. Numerical examples are used to demonstrate the proposed method. Various experimental data under variable amplitude loading are collected for model validation.

Keywords: fatigue crack growth, probabilistic, inverse first-order reliability method, random loading

Nomenclature:

C, m = Material parameters in fatigue crack growth criteria

a, a_i = crack length, initial crack length in cycle i , respectively

$\Delta\sigma, \Delta\sigma_i$ = Stress range, stress range in cycle i, respectively

R, R_i = Stress ratio, stress ratio in cycle i, respectively

N_i, N_{total} = Number of fatigue cycle in cycle i, total fatigue cycle respectively

$\Delta\sigma_{eq}, R_{eq}$ = Equivalent stress range, equivalent stress ratio, respectively

$\Delta\sigma_{eq}^*$ = is the equivalent stress level considering the load interaction effect

η = factor for the load interaction

$g()$ = function to include stress ratio

$p_i(R_i, \Delta\sigma_i)$ = occurrence probability of stress range and stress ratio

1. Introduction

Fatigue failure is one of most common failure modes for materials and structures. Structures usually experience different random variable load spectrums during their service life. The applied fatigue cyclic loading [1] is stochastic in nature, which changes the stress amplitude and stress ratio throughout the entire life of the structure. One big challenge in fatigue crack growth prediction is the proper inclusion of random loading history effects, because different loading sequences may induce different load-interaction effects [2]. It may accelerate or decelerate the fatigue crack growth. During the last few decades, many studies have been performed to investigate the retardation of crack growth caused by single or multiple overloads [3-5]. Different models have been developed: yield zone models [6, 7], crack closure models [8-11] and strip yield models [9, 11, 12]. These models focus on different mechanism explanation of loading interaction effect and used different types of variable block loadings for model validation. Realistic random loading cases and the statistical

description of loading interaction effects have not been fully investigated in the past. Due to the complicated and nonlinear nature of random loading interaction, a cycle-by-cycle simulation is generally required for each different loading history. This approach is computationally expensive for probabilistic analysis, which usually requires a large number of Monte Carlo simulations. In view of this, the objective of this paper is to develop an efficient probabilistic methodology for fatigue crack growth prediction under general random variable amplitude loadings. The key idea is to derive an equivalent stress transformation based on the statistical description of the random loading, such as the probabilistic distribution of applied stress range and stress ratio. The variable amplitude loading crack growth problem is reduced to an equivalent constant amplitude crack growth problem, which greatly facilitates the integration for crack length prediction.

Fatigue reliability is a time-dependent reliability problem and different metrics can be used to describe the random nature of fatigue damage. One common approach is to calculate the reliability/failure probability at a specified life [13-16]. This approach is very useful for engineering design against fatigue since the service life is usually given in design problems. Both simulation-based method and the analytical probabilistic method (e.g., first-order reliability method (FORM)) can be used for this purpose [13]. Another approach is the probabilistic life prediction, i.e. the remaining life estimation at a specified reliability level. This measure is very useful for damage prognosis and condition-based maintenance and is the focus of the current study. Direct Monte Carlo simulation can be used for probabilistic fatigue prediction, but is

time-consuming for cycle-by-cycle fatigue crack growth analysis. Efficient methods for the probabilistic fatigue life prediction are the key objective of the proposed study and the inverse reliability method is proposed for this purpose. The authors have recently developed a probabilistic crack growth analysis using inverse FORM method under constant amplitude loadings [17]. This method will be used for probabilistic analysis.

This paper is organized as follows. First, the proposed equivalent stress transformation is derived for some special variable amplitude histories without considering the load interaction effect. Numerical examples are demonstrated to show the feasibility of the proposed equivalent stress transformation concept. Next, a small time scale fatigue crack growth model is briefly discussed and is used to obtain a correction factor in the proposed equivalent stress transformation to consider the load interaction effect. Following this, uncertainty quantification of material variability is performed and an efficient numerical algorithm for probabilistic crack growth is implemented using the inverse FORM calculation. Model predictions are compared with existing experimental data for model validation. Finally, some conclusions and future work are given based on the current investigation.

2. Equivalent stress transformation without load interaction

2.1 Basic concept of the equivalent stress transformation

There are several different functions to describe the fatigue crack growth rate curves, such as Paris' model [18, 19], Forman's model [20] and NASGROW equation [21]. Without loss of generality, a generic function of crack growth rate curve can be expressed as

$$da/dN = f(\Delta\sigma, R, a) \quad (1)$$

Eq. (1) can be reformulated as

$$dN = \frac{1}{f(\Delta\sigma, R, a)} da \quad (2)$$

For an arbitrary fatigue cycle i , the increment of crack length can be obtained by integrating both sides of Eq. (2).

$$N_i = \int_{a_i}^{a_{i+1}} \frac{1}{f(\Delta\sigma_i, R_i, a)} da \quad (3)$$

where a_i is the crack size at the beginning of cycle i and a_{i+1} is the crack size at the beginning of cycle $i+1$. The total fatigue life N under arbitrary random loading history is the summation of N_i and can be written as

$$N_{total} = \sum_{i=0}^n N_i = \sum_{i=0}^n \int_{a_i}^{a_{i+1}} \frac{1}{f(\Delta\sigma_i, R_i, a)} da \quad (4)$$

where a_0 is the initial crack size and a_n is crack length at fatigue cycle N .

The main objective of this paper is to find an equivalent crack growth process under constant amplitude loading, which produces a similar crack length with that of the true random loading case. In this ideal crack growth process, the stress level is constant and is the proposed equivalent stress level (ESL). It should be noted that the concept of equivalent stress is not new and has been discussed for block loading conditions using Walker's equation for stress ratio correction. The current study extend this concept to random loading cases using probability distribution function and includes the stress ratio effect using a generic function [20].

The equivalent stress level can be expressed as

$$N_{total} = \int_{a_0}^{a_{n+1}} \frac{1}{f(\Delta\sigma_{eq}, R_{eq}, a)} da \quad (5)$$

The equivalent stress level can be obtained by equaling Eq. (4) and Eq. (5) as

$$\int_{a_0}^{a_{n+1}} \frac{1}{f(\Delta\sigma_{eq}, R_{eq}, a)} da = \sum_{i=0}^n \int_{a_i}^{a_{i+1}} \frac{1}{f(\Delta\sigma_i, R_i, a)} da \quad (6)$$

Eq. (6) is the proposed equivalent stress transformation and it can be applied to different types of crack growth models. For any arbitrary functions of $f()$, the analytical solution is not apparent and discussions of some special cases are given below.

2.2 Special cases of equivalent stress transformation

The stress range and stress ratio are the two major controlling factors in describing the general variable amplitude loading conditions. Several special cases of the equivalent stress transformation are discussed below.

Case 1: fixed stress ratio

A simple case for fixed R ratio is illustrated first for two different loading cycles, as shown in Fig. 1. The solid line represents an arbitrary variable amplitude loading (two cycles), and the dashed line represents the equivalent loading. Both the variable and constant loadings are under the same constant stress ratio (i.e., stress ratio of zero in this case). These two loadings have the same initial and final crack size. The fatigue crack growth caused by the equivalent stress range is the same as that caused by the two arbitrary loading cycles (Eq. (7)). The crack increments for the true loading history and the equivalent constant amplitude loading can be expressed as

$$\begin{cases} N_{total} = N_1 + N_2 = \int_{a_0}^{a_1} \frac{1}{f(\Delta\sigma_1, R, a)} da + \int_{a_1}^{a_2} \frac{1}{f(\Delta\sigma_2, R, a)} da \\ N_{total} = \int_{a_0}^{a_2} \frac{1}{f(\Delta\sigma_{eq}, R, a)} da \end{cases} \quad (7)$$

To further simplify the discussion, a modified Paris law is used to derive the analytical solution of the equivalent stress. The modified Paris law is expressed as

$$\frac{da}{dN} = C(\Delta K)^m = g(R)(\Delta K)^m \quad (8)$$

where C and m are the fitting parameters in the Paris law. Parameter C is expressed as a generic function of applied stress ratio R . For the case 1, the stress ratio is fixed and C is a constant. $\Delta K_i = \Delta\sigma_i \sqrt{\pi a_i}$. This stress intensity factor (SIF) solution is for a center through crack in an infinite plate as a demonstration example. Other SIF solutions can be used, for example, by including a geometric correction factor for finite width plate.

Using Eq. (7) and the modified Paris law, the fatigue life N_i under the constant stress amplitude $\Delta\sigma_i$ can be rewritten as

$$N_i = \frac{2\Delta\sigma_i^{2-m}\pi^{1-\frac{m}{2}}}{C\Delta\sigma_i^2\pi(2-m)} (a_{i+1}^{1-\frac{m}{2}} - a_i^{1-\frac{m}{2}}) \quad (9)$$

Substituting Eq. (9) to Eq. (7), a relationship between the equivalent stress level and the variable loading can be developed as

$$N_1\Delta\sigma_1^m + N_2\Delta\sigma_2^m = (N_1 + N_2)\Delta\sigma_{eq}^m \quad (10)$$

If p_1 and p_2 are the occurrence probability of these two variable loadings, i.e., $p_1 = N_1/(N_1 + N_2)$ and $p_2 = N_2/(N_1 + N_2)$, Eq. (10) can be expressed as

$$\Delta\sigma_{eq} = (p_1(\Delta\sigma_1)^m + p_2(\Delta\sigma_2)^m)^{\frac{1}{m}} \quad (11)$$

This solution can be easily extended to include many load cycles and the general solution can be expressed as

$$\Delta\sigma_{eq} = \left(\sum_1^n p_i (\Delta\sigma_i)^m \right)^{\frac{1}{m}} \quad (12)$$

A numerical example of fatigue crack growth prediction is shown in Fig. 2. The material is Al-7075-T6 with an initial crack of 1.27 mm. The probability density function (PDF) of the stress range is shown in Fig. 2 (a), which follows a normal distribution with a mean value of 200 MPa and a standard deviation of 20 MPa. The first 50 of 10000 cycle random loading is shown in Fig. 2 (b). The stress ratio is a constant and equals to -0.5. Using the equivalent stress transformation (Eq. (12)), the fatigue crack prediction can be predicted. A comparison with the cycle-by-cycle calculation is shown in Fig. 2 (c). The solid line is the fatigue crack growth curve under the true random loading history and the dots are the fatigue crack growth under the equivalent constant amplitude stress loading. Although some small discrepancy of fatigue crack growth curve can be seen, the same final crack size can be obtained.

Case 2: fixed stress range

The above discussion is for variable loading cases with a fixed stress ratio. Another simple case is illustrated here, in which the stress range is fixed. As mentioned above, the parameter C in the modified Paris law is the a function of stress ratio (i.e., $C = g(R)$). For fixed stress range, the fatigue life can be rewritten as:

$$N_i = \frac{g(0)}{g(R_i)} \frac{2\Delta\sigma^{2-m} \pi^{\frac{1-m}{2}}}{g(0)\Delta\sigma^2 \pi(2-m)} (a_{i+1}^{1-\frac{m}{2}} - a_i^{1-\frac{m}{2}}) \quad (13)$$

First, only two variable loading histories are considered. A relationship between the equivalent stress (under stress ratio zero) and the variable loading can be developed.

$$\Delta\sigma_{eq} = \left(\frac{N_1}{N_{total}} \frac{g(R_1)}{g(0)} + \frac{N_2}{N_{total}} \frac{g(R_2)}{g(0)} \right)^{\frac{1}{m}} \Delta\sigma = \left(p_1(R_1) \frac{g(R_1)}{g(0)} + p_2(R_2) \frac{g(R_2)}{g(0)} \right)^{\frac{1}{m}} \Delta\sigma \quad (14)$$

where p_1 and p_2 are the occurrence probability of the two stress ratios. For more general cases of many fatigue cycles, the equivalent stress ratio can be described as

$$\Delta\sigma_{eq} = \left(\sum_1^n \frac{N_i}{N_{total}} \frac{g(R_i)}{g(0)} \right)^{\frac{1}{m}} \Delta\sigma = \left(\sum_1^n p_i(R_i) \frac{g(R_i)}{g(0)} \right)^{\frac{1}{m}} \Delta\sigma \quad (15)$$

A numerical simulation is performed to verify the proposed equivalent stress level. Same material properties as the one used in the last section is used. The random loading has a constant stress range of 200 MPa and the stress ratio follows a normal distribution. The mean value and standard deviation of stress ratio are -1 and 0.1 respectively. The histogram of 10000 cycle random loading is shown in Fig. 3 (a). A demonstration of the first 50 cycles of fatigue loading is shown in Fig. 3(b). Fatigue crack growth prediction has been done using the equivalent stress level (Eq. (15)). A comparison with cycle-by-cycle calculation is shown in Fig. 3 (c). The solid line is the fatigue crack growth curve under the true random loading history and dots are the fatigue crack growth under equivalent stress range. Good agreement of the final crack size can be observed in Fig. 3(c).

Case 3: varying stress range and stress ratio

Above two special cases assume one of the applied loading parameters (e.g., stress range or stress ratio) is fixed. A general case is discussed here if both of them

are random variables. A joint distribution of them is required for the derivation. In this case, the crack growth for any arbitrary cycle is determined by the following equation.

$$N_i = \int_{\Delta a_i}^{\Delta a_{i+1}} \frac{1}{g(R_i)(\Delta \sigma_i \sqrt{\pi a})^m} da = \frac{g(0)}{g(R_i)} \int_{\Delta a_i}^{\Delta a_{i+1}} \frac{1}{g(0)(\Delta \sigma_i \sqrt{\pi a})^m} da \quad (16)$$

Following the same procedure, the general equivalent stress can be expressed as

$$\Delta \sigma_{eq} = \left(\sum_1^n \frac{N_i}{N_{total}} \frac{g(R_i)}{g(0)} \Delta \sigma^m \right)^{\frac{1}{m}} = \left(\sum_1^n p_i(R_i, \Delta \sigma) \frac{g(R_i)}{g(0)} \Delta \sigma^m \right)^{\frac{1}{m}} \quad (17)$$

where $p_i(R_i, \Delta \sigma_i)$ is the joint distribution of the stress range and the stress ratio. Eq. (17) is the generalized equivalent stress transformation without considering the loading interaction effect.

A numerical example is applied to the general case where both stress range and stress ratio varies. A joint distribution (Gaussian) of the stress range (mean: 200 MPa, std: 20 MPa) and the stress ratio (mean:-1, std: 0.1) is shown in Fig. 4 (a). The correlation coefficients of stress range and stress ratio is assumed to be 0.5. The first 50 cycles of a random 5000 loading history is shown in Fig. 4 (b). Fatigue crack prediction has been performed for this joint-distributed stress range and stress ratio. Comparison with cycle-by-cycle calculation is shown in Fig. 4 (c). Satisfactory results are obtained.

3. Equivalent stress transformation with load interaction

Previous discussion focuses on the equivalent stress transformation without considering load interaction. It is well known that the “memory” effect exists for fatigue crack growth and the coupling effect has to be considered. In this section, the previous developed equivalent stress model is extended to include the load interaction

effect, such as the overload retardation and underload acceleration. The modification is based on a recently developed small time scale formulation of fatigue crack growth [22] and a load interaction correction factor.

A new small time scale model has been developed by Lu and Liu [22]. This method is based on the incremental crack growth at any time instant within a cycle, and is different from the classical reversal-based fatigue analysis. This methodology is based on the interaction of forward and reverse plastic zone and has been validated under various variable amplitude loadings, such as a combination of overload and underload. The small time scale method is briefly described below. Detailed derivation can be found in the referred paper [22].

The developed incremental crack growth model is schematically shown in Fig. 5. The model is developed based on the geometric relationship between the crack tip opening displacement (CTOD) and the instantaneous crack growth kinetics. Considering the geometry of crack tips at two time instants (t and $t + dt$), the relationship between the CTOD increment $d\delta$ and the crack growth da can be expressed as

$$da = \frac{\varpi \tan(\theta)}{2} d\delta = W d\delta \quad (18)$$

where $W = \frac{\varpi \tan(\theta)}{2}$ and θ is the crack tip opening angle (CTOA). It should be noted that Eq. (18) assumes the infinitesimal crack growth.

Using several hypotheses about the non-uniform crack growth kinetics within one loading cycle, a general instantaneous crack growth rate at any time can be expressed as

$$\dot{a} = H(\dot{\sigma}) \cdot H(\sigma - \sigma_{ref}) \cdot \frac{2W\lambda\sigma}{1 - W\lambda\sigma^2} \cdot \dot{\sigma} \cdot a \quad (19)$$

where $H(x) = \begin{cases} 1, & \text{if } x > 0 \\ 0, & \text{if } x \leq 0 \end{cases}$ and σ_{ref} is the lower integration limit. Eq. (19)

includes two hypotheses: 1) there is no crack growth during the unloading path (see the term of $H(\dot{\sigma})$); 2) there is no crack growth during the initial loading path (see the term of $H(\sigma - \sigma_{ref})$). Detailed justification of these hypothesis and validation under uniaxial loadings can be found in [23]. The crack length at any arbitrary time can be calculated via direct time integration over both sides of Eq. (19). The load interaction effect can be predicted and explained using the small time scale model. It should be noted that any mechanism-based fatigue crack growth model can be used to include the load interaction effect. The small time scale model is selected in this study to show the overall methodology of the proposed equivalent stress transformation.

The key idea of this paper is the equivalent stress transformation. A modification of the equivalent stress transformation is proposed to include the load interaction effect. The equivalent stress transformation considering the load interaction effect is defined as

$$\Delta\sigma_{eq}^* = \eta\Delta\sigma_{eq} \quad (20)$$

where $\Delta\sigma_{eq}^*$ is the equivalent stress level considering the load interaction effect and $\Delta\sigma_{eq}$ is calculated using Eq. (17) without considering the load interaction term. η is the factor for the load interaction effect and depends on specific loadings and material properties. This factor can be calibrated by the cycle-by-cycle simulation results. Details are shown below for deterministic variable amplitude loading and random

variable amplitude loading cases.

If the applied variable loading spectrum is deterministic (i.e., the future loading sequence is known), the load interaction factor η is a deterministic variable. The calibration of η can be done by minimizing the crack length prediction error of the equivalent stress level and the cycle-by-cycle simulation results using the small time scale model. This procedure is based on the least square fitting. An example is shown below in Fig. 6. Fig. 6(a) shows the deterministic loading spectrum (i.e., three repeated overload block spectrum). Fig. 6(b) shows the crack length predictions using the cycle-by-cycle simulation (triangle symbols) and the prediction results using the equivalent stress transformation (solid line). Standard searching algorithms can be used to find η to minimize the difference between these two predictions. If retardation effect is dominant, η will be less than 1. If the acceleration effect is dominant, η will be larger than 1. If no significant load interaction effect exists, η will be close to 1.

Above discussion is for simple repeated block loading, where the future load sequence is known. If the specimen is under truly random loading, where the future load sequence is unknown, the load interaction factor η becomes a random variable. In this case, several calibration using random generated loading histories are required. For each generated loading history, one η value will be calibrated. All calibrated η values can be used to calculate the statistics of η . In the probabilistic fatigue crack growth analysis shown below, η is an input random variable including the future loading uncertainties. An example has been demonstrated for variable loading

with unknown sequence. The variable loading is the same as shown in Fig. 6 (a) with unknown $n1$, $n2$ and $n3$. The summation of $n1$, $n2$ and $n3$ equals to 1997. Different crack length simulations with random combinations of $n1$, $n2$ and $n3$ are been generated first. Load interaction factor η is then calibrated for each case using least square regression. The calibrated η values can be fitted to a probability distribution. The empirical cumulative distribution function and fitting results are shown in Fig. 7. Once the distribution of η is found, the fatigue crack growth with unknown loading sequence can be predicted. Details of the model validation are discussed in Sec. 5.2.

4. Probabilistic crack growth prediction using Inverse FORM

Reliability analysis focuses on the probability of failure at a given spatial coordinate, which is made up of multi-dimensional variates, while inverse reliability analysis focuses on the coordinate in the multi-dimensional space at a certain reliability level. Simulation-based methods are the most traditional method; however, the computational efficiency can not satisfy the most current engineering projects. Analytical method such as first-order reliability (FORM) [24, 25] or second-order reliability method (SORM) are widely used numerical technique due to their efficiency and accuracy. Form method are widely applied in reliability analysis [26-28] as well as inverse reliability analysis.

FORM method requires a performance function to describe the either physical or no-physical phenomena. This performance function can be an explicit function, e.g., mechanical model, mathematical model, or can be an inexplicit function, which is just

based on many observations of a phenomena. A limit state function is expressed as a function of two sets of Gaussian variables x and y , as shown below:

$$g(x, y) = 0 \quad (21)$$

where x is a multi-dimensional random variable vector and represents material properties, loadings, and environmental factors, etc. y is the index variable vector, e.g., time, spatial coordinates and displacement. Transformation [29] are required for non-Gaussian variables to their equivalent standard normal space.

$$\|x\| = \beta \quad (22)$$

$$p_f = \Phi(-\beta) \quad (23)$$

where β is defined as the distance from origin to the most probable point (MPP) in the standard normal space. The failure probability P_f can be calculated using the cumulative distribution function (CDF) Φ of the standard Gaussian distribution. β is a non-negative value and the same value of β may indicate different failure of probability.

For the failure probability larger or equal to 50%, at the MPP the vector x is in the same direction with the normal direction at MPP, while for the rest case with failure probability less than 50%, the vector x is in the opposite direction with the normal direction at MPP and the situation can be described as:

$$\frac{x}{\|x\|} = \pm \frac{\nabla_x g(x, y)}{\|\nabla_x g(x, y)\|} \quad (24)$$

where $\nabla_x g(x, y)$ is the normal vector at MPP. The plus and minus sign represent P_f larger than 50% and less than 50%, respectively.

The overall objective of the FORM method is to find a non-negative function

satisfying all constraint conditions specified in Eq. (22-25). The limit state function is expanded around random variable vector x_0 using first-order Taylor's series expansion, and the indexing variable vector y is fixed.

$$g(x, y) = g(x_0, y_0) + \nabla_x g(x_0, y_0)(x - x_0) + O(x) = 0 \quad (25)$$

The increments of x and y can be expressed as

$$\Delta_1 = \begin{bmatrix} \frac{[\nabla_x g(x_0, y_0) \cdot x_0] - g(x_0, y_0)}{\|\nabla_x g(x_0, y_0)\|^2} \nabla_x g(x_0, y_0) - x_0 \\ 0 \end{bmatrix} \quad (26)$$

Using first order Taylor's series expression, the limit state function can be expanded around x and y as

$$g(x, y) = g(x_0, y_0) + \nabla_x g(x_0, y_0)(x - x_0) + \nabla_y g(x_0, y_0)(y - y_0) + O(x_0, y_0)(x - x_0) = 0. \quad (27)$$

The new x can be obtained by rewrite Eq. (24),

$$x = \pm \|x_0\| \frac{\nabla_x g(x_0, y_0)}{\|\nabla_x g(x_0, y_0)\|} \quad (28)$$

Substitue Eq.(28) into Eq.(27), the increments of x and y can be expressed as

$$\Delta_2 = \begin{bmatrix} -x_0 \pm \|x_0\| \frac{\nabla_x g(x_0, y_0)}{\|\nabla_x g(x_0, y_0)\|} \\ \frac{[\nabla_x g(x_0, y_0) \cdot x_0] - g(x_0, y_0) \pm \|x_0\| \frac{\nabla_x g(x_0, y_0)}{\|\nabla_x g(x_0, y_0)\|}}{\nabla_y g(x_0, y_0)} \end{bmatrix} \quad (29)$$

An analytical search algorithm is expressed as Eq. (30)

$$(x, y) = (x_0, y_0) + (a_1 \Delta_1 + a_2 \Delta_2) \quad (30)$$

$$a_1 + a_2 = 1 \quad (31)$$

where a_1 and a_2 are non-negative value and represent the weight of each search directions. Eq. 32 is a general solution for both forward reliability and inverse

reliability. For forward reliability method, a_1 equals to 1, and a_2 equals 0; while for inverse reliability method, a_1 and a_2 can be any non-negative values which satisfy Eq. (31). Different combinations of a_1 and a_2 result different convergence speed.

The convergence criterion for the numerical search algorithm is

$$\frac{(\|x - x_0\|^2 + \|y - y_0\|^2)^{\frac{1}{2}}}{(\|x\|^2 + \|y\|^2)^{\frac{1}{2}}} \leq \varepsilon \quad (32)$$

where ε is a small value and indicates that the relative difference between two numerical solutions is small enough to ensure the convergence.

5. Validation with experimental data

In this section, experimental validation of the proposed equivalent stress transformation is performed. The validation is performed for two types of loadings: 1) deterministic variable loading with known future loading sequence; 2) random variable loading with unknown future loading sequence.

For the current problem, the limit state function is defined as

$$g(C, K_c, \eta, N) = \log \left(\int_{a_i}^{a_c} \frac{1}{C[\Delta K]^m} \left(1 - \frac{K_{\max}}{K_c}\right) da \right) - \log(N) \quad (33)$$

The random variables can be the parameters C , the critical stress intensity factor K_c and the load interaction factor η in the fatigue crack growth model. It is assumed that the C , K_c and η follow log-normal distribution. In the current study, C , K_c and η are assumed to be independent random variables since each of them are corresponding to very different failure mechanisms. Further studies of the random variable selection and their statistical distributions and correlations are required. The

proposed study aims to illustrate the application of the inverse FORM method and uses above mentioned simplifications.

5.1 Model validation with known loading sequence

Several experimental data are collected from open literature for model validation. The material is aluminum 7075-T6. The constant amplitude loading testing is shown in Fig. 8 for Al-7075 and fitted statistical distribution of material parameters is listed in Table 1. The experimental data are reported in [30]. A summary of the properties of the specimens used for the collected experimental data are listed in Table 2.

Experimental data of Al 7075-T6 [30] under two blocks loading spectrum are used for model validation. A schematic illustration of the two blocks loading is shown in Fig. 9. p and n in Fig. 9 controls the number of cycles at the high amplitude and the low amplitude, respectively. Eight sets of experimental different block loadings (two constant and six variable amplitude loadings) are used for model validation and are plotted in Fig.10. p and n values for each spectrum loading are shown in the legend.

In Fig. 10, the fatigue crack growth prediction has been performed for Al-7075-T6. Both one thousand samples of Monte Carlo simulation and the inverse FORM method are used to calculate the probabilistic fatigue crack distribution. In Fig. 10, the fatigue crack growth prediction results for Al-7075 have been shown for 2 constant amplitude loading cases ((a),(b)) and 6 variable amplitude loading cases ((c)~(h)). The triangles shown in Fig. 10 are the experimental data [30]. The solid lines and the dashed lines represent median prediction of fatigue crack growth and 90% confidence bounds using Monte Carlo simulation, respectively. The dots shown in Fig. 10 are for the results of median and 90% confidence bounds using the inverse FORM

method. It is shown that the inverse FORM results agree well with Monte-Carlo simulation for the median fatigue life prediction and 90% confidence bounds. Both methods capture the major trends of fatigue life curves.

5.2 Model validation with unknown future loading spectrums

Above validation section uses variable amplitude loading with fully-known loading sequence. Thus, uncertainties from loading spectrums do not exist. In realistic application, the loading statistical information may be available from existing database or field measurement. However, the true loading sequence for particular structure is unknown. Thus, the uncertainties from unknown future loading sequences may contribute to the overall scatter of the probabilistic fatigue crack growth prediction. In this section, model validation has been done with unknown future loading sequences. Experimental data has been collected for Al-7075-T6 under variable loading with 6% overload [31]. A summary of the properties of the specimens used for the collected experimental data are listed in Table 3. The variable amplitude loading testing is shown in Fig. 11. P_{max} and P_{min} of the load cycles are 2000N and 200N, respectively. The peak value $P_{max,ol}$ for the overload cycle is 2400N for the overload ratio 1.2. Seven specimens are tested under random loading sequences. In another word, the statistics of these seven loading spectrum are same (i.e., all with 6% overload), but the sequence is different from each other. The block sequences of the testing group are listed in Table 4.

In the current study, both the overload occurrence probability and the overload ratio are constants. Hence, the loading sequence controls the uncertainties of the fatigue crack growth. In this case, the coefficient η can be written as an explicit

function of loading sequences. First, seven different loading spectrums with 6% overload have been generated first. For each generated loading history, one η value will be calibrated. All calibrated η values can be used to calculate the statistics of η . In the probabilistic fatigue crack growth analysis shown below, η is an input random variable including the future loading uncertainties. The statistic of loading factor η can be easily calculated and applied into the probabilistic fatigue crack growth prediction.

Experimental data under different loading spectrums has been shown in Fig. 12. Fatigue crack growth using one thousand Monte-Carlo simulation and the inverse FORM have been applied for probabilistic fatigue crack growth analysis. The solid lines and the dashed lines represent median prediction of fatigue crack growth and 95% confidence bounds using Monte Carlo simulation, respectively. The red dots are the inverse FORM results. It can be observed that the inverse FORM method results match well with the MC results. The 95% confidence bounds cover all the experimental data.

5.3 Computational efficiency

A summary of computation time using three different approaches are shown in the Table 5. The computations are performed using the same PC: dual core (Intel 6600) with 4gb rams and windows 7 OS. MATLAB 2009b is the program used in the current study. For cycle-by-cycle simulation, the computation time for single simulation run is about 5000 hours (estimated). Exact time for 1000 MC simulation using the cycle-by-cycle simulation is only estimated. It can be easily observed that, the MC simulation using the equivalent stress level is much more efficient. The most efficient

one is the equivalent stress level concept with the inverse FORM. The computational time is several magnitudes less than both cycle-by-cycle and equivalent-stress-level-based MC simulation. Thus, the proposed method (equivalent stress level with inverse FORM) is very useful for real-time damage prognosis. It should be noted that a large number of MC simulation is required for very low failure probability (e.g., one million samples for 0.001% failure probability). In that case, the ratio of computational time of the proposed method and the direct MC will be even larger.

6. Conclusion

In this paper, an efficient probabilistic methodology is proposed for fatigue crack growth prognosis. The proposed method simplifies the fatigue crack growth analysis under general random loadings and does not need cycle-by-cycle calculation. Analytical inverse FORM method avoids large number of simulations and further enhances the computational efficiency. The advantage makes it very suitable for real-time damage prognosis. Extensive experimental data for Al-7075-T6 under different loading spectrums are used to validate the proposed methodology. Generally, the model predictions agree with experimental observations well. Several conclusions can be drawn based on the current investigation.

- Equivalent stress transformation is verified with direct cycle-by-cycle simulation and is very effective to reduce the random loading crack growth problem to an equivalent constant loading crack growth problem.

- Several magnitudes of computational time can be saved combining the equivalent stress transformation and the inverse FORM method for probabilistic analysis.

Current study focuses on some simple overload spectrums for model validation. Future research is required to validate or modify the proposed model under more complex loading spectrums. Only limited number of specimens is performed under each loading cases. It will be great to have a large number of specimens to fully validate the statistical crack growth behavior in the future.

Acknowledgement

The research reported in this part was supported by funds from Air Force Office of Scientific Research: Young Investigator Program (Contract No. FA9550-11-1-0025, Project Manager: Dr. David Stargel). The support is gratefully acknowledged.

References

1. Pommier, S., *Cyclic plasticity and variable amplitude fatigue*. International Journal of Fatigue, 2003. **25**(9-11): p. 983-997.
2. Mikheevskiy, S. and G. Glinka, *Elastic-plastic fatigue crack growth analysis under variable amplitude loading spectra*. International Journal of Fatigue. **31**(11-12): p. 1828-1836.
3. Corbly, D.M. and P.F. Packman, *On the influence of single and multiple peak overloads on fatigue crack propagation in 7075-T6511 aluminum*. Engineering Fracture Mechanics, 1973. **5**(2): p. 479-497.
4. Venkateswara Rao, K.T. and R.O. Ritchie, *Mechanisms for the retardation of fatigue cracks following single tensile overloads: behavior in aluminum-lithium alloys*. Acta Metallurgica, 1988. **36**(10): p. 2849-2862.
5. Mohanty, J.R., B.B. Verma, and P.K. Ray, *Prediction of fatigue crack growth and residual life using an exponential model: Part II (mode-I overload induced retardation)*. International Journal of Fatigue, 2009. **31**(3): p. 425-432.
6. Willenborg J, E.R., Wood RA, *A Crack Growth Retardation Model Using an Effective Stress Concept*. 1971, Air Force Flight Dynamics Laboratory: Wright-Patterson Air Force Base, Ohio.
7. Wheeler, O.E., *Spectrum loading and crack growth*. J. Basic Eng., Trans. ASME, 1972. **94**(1): p. 181-186.
8. Elber, W., *The significance of fracture crack closure*. ASTM Special Technical Publication 486,

- American Society for Testing and Materials ed. Damage tolerance in aircraft structures. 1971, Philadelphia. 230-242.
9. Newman, J.C., *A crack closure model for predicting fatigue crack growth under aircraft spectrum loading*. Methods and models for predicting fatigue crack growth under random loading, ASTM Special Technical Publication 748, American Society for Testing and Materials. 1981, Philadelphia 53-84.
 10. Koning, A.U.d. *A simple crack closure model for prediction of fatigue crack growth rates under variable-amplitude loading*. in *Fracture Mechanics: Thirteenth Conference, ASTM STP 743*. 1981: American Society for Testing and Materials.
 11. Ray, A. *A state-space model of fatigue crack growth for real-time structural health management*. in *Digital Avionics Systems Conferences*. 2000.
 12. de Koning AU, v.d.L.H., *Prediction of fatigue crack growth rates under variable loading using a simple crack closure model*. 1981, NLR MP 81023U Amsterdam.
 13. Liu, Y. and S. Mahadevan, *Efficient methods for time-dependent fatigue reliability analysis*. AIAA Journal, 2009. **47**(3): p. 494-504.
 14. Liu, Y. and S. Mahadevan, *Probabilistic fatigue life prediction using an equivalent initial flaw size distribution*. International Journal of Fatigue, 2009. **31**(3): p. 476-487.
 15. Kujawski, D., *A fatigue crack driving force parameter with load ratio effects*. International Journal of Fatigue, 2001. **23**(Supplement 1): p. 239-246.
 16. NASA, *Fatigue crack growth computer program NASGRO Version 3.0-Reference manual*. JSC-22267B, NASA, Lyndon B. Johnson Space Center, Texas, 2000.
 17. Xiang, Y. and Y. Liu, *Application of inverse first-order reliability method for probabilistic fatigue life prediction*. Probabilistic Engineering Mechanics. **26**(2): p. 148-156.
 18. Paris, P. and F. Erdogan, *A critical analysis of crack propagation laws*. J. Basic Eng. Trans. ASME, 85, 1963: p. 528-553.
 19. Paris, P. and M. Gomez, *A rational analytic theory of fatigue*. Trends Eng, 1961. **13**(9-14).
 20. Dowling, N.E., *Mechanical behavior of materials : engineering methods for deformation, fracture and fatigue*. 3rd ed. 2007, Upper Saddle River, NJ, London: Pearson Prentice Hall ; Pearson Education. xvii, 912 p.
 21. NASA, *Fatigue crack growth computer program NASGRO Version 3.0-Reference manual*. JSC-22267B, NASA, Lyndon B. Johnson Space Center, Texas, 2000.
 22. Lu, Z. and Y. Liu, *Small time scale fatigue crack growth analysis*. International Journal of Fatigue. **32**(8): p. 1306-1321.
 23. Zizi Lu and Y. Liu, *Small time scale fatigue crack growth analysis*. International Journal of Fatigue, 2010. **32**(8): p. 1306-1321.
 24. Xiang, Y. and Y. Liu, *Application of inverse first-order reliability method for probabilistic fatigue life prediction*. Probabilistic Engineering Mechanics. **In Press, Accepted Manuscript**.
 25. Xiang, Y. and Y. Liu, *Inverse first-order reliability method for probabilistic fatigue life prediction of composite laminates under multiaxial loading*. ASCE Journal of Aerospace Engineering, 2011. **24**(2): p. 189-198.
 26. Thorndahl, S. and P. Willems, *Probabilistic modelling of overflow, surcharge and flooding in urban drainage using the first-order reliability method and parameterization of local rain series*. Water Research, 2008. **42**(1-2): p. 455-466.
 27. Skaggs, T.H. and D.A. Barry, *Assessing uncertainty in subsurface solute transport: efficient*

- first-order reliability methods*. Environmental Software, 1996. **11**(1-3): p. 179-184.
28. Cizelj, L., B. Mavko, and H. Riesch-Oppermann, *Application of first and second order reliability methods in the safety assessment of cracked steam generator tubing*. Nuclear Engineering and Design, 1994. **147**(3): p. 359-368.
29. Rackwitz, R.a.F., B, *Note on Discrete Safety Checking When Using Non-Normal Stochastic Models for Basic Variables*. Load Project Working Session, MIT, Cambridge, MA, June 1976.
30. Porter, T.R., *Method of analysis and prediction for variable amplitude fatigue crack growth*. Eng. Fract. Mech, 1972. **4**: p. 717-736.
31. Lu, Z. and Y. Liu, *Experimental investigation of random loading sequence effect on fatigue crack growth*. Materials & Design, 2011. **32**(10): p. 4773-4785.

Appendix 8: Accomplishments for Task 2.3

Probabilistic fatigue damage prognosis of lap joint using Bayesian updating

Abstract. In this paper, a general framework for probabilistic prognosis and uncertainty reduction under fatigue cyclic loading is proposed. First, the general idea using the Bayesian updating in prognosis is introduced. Several sources of uncertainties are discussed and included in the Bayesian updating framework. An equivalent stress level model is discussed for the mechanism-based fatigue crack growth analysis, which serves as the deterministic model for the lap joint fatigue life prognosis. Next, an in-situ lap joint fatigue testing with pre-installed piezoelectric sensors is designed and performed to collect experimental data. Signal processing techniques are used to extract the damage features for the crack length estimation. Following this, the proposed methodology is demonstrated using the experimental data under both constant and variable amplitude loadings. Finally, detailed discussion on validation metrics and sensitivity analysis of the proposed prognosis algorithm is given. Several conclusions and future work are drawn based on the proposed study.

1. Introduction

There are various types of uncertainties for the remaining life prediction of structural components, such as measurement uncertainty, mechanism modeling uncertainty, modeling parameter uncertainty, and detection model uncertainty. In order to reasonably perform the damage prognosis and health management, these

uncertainties need to be quantified and managed for accurate prognosis and decision-making. Bayesian updating algorithm ([1-3]) plays an important role in the uncertainty incorporation. The model parameters are considered as random variables, whose probability distribution is updated as more and more information is available from the target system. Before conducting the damage prognosis, the current health condition [4, 5] of the target system needs to be assessed. There are many non-destructive evaluation (NDE) methods available for fatigue damage diagnostics, such as thermograph (Hung 1996)[6], ultrasonics [7], X-ray CT [8], etc. With the development of Lamb wave-based damage detection methods, piezoelectric sensors have been widely used [9-15] for structural health monitoring because of their low cost and high efficiency [16]. The built-in piezoelectric sensors are an ideal way to detect invisible fatigue crack growth in metal structures [17] and internal delamination in composite components [18]. However, most of the existing studies focus on the simple plate components with without complex local geometrical features. Extending these detection methods to more complex structural components (e.g., lap joints) and considering uncertainties requires further attention.

Two major approaches were used for prognosis: data-driven and mechanism-based approaches. The proposed study uses the mechanism-based approach for prognosis. Paris' law [19] is one of the most widely used fracture mechanics-based model for fatigue life prediction. Several modified versions of the Paris' law have been reported in the literature, such as the modification for the near threshold crack growth [20, 21], small/short cracks growth [22, 23], and crack closure

model [24]. Most of these studies are difficult to be applied to random variable spectrum loadings. An Equivalent Stress Level model [25] was suggested that can efficiently calculate the fatigue crack growth under variable amplitude loadings.

The paper is organized as follows. First, a prognosis framework is introduced based on the Bayesian updating. Next, a piezoelectric sensor based lap joint fatigue testing is introduced and the corresponding detection models are presented and compared. Following this, the proposed prognosis method is demonstrated using the experimental measured signals for different specimens under different loadings. Finally, the prognosis performance is validated using prognosis metrics and prognostic sensitivity is analyzed numerically.

2. Model development

2.1. Background of the Bayes' theorem and uncertainty updating

In the prognosis problem, the newly observed information can be incorporated to obtain a better knowledge about the system, including its parameter distribution, model accuracy, and future performance. Recently, Bayes' theorem has been extensively used in various engineering fields for prognosis [26] [27]. The Bayes' theorem is to update the distribution of the interested parameters with the in-situ system responses. The posterior distribution of the parameters can be obtained by combining the information of its prior guess and the belief about the current system response. In the Bayesian updating, model parameters are considered as random

variables, which can be updated using the in-situ observation data x' . The posterior distribution of the parameters can be express as

$$q(\theta) \propto p(\theta)p(x'|\theta) \quad (1)$$

where $p(\theta)$ is the prior distribution of the model parameter. θ can be a vector for multiple parameters. $p(x'|\theta)$ is the likelihood function. $q(\theta)$ is the posterior distribution of model parameter. In the Bayesian updating, model uncertainties and measurements uncertainties are incorporated in the construction of the likelihood function. Details are shown below.

In the prognosis problem, the sources of uncertainties usually include, but not limited to, the mechanism modeling uncertainty, the model parameter uncertainty, and the measurement uncertainty. Consideration of these uncertainties is essential for providing an informative inference and prognosis of the target system. For fatigue problems, the crack propagation is not a smooth and stable process, thus a good choice of the mechanism model to express the crack growth plays a vital role to predict the remaining fatigue life. The parameters uncertainties in the mechanism model will propagate to the prognosis results. Additionally, measurement uncertainties are determined by the measuring technique. Moreover, if the target system response is obtained by other measurements, such as signals, the uncertainties may be induced by the detection model used to predict the target system response.

Consider a generic mechanism model to describe the time-dependent behavior of a system

$$x_t = M(N, \theta) \quad (2)$$

where x_t is the target system response at time t (e.g., the crack length in fatigue problem) N is the index variable (i.e., non-random), such as time and spatial coordinates). θ is a vector for model random parameters. Due to the experimental measuring uncertainties, the testing measurement for the system response can be described by introducing a measurement noise ϵ_1 , i.e.,

$$x' = x_t + \epsilon_1 \quad (3)$$

In some engineering applications, the system response cannot be directly measured and needs to be inferred from other types of signals. For example, the crack in a component cannot be easily measured directly using optical method due to the inaccessible locations of these cracks. Features from NDT sensor signal can be used to infer the crack length. In this case, the inference becomes the detection model and itself will have additional uncertainties (e.g., data reduction scheme in the feature extraction or regression analysis for the correlation between features and system responses). If a certain detection model $D(F)$ using received signal features F is used to infer the system response, the detection model can be expressed as

$$D(F) = x' + \epsilon_2 \quad (4)$$

where a random variable ϵ_2 is used to describe the detection model uncertainties. To update the target system using the detected system response, the likelihood function $p(D(F)|\theta)$ needs to be constructed. In the following section, the likelihood

function is formulated for given mechanism model and the detection model. The above described uncertainties are included in the likelihood function.

The probability distribution of ϵ_1 is represented as $p(\epsilon_1|\theta) = f_1(\epsilon_1)$ and the probability of detection model error ϵ_2 is $p(\epsilon_2|\theta) = f_2(\epsilon_2)$. The conditional probability of $p(D(F)|\theta)$ can be obtained by marginalizing the joint probability $p(D(F), x', \epsilon_2|\theta)$ over x' and ϵ_2 , which is given as

$$p(D(F)|\theta) = \iint_{x', \epsilon_2} p(D(F), x', \epsilon_2|\theta) dx' d\epsilon_2 = \iint_{x', \epsilon_2} p(x'|\theta) p(\epsilon_2|\theta) p(D(F)|x', \epsilon_2, \theta) dx' d\epsilon_2 \quad (5)$$

Based on Eq. (4)

$$p(D(F)|x', \epsilon_2, \theta) = \delta(D(F) - x' - \epsilon_2) \quad (6)$$

Substitute the above equation into Eq. (5)

$$p(D(F)|\theta) = \int_{x'} p(x'|\theta) f_2(D(F) - x') dx' \quad (7)$$

In Eq. (7), the probability $p(x'|\theta)$ needs to be determined. Based on Eq. (2) and Eq.(4), we can get the equation $x' = M(N, \theta) + \epsilon_1$. The conditional probability of $p(x'|\epsilon_1, \theta)$ can be expressed as

$$p(x'|\epsilon_1, \theta) = \delta(x' - M(N, \theta) - \epsilon_1) \quad (8)$$

Following the same procedure in Eq. (5), the conditional probability $p(x'|\theta)$ can be calculated by marginalizing over ϵ_1

$$p(x'|\theta) = \int_{\epsilon_1} p(\epsilon_1|\theta) p(x'|\epsilon_1, \theta) d\epsilon_1 = \int_{\epsilon_1} p(\epsilon_1|\theta) \delta(x' - M(N|\theta) - \epsilon_1) d\epsilon_1$$

$$= f_1(x' - M(N, \theta)) \quad (9)$$

Substitute Eq. (9) into Eq. (7)

$$\begin{aligned} p(D(F)|\theta) &= \int_{x'} p(x'|\theta) f_2(D(F) - x') dx' = \\ &= \int_{x'} f_1(x' - M(N, \theta)) f_2(D(F) - x') dx' \quad (10) \end{aligned}$$

It can be seen that the condition probability $p(D(F)|\theta)$ is the convolution between probability distribution $f_1(\epsilon_1)$ and $f_2(\epsilon_2)$. General solution for Eq. (10) is not apparent. To further simplify the calculation, it is assumed that $f_1(\epsilon_1)$ and $f_2(\epsilon_2)$ are independent Gaussian distributions [28, 29]. If the two errors are all Gaussian random noise with standard deviation σ_{ϵ_1} and σ_{ϵ_2} , the convolution of the two Gaussian probability distribution can be expressed as

$$p(D(F)|\theta) = \frac{1}{\sqrt{2\pi(\sigma_{\epsilon_1}^2 + \sigma_{\epsilon_2}^2)}} \exp\left(-\frac{1}{2} \frac{(D(F) - M(N, \theta))^2}{\sigma_{\epsilon_1}^2 + \sigma_{\epsilon_2}^2}\right) \quad (11)$$

2.2. In the Bayesian updating, the Markov-Chain Monte-Carlo (MCMC) method is used to draw samples. Since MCMC method is well documented in the open literature. No detailed discussion is given to save the space. *Fatigue crack growth model*

The proposed model is based on the equivalent transformation of a random loading to constant loading. It should be noted that the proposed methodology is generic and applicable to different types of mechanism models. For example, several mechanism models are available to describe the fatigue crack growth data under constant amplitude loading, such as Forman's model [30], NASGROW model [31], and Paris' law [19]. The used equivalent stress model is very efficient for the random

variable loadings without the cycle-by-cycle calculation and has been validated with different sets of experimental data. In the equivalent stress fatigue crack growth model, a generalized crack growth rate curve is assumed as

$$\frac{da}{dN} = f(\Delta\sigma, R, a) \quad (12)$$

For arbitrary crack growth, the fatigue cycles can be calculated by integrating both sides of Eq. (12).

$$N_i = \int_{a_i}^{a_{i+1}} \frac{da}{f(\Delta\sigma, R, a)} \quad (13)$$

where a_i is the crack size before N_i cycles and a_{i+1} is the crack size after N_i cycles. The total fatigue life N_{total} under arbitrary random loading history is the summation of N_i and can be written as

$$N_{total} = \sum_0^n N_i = \sum_0^n \int_{a_i}^{a_{i+1}} \frac{da}{f(\Delta\sigma_i, R_i, a)} \quad (14)$$

where a_0 is the initial crack size and a_n is crack length at fatigue cycle N_n . The above discussion is for constant amplitude loading. For random variable loading, the proposed model tries to find an equivalent constant amplitude loading crack growth process under which the fatigue life obtained is the same with that of the true random loading case. The fatigue life of this equivalent crack growth process can be expressed as

$$N_{total} = \int_{a_0}^{a_{n+1}} \frac{da}{f(\Delta\sigma_{eq}, R_{eq}, a)} \quad (15)$$

The equivalent stress level can be obtained by equaling Eq. (14) and Eq. (15) as

$$\sum_0^n \int_{a_i}^{a_{i+1}} \frac{da}{f(\Delta\sigma_i, R_i, a)} = \int_{a_0}^{a_{n+1}} \frac{da}{f(\Delta\sigma_{eq}, R_{eq}, a)} \quad (16)$$

Theoretically, Eq. (16) can be applied to any type of crack growth model. The detailed derivation for modified the Paris model is given below.

To incorporate the stress ratio effect, the Paris' law is modified as

$$\frac{da}{dN} = C(\Delta K)^m = g(R)(\Delta K)^m \quad (17)$$

where C and m are the fitting parameters in the Paris' law. Parameter C can be expressed as kb^R , where k and b are fitted by experimental data under different load ratios. Using Eq. (13) and the modified Paris' law, the fatigue life N_i can be rewritten as

$$N_i = \int_{a_i}^{a_{i+1}} \frac{1}{g(R_i)(\Delta\sigma_i\sqrt{\pi a})^m} da = \frac{g(0)}{g(R_i)(\Delta\sigma_i)^m} \int_{a_i}^{a_{i+1}} \frac{1}{g(0)(\sqrt{\pi a})^m} da \quad (18)$$

Given two constant loading spectrums in one block, the relationship between the equivalent stress level and the variable amplitude loading can be described as

$$N_1 \frac{g(R_1)(\Delta\sigma_1)^m}{g(0)} + N_2 \frac{g(R_2)(\Delta\sigma_2)^m}{g(0)} = (N_1 + N_2)(\Delta\sigma_{eq})^m \quad (19)$$

$$\Delta\sigma_{eq} = \left(\frac{N_1}{N_1+N_2} \frac{g(R_1)(\Delta\sigma_1)^m}{g(0)} + \frac{N_2}{N_1+N_2} \frac{g(R_2)(\Delta\sigma_2)^m}{g(0)} \right)^{\frac{1}{m}} \quad (20)$$

where N_1 and N_2 are the two constant loading cycles in one block. Following the same procedure, the generalized equivalent stress can be expressed as

$$\Delta\sigma_{eq} = \left(\sum_1^n \frac{N_i}{N_{total}} \frac{g(R_i)(\Delta\sigma_i)^m}{g(0)} \right)^{\frac{1}{m}} \quad (21)$$

For the equivalent loading condition, the parameters k and m should be calibrated for specific specimens and are treated as random variables.

To precisely predict the fatigue life, an initial crack length is needed as input to the crack growth model. An equivalent initial flaw size (EIFS) concept [32] is applied to calculate the crack length for a given number of load cycles. In the probabilistic crack growth analysis, the EIFS and the parameter k for variable loading m are three random variables and will be updated. The initial estimation of EIFS can be calculated as [33]

$$a = \frac{1}{\pi} \left(\frac{\Delta K_{th}}{\Delta \sigma_f Y} \right)^2 \quad (22)$$

where Y is a geometry correction factor depending on specimen geometry and crack configuration, $\Delta \sigma_f$ is fatigue limit, and ΔK_{th} is the threshold stress intensity factor. For lap joints, the corresponding detailed solution for Y is given in [34].

As a short summary, the schematic diagram of the Bayesian updating framework for fatigue crack growth analysis is shown in Fig. 1. The corresponding prior distributions for model parameters are shown in Table .1. The probabilistic remaining useful life can be used calculated using the samples from the MCMC simulation.

3. Lap joint fatigue testing using a piezoelectric sensor network

In this section, the proposed methodology in section 2 is demonstrated using lap joint testing and model predictions are compared with experimental observations. Details are shown below.

3.1. Experiment Setup

The experimental setup for damage prognosis of riveted lap joint coupons consists of three major modules: sensing and data acquisition system, optical fatigue crack measurement system, and fatigue cyclic loading system (Figure 2). Sensing and data acquisition system generates a 3.5 cycles tone burst lamb wave from Piezoelectric (PZT) actuators and records the corresponding signal received by PZT sensors. Optical crack measurement system uses a traveling microscope to measure the crack length after a certain number of loading cycles at regular intervals. The specimen is subjected to tensile cyclic loading using a hydraulic testing machine. The experiment setup is shown in figure 1. The coupons were subjected to two types of loading spectrums: constant block loading and variable block loading as shown in figure 3.

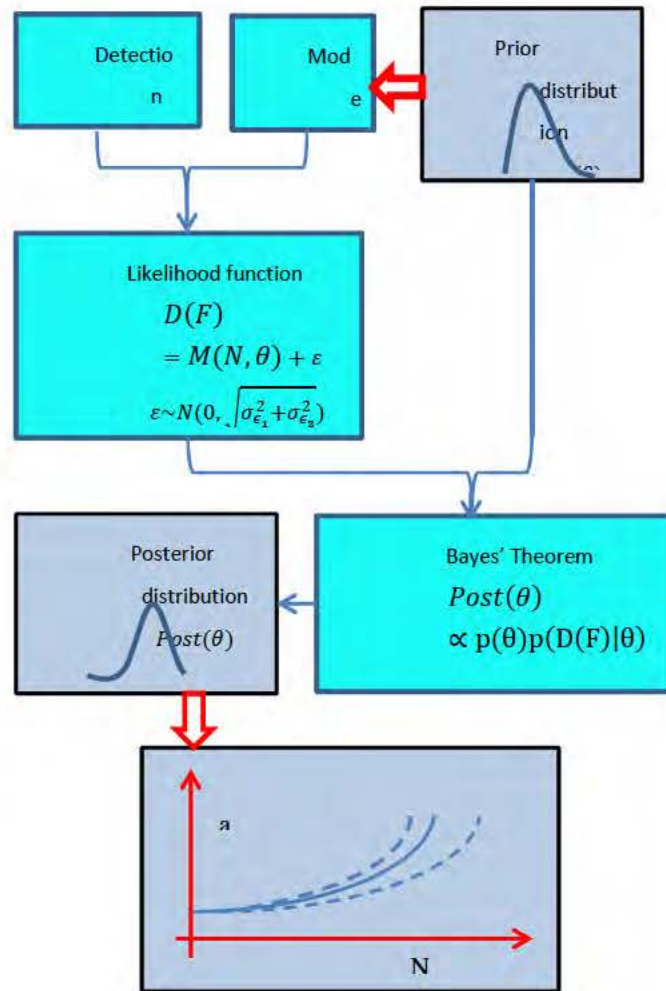


Figure 1.The overall prognosis framework using Bayesian Updating

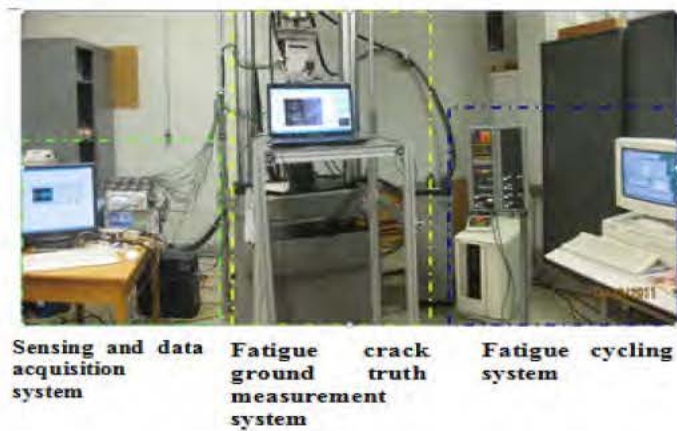


Figure 2.Systematic flow chart for the damage diagnosis system for lap joint

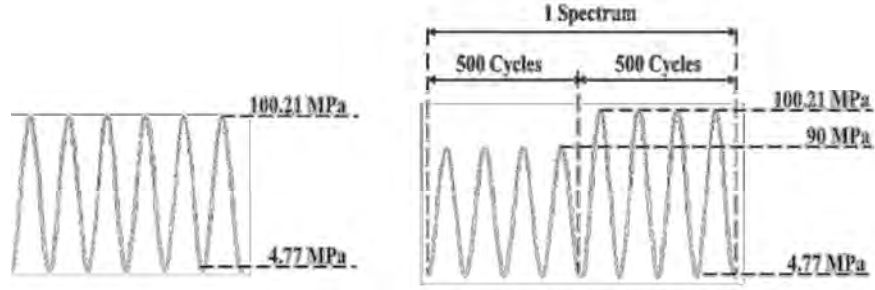


Figure 3. Loading spectrum. a) Constant loading; b) Variable loading

3.2. Specimen Geometry and Sensor Layout Design

The riveted panels are made of 0.063 inch Al 2024-T3 sheets that were originally provided by NRC, Canada. For repeatability, additional coupons were manufactured at NASA. Three rows of rivets are embedded in the panels. The detailed geometry is shown in figure 4 and corresponding mechanical properties of the material are shown in table 1. Multiple specimens are tested to show the reproducibility of the proposed method and to include the effect of uncertainties among different specimens. Detailed information for the specimens are shown in Table XXX.

The experimental results have shown that the major crack always appears at the countersunk hole in the first row. Therefore, the first row is considered as the target region for damage detection. The actuators and the sensors are placed on the opposite sides of the first row. This ensures the crack would be on the direct wave path of the sensor-actuator pairs whenever it appears. To employ a pitch-catch method [35], PZTs acting as actuators and sensors are glued on the two sides of the rivet holes. The corresponding sensor network configuration is shown in figure 5. Red dots represent actuators away from the target region and the green dots represent sensors near the

target region. Each pair of sensors can interrogate the damage information on their direct wave path.

Table 1. Mechanical properties of Al2024-T3

Material	Yield strength (Mpa)	Elastic modulus (Mpa)	σ_u (Mpa)	ΔK_{th} (Mpa $m^{0.5}$)
Al2024-T3	360	72000	490	1.1164

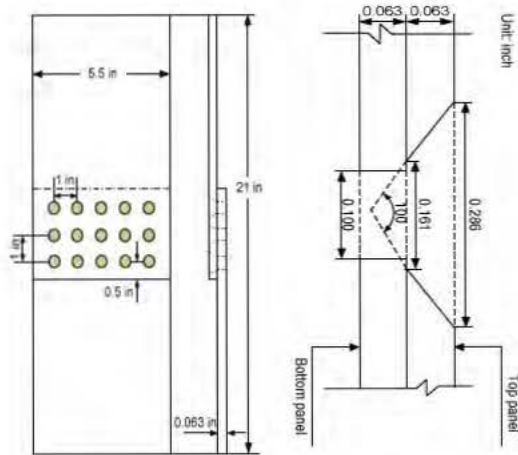


Figure 4. Geometry of the lap joint and detailed dimension of the connection part

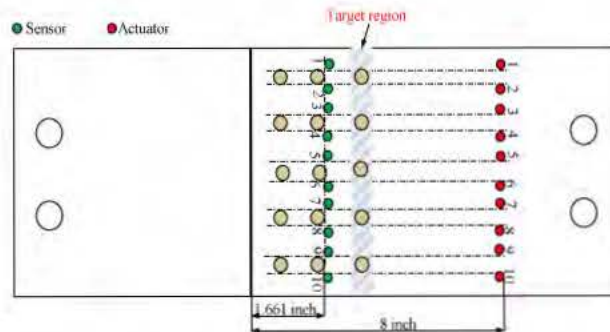


Figure 5. Sensor network layout for damage detection on riveted lap joint

3.3. Experimental Result and Data Processing

In this study, a Hamming-windowed sinusoidal tone burst with 3.5 cycles was used as the actuating signal. The central frequency of this signal was set at 200kHz, as shown in figure 6. After installing the specimen on the hydraulic machine, the baseline signal for normal condition is collected first. Further data are collected periodically and the traveling microscope is used to measure the surface crack length at regular intervals. Figure 7 illustrates a typical signal obtained for specimen T4 subjected to the constant amplitude loading. With further signal processing, changes in selected features (phase change, correlation coefficient, and amplitude change) are calculated. The amplitude change reflects the energy dissipation due to the crack. The phase angle change is due to the traveling distance change due to the crack. The correlation coefficient change reflects the signal perturbation due to the new waves generated at the crack surfaces (Raghavan and Cesnik 2007). All of these feature changes can be obtained by comparing the received signals under normal and defect condition. Detailed description is given in the open literatures [36-38]. The relationship between trends in features and crack length is shown in figure 8.

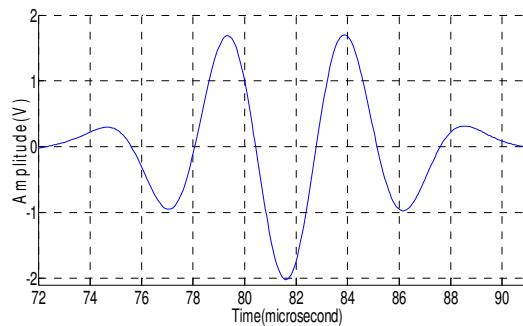


Figure 6. A tone burst signal of 3.5 cycles with 200kHz central frequency

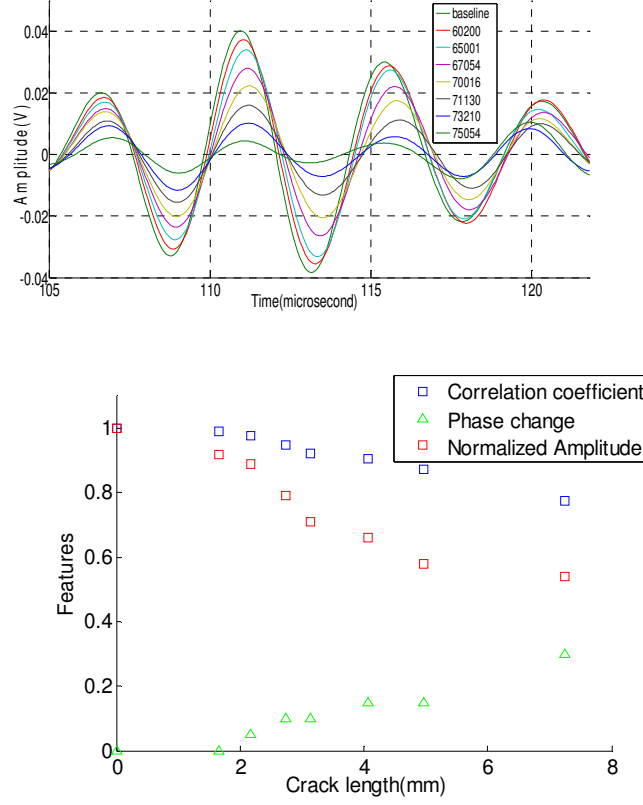


Figure 7.Received signal for specimen T4

Figure 8.The relationship between signal features and crack length

3.4. Detection model

3.4.1. Linear Regression model

As shown in figure 8, all features exhibit monotonic relationships with increasing crack length. Thus, all three features are potentially good candidates for the detection. A linear regression model is used to combine all three feature and to predict the crack length Using datasets from several testing specimens, a linear regression is is shown in Eq. (24), which is trained using datasets from five different specimens (T1, T2, T3, T4, and T5). Table 2 lists the regression coefficients for this formulation.

$$a = B + \beta_1 x + \beta_2 y + \beta_3 z \quad (24)$$

where a is the detected crack length, x is the correlation coefficient, y is the phase change variable, and z is the normalized amplitude.

Table 2. Coefficients for linear regression model

Coefficients	Value
B	4.23
β_1	1.98
β_2	4.23
β_3	-4.79

Using the diagnostic model described above, detected crack length for other specimens can be obtained. figure 9 shows experimentally measured crack lengths and the detection results for the two specimens (NRC T6 and variable loading T7). It can be observed that detection results show good agreement with experimentally measured crack length in general.

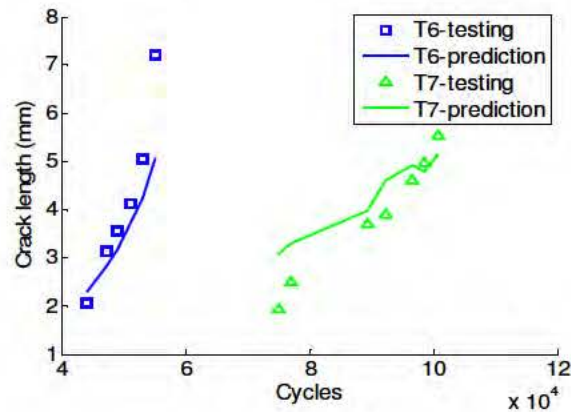


Figure 9. Measurement and detection model prediction using linear regression model

3.4.2. Quadratic regression model

Following the same procedure as the above discussed linear regression model, the quadratic detection model is given as Eq. (25). This model is trained by datasets from five different specimens (T1,T2,T3 T4, and T5). The corresponding coefficients for this model are listed in table 3.

$$a = A + \alpha_1 x + \alpha_2 y + \alpha_3 z + \alpha_4 xy + \alpha_5 xz + \alpha_6 yz + \alpha_7 x^2 + \alpha_8 y^2 + \alpha_9 z^2 \quad (25)$$

Table 3.Coefficients for second order multivariate regression

Coefficients	Value
A	7.92
α_1	-2.77
α_2	-2.69
α_3	-9.41
α_4	0.529
α_5	-5.19
α_6	10.0
α_7	6.21
α_8	0.67
α_9	3.50

Using the quadratic regression model described above, detected crack length for various specimen can be obtained. The measurement and model prediction of specimen T6 and T7 are shown in figure 10.

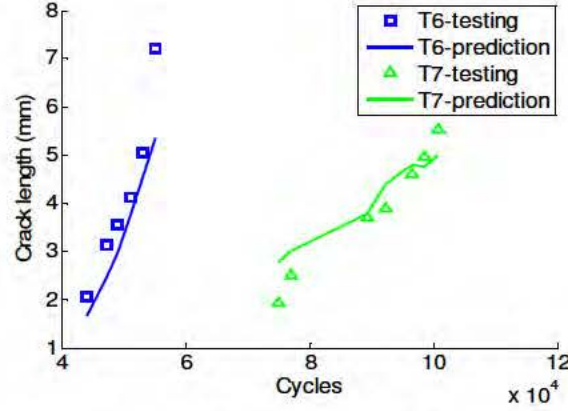


Figure 10.Measurement and detection model prediction using Quadratic regression model

3.4.3. Gaussian Regression model

Gaussian process regression is a generalization of the Gaussian probability distribution [39]. Random variables, such as scalars or vectors (for multivariate distributions) are considered using a probability distribution. Given a dataset $D = \{X_1, X_2, \dots, X_k | X_i \in R^D\}$ and $y = \{y_1, y_2, \dots, y_k\}$, the system measurement y can always be considered as a sample from a multivariate Gaussian distribution. The Gaussian process can be specified by its mean function and the covariance function as

$$m(X) = E(f(X)) \quad (26)$$

$$k(X, X') = E[(f(X) - m(X))(f(X') - m(X'))] \quad (27)$$

With an appropriate choice of mean function, covariance function, the function $y = g(x)$ can be defined as $g(x) \sim GP(m(x), k(x, x'))$. In comparison with several mean and covariance functions, the mean function and covariance function are chosen as

$$m(X) = ([\gamma_1 \ \gamma_2 \ \dots \ \gamma_D]X + \gamma_0)^2 \quad (28)$$

$$k(X, X') = \sigma_f^2 f_d(r_d) \exp(-r_d) \quad (29)$$

$$r_d = \sqrt{\frac{d}{l^2} (X - X')^T (X - X')}$$

where $\gamma_0 \cdots \gamma_D$, σ_f , l are parameters need to be tuned to maximize the likelihood function. The detailed discussion of its application can be found in [39]. Since the signal feature space is in dimension 3 (Correlations coefficient, Phase change, and Amplitude), function $f_d(t)$ is chosen as $f_3(t) = 1 + t$. Following the previous procedure, this model is trained using datasets for (T1, T2, T3, T4, and T5), the datasets for T6 and T7 are used as validation. The results are shown in figure 11.

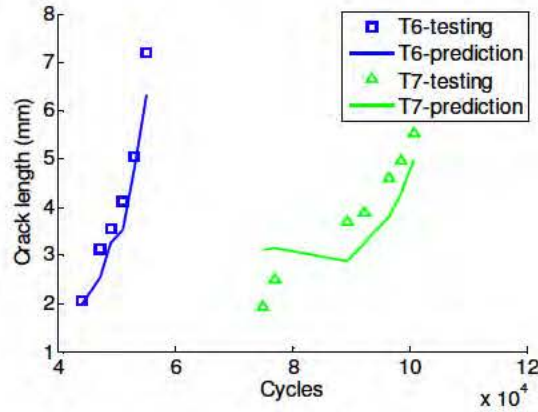


Figure 11.Measurement and detection model prediction for specimens using GP regression model

Based on the above discussion of detection models, the relevant measures of goodness of fit statistics can be obtained, which are given as

Table 3.Comparison of regression statistic for different regression models

	R square	Standard error
Linear regression model	0.909010	0.681268

	R square	Standard error
Quadratic regression model	0.961062	0.508134
Gaussian Regression model	NA	0.611133

By comparing the above three detection models, the Quadratic regression model gives the smallest standard error and the largest R square value. In the following section, the corresponding model detection results are used in the Bayesian updating and the prognosis sensitivity respect to measurement noise is discussed.

4. Lap joint fatigue damage prognosis using Bayesian updating

4.1. Constant Loading Case

Based on the prognostic method discussed before, the detected crack length from the above Quadratic model is used to update the model parameters, and then predict the remaining useful fatigue life (RUL). To validate the prognosis result, the optically measured crack length is considered as the ground truth . Figure 12 shows the prior belief and figure 13 shows the updated results from the proposed prognosis method. Blue solid line is the median prediction using the prior distribution. Hollow rectangular points are the optically measured crack length and are considered as the true crack length. Black solid points are the crack estimation from the Lamb wave-based damage detection method.

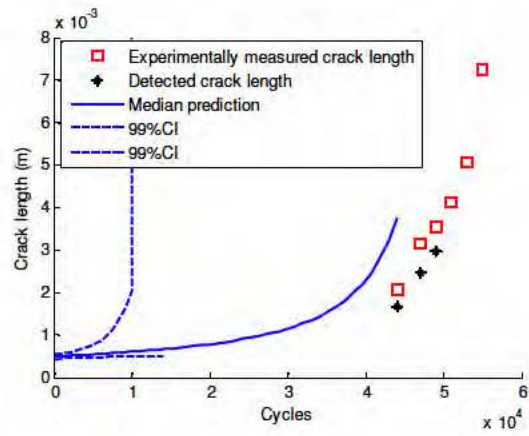
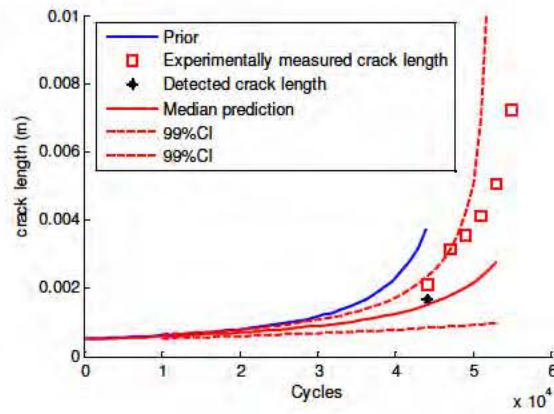
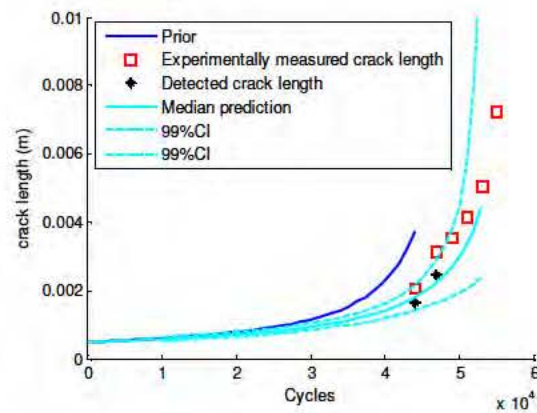


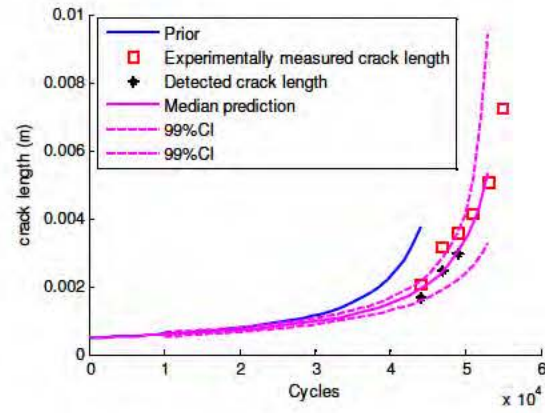
Figure 12. Prior belief and dataset for T6



a.



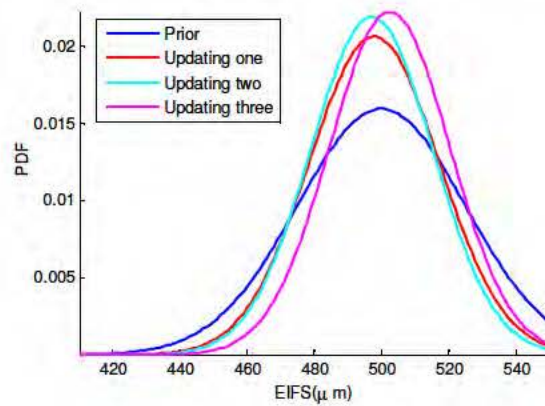
b.



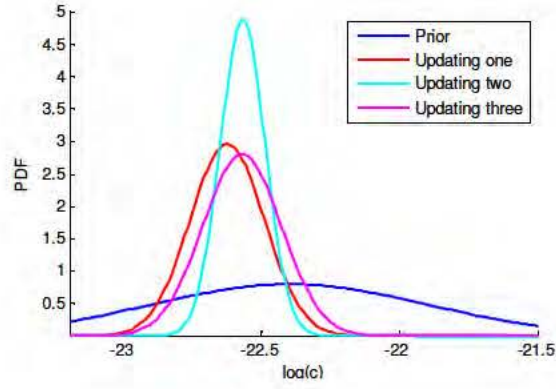
c.

Figure 13. Bayesian updating result. a), Updating one. b), Updating two. c), Updating three.

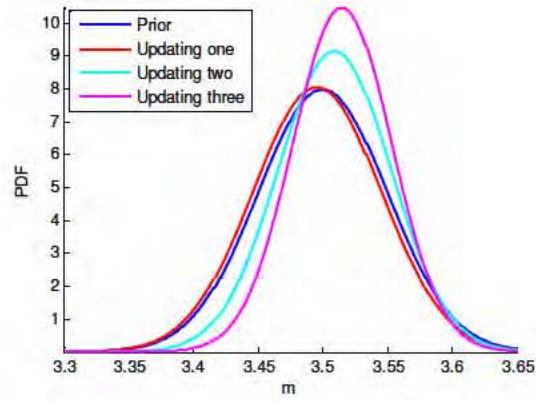
From figure 13, it can also be seen that the median prediction trend gets closer to the testing dataset with additional updating using detection data. The uncertainty bounds become narrower with additional updating, which indicates the effectiveness of the Bayesian updating method in reducing prognostic uncertainties. This trend can also be observed in the updated parameter distribution, shown in figure 14.



a.



b.



c.

Figure 14.Parameter updating result. a), Updated EIFS. b), Updated $\log(c)$. c),

Updated m

4.2. Variable Loading Case

Following the same procedure as described in Section 4.1., the prognosis is carried out for variable amplitude loading case. The detected crack length from the Quadratic regression model is used as the updating dataset. Figure 15 shows the prior belief and two sets of data (i.e., crack length measurement from optical microscope

and those from Lamb wave detection). Figure 15 shows the updated results using the proposed prognosis method.

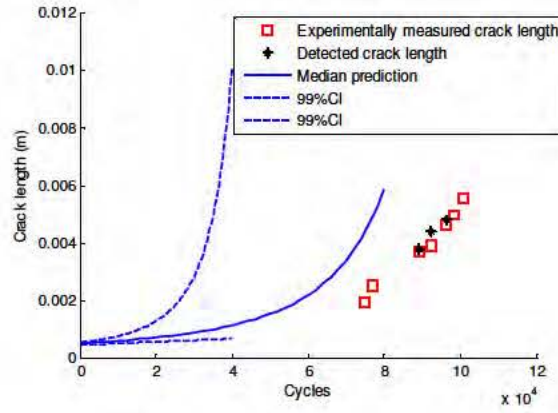
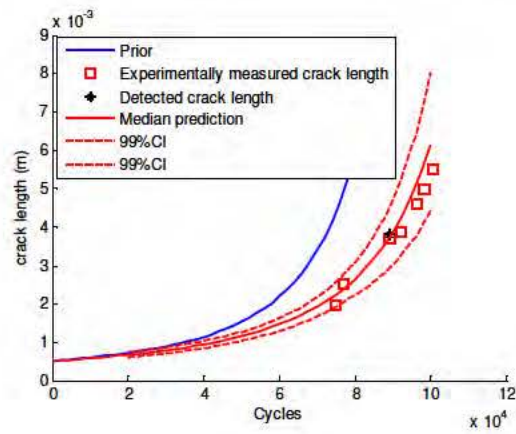
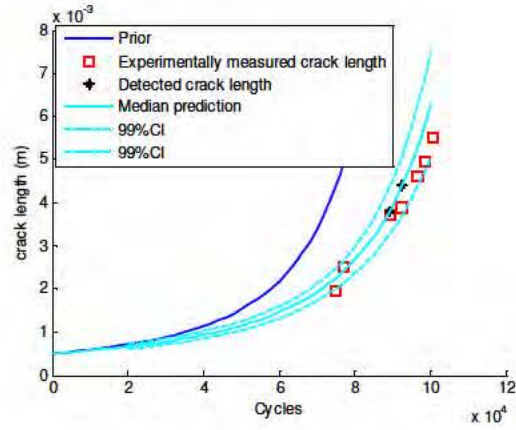


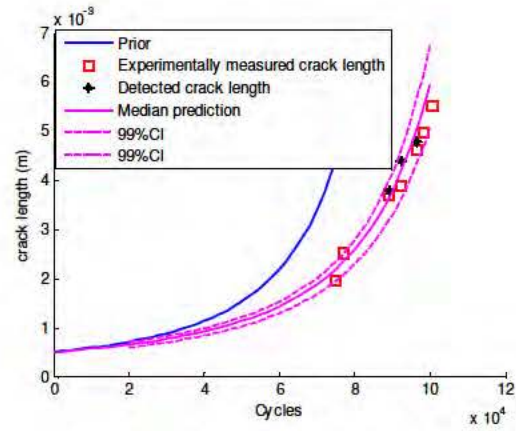
Figure 15. Prior belief and dataset for T7



a.



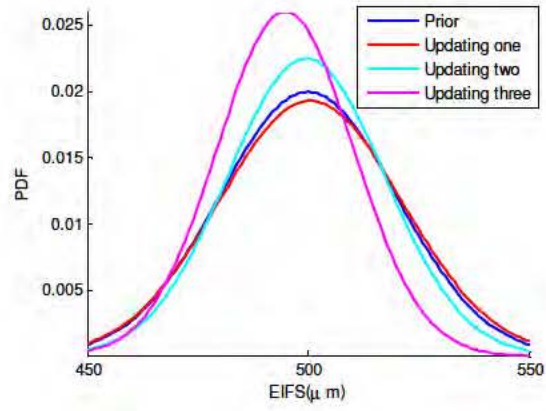
b.



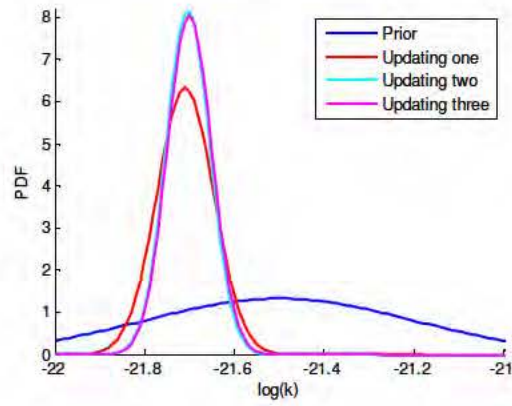
c.

Figure 16. Bayesian updating results with. a), Updating one. b), Updating two. c), Updating three.

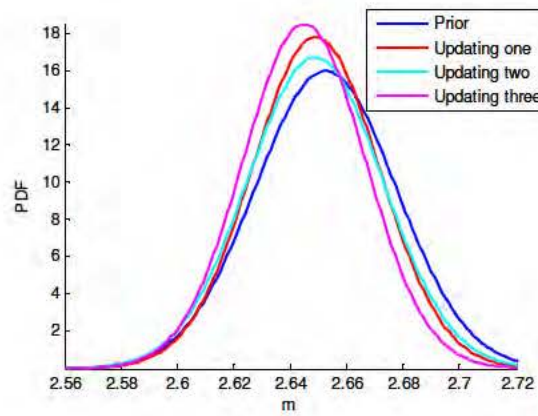
From the above figures, a similar trend can be observed for the updated crack growth trajectory as well as for the constant amplitude loading case. The 99% confidence bound is reduced when additional updating is performed. Figure 17 shows the updated parameters distribution. The distribution of the updated parameters converges as more detected data is used in the Bayesian updating.



a.



b.



c.

Figure 17.Parameter updating result. a), Updated EIFS. b), Updated $\log(k)$. c),

Updated m

5. Prognostic Performance Evaluation and sensitivity analysis

To evaluate the performance of the prognostic model, prognostic metrics are employed. A detailed discussion of metrics-based model validation can be found in [40]. Several relevant metrics, such as Prognostic Horizon (PH), $\alpha - \lambda$ Accuracy, Relative Accuracy (RA), Cumulative Relative Accuracy (CRA), and Convergence are discussed in that publication. In this paper, Prognostic Horizon is used to assess prognostic algorithms performance. The Prognostic Horizon describes the length of time before end-of-life (EoL) when a prognostic algorithm starts predicting with desired accuracy limits. The limit is expressed using an α -bound given by $\pm\alpha \cdot t_{\text{EoF}}$. In contrast, $\alpha - \lambda$ Accuracy determines whether prediction accuracy is within desired accuracy levels (specified by α) at a given time. The smaller α means the higher desired accuracy. The red dot represents the time when the Bayesian updating is applied. The prognosis performance validation for constant loading case and variable loading case is shown below.

- Constant loading prediction performance assessment

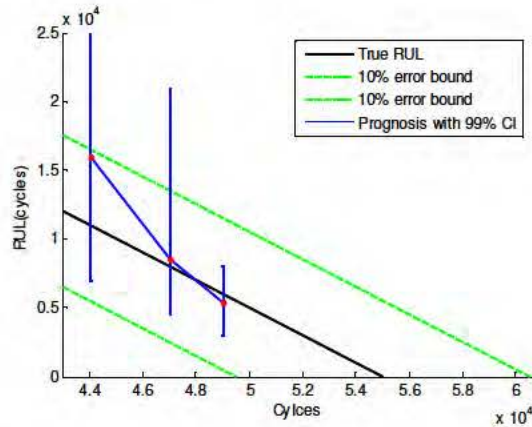


Figure 18.Prognostic performance validation for constant loading

Figure 18 shows that the excellent median prediction is obtained after each updating. The 99% RUL prediction interval enters the 10% error bound at the third updating, so the proposed prognostic method can provide a satisfactory prediction of RUL.

- Variable loading prediction performance assessment

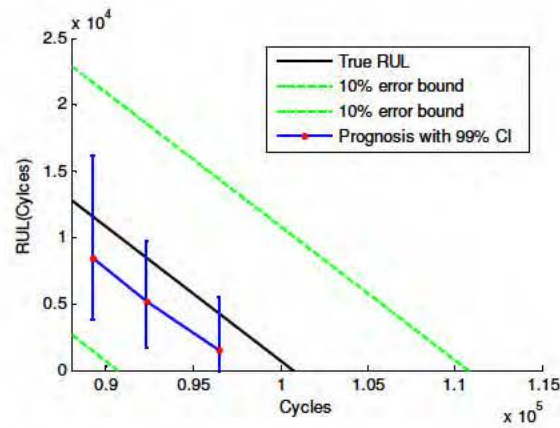


Figure 19.Prognostic performance validation for variable loading

From figure 19, the same trend can be observed. The 99% RUL interval prediction enters the 10% error bound after each updating. With additional updating, the confidence bound is reduced as given more information. Therefore, the updating result can provide an informative RUL prediction at earlier stage of the whole lifecycle.

6. Conclusion

In this paper, an integrated fatigue damage diagnostics and prognostics methodology is proposed, which combines a piezoelectric sensor network-based damage detection method, physics-based fatigue crack propagation model, and a

Bayesian updating framework. The proposed method is demonstrated and validated using fuselage lap joints test datasets. Finally, the model predictions are evaluated using prognostic metrics quantitatively. Based on the results obtained, several conclusions can be drawn:

1. By properly interpreting the features changes of the received signal, the proposed diagnostic model provides a reasonable estimate of the crack length in lap joints.
2. The accuracy of crack length prediction is different for different detection models. Based on the comparison of the regression statistics, the Quadratic regression model shows a better result in the current study.
3. Bayesian updating can represent and manage the uncertainties introduced by model parameters and detection model. Additional measurements can greatly reduce prognostic uncertainties.

The current work focused on the damage size estimation for a known damage location identified based on hot spot identification (and consequent sensor placement). Further efforts are required to provide capability for more general crack location methods and to extend the proposed methodology to other structural components. Last but not the least, this work assumed presence of a single major crack for predictions. Further studies are required to consider multiple site cracks and their interactions.

Reference

1. Dempster, A., *A generation of Bayesian inference*. Classic Works of the Dempster Shafer Theory of Belief Functions, 2008: p. 73-104.

2. Box, G. and G. Tiao, *Bayesian inference in statistical analysis*. Wiley New Work, 1992.
3. Gilboa, I. and D. Schmeidler, *Updating ambiguous beliefs*. Morgan Kaufmann Publishers Inc, 1992: p. 143-162.
4. Chong, K.P., *Health monitoring of Civil structures* J. Intell. Mater. Syst. Struct, 1999. **9**(11): p. 892-898.
5. Masri, S.F., et al., *Application of a web-enabled real-time structural health monitoring system for civil infrastructure systems*. Smart MATER. STRUCT., 2004. **13**(6): p. 1269-1283.
6. Koruk, M., & Kilic, M., *The usage of IR thermography for the temprature measurements inside an automobile cabin*. International Communication in Heat and Mass Tansfer, 2009. **36**(872-877).
7. Kazys, R. and L. Svilainis, *Ultrasonic detection and characterization of delaminations in thin composite plates using signal processing technique*. Ultrasonics, 1997. **35**: p. 367-383.
8. Nicoletto, G., G. Anzelotti, and R. Konecn, *X-ray computed tomography vs. metallography for pore sizing and fatigue of cast Al-alloys*. Pocedia Engineering, **2**: p. 547-554.
9. Giurgiutiu, V., *Lamb wave generation with piezoelectric wafer active sensors for structural health monitoring*. Smart Structures and Materials 2003. **5056**: p. 111-122.

10. Giurgiutiu, V., *Tuned Lamb wave excitation and detection with piezoelectric wafer active sensors for structural health monitoring*. Journal of Intelligent Material Systems and Structures, 2005. **16**(4): p. 291.
11. Santoni, G.B., L. Yu, and B. Xu, *Lamb wave-mode tuning of piezoelectric wafer active sensors for structural health monitoring*. Journal of Vibration and Acoustics, 2007. **129**: p. 752.
12. Lemistre, M. and D. Balageas, *Structural health monitoring system based on diffracted Lamb wave analysis by multiresolution processing*. Smart materials and structures, 2001. **10**: p. 504.
13. Monkhouse, R., P. Wilcox, and P. Cawley, *Flexible interdigital PVDF transducers for the generation of Lamb waves in structures*. Ultrasonics, 1997. **35**(7): p. 489-498.
14. Ward, M.D. and D.A. Buttry, *In situ interfacial mass detection with piezoelectric transducers*. Science, 1990. **249**(4972): p. 1000.
15. Giurgiutiu, V., A. Zagrai, and J.J. Bao, *Piezoelectric wafer embedded active sensors for aging aircraft structural health monitoring*. Structural Health Monitoring, 2002. **1**(1): p. 41-61.
16. Constantin, N., S. Sorohan, and M. Gavan, *Efficient and low cost PZT network for detection and localization of damage in low curvature panels*. Journal of Theoretical and Applied Mechanics, 2011. **49**(3): p. 685-704.

17. Ihn, J.-B. and F.-K. Chang, *Detection and monitoring of hidden fatigue crack growth using a built-in piezoelectric sensor/actuator network: I. Diagnostics*. Smart Mater. Struct. , 2004. **13**: p. 609-620.
18. JR, C.H.K. and F.-K. Chang, *Identifying delamination in composite beams using built-in piezoelectrics*. J. Intell. Mater. Syst. Struct, 1993. **6**: p. 649-72.
19. Paris, P. and F. Erdogan, *A critical analysis of crack propagation laws*. Journal of Basic Engineering, Transactions of the American Society of Mechanical Engineers, 1963: p. 528-534.
20. Laird, C., *Mechanisms and theories of fatigue*. Fatigue Microstruct., 1979: p. 149-203.
21. Forman, R., *Numerical analysis of crack propagation in cyclic-loaded structures*. J Basic Eng 1967. **89**: p. 459-64.
22. Kitagawa, H. and S. Takahashi, *Applicability of fracture mechanics to very small cracks or cracks in the early stage*. ASM. In: Proceedings of the second international conference on mechanical behaviour of materials, 1979: p. 627-31.
23. Ritchie, R. and J. Lank, *Small fatigue cracks: a statement of the problem and potential solutions*. Mater. Sci. Eng., 1996. **84**: p. 11-6.
24. Elber, W., *Fatigue crack closure under cyclic tension*. Eng. Fract. Mech., 1970. **21**: p. 37-45.

25. Lu, Z. and Y. Liu, *Small time scale fatigue crack growth analysis*. International Journal of Fatigue, 2010. **32**(8): p. 1306-1321.
26. Press, S., *Subjective and objective Bayesian statistics: principles, models, and applications*. Wiley-Interscience, Hoboken, NJ, 2003.
27. Caticha, A. and A. Giffin, *Updating probabilities. Bayesian Inference and Maximum Entropy Methods in Science and Engineering*. AIP Conf. Proc, 2006. **31**: p. 872.
28. Adam, M.T., *G104-A2L Guide for estimation of measurement uncertainty in testing*. American Association of Laboratory Accreditation Manual, 2002: p. 10-18.
29. Bell, S., *A Beginner's Guide to Uncertainty of Measurement*. The National Physical Laboratory, 2001. **2**: p. 9-16.
30. Dowling, N.E., *Mechanical behavior of materials : engineering methods for deformation, fracture and fatigue*. 3rd ed2007, Upper Saddle River, NJ,London: Pearson Prentice Hall ;Pearson Education. xvii, 912 p.
31. NASA, *Fatigue crack growth computer program NASGRO Version 3.0-Reference manual*. JSC-22267B, NASA, Lyndon B. Johnson Space Center, Texas, 2000.
32. Liu, Y. and S. Mahadevan, *Probabilistic fatigue life prediction using an equivalent initial flaw size distribution*. International Journal of Fatigue, 2009. **31**(3): p. 476-687.

33. El, H.M., T. Topper, and K. Smith, *Prediction of nonpropagating cracks*. Eng. Fract. Mech., 1979. **11**: p. 573-84.
34. hijazi, A.L., B.L. Smith, and T.E. Lacy, *Linkup strength of 2024-T3 bolted lap joint panels with multiple-site damage*. Journal of Aircraft, 2004. **41**(2): p. 359-364.
35. Raghavan, A. and C.E.S. Cesnik, *Review of guided-wave structural health monitoring*. Shock and Vibration Digest, 2007. **39**(2): p. 91-116.
36. Zhao, X., et al., *Active health monitoring of an aircraft wing with embedded piezoelctric sensor/actuator network:I.Defect detection, localization and growth monitoring* Smart MATER. STRUCT., 2007. **16**(1208-17).
37. Wang, Q. and S. Yuan, *Baeline-free imaging method based on new pzt sensor arrangements*. Journal of Intelligent Material Systems and Structures, 2009. **20**(1663-1673).
38. SU, Z. and L. Ye, *Identification of damage using Lamb waves*. Springer, 2009. **LNACM 48**: p. 195-254.
39. Rasmussen, C.E. and C.K.I. Williams, *Gaussian Process for Machine Learning*. The MIT press, 2006.
40. Saxena, A., et al., *Metrics for evaluating performance of prognostic techniques*. In Aerospace conference, 2009 IEEE, 2008: p. 1-13.